# ABSTRACT

**Development of Enzymatic $H_2$ production and $CO_2$ Reduction Systems**

*Thomas W. Woolerton, Christ Church*

*A Thesis submitted for the degree of D. Phil, Trinity Term 2012*

One of today's most pressing scientific challenges is the conception, development and deployment of renewable energy technologies that will meet the demands of a rapidly increasing population. The motivation is not only dwindling fossil fuel reserves, but also the necessary curtailment of emissions of the greenhouse gas carbon dioxide (a product of burning fossil fuels). The sun provides a vast amount of energy (120,000 TW globally), and one major challenge is the conversion of a fraction of this energy into chemical energy, thereby allowing it to be *stored*. Dihydrogen ($H_2$) that is produced from water is an attractive candidate to store solar energy (a 'solar fuel'), as are high energy carbon-containing molecules (such as CO) that are formed directly from carbon dioxide.

One key aspect is the development of *catalysts* that are able to offer high rates and efficiencies. In biology, some microbes acquire energy from the metabolism of $H_2$ and CO. The biological catalysts - enzymes - that are responsible are hydrogenases (for the oxidation of $H_2$ to protons); and carbon monoxide dehydrogenases (CODHs, for the oxidation of CO to $CO_2$). These redox enzymes, containing nickel and iron as the only metals, are extraordinary in terms of their catalytic characteristics: many are fully reversible catalysts and offer very high turnover frequencies (thousands per second are common), with only tiny energy input requirements.

This Thesis uses a hydrogenase from the bacterium *Escherichia coli*, and two CODHs from the bacterium *Carboxydothermus hydrogenoformans*, as the catalysts in $H_2$ production and $CO_2$ reduction systems. Chapter 3 describes the concept and development not of a solar fuel system, but of a device that catalyses the water-gas shift reaction (the reaction between CO and water to form $H_2$ and $CO_2$) - a process of major industrial importance for the production of high purity $H_2$. Chapters 4, 5 and 6 detail photochemical $CO_2$ reduction systems that are driven by visible light. These systems, operating under mild, aqueous conditions, involve CODHs attached either to $TiO_2$ nanoparticles that are sensitised to visible light by the co-attachment of a ruthenium-based dye complex, or to cadmium sulfide nanomaterials that, having a narrow band gap, are inherently photoexcitable by visible light.

The motivation here is not the construction of technological devices; indeed, the enzymes that are used are fragile, highly sensitive to oxygen, and impossible to scale to industrial levels. Rather, the drivers are those of scientific curiosity (can the incorporation of these remarkable biological catalysts enable the creation of outstanding solar fuel devices?), and of producing systems that serve as benchmarks and inspiration for the development of fully synthetic systems that are robust and scalable.

# ACKNOWLEDGEMENTS

Thanks must firstly go to Fraser, for offering me a place in his research group, and for continued support and encouragement throughout my D. Phil. I am truly grateful for having had the opportunity to work in his group; it has provided an incredibly rich education, and I have gained so much more than a scientific training. I am also indebted to Dr Kylie Vincent, whose supervision in the year of my Master's project played a large part in my decision to pursue a D. Phil.

Thanks to all of the members of the Armstrong Group who I have had the joy of working with over the past few years, both for discussions and help in the lab, and also for making the third floor of the ICL such a brilliant place to be. In particular, thanks to Alison, Gopan, Vincent, Philip, Bonnie, Edgar, Suzannah, Maxie, Sally, Carina, Andreas, Oli, Greg and Elena. Special thanks to Annemarie, who provided so much support, to Holly, for major MS Word-based help, and to Yatendra, with whom I have been so lucky to work closely with for the last year.

Thanks to my Part II students, Oliver Lazarus and Sally Sheard, for all their hard work. I learnt so much from the experience of supervising your projects. Thanks for putting up with me!

I am also grateful to the support staff in the ICL who made my work possible and came to my rescue many times with fixing broken equipment: Paul and Nenad in electronics, Ashleigh, Terri the glassblower, and Pam and the team in the office. Thanks also to Christ Church, the EPSRC, and the Dowager Countess Eleanor Peel Trust Fund for financial support.

Finally, huge thanks to my friends and family, without whose support this D. Phil would never have been possible.

# COLLABORATIONS

The protein samples used in this Thesis were kindly donated by collaborators. *Eschericia coli* hydrogenase 2 was supplied by Dr Michael Lukey (Armstrong Group, University of Oxford); *Carboxydothermus hydrogenoformans* carbon monoxide dehydrogenase I and II were supplied by Elizabeth Pierce (Ragsdale Group, University of Michigan).

Some of the experiments in section 3.5.2 were performed by Oliver Lazarus under my supervision, and some of the experiments in sections 4.2.6.3, 5.2.3.1, 5.2.4.2, 5.2.5, 5.3.1.2 and 6.3.2 were performed by Sally Sheard, also under my supervision.

The electron microscopy in sections 4.2.2.1 and 6.4.1 was carried out by Dr Jamie Warner (Department of Materials, University of Oxford), and that in Appendix A5 was carried out by Dr Robert Gilbert (Division of Structural Biology, University of Oxford),

The cadmium sulfide nanomaterials in section 6.4.1 were synthesised by Dr Yatendra Chaudhary (Armstrong Group, University of Oxford).

# PUBLICATIONS

1. *How light-harvesting semiconductors can direct the electrochemical bias of attached enzymes in favour of $H_2$ production and $CO_2$ reduction*. Yatendra S. Chaudhary, **Thomas W. Woolerton**, Juan C. Fontecilla-Camps, Stephen W. Ragsdale and Fraser A. Armstrong, *Submitted*, **2012**.
2. *Enzyme and bio-inspired electrocatalysts in solar fuel devices*. **Thomas W. Woolerton**, Sally Sheard, Elizabeth Pierce, Stephen W. Ragsdale and Fraser A. Armstrong, *Energy Environ. Sci.*, **2012**, *5*, 7470-7490.
3. *Visible light-driven $CO_2$ reduction by enzyme coupled CdS nanocrystals*. Yatendra S. Chaudhary, **Thomas W. Woolerton**, Christopher S. Allen, Jamie H. Warner, , Elizabeth Pierce, Stephen W. Ragsdale and Fraser A. Armstrong, *Chem. Commun.*, **2012**, *48*, 58-60.
4. *$CO_2$ photoreduction at enzyme-modified metal oxide nanoparticles*. **Thomas W. Woolerton**, Sally Sheard, Elizabeth Pierce, Stephen W. Ragsdale and Fraser A. Armstrong, *Energy Environ. Sci.*, **2011**, *4*, 2393-2399.
5. *Efficient and clean photoreduction of $CO_2$ to CO by enzyme-modified $TiO_2$ nanoparticles using visible light*. **Thomas W. Woolerton**, Sally Sheard, Erwin Reisner, Elizabeth Pierce, Stephen W. Ragsdale and Fraser A. Armstrong, *J. Am. Chem. Soc.*, **2010**, *132*, 2132-2133.
6. *Water-gas shift reaction catalyzed by redox enzymes on conducting graphite platelets*. Oliver Lazarus, **Thomas W. Woolerton**, Alison Parkin, Michael J. Lukey, Erwin Reisner, Javier Seravalli, Elizabeth Pierce, Stephen W. Ragsdale, Frank Sargent, and Fraser A. Armstrong, *J. Am. Chem. Soc.*, **2009**, *131*, 14154-14155.
7. *Oxidation of dilute $H_2$ and $H_2/O_2$ mixtures by hydrogenases and Pt*. **Thomas W. Woolerton**, Kylie A. Vincent, *Electrochimica Acta*, **2009**, *54*, 5011-5017.

# SYMBOLS & ABBREVIATIONS

| | |
|---|---|
| Å | angstrom = $10^{-10}$ m |
| A | Ampere |
| *A* | surface area of an electrode *or* absorption (according to context) |
| atm. | atmosphere |
| ATP | adenosine triphosphate |
| *c* | speed of light = 3.0 x $10^{8}$ $ms^{-1}$ |
| CB | conduction band |
| *Ch* | *Carboxydothermus hydrogenoformans* |
| CODH | carbon monoxide dehydrogenase |
| Cys | cysteine |
| Da | Dalton |
| DFT | density functional theory |
| *Dg* | *Desulfovibrio gigas* |
| DSSC | dye-sensitised solar cell |
| *E* | electrode potential |
| $e^-$ | electron |
| $E_a$ | activation energy |
| *Ec* | *Escherichia coli* |
| *Ec*Hyd2 | *Escherichia coli* hydrogenase 2 |
| $E_{eq}$ | equilibrium (zero current) potential |
| EM | electron microscopy |
| EPR | electron paramagnetic resonance |
| $E^o$ | standard reduction potential |
| *F* | Faraday's constant = 96,485 C $mol^{-1}$ |
| FNR | ferredoxin-NADP-oxidoreductase |
| g | gram *or* the gravitational constant (according to context) |
| GC | gas chromatography *or* gas chromatograph (according to context) |
| HTS | high temperature shift |
| *H* | enthalpy |
| *h* | Planck's constant = 6.626 × $10^{-34}$ J s |
| h | hour |
| *i* | current |
| ITO | indium tin oxide |
| IUPAC | International Union of Pure and Applied Chemistry |
| *j* | flux |
| K | Kelvin |
| k | kilo |
| *k* | rate constant |
| $k_B$ | the Boltzmann constant = 1.38 × $10^{-23}$ J $K^{-1}$ |
| $K_h$ | hydration constant |
| $K_M$ | Michaelis constant |
| L | litre |

| | |
|---|---|
| LTS | low temperature shift |
| m | milli or metre (according to context) |
| M | mol $dm^{-3}$ |
| min | minute |
| MLCT | metal-to-ligand charge transfer |
| mol | mole |
| *Mt* | *Moorella thermoacetica* |
| n | nano |
| *n* | number of electrons |
| $NAD^+$/NADH | nicotinamide adenine dinucleotide (oxidised/reduced) |
| $NADP^+$/NADPH | nicotinamide adenine dinucleotide phosphate (oxidised/reduced) |
| NMR | nuclear magnetic resonance |
| OEC | oxygen-evolving complex |
| PFE | protein film electrochemistry |
| PG | pyrolytic graphite |
| PGE | pyrolytic graphite edge-plane |
| ppm | parts per million |
| *Q* | reaction quotient |
| *R* | the gas constant = 8.314 J $K^{-1}$ $mol^{-1}$ |
| RDE | rotating disk electrode |
| rpm | revolutions per minute |
| *Rr* | *Rhodospirillum rubrum* |
| *S* | entropy |
| s | second |
| SCE | saturated calomel electrode |
| SEM | scanning electron microscopy |
| SHE | standard hydrogen electrode |
| *T* | temperature |
| TEM | transmission electron microscopy |
| TOF | turnover frequency |
| TON | turnover number |
| *v* | frequency |
| V | volt |
| VB | valence band |
| *vs.* | *versus* |
| W | watt |
| WGS | water-gas shift |
| w/v | weight/volume |
| $\Gamma$ | electroactive coverage |
| $\Delta G^{\neq}$ | free energy of activation |
| Ω | ohm |
| ºC | degree Celsius |

# TABLE OF CONTENTS

# 1 INTRODUCTION

## 1.1 SUSTAINABLE ENERGY, THE SOLAR OPPORTUNITY, AND EXISTING SOLAR TECHNOLOGIES

The combination of rapidly increasing human population and economic growth means that energy supply is undoubtedly one of the most important global issues of the 21st century. Compared to 2001 levels, global demand for energy is predicted to double by 2050 and more than triple by 2100.[1] This increasing energy requirement coincides with the depletion of coal, oil and natural gas ('fossil fuels,' today's primary energy sources), and so there is now a global drive to develop technologies to harness alternative forms of energy. Growing concern over the environmental impact of carbon dioxide emissions (a result, of course, of burning the aforementioned fossil fuels) necessitates that energy solutions must also be *clean*; that is, they should not lead to further environmental damage.

By far, the largest renewable energy source is sunlight. The rate of energy supply to the Earth's surface from the sun is 120,000 TW, far exceeding today's global human power requirement (~16 TW in 2009),[2] and almost certainly sufficient to meet the imaginable needs of any future generations. The potential of solar is often highlighted by two fashionable statistics: at today's 16 TW requirement, the amount of solar energy striking the Earth's surface in *one hour* is almost enough to satisfy the energy demand for a *whole year*; and using 1% of the Earth's surface to convert solar energy with 10% efficiency would easily satisfy demand for at least the next 50 years.[3] In contrast, no other single renewable source is large enough to have major impact, even if implemented aggressively: it is estimated that harnessing wind energy can provide ~ 2-4 TW, tidal energy less than 2 TW, and geothermal < 3 TW.[3] Energy conversion of sunlight into biomass, taking advantage of photosynthesis in plants, has been exploited by humans for millennia but is not a realistic solution today

because of the competition for land space with food crops.[4] Even using fast-growing plants such as switchgrass would require the use of 10% of the Earth's land, corresponding to almost all of the remaining cultivable land not currently used for growing food crops.[3] Of course, this is not to suggest that renewables other than solar are not worth pursuing – wind, tidal, geothermal and others are likely to be important components in the global 'energy mix' in at least the medium term future. This is especially true when the resources available to specific countries are considered; for example, Iceland takes advantage of its geothermal resources,[5] and wind turbines in Denmark provided 26% of grid electricity in 2010.[6] However, it is reasonable to propose that the single natural resource having the greatest potential to meet a terawatt-scale demand is solar.

To date, most efforts to harness solar energy have been through the development of technologies for the conversion of photons to electricity using photovoltaic (PV) cells. The light absorbing component of the majority of commercial cells is silicon, and in most cases electricity is generated on a 'microgeneration' scale to power residential homes and other buildings.[7,8] This technology is reasonably mature: Si cells were developed in the 1980s and the best research cells now have efficiencies of around 20%,[9] although commercial modules are considerably lower. The global photovoltaic industry is substantial and growing rapidly; it was worth $US 91.6 billion in 2011 and this figure is predicted to rise to $US 130 billion by 2021.[10] In 2010, the total worldwide capacity of installed units was 23 GW,[11] and although this corresponds to less than 0.2% of the global power requirement there is also potential for growth through the emergence of different kinds of PV technologies that are not Si-based. 'Third-generation' PV cells (known as dye sensitised solar cells (DSSCs), or Grätzel cells) use mesoporous thin films of wide band gap metal oxide nanoparticles that are

sensitised to visible light by the attachment of transition metal-based complexes (dyes).[12-14] The working principle of these cells will be discussed later (section 1.6.2), as it is relevant to much of the research detailed in this Thesis. A third class of photovoltaics is organic photovoltaic cells, which use polymeric organic semiconductors (compounds that contain delocalised π electron systems).[15-17] These materials have very high absorption coefficients (> 100 $cm^{-1}$),[18] but the cells currently suffer from poor stabilities towards $O_2$ and water and therefore have lifetimes of less than a year. Both DSSCs and organic photovoltaic cells are the focus of intensive ongoing research because the efficiencies are still relatively low (maximum research cell efficiencies are 11.4% and 10.1%, respectively).[9] Nevertheless, they share a common advantage over silicon photovoltaics in terms of manufacturing costs because existing, high through-put techniques developed in the printing industry can be adapted for their large-scale production.

## 1.2 ENERGY STORAGE AND 'SOLAR FUELS'

The diurnal cycle and the seasonal and geographic variations in sunlight lead to a complexity associated with solar energy. Although photovoltaics are well suited to many situations, the energy requirements of humans are largely incompatible with the variations in solar flux, and as a result there is an unquestionable need to convert solar energy to *fuels*[*] that can be stored and transported, ideally using existing infrastructure. Figure 1A shows a breakdown of the final forms of energy (worldwide) at the point of use. Electricity accounts for less than one fifth of consumption, and the remaining sections are all *stored* forms of energy (fuels). The

[*] Technically, the term 'fuel' is not wholly accurate here (a fuel must exist as a substance in the Earth that is mineable, or be directly obtainable from a mineable resource). However, the term is now established in the field of artificial photosynthesis as an acceptable description of energy carriers such as $H_2$, and it is used throughout this Thesis in this sense.

majority of the stored forms are fossil fuels: oil (41.3%, used mainly for transport), natural gas (15.2%, used mainly for heating and cooking), and coal/peat (10.0%, mainly heating). Batteries offer one solution, allowing electrical energy to be stored and released when required. Although batteries are superb in certain applications – specifically, those that have low power requirements or in portable devices - their energy densities are very low compared to chemical fuels (Figure 1B).

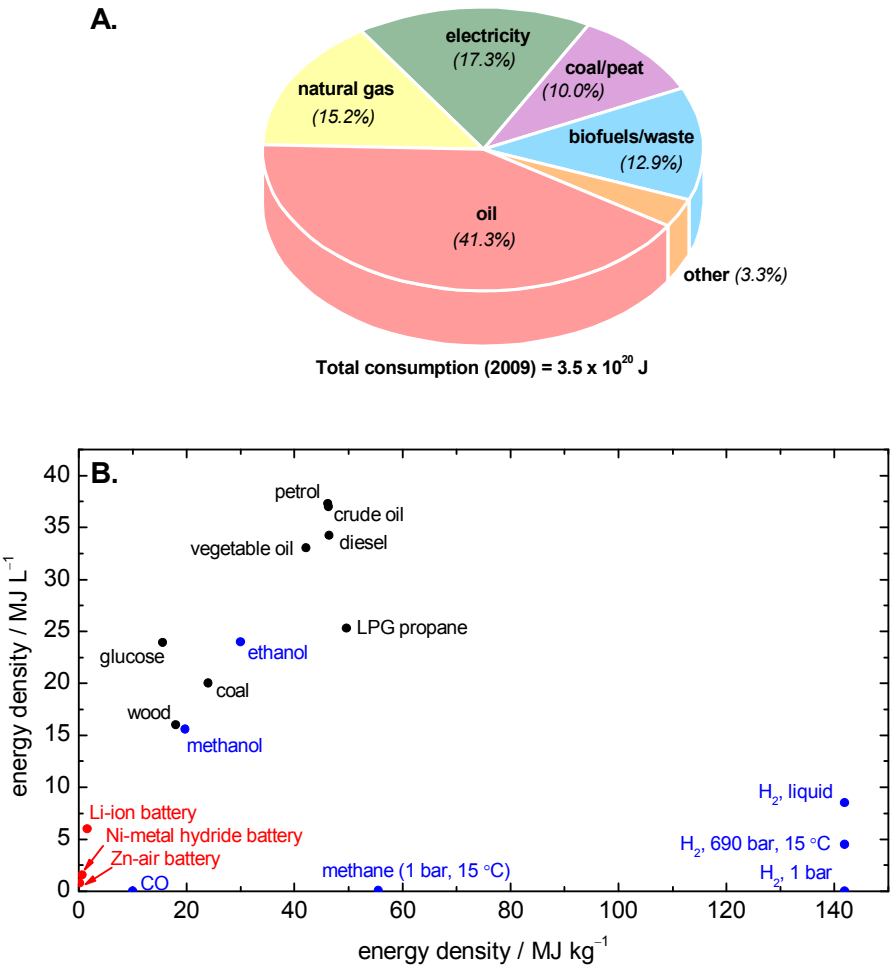


**Figure 1 The requirement for fuels.** (A) Breakdown of worldwide final forms of energy consumption in 2009. 'Other' includes geothermal, wind and solar. Data from International Energy Agency - Key World Energy Statistics, 2011.[2] (B) Energy densities of selected fuels, and of batteries (red). Highlighted in blue are common targets from feedstocks of $CO_2$ and/or water (see later).

Despite the low energy densities, battery-powered vehicles (mainly cars) are now widely available, although their market-share remains low. One of the key reasons for this – resulting from the inadequacy of the batteries - is their low range (~ 100 miles),[19] and for this reason electric vehicles (EVs) are only really suited to city driving and short journeys. Also, while EVs do not emit pollutants or greenhouse gases at the point of use, they are only a clean technology if the electricity used to charge the battery is generated from renewable sources.[†] The superiority of today's most common vehicle fuels (petrol and diesel) is clear from their positions in the Figure 1B plot. High energy densities mean that the distances that can be travelled on a single tank of fuel are large, and, although 'peak oil' (the point in time at which the rate of extraction is at its maximum) is widely believed to have now passed,[20-22] oil has in recent history been abundant and readily available.

Highlighted in blue in Figure 1B are fuels that may, theoretically at least, be target synthetic products from $CO_2$ and/or water. These are ideal feedstocks for fuel production: water is a virtually limitless resource, and $CO_2$ is a product of fossil fuel combustion. Collection of water is trivial, but the capture of $CO_2$ - a gas, present in the atmosphere at a very low (albeit dangerously increasing) level - poses a significant challenge. An obvious strategy is to contain flue gas from conventional coal and gas-fired power stations,[23-25] and an alternative is to sequester and concentrate $CO_2$ from the atmosphere.[26,27] Assuming capturing technologies to be realisable, the conversion of $CO_2$ back to energy-rich fuels is a highly attractive prospect because it 'closes the loop' on this anthropogenic carbon cycle. Dihydrogen ($H_2$) has a very large energy density per unit mass, but in its gaseous form its energy density per

[†] Admittedly, electric engines perform at ~75% efficiency compared to ~20% for internal combustion engines, so even if the batteries are charged with electricity generated in a coal-fired power station, they still offer an advantage over conventional cars.

unit volume is poor, and even after compression to 690 bar the volumetric energy density does not exceed that of the best batteries. Liquefying $H_2$ (an energetically expensive process) provides a further improvement, but it still offers less than a third of the energy density of crude oil. The most desirable targets of the 'synthesisable' fuels are probably methanol or ethanol, because these are liquids under ambient conditions.

Figure 2 shows idealised, 'closed-loop' systems for the production and use of fuels prepared from $CO_2$ and/or water. The scheme is not a comprehensive representation of all available options; I have chosen to show the activation of $CO_2$ to CO (this reaction is a core focus of this Thesis) followed by further processing to liquid fuels, but equally viable is the direct reduction of $CO_2$ to methanol. One may reasonably argue that one-step production of methanol directly from $CO_2$ is a more attractive target, but CO also has major value as a chemical feedstock for many industrial processes (see section 1.3).

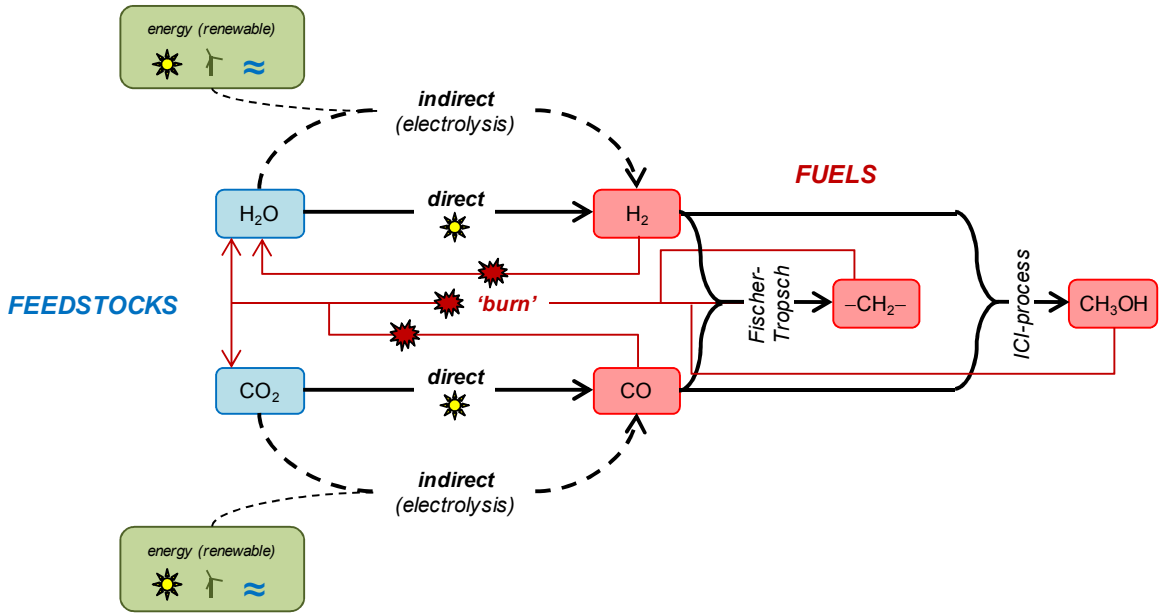


**Figure 2 Idealised, closed-loop systems for sustainable and clean cycling of fuels.** *Indirect* routes use clean electricity to electrochemically produce $H_2$ (from $H_2O$) or CO (from $CO_2$). These can then be used as fuels themselves ('burnt' in fuel cells), or converted into liquid fuels ('$-CH_2-$') by established Fisher-Tropsch processing. *Direct* routes bypass the requirement for electricity, and use solar energy to drive fuel production either by artificial photosynthetic processes (involving photoinduced charge separations in light-sensitive materials), or by solar-thermal processes.

The scheme shows that routes to fuels can proceed through two types of pathway. *Indirect* routes use electricity to electrochemically reduce $H_2O$ to $H_2$, or $CO_2$ to CO ($CO_2$ may also be converted to other reduction products, although these are not shown here). The electricity could be produced from sunlight at photovoltaic cells, or indeed could be generated from other renewable sources. The $H_2$ or CO can then be 'burned' in fuel cells, with the products ($H_2O$ or $CO_2$) theoretically being recycled in future fuel production. Alternatively, $H_2$ and CO can be combined through well established Fisher-Tropsch processes to make liquid fuels.[28] The latter is arguably more practical for the reasons of fuel density already discussed, and because fuel distribution and storage infrastructure already exists for liquid fuels. Again,

the products ($CO_2$ and $H_2O$) of burning these liquid fuels (represented as '$-CH_2-$' in Figure 2) can, in principle, be recycled. Another option is to convert CO into methanol by the $CuO/ZnO/Al_2O_3$-catalysed ICI-process.[29]

Alternative strategies are *direct* solar conversions to $H_2$ or CO. From a scientific standpoint this is a far more elegant objective than the previously outlined indirect approach, and a direct route has the opportunity to avoid the efficiency losses of multi-step processes. Direct conversion processes may be divided into two groups, both of which can be driven by sunlight: thermochemical and artificial photosynthetic. Fuels produced by direct processes with sunlight as the energy source are now commonly referred to as *solar fuels*.

### 1.2.1 THERMOCHEMICAL SOLAR FUEL PRODUCTION

Thermochemical solar fuel production is important because systems of this kind are close to being implemented industrially, and, although not a main focus of this Thesis, it is therefore appropriate that they are discussed here.

Thermolysis is the process by which a compound decomposes upon heating, and can be applied to water to produce $H_2$, or to $CO_2$ to form CO or C.[30] In the absence of catalysts, extremely high temperatures (several thousands of degrees) are required for the process to occur at an appreciable level, but metal oxide catalysts can be used to lower the necessary temperatures. The catalysts most commonly used for $H_2$ production are $CeO_2$, $Fe_3O_4$ or ZnO,[31-33] and the latter two have also been used for $CO_2$ thermolysis.[34,35] Sunlight can be used as the source of heat through the use of mirrors to concentrate sunlight onto a reactor into which the starting material is fed, and this method of heat generation is the same as that

used in 'solar thermal' systems that use the heat to create steam to drive conventional generators. These (electricity generating) systems are already at a commercial level, with most plants being in Spain (*e.g.* PS10 in Seville, 11 MW capacity)[36] and the USA (*e.g.* Nevada Solar One, 64 MW capacity).[37]

Two separate redox steps are involved in metal oxide-catalysed thermolysis. Firstly, the catalyst is thermally reduced, with concomitant release of $O_2$. This is an endothermic process that is run at very high temperature (~ 2000 ºC), and at low pressure (100 – 200 mbar). $H_2$ (from water) or CO (from $CO_2$) is then released upon re-oxidation of the metal, and this is a lower temperature step which is typically run at 400 – 600 ºC.[31] By splitting the overall reactions into two steps that can be carried out in separate reactors, the issue of separation of $O_2$ and $H_2$/CO is resolved. Using $M_xO_y$ as the general formula of the metal oxide catalyst, the process can be summarised as follows:

| | | |
|---|---|---|
| 1. | High temperature reduction: | $M_xO_y + heat \rightarrow xM + (y/2)O_2$ |
| 2a. | Low temperature oxidation with $H_2O$: | $xM + yH_2O \rightarrow M_xO_y + yH_2$ |
| | *or* | |
| 2b. | Low temperature oxidation with $CO_2$: | $xM + yCO_2 \rightarrow M_xO_y + yCO$ |
| | | $xM + (y/2)CO_2 \rightarrow M_xO_y + (y/2)C$ |

This method of solar fuel production is as much an engineering challenge as it is a chemical one, with a high proportion of the research in the field dedicated to the design of solar furnaces and heliostats (arrays of mirrors that constantly rotate to track the sun, thereby continuously reflecting sunlight towards the reactor). The complex infrastructure required is generally expensive, and the high operating temperatures lead to issues of material stability and lifetime.[31,38] The requirement for high concentrations of direct sunlight dictate that, as is

the case for solar thermal systems for steam-powered generation of electricity, thermolysis pilot plants are only feasible in sunny locations.[39]

Co-feeding water and $CO_2$ produces synthesis gas (a mixture of $H_2$ and CO),[40] and recent results have shown that the $H_2$:CO composition can be controlled in the range by varying the water:$CO_2$ ratio.[41] The synthesis gas can then be fed directly through to Fischer-Tropsch reactors for liquid fuel production.[28]

### 1.2.2 SOLAR FUELS FROM ARTIFICIAL PHOTOSYNTHESIS

A major disadvantage of solar-driven thermochemical fuel production is that it requires direct and *focusable* sunlight. In contrast, light-induced charge separation processes do not require direct sunlight (indeed, photovoltaic cells can operate even under dull conditions). The approach of fuel production *via* light-induced charge separation is termed *artificial photosynthesis*,[42-48] so-called because these systems are inspired by the processes involved in natural photosynthesis. The natural process occurs in plants and some bacteria, and involves the reduction of $CO_2$ to carbohydrates and other carbon-rich products in a process that, overall, is highly complex.[49-51] Briefly, two photosystems are involved. At photosystem II, the chlorophyll P680 absorbs light to form an excited state (P680*) which transfers electrons through an electron transport chain to a second photosystem, photosystem I. Here, a second chlorophyll (P700) is photoexcited, with the excited state transferring electrons through another electron transport chain to ferredoxin-NADP-oxidoreductase (FNR). At FNR, $NADP^+$ is reduced to NADPH, which is an electron source for the reduction of $CO_2$ in the Calvin cycle.[52,53] The electron source is water, which is oxidised to $O_2$ at the oxygen-

evolving complex (OEC) in photosystem II, the active site of which contains an $Mn_4CaO_5$ cluster.[54,55]

Artificial photosynthetic systems do not aim to replicate the highly intricate natural system, but instead draw inspiration from its overall 'design' and the light harvesting and charge separation steps. Figure 3 shows, schematically, the general approach of an artificial system based on a photoexcitable material or compound (D). Following light absorption and charge separation the electron, if sufficient in energy, can be used for reduction of an oxidised moiety to a reduced compound (a fuel). The hole is quenched by an electron donor, which becomes oxidised. For the same reasons as outlined earlier, the most attractive and obvious fuel targets are $H_2$ (from protons or water), or $CO_2$ reduction products.

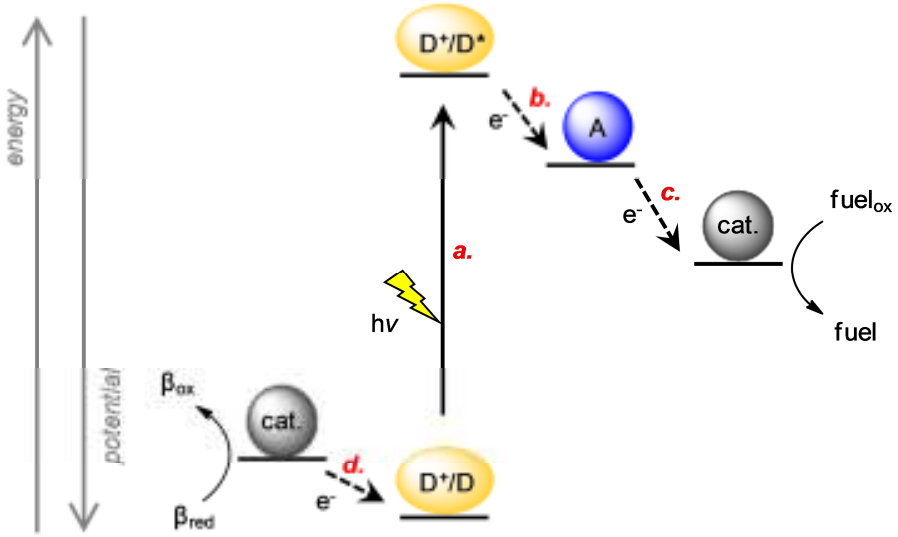


**Figure 3 A general scheme for the design of an artificial photosynthesis system, based on photoinduced charge separation between donor and acceptor units.** D represents a light-sensitive moiety, which when excited by a photon of sufficient energy (process *a.*) is able to spontaneously inject an electron into an acceptor, A (process *b.*). Transfer of electrons to a suitable reductive catalyst (process *c.*) enables reduction of a feedstock ('$fuel_{ox}$', either $H_2O$ or $CO_2$) to a fuel ($H_2$ or reduced carbon compounds). $\beta_{red}$ represents an oxidisable species (ideally $H_2O$) that quenches $D^+$, regenerating the ground state D.

The donor (D) and acceptor (A) units are not necessarily separate physical components. For example, in a semiconductor particle under band gap irradiation (see section 1.6.1) electrons are excited from the valence band to the conduction band; in this instance the valence band is (conceptually) the donor, and the conduction band the acceptor. To summarise Figure 3, energy from photons induces a charge separation; the reductive catalyst then effects a reduction of the feedstock ('$fuel_{ox}$,' either $H_2O$ or $CO_2$) to a fuel ($H_2$ or reduced carbon compounds), and the oxidised donor is reduced back to its initial state by an electron donor ($\beta_{red}$). In view of scale-up of such a system to a commercial or industrial level, the electron donor species must be widely abundant and low cost. Water, in principle, is the ideal candidate but both kinetic and thermodynamic factors mean that its oxidation (requiring four electrons to produce $O_2$) is highly challenging.[56,57] The OEC in photosystem II is therefore of great interest, because it provides a blueprint for the design of artificial water oxidation catalysts.[58-64] Researchers often use 'sacrificial' electron donors (typically amines or ascorbate) that are able to quench the oxidised light absorber more readily than water, and this allows focus on the fuel forming reaction. Similarly, to focus on water oxidation catalysts, sacrificial electron acceptors such as $S_2O_8^{2-}$, $Ag^+$ or $Fe^{3+}$ may be used.

## 1.3 CARBON MONOXIDE AS AN INDUSTRIAL FEEDSTOCK

In addition to CO having value as a fuel, or at least as a pre-cursor to liquid fuels, it is an important chemical feedstock for various industrial reactions. The BP Chemicals-developed Cativa process[65,66] (an improved version of the Monsanto process)[67] is the principal industrial route to acetic acid, proceeding *via* the carbonylation of methanol in the presence of an iridium-based catalyst and HI. In 2000, the world demand for acetic acid was around

6 million tonnes per year, and 60% of this was prepared by the carbonylation route.[65] In the 'oxo' reaction[68] hydroformylation of olefins is achieved by their reaction with CO and $H_2$ to produce $C_3 - C_{15}$ aldehydes (themselves important precursors to amines, carboxylic acids and primary alcohols). Carbon monoxide is also used extensively in the Mond process for nickel purification.[69]

The Fischer-Tropsch process[28] has already been mentioned within the context of producing liquid fuels, but it is also a key process for the manufacture of a wide range of chemicals. Here, the components of 'synthesis gas' (CO and $H_2$) react together to form liquid alkanes, olefins, methanol and/or higher alcohols. The reaction may be summarised as:

$$x\mathrm{CO} + y\mathrm{H_2} \rightarrow \text{`}\mathrm{-CH_2-}\text{'} \text{ products}$$

The product mixture depends on the exact conditions of the reactions, which may be run at temperatures between 170 and 400 ºC, with metal oxide catalysts (*e.g.* FeO, $ThO_2$, MgO). The synthesis gas itself is prepared from one of two routes, both of which are unsustainable: coal gasification ($C + H_2O \rightleftharpoons CO + H_2$) or from steam reformation of natural gas ($CH_4 + H_2O \rightleftharpoons CO + 3H_2$). The latter process is also a major route to industrial hydrogen production, and in this case the overall yield of $H_2$ is increased by the water-gas shift reaction ($CO + H_2O \rightleftharpoons H_2 + CO_2$), which is the focus of chapter 3.

## 1.4 PRINCIPLES OF ELECTROCHEMICAL ACTIVATION OF $CO_2$

There are a number of approaches to the activation of $CO_2$ to useful compounds. In reductive hydrogenations, methanol[70-72] and methane (the Sabatier reaction)[73] can both be formed from reactions of $CO_2$ with $H_2$ at high temperatures and/or pressures. The reaction to produce

methanol has a moderate yield of less than 40% at 200 ºC, using a $Cu/ZnO/Al_2O_3$ catalyst,[74-77] and the Sabatier reaction typically uses nickel, ruthenium or rhodium catalysts.[78] The hydrogen required for these reactions must come from the unsustainable stream reformation of natural gas, or from energy-intensive water splitting (either electrochemical, thermal or photolytic).

An alternative method that avoids the requirement for such processes is *direct electrochemical* reduction of $CO_2$, although this approach presents challenges on both thermodynamic and kinetic grounds. Since $CO_2$ is a molecule of low chemical reactivity and high stability ($\Delta G^{\ominus}$ = -394 kJ mol$^{-1}$, *c.f.* -137 kJ mol$^{-1}$ for CO),[79,80] significant energy input is required for its 'fixation'. It is a linear molecule in which the carbon is weakly electrophilic and the oxygen atoms are weak Lewis bases. Reactions usually occur *via* nucleophilic attack of the carbon. The standard redox potentials, corrected to pH 7 and 25 ºC for the one, two, four, six and eight electron reductions are shown below.[81]

| | |
|---|---|
| $CO_2 + e^- \rightarrow CO_2^{\bullet -}$ | $E$ = -1.90 V |
| $CO_2 + 2H^+ + 2e^- \rightarrow CO + H_2O$ | $E$ = -0.53 V |
| $CO_2 + 2H^+ + 2e^- \rightarrow HCO_2H$ | $E$ = -0.61 V |
| $CO_2 + 4H^+ + 4e^- \rightarrow HCHO + H_2O$ | $E$ = -0.48 V |
| $CO_2 + 6H^+ + 6e^- \rightarrow CH_3OH + H_2O$ | $E$ = -0.38 V |
| $CO_2 + 8H^+ + 8e^- \rightarrow CH_4 + 2H_2O$ | $E$ = -0.24 V |

The one-electron reduction to the $CO_2^{\bullet -}$ radical is heavily uphill ($E$ = -1.90 V), due to the large reorganisation energy required to bend the linear $CO_2$ molecule. When (or if) this radical is formed, there are four possible routes:[82] (1) addition of a second electron to form $CO_2^{2-}$ ($E$ = -1.2 V);[83] (2) reaction with water to form $HCO_2^{\bullet}$, followed by addition of a

second electron to give formate; (3) reaction with $CO_2$ to form $OCOCO_2^{\bullet-}$, then addition of a second electron to give CO and $CO_3^{2-}$; or finally (4) self-coupling with a second $CO_2^{\bullet-}$ to form $C_2O_4^{2-}$ (oxalate). The distribution of products is sensitive to the concentration of $CO_2$ and the reaction conditions (in the presence of water the major product is formate).[84,85] The final route to form oxalate is highly attractive because a carbon-carbon bond is formed, which is the starting point for the synthesis of a multitude of further organic products.

The multi-electron conversions all have much more positive reduction potentials and are therefore considerably more appealing from an energetic perspective, but the difficulty is now one of kinetics because of the requirement for electron and proton transfers to be coupled. The activation energies (kinetic barriers) for these processes are high, so catalysts are required in order to achieve reasonable rates.

The electrochemical processes just described are closely related to *photo*electrochemical reduction of $CO_2$, because here photons are captured and converted into separated charges (holes and electrons). The electrons effect the reduction reaction(s), with the positively charged 'holes' usually extracted by sacrificial electron donors that become oxidised. In either broad category (electrochemical or photoelectrochemical), efforts have been made to prepare catalysts both to overcome the aforementioned kinetic barriers, and also to allow the formation of single reduction products. The latter relates not only to avoiding mixtures of carbon products but also to preventing the reduction of protons to $H_2$, which is a pervasive challenge in the field.

## 1.5 ELECTROCATALYSTS FOR $CO_2$ REDUCTION

(Photo)electrocatalysts for $CO_2$ reduction can be divided into four main groups: (1) homogeneous, light-absorbing transition metal complexes; (2) semiconductor-based systems (either in the form of photocathodes, or particulate systems); (3) metal electrodes; and (4) catalysts coupled to 'inert' electrodes, either through being directly attached to the electrode surface, or though diffusion-controlled processes in the electrolyte solution. Groups (1) and (2) describe firm photocatalysts; groups (3) and (4), while referring to (light-insensitive) electrocatalysts that are usually investigated through standard electrochemical techniques, may become light-driven if the catalyst is incorporated into a light sensitive moiety such as a semiconductor particle, or if the electrons supplied to the cathode originate from photovoltaic processes. In many instances, the source of electrons is irrelevant to the principle of operation of the catalyst. Catalysis at bare (unmodified) metal electrode surfaces, and 'classic' electrocatalysts (categories 3 and 4 identified above) shall now be reviewed. Focus will return to semiconductor particle-based assemblies (2) in section 1.6.

### 1.5.1 $CO_2$ REDUCTION AT METAL ELECTRODES

The simplest electrochemical system for $CO_2$ reduction is a bare metal electrode, and a wide range of metals have been investigated for this purpose.[86,87] The nature of the metal determines both the yield and the product distribution, with one major issue in aqueous systems being that of competing proton reduction to form $H_2$. As electrocatalysts for $CO_2$ reduction, the metals can be summarised by dividing them into groups according to their major products. In the cases of Pb, Hg, In, Sn, Cd and Tl the major product is formate, but potentials significantly beyond the thermodynamic reduction potential are necessary (applied

$E$ < -1.5 V *vs.* SHE).[88] Ni, Fe, Pt and Ti all fail to show any significant carbon products, the reason being that although $CO_2$ is reduced to CO at these surfaces, the metal-CO adsorption strengths are so high that the product is not released.[86] Instead (in aqueous electrolytes) $H_2$ is formed, the overpotential for which is more moderate. In contrast, Au, Ag, Zn, Pd and Ga all form CO as the major product, since CO is bound less tightly.

Despite the fact that large overpotentials are still required, the best metal electrode for $CO_2$ reduction is, by some margin, copper.[89,90] Although mixtures of products are formed, this is the only electrode capable for forming products more reduced than CO and formate: $CH_4$ and $C_2H_4$ dominate at sufficiently negative potentials (when overpotentials in excess of 1 V are applied);[57,58] at less negative potentials the major products are CO and formate. Under all conditions, however, mixtures remain unavoidable. The precise mechanism of $CO_2$ reduction to highly reduced compounds at copper surfaces remains elusive, and curiously, methanol production has never been observed (this is interesting because the gas-phase methanol synthesis reaction – which uses copper catalysts - produces methanol from mixtures of $CO_2$, CO and $H_2$).[91] The key step in the formation of the hydrocarbons is protonation of bound CO to form bound CHO, and it is now clear from density functional theory calculations that the strength of CO adsorption relative to the ability of the metal surface to stabilise adsorbed CHO is key.[92]

The issue of competing $H_2$ production can be solved by switching from aqueous to organic electrolytes, from which protons can be excluded or the concentration controlled in order to influence the product distribution. An extra advantage is that the solubility of $CO_2$ is much

higher in organic solvents than in water (example solution concentrations of $CO_2$ at 1 atm. at 25 ºC are 0.199 M (in DMF) and 0.205 M (in THF), compared to 0.033 M in water).[93]

## 1.5.2 OTHER ELECTROCATALYSTS FOR $CO_2$ REDUCTION

### 1.5.2.1 METAL COMPLEXES WITH BIPYRIDYL LIGANDS

The first major group of $CO_2$ reduction electrocatalysts is transition metal complexes having bipyridyl ligands. The first example, published by Lehn in 1984 was $Re(bpy)(CO)_3Cl$ (bpy = 2,2'-bipyridine),[94] which had actually been designed as a photosensitiser before its $CO_2$ reducing ability was observed. In a 9:1 DMF:$H_2O$ solution $CO_2$ was reduced to CO at -1.25 V *vs.* SHE, and although there was good selectivity over $H_2$ production, the turnover frequency (TOF) of 21.4 $h^{-1}$ was poor. Since this report, electrocatalysis by numerous other transition metal-bipyridyl complexes has been observed, mainly using Re,[95,96] Ru,[97-102] Rh[102] and Os.[103,104] The Tanaka complex[97] $[Ru(bpy)_2(CO)_2]^{2+}$ is fairly typical and its mechanism for $CO_2$ reduction (Scheme 1) is as follows: the complex is reduced by two electrons, and loses CO to form a neutral complex. $CO_2$ then binds through the carbon atom to form a $\eta^1$-adduct, which is then protonated to give $[Ru(bpy)_2(CO)(COOH)]^+$. A second proton is then added before water is lost, regenerating the catalyst. Like the original Lehn complex, the process is inefficient (a potential of -1.40 V *vs.* SCE is required) and the turnover number (TON) of 26.2 is low, and these are common characteristics from which these metal-bipyridyl catalysts generally suffer.[105]

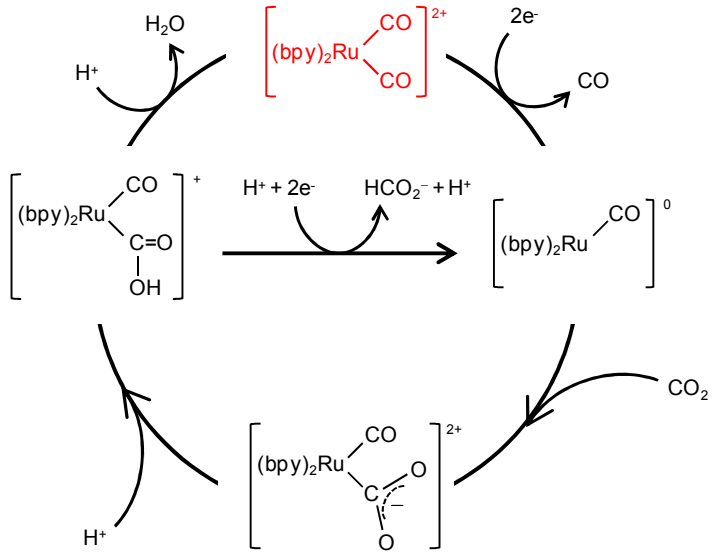


**Scheme 1 The proposed mechanism of $CO_2$ reduction to CO by the Tanaka catalyst,[97] $[Ru(bpy)_2(CO)_2]^{2+}$.**

### 1.5.2.2 TRANSITION METAL PHOSPHINE COMPLEXES

More promising are transition metal phosphine complexes. The first electrocatalyst of this kind was $Rh(dppe)_2Cl$ (dppe = 1,2-bis(di-phenylphosphino)ethane), which was shown by Wagenknech *et al.* to produce CO in DMF at -1.55 V *vs.* SCE,[106] but the most intensive research into polydentate phosphine catalysts has since been done by the Dubois group with a focus on complexes having Pd as the metal centre.[107-110] Significant improvement has been made over the original $Rh(dppe)_2Cl$ complex in terms of lowering the overpotential requirement. The Dubois suite of electrocatalysts use tridentate phosphine ligands, with the active catalytic species having a weakly coordinated solvent molecule in the fourth square planar position, *e.g.* $[Pd(triphos)(NCMe)](BF_4)_2$. The major product is CO. Catalytic rate constants of these complexes are between 5 - 300 $M^{-1}$ $s^{-1}$ and the overpotentials for CO

production (100 – 300 mV) are moderate, although they suffer from low TONs of around 10-100.[108,111]

The proposed catalytic cycle[108] for $CO_2$ reduction by $[Pd(triphos)(NCMe)](BF_4)_2$ is shown in Scheme 2. Following reduction by a single electron, $CO_2$ is bound to form a 5-coordinate complex. Addition of a proton forms the metallocarboxylic acid, and reduction by a second electron results in dissociation of the solvent molecule. A second proton then leads to loss of water, before another solvent molecule displaces CO and reforms the catalyst.

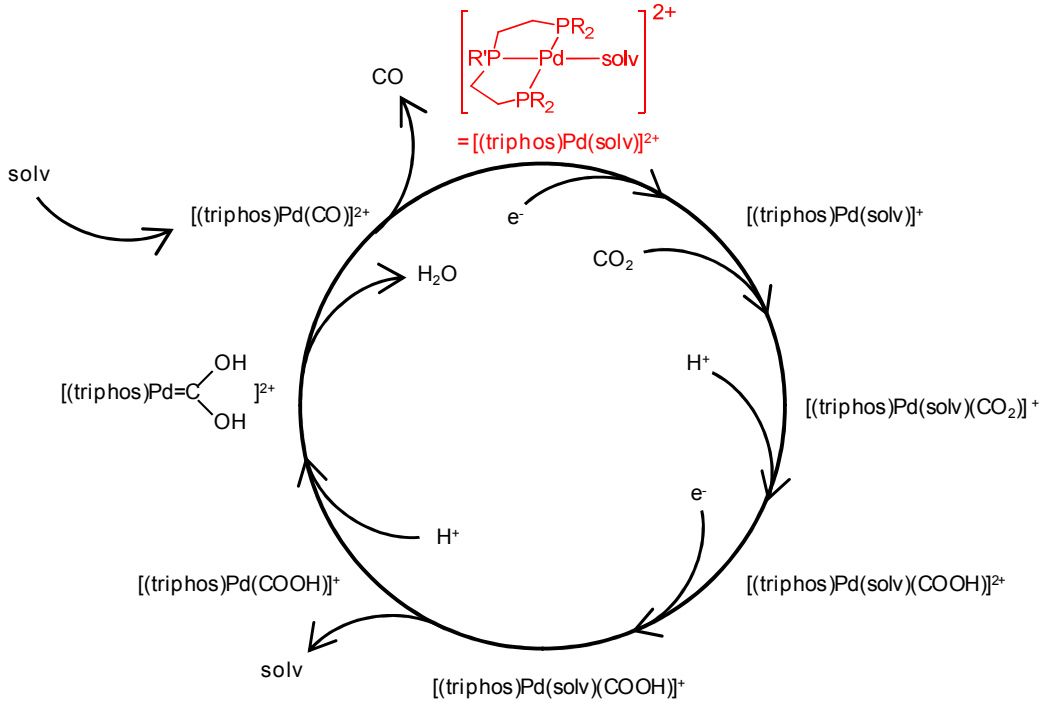


**Scheme 2 The proposed mechanism of $CO_2$ reduction to CO by the Dubois Pd-based $CO_2$ reduction electrocatalyst.[108]**

A promising development in this category of electrocatalysts was the preparation of *bimetallic* Pd complexes, and when methylene was used as the bridging group (as shown in

Figure 4)[112] the rate constant was increased over those of the monometallic catalysts (5 – 300 $M^{-1}$ $s^{-1}$)[111] by around three orders of magnitude. This was interpreted as being indicative of cooperative binding of $CO_2$. Reversible reduction of $CO_2$ in biology is catalysed by enzymes called carbon monoxide dehydrogenases (CODHs). While these will be discussed in detail later (section 1.7), it is interesting to note that the bimetallic Dubois Pd catalyst shares key features with the [Ni4Fe-4S] active site cluster of the CODH that is found in anaerobic organisms. Firstly, in the enzyme, $CO_2$ is also bound cooperatively (nickel acts as a Lewis base, binding the electrophilic carbon, and a dangling Fe atom is a Lewis base coordinating one of the oxygen atoms); and secondly, when $CO_2$ is bound a stable seven-membered ring is formed in both of the catalysts. Despite the impressive catalytic rates ($k > 10^4$ $M^{-1}$ $s^{-1}$), the TON for the bimetallic Dubois catalyst in Figure 4 was low – around 10 – and it was thought that this was due to deactivation on account of metal-metal (Pd-Pd) bond formation, which has a higher tendency to occur for second and third row transition metals.

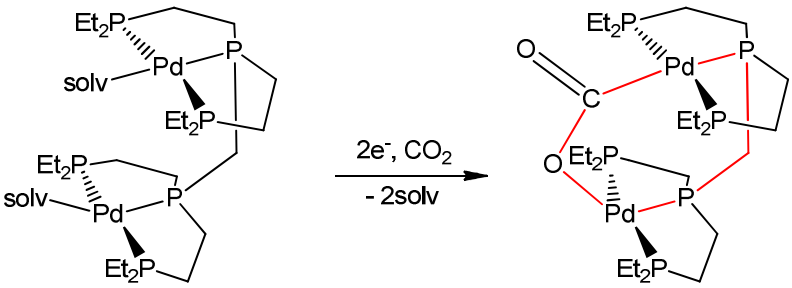


**Figure 4 Dubois bimetallic-Pd $CO_2$ reduction catalyst,[112] $[Pd_2(CH_3CN)_2(eHTP)](BF_4)_4$, where eHTP = $(Et_2PCH_2CH_2)_2PCH_2P(CH_2CH_2PEt_2)_2$.** Here, solv = $CH_3CN$. A stable seven-membered ring, highlighted in red, in formed upon binding $CO_2$.

#### 1.5.2.3 METAL COMPLEXES WITH MACROCYCLIC LIGANDS

Some of the earliest work with this kind of catalyst was done by Eisenberg *et al.* in 1980, who observed CO production by tetra-azomacrocyclic complexes of nickel and cobalt when potentials between -1.3 and -1.6 V *vs.* SCE were applied.[113] TOFs were poor: 2 – 9 $h^{-1}$ at 23 ºC, and $H_2$ was also produced (the solvent systems used were either water or 2:1 water:acetonitrile).

A major breakthrough was made a few years later by Sauvage who used $Ni^{II}$(cyclam) complexes to achieve highly selective reduction of $CO_2$ to CO in water, at fast rates (TOFs of around 1000 $h^{-1}$) and with very little degradation of the catalyst, even after $10^4$ turnovers.[114-116] The required overpotentials were still moderately large, however (potentials of around -1 V *vs.* SHE were applied, corresponding to overpotentials of about 0.5 V), and an Hg electrode surface was essential, onto which the cyclam complex (specifically, the reduced $Ni^{I}$(cyclam) form) adsorbed.[117]

Another notable group of catalysts in this class is iron(0) porphyrins, which were also found to form CO.[118] Weak acid increased efficiencies and lifetimes of catalysis, although this did not result in production of significant amounts of $H_2$.[119] Like the nickel cyclam complexes, turnover frequencies were relatively high (350 $h^{-1}$), and stability of the catalyst was good with only 1% decay per catalytic cycle. Again, mercury electrodes and relatively high potentials (-1.5 V *vs.* SCE) were required. Nevertheless, the selective production of a single product by this and the nickel cyclam represents an important advantage over the other electrocatalysts that have been discussed.

#### 1.5.2.4 PYRIDINIUM ION

The pyridinium ion, uniquely, has been found by Bocarsly *et al.* to catalyse the six-electron reduction of $CO_2$ to methanol with very little overpotential requirement.[120] The catalyst acts as a *one*-electron shuttle between the electrode and the carbon species, in an approach that contradicts the conventional method of designing catalysts to effect multiple, proton-coupled electron transfers. The detailed mechanistic study revealed the catalytic route to proceed through various pyridinium-carbon coordinative interactions in inner-sphere-type electron transfers, *i.e.* the process is not one of simple outer-sphere electron transfers.[121] Overpotentials of just 200 mV have been found to be sufficient, with the catalysis being first order in both pyridinium and $CO_2$.[122]

Despite there still being some product distribution, this simple, metal-free catalyst appears to be particularly promising, and it has been demonstrated to work in an aqueous, light-driven system forming only methanol.[123] The photoelectrochemical cell used a p-type GaP photoelectrode, and even when potentials more *positive* than the thermodynamic $CO_2/CH_3OH$ reduction potential were applied, methanol was formed with good selectivity at quantum yields of around 2% when using visible (465 nm) light.

Table 1 summarises the main types of electrocatalysts for $CO_2$ reduction.

**Table 1** Summary of various categories of electrocatalyst for $CO_2$ reduction

| category | main products | advantages | disadvantages | references |
|---|---|---|---|---|
| *unmodified metal electrodes* | CO, $HCOO^-$, $H_2$ (in water); $CH_4$ and $C_2H_4$, EtOH (Cu only) | simplicity; Cu is only electrocatalyst capable of forming large amounts of hydrocarbons (*i.e.* $CH_4$ and $C_2H_6$) | competing $H_2$ production in water; very high overpotential requirements | 86-92,124 |
| *metal bipyridyl complexes* | CO, $HCOO^-$ (and $H_2$ in water) | | low turnover rates/numbers; high overpotential requirements | 94-104 |
| *transition metal phosphine complexes* | CO (and $H_2$ in water) | moderate overpotentials (100-300 mV); fast rates (at least specific examples of) | low TONs (< 100) | 106-112 |
| *metal macrocycles* | CO (and often $H_2$ in water) | fast rates (up to $10^4$ $h^{-1}$; high stabilities | Hg electrode surface required; high overpotential requirements (> 0.5 V) | 113-119 |
| *pyridinium ion* | $CH_3OH$ (mainly), HCOOH, HCHO | only catalyst to form methanol; low overpotential requirement (~ 200 mV) | only demonstrated to work with a limited range of electrode surfaces | 120-123 |

## 1.6 PHOTOELECTROCATALYTIC SYSTEMS FOR $CO_2$ REDUCTION

In order to form a light-driven system for reductive $CO_2$ activation, the electrocatalysts summarised in Table 1 must be coupled to a light capturing system that is able to transfer this energy to the catalyst in the form of reductive electrons. Broadly, there are four approaches through which this may be achieved.

Firstly, as briefly mentioned above for the case of pyridinium-catalysed $CO_2$ reduction, a photoelectrochemical cell can be prepared by using a light-sensitive material (typically a

semiconductor) as the cathode. The catalyst may be present in the electrolyte solution or directly attached to the electrode, and irradiation with light provides electrons for the reduction process. At an anodic counter electrode, oxidation of a sacrificial solution species supplies electrons to regenerate the photocathode.

As a second option, homogeneous systems can be prepared, involving a light harvesting species such as a transition metal complex (*e.g.* $[Ru(bpy)_3]^{2+}$) and a molecular catalyst in solution. The photoexcited light harvester reduces the catalytic species, often *via* a mediator such as methyl viologen. The oxidised light absorber is regenerated through reduction by a sacrificial electron donor.

Thirdly, it is possible for the light harvester and catalyst to be the same molecule/complex, such as $Re(CO)_3(bpy)X$-based complexes,[105] and finally there is a group of $CO_2$ reduction photocatalysts that use colloidal suspensions of semiconductor particles (typically on the nanometre scale). Although $CO_2$ reduction has been reported at unmodified semiconductors, a 'co-catalyst' is usually present, and this may be in solution phase or attached to the semiconductor particles to form a heterogeneous system. The first three strategies will be discussed no further here. More relevant to this Thesis is the final category of semiconductor particle-based systems, which is now considered.

### 1.6.1 SEMICONDUCTOR PARTICLE-BASED SYSTEMS

Semiconductors are sensitive to light; photons of sufficient energy promote electrons from the valence band to the conduction band, resulting in formation of an exciton (an electron-hole pair).[125] For this process to occur, the energy of the photon must exceed the band gap of

the semiconductor material (that is, the difference in energy between the valence and conduction bands). If these charge carriers avoid non-productive recombination and instead separate and migrate to the surface of the material, they can be useful for redox reactions, and therefore semiconductors have been a subject of major interest for their application in artificial photosynthetic systems, both for production of $H_2$ from protons and for $CO_2$ reduction. Figure 5 shows the principle of light-driven $CO_2$ reduction at a semiconductor particle.

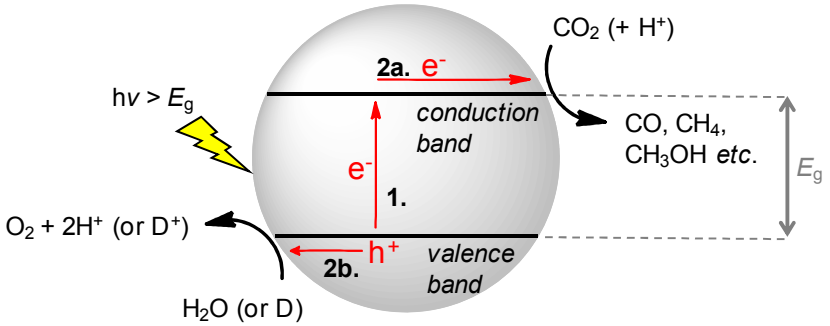


**Figure 5 Schematic representation of $CO_2$ reduction at the surface of a semiconductor particle.** Absorption of photons of energy exceeding the band gap ($E_g$) of the semiconductor excites electrons from the valence band to the conduction band (process 1.), resulting in an electron-hole pair (an exciton). The electrons and holes ($h^+$) migrate to the particle surface (2a. and 2b.), whereupon they effect reduction of $CO_2$ to reduced carbon compounds, and oxidations. Ideally, the reductant being oxidised by valence band holes is $H_2O$, but in many cases is a sacrificial species such as an amine (represented by D).

Inoue *et al*. were the first to report, in 1979, that suspensions of various wide band gap semiconductor particles photocatalyse the reduction of $CO_2$ with water to produce mixtures of products.[126] Typical reduction products at semiconductor suspensions are CO, formic acid, formaldehyde, methanol and methane, all of which require the transfer of multiple electrons and (with the exception of CO) protons. The mechanism of $CO_2$ reduction at semiconductor

surfaces is not always clear, although Savéant and Hori have proposed pathways for the formation of CO *via* the $CO_2^{\bullet-}$ species (Figure 6).

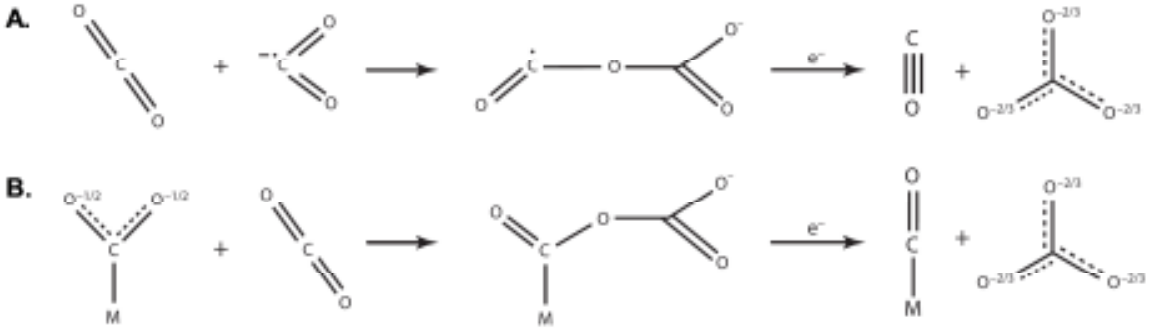


**Figure 6 Mechanisms proposed by Savéant (A) and Hori (B) for reduction of $CO_2$ to CO in low proton concentrations or high $CO_2$ concentrations.** Figure reproduced from reference [127].

The most commonly used semiconductor material is $TiO_2$, despite the fact that the conduction band is more mildly reducing than other semiconductors (Figure 7). Being cheap, non-toxic, stable and widely abundant means that it is an appropriate material for use in systems that must eventually operate on a global scale. *Anatase* $TiO_2$, having a band gap of 3.2 eV,[128] is generally considered to be the most photocatalytically active form. An excellent 2009 review article by Indrakanti *et al.* summarises $TiO_2$-based photocatalysts for $CO_2$ reduction.[129] The wide band gap requires photons of wavelength shorter than 386 nm to excite electrons into the conduction band, and many reports of $CO_2$ photoreduction at $TiO_2$ therefore use UV light sources. There are several strategies that can be employed to sensitise $TiO_2$ towards visible wavelengths, and these are discussed in section 1.6.2.

To date, heterogeneous *co-catalysis* at semiconductor particles is fairly primitive. The most prominent method of increasing the $CO_2$ reduction photocatalytic activity of $TiO_2$

nanoparticles in suspension has been to include deposits of transition metals, including Cu,[130-137] Pt[138-140] and Ru,[141] on the semiconductor surface. This fairly simple approach is primarily based on the metallic clusters acting as trapping sites for electrons (thereby decreasing the number of electron-hole recombinations), although the catalytic enhancement observed through the use of copper may also be attributed to the previously discussed electrocatalytic ability of this metal for multi-electron reductions of $CO_2$ (section 1.5.1).

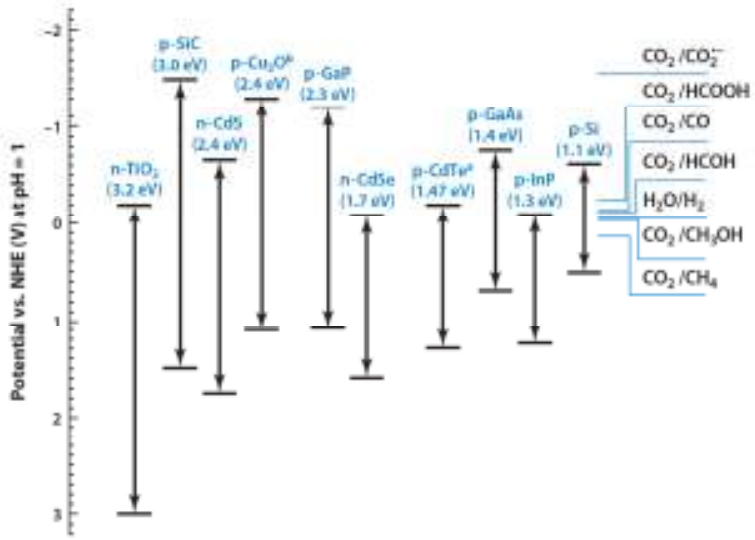


**Figure 7 Positions of the conduction and valence bands of several semiconductors at pH = 1 *vs.* NHE.** Thermodynamic potentials for $CO_2$ reduction to different products at pH = 1 *vs.* NHE are shown beside the band edge positions of semiconductors. Figure reproduced from reference [127].

### 1.6.2 TRANSITION METAL COMPLEXES FOR SENSITISATION OF WIDE BAND GAP SEMICONDUCTORS TO VISIBLE LIGHT

The wide band gap of $TiO_2$ means that only a small percentage of the solar spectrum (towards the high energy, UV end) is useful for photoinduced charge separation. Photochemical devices based on $TiO_2$ (and other wide band gap semiconductors such as ZnO) are therefore often subjected to various strategies to enable the use of *visible* light as

the energy source. These include doping with impurities[142-145] and coupling with other materials that themselves have narrow band gaps (*e.g.* CdS,[146-148] CdSe,[149] $V_2O_5$[150]), but the most heavily pursued approach is to attach a transition metal dye complex (often referred to as a photosensitiser) to the $TiO_2$ surface.[151-156] The sensitisation of $TiO_2$ to visible wavelengths using transition metal dyes is the basis of dye-sensitised solar cells (DSSCs),[12-14] which were mentioned earlier as alternatives to silicon-based photovoltaics. The most commonly used dyes in DSSCs are those based on ruthenium tris-bipyridyl, *i.e.* $[Ru(bpy)_3]^{2+}$, and extensive reviews cover the photochemistry of such complexes.[157,158] The ground state of $[Ru(bpy)_3]^{2+}$ is very stable due to the $d^6$ electron count and the chelation of the bipyridine ligands. The lowest energy transition is a metal-to-ligand charge transfer (MLCT) process, in which one of the $d\pi^6$ electrons in a Ru-based orbital (the HOMO) is excited into one of the empty bipyridine-based $\pi^*$ orbitals (the LUMO). A simplified molecular orbital level diagram showing this transition is drawn in the bottom half of Figure 8, along with other possible transitions: a 'metal-centred' (MC) transition of one of the Ru-based $d\pi^6$ electrons into a Ru-based $\sigma^*$ orbital, and a 'ligand-centred' (LC) transition from the bipyridine-based $\pi$ bonding orbital into the $\pi^*$ LUMO. The MC transition is symmetry-forbidden, and hence it has a low extinction coefficient and the absorbance shown in the spectrum (panel A) is weak.

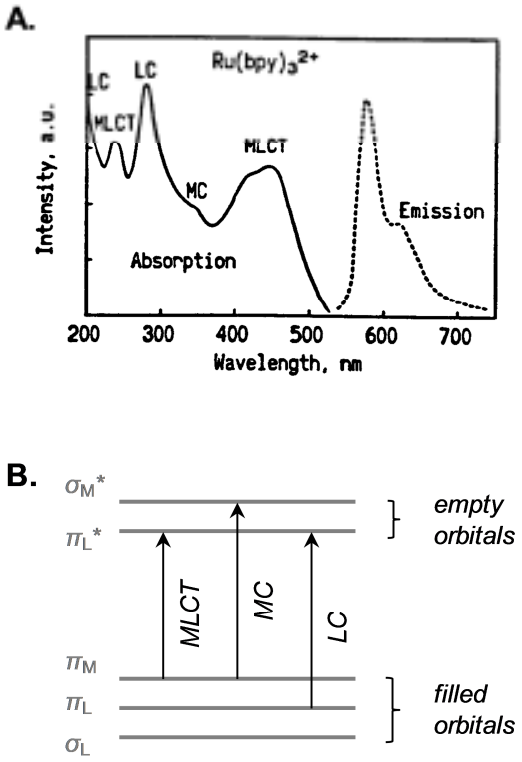


**Figure 8 Electronic transitions in ruthenium tris-bipyridyl complexes.** (A) Electronic absorption (in water) and emission (in ethanol) spectra of $[Ru(bpy)_3]^{2+}$. Reproduced from reference [158]. (B) Schematic representation of a molecular orbital level diagram to show the possible light-induced electronic transitions that lead to the absorbance bands in the spectrum in (A). MLCT = metal-to-ligand charge transfer; MC = metal centred transfer; LC = ligand-centred transfer. Subscripts M and L indicate whether the orbital energy level is mainly metal-based or ligand-based, respectively.

The selection rule of $\Delta S = 0$ (no change of electron spin is permitted between ground and excited states) means that the MLCT process results in a singlet state. However, owing to the 'heavy atom effect' of the ruthenium centre, this singlet state (termed $^1$MLCT) is able to relax to the lower energy *triplet* state ($^3$MLCT) through intersystem crossing; the singlet and triplet states have the same orbital occupation, but differ in the electron spin pairings. For ruthenium tris-bipyridine, intersystem crossing occurs with high efficiency (close to 100%),

and its triplet state has a long lifetime (~ 1 μs in water)[159] because relaxation back to the singlet ground state is a slow process owing to the $\Delta S = 0$ selection rule.

The general principle of operation of a $TiO_2$-based DSSC is shown in Figure 9, together with an outline of the steps involved in the overall conversion of solar energy to electrical current. The photoanode consists of a mesoporous layer of $TiO_2$, providing a high surface area for maximum light absorption. The photosensitiser species (S) is attached to the surface of $TiO_2$; upon absorption of a photon of sufficient energy the dye is photoexcited through the previously discussed MLCT process. The next step is electron injection into the conduction band of $TiO_2$, and this may occur either from $^1$MLCT or from $^3$MLCT. Injection from $^1$MLCT typically occurs on a sub-picosecond timescale;[160-163] injection from $^3$MLCT typically occurs within the timescale of tens of picoseconds or longer,[164,165] since it is at lower energy than the singlet state. However, since the previously mentioned intersystem crossing from $^1$MLCT to $^3$MLCT is fast (~ 100 fs)[166] and the triplet state is so long-lived, injection from the triplet state is generally understood to be the dominant pathway. Regardless of which pathway occurs, electron injection results in oxidation of the dye, and this is reduced back to its original oxidation state by a species that is present in the electrolyte for this purpose. Typically this is iodide, which is oxidised to triiodide ($I_3^-$). Once the electron is in the conduction band of $TiO_2$ it migrates through the mesoporous network to a conducting glass back contact, and is conducted through the external circuit as the electrical current. At the counter electrode, the electrons reduce iodine back to iodide, and this redox couple is continually cycled in this way.

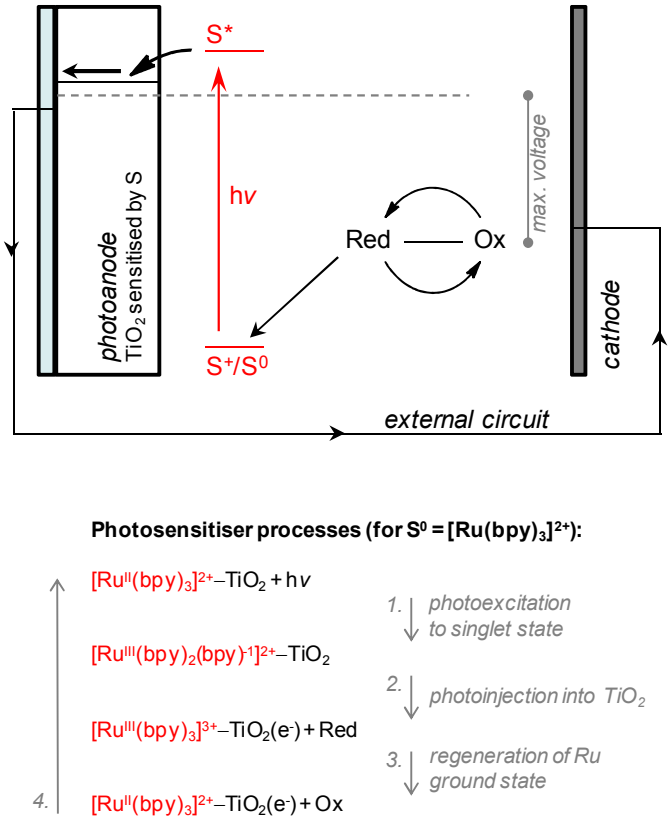


**Figure 9 Schematic representation of the principle of operation of a dye-sensitised solar cell (DSSC).** The photoanode is mesoporous $TiO_2$ sensitised with a transition metal dye complex (S). Upon absorption of a photon, S is photoexcited and injects an electron into the $TiO_2$ electrode, which enters the external circuit through the conducting glass backing plate (light blue). The oxidised photosensitiser is returned to the ground state by reduction by the reduced form of a mediator (Red); the oxidised mediator (Ox) is cycled back to Red by an electron from the external circuit. The equations describe the main processes involved in the overall conversion of solar to electrical energy. $TiO_2(e^-)$ represents a photoinjected electron in $TiO_2$. The maximum cell voltage depends on the potential difference between the Ox/Red couple and the Fermi level of $TiO_2$.

Dye-sensitisation of $TiO_2$ is, in principle, applicable to solar fuel production at semiconductors, although to date there exist only very few examples of such an approach for photocatalytic $CO_2$ reduction.[137,167,168] Ozcan *et al.* modified films of Pt-impregnated $TiO_2$ with dyes including $[Ru(bpy)_3]^{2+}$, reporting methane as the only product under visible light.[137,167] A more advanced photoreactor, using catalyst-coated optical fibers, was reported

by Nguyen *et al.*; here, $TiO_2$ was doped with Cu and Fe and sensitised with [Ru(2,2'-bipyridyl-4,4'-dicarboxylate)$_2$-(NCS)$_2$]$^{2+}$ (the well known 'N3' dye) to produce mixtures of methane and ethane.[168]

## 1.7 $CO_2$ FIXING IN BIOLOGY

Carbon dioxide is produced on an enormous scale by aerobic metabolism in animals, plants and microorganisms. The carbon cycle, broadly speaking, is finely balanced: approximately the same amount of $CO_2$ that is emitted (around $10^{17}$ g each year)[169] is taken up and used by plants and certain microorganisms in various '$CO_2$ fixation' pathways. The main route is through the Calvin cycle,[162,163] in which the $CO_2$ fixation step in the 'dark reactions' of photosynthesis is catalysed by the enzyme ribulose 1,5-biophosphate carboxylase (known as 'Rubisco', thought to be Earth's most abundant protein). This will not be discussed further in this Thesis. A second major route (there are six in total)[170,171] is the Wood-Ljungdahl or reductive acetyl-CoA pathway.[172,173] Here, $CO_2$ is reduced to CO, which is then combined with a methyl group and Coenzyme A to form acetyl-Coenzyme A, a biosynthetic building block and a source of ATP. The latter step is catalysed by acetyl-Coenzyme A synthase (ACS), the active site of which can be described as a binuclear NiNi centre bridged to a [4Fe-4S] cluster.[174,175] The first step in this process - reduction of $CO_2$ to CO - is catalysed by an enzyme called carbon monoxide dehydrogenase (CODH).‡ The CODH and ACS enzymes that are involved in the Wood-Ljungdahl pathway form a tight, 'bifunctional' CODH/ACS complex, shown in Figure 10.[176]

‡ The name 'carbon monoxide dehydrogenase' is a misnomer, since CO cannot, of course, be dehydrogenated. The enzyme could more usefully have been termed 'carbon monoxide oxidoreductase.'

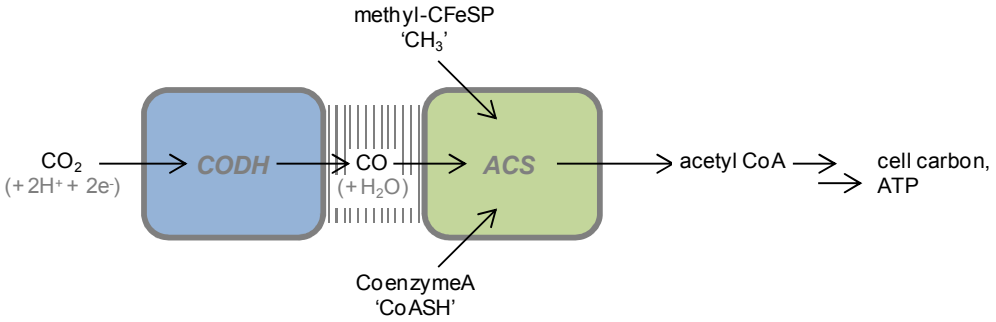


**Figure 10 Representation of the carbonyl branch of the Wood-Ljungdahl pathway for fixation of $CO_2$ into acetyl CoenzymeA using a 'bifunctional' CODH/ACS complex.** $CO_2$ is reduced to CO by CODH, which is then condensed with CoenzymeA and a methyl group by ACS to form acetyl-CoenzymeA. This is a biosynthetic building block and the source of ATP. The methyl group comes from the methyl branch of the pathway (not depicted), which involves the six-electron reduction of $CO_2$ to $CH_3$-$H_4$folate. The electrons used in the CODH-catalysed reduction of $CO_2$ may come from hydrogenase-catalysed $H_2$ oxidation, or pyruvate oxidation catalysed by pyruvate ferredoxin oxidoreductase.[176] A gas channel between the CODH and ACS units prevents the escape of CO.[177,178]

*Monofunctional* CODHs (that is, CODHs that are *not* part of a CODH/ACS complex) also exist, and these play a crucial role in energy generation (production of low potential electrons) in a range of microbial organisms that use CO as an energy source.[176] There are two main categories: Mo-CODH (in aerobes), in which the active site is a CuSMo-pterin,[179-181] and Ni-CODH (in anaerobes), in which the active site is a [Ni4Fe-4S] cluster.[182,183] There are thus three main categories of CODH, and these are summarised in Table 2.

**Table 2** Types of CODH

| category | reaction catalysed | metal centres[a] |
|---|---|---|
| *aerobic* Mo-CODH[179-181] | $CO + H_2O \rightarrow CO_2 + 2H^+ + 2e^-$ | CuSMo-pterin |
| *anaerobic* Ni-CODH | $CO + H_2O \rightarrow CO_2 + 2H^+ + 2e^-$ | D-cluster, [4Fe-4S]; 2 x B-cluster, [4Fe-4S]; 2 x C-cluster, [Ni4Fe-4S] |
| *anaerobic* CODH/ACS[184] | $CO_2 + 2H^+ + 2e- \rightarrow CO + H_2O$; CO + '$CH_3$' + CoASH → acetyl-Coenzyme A | D-cluster, [4Fe-4S]; 2 x B-cluster, [4Fe-4S]; 2 x C-cluster, [Ni4Fe-4S]; Ni-Ni-[4Fe-4S] |

[a] See section 1.7.1.1 for further details.

Turnover frequencies of up to 40,000 $s^{-1}$ have been measured for CO oxidation by Ni-CODH from the organism *Carboxydothermus hydrogenoformans* (*Ch*),[185] although the rate of $CO_2$ reduction is around ten times slower. This is unsurprising, given the aforementioned biological role of monofunctional CODH as a CO-oxidiser. The oxygen tolerant Mo-CODH from *Oligotropha carboxidovorans* is considerably slower (~50 $s^{-1}$).[186] This Thesis is concerned only with the monofunctional and anaerobic Ni-CODH. The structure and catalytic characteristics of this enzyme, which is completely inactivated by exposure to $O_2$,[185,187,188] are described in more detail in section 1.7.1. One of the most intensely studied Ni-CODH-containing organisms is the earlier mentioned thermophilic eubacterium *Carboxydothermus hydrogenoformans*. This species, which was isolated in a hot swamp on a volcanic island off the east coast of Russia,[189] grows at temperatures between 40-78 ºC and is able to grow chemolithoautotrophically with CO as the only source of carbon and energy. It expresses five CODH enzyme complexes, termed $CODH_{I-V}$, all of which have a [Ni4Fe-4S] active site.[190] The roles of $CODH_I$ and $CODH_{II}$ (the two CODHs used in this Thesis) are the

best understood, and these are represented in Figure 11 in terms of their roles in the bacterial cell. Note that from this point onwards the prefix 'Ni-' is not always used, and 'CODH' always refers to the monofunctional, anaerobic Ni-CODH enzyme.

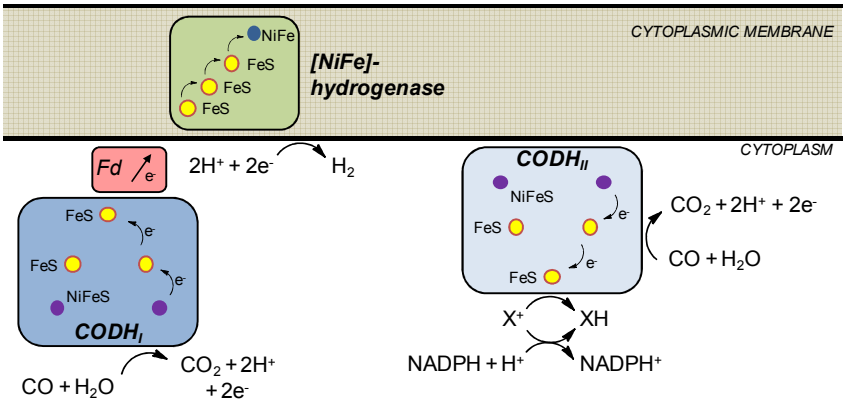


**Figure 11** Scheme showing the roles of $CODH_I$ and $CODH_{II}$ in *Carboxydothermus hydrogenoformans*. Both enzymes are membrane-associated. $CODH_I$ is used for energy generation; electrons released from CO oxidation are coupled to a [NiFe]-hydrogenase (see section 1.8), with electron transfer mediated by a ferredoxin (Fd). $CODH_{II}$ has a separate function, using the electrons released from CO oxidation for anabolic purposes, including $NADP^+$ reduction. Figure adapted from reference [185].

Both $CODH_I$ and $CODH_{II}$ are membrane-associated, and catalyse the same reaction (oxidation of CO to $CO_2$) with approximately the same activity.[185] The role of $CODH_I$ is to provide the cell with energy by using CO as a fuel. It is coupled to a [NiFe]-hydrogenase (these are discussed in section 1.8) by a ferredoxin, and electrons released from the oxidation of CO are transferred to the hydrogenase, which reduces protons to $H_2$. The overall reaction is:

$$CO + H_2O \rightarrow CO_2 + H_2 \qquad (\Delta G = -20 \text{ kJ mol}^{-1})$$

$CODH_{II}$ in the main part serves a different purpose, which is to provide electrons for anabolic purposes, reducing $NADP^+$ to NADPH. A cytoplasmic coupling factor ($X^+/XH$ in Figure 11) is required for this to occur, and it is likely that this is a ferredoxin:$NADP^+$ oxidoreductase.[185]

## 1.7.1 Ni-CODH: A HIGHLY SPECIALISED CATALYST FOR INTERCONVERSION OF CO AND $CO_2$

### 1.7.1.1 Ni-CODH STRUCTURE

X-ray crystal structures of Ni-CODH from *Ch*,[191,192] *Rhodospirillum rubrum* (*Rr*) [193] and *Moorella thermoacetica* (*Mt*, formerly known as *Clostridium thermoaceticum*)[175,177] have been reported. The Ni-CODH structure in each case is very similar. The crystallography of *Ch* $CODH_{II}$ by Dobbek *et al*. revealed the enzyme to be a heart-shaped homodimer (Figure 12) containing five metal clusters.[191,192] A [4Fe-4S] cluster, termed the D-cluster, is shared between the two subunits and is positioned close to the surface of the protein. This is the entry and exit points for electrons, which (for the natural CO-oxidation direction of catalysis in the monofunctional enzyme) are transferred to or from the electron acceptor (ferredoxin, flavodoxin *etc*.). Each subunit then contains another [4Fe-4S] cluster (B-cluster) that links the D-cluster to the active site (C-cluster), which is a [Ni4Fe-4S] cluster. The D- and B-clusters therefore 'wire' the buried active site to the surface of the protein. The separations of the D-/B-, and B-/C-clusters are shorter than 11 Å,[191] facilitating rapid electron transfer, and, although it is not clear from the dimeric crystal structure, it is actually the B-cluster of the *adjacent* subunit that mediates electron transfer between the D-cluster and the C-cluster. A hydrophobic channel (to deliver CO) and a solvent channel (to deliver $H_2O$) converge close to the Ni atom of the active site.[191] A histidine-lined tunnel also begins near the C-cluster and

continues to the surface of the protein, and it has been proposed that this facilitates the delivery of protons to the solvent.[191,193]

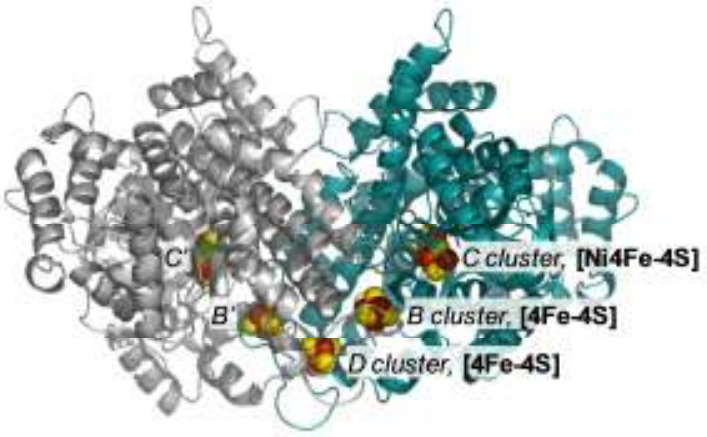


**Figure 12 The crystal structure of *Ch* $CODH_{II}$ (PDB code: 1SUF).** The protein has a mass of 136.6 kDa ($CODH_I$ is 137.0 kDa) and overall dimensions of around 88 x 63 x 60 Å.[191] The structure comprises a homodimer, with the two units shown in different colours.

The C-cluster is a [Ni4Fe-4S] unit, which can be considered as a [3Fe-4S] cluster connected to a NiFe binuclear site.[191,192] Figure 13 shows the C-cluster (the active site) with $CO_2$ bound: the carbon is coordinated to Ni which acts as a Lewis base, and one of the oxygens is coordinated by the Lewis-acidic, 'dangling' Fe. The crystallography at three different potentials provided significant insight into the catalytic mechanism (see later), through observation of the C-cluster in different states.[192] The Ni atom is in an approximately square planar coordination environment: it is bridged by two sulfurs of the cluster and a cysteine, with the fourth position being occupied by either water or substrate ($CO/CO_2$). The dangling Fe is coordinated by histidine and cysteine ligands.

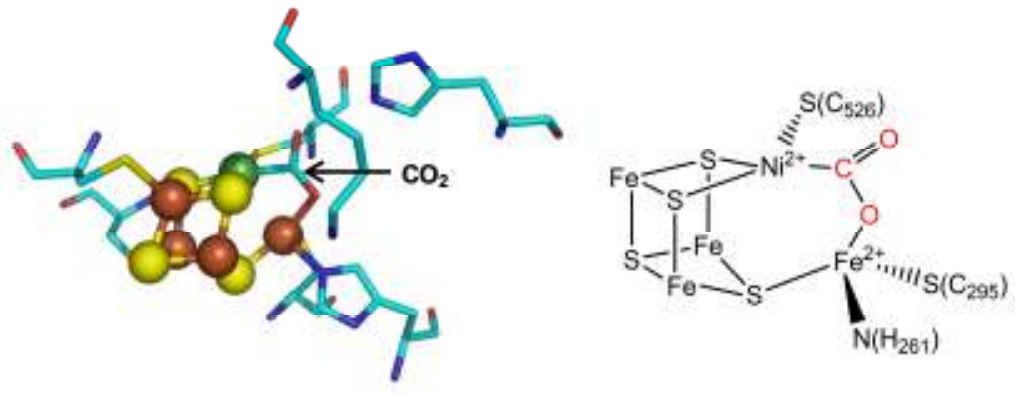


**Figure 13 The active site (ºC-cluster) of CODH, shown with $CO_2$ bound.** In the representation on the left, the Ni atom is shown in green, Fe in red and S in yellow. The cluster can be considered as a [3Fe-4S] cluster connected to a NiFe binuclear site, in which the Ni atom is in an approximately square planar coordination environment.

In the original 2001 paper detailing the characterisation of the $CODH_{II}$ active site, a sulfur atom was shown to be bridging the Ni and dangling Fe atoms, and it was thought that this was in some way necessary for catalysis.[191] However, subsequent crystallography with $CO_2$,[192] water[194] and cyanide[194] bound at the active site does *not* show a sulfur in this position, and it is now understood that any such bridging sulfur must be reductively or chemically replaced before the enzyme is catalytically active.[195]

#### 1.7.1.2 CODH STATES AND CATALYTIC CYCLE

Studies using a technique called protein film electrochemistry (PFE, which is described in detail in section 2.1.1) have demonstrated the bi-directional catalytic ability of *Ch* $CODH_I$, *i.e.* it is able to catalyse both CO oxidation and $CO_2$ reduction when immobilised on a pyrolytic graphite surface,[196] despite the fact that, as previously stated, its biological function is energy generation through CO oxidation. More recent work on the same enzyme has demonstrated the inhibitory effects on the catalytic activity of various small molecules, some

of which only have an effect within a certain potential range and must therefore be targeting certain states of the C-cluster.[197] One of these inhibitory species is sulfide, and the negative effect on catalysis is commensurate with the previously mentioned understanding that any such sulfur bridging the Ni and dangling Fe must be removed before the enzyme has catalytic activity.

Various techniques have been used to study the catalytic mechanism and redox states of Ni-CODHs from *Rr*,[198-202] *Mt*[175,177,182,198,203-211] and *Ch*.[191,192,198,203,204,212] There are four states of the C-cluster that are common to Ni-CODHs: $C_{ox}$, $C_{red1}$, $C_{int}$ and $C_{red2}$, the interconversions between which are shown in Figure 14.

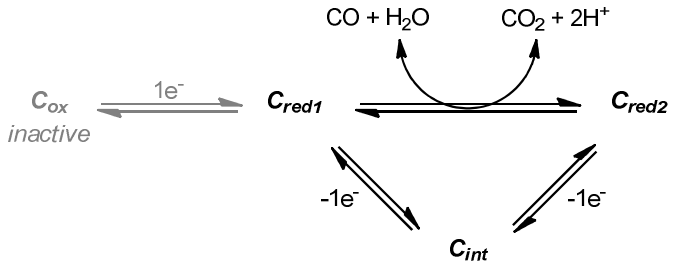


**Figure 14 The different states of Ni-CODH.**

Electron paramagnetic resonance (EPR) spectroscopy can be used to study the C-cluster: $C_{red1}$ and $C_{red2}$ are EPR-active, whereas $C_{ox}$ is EPR-silent. It is EPR spectroscopy that provides evidence for the C-cluster being the active site: the spectrum changes from that of the $C_{red1}$ state to that of the $C_{red2}$ state at a rate matching that of CO oxidation[213] (further evidence stems from the fact that the inhibitor cyanide has been observed to bind at the C-cluster).[211] The midpoint potentials for the one-electron reductions of $C_{ox}$ to $C_{red1}$ and of $C_{red1}$ to $C_{red2}$ are -200 mV and -530 mV respectively.[214] As described earlier, the C-cluster

can be considered as a [3Fe-4S] cluster connected to a NiFe binuclear site; in this depiction, the diamagnetic $C_{ox}$ state is proposed to comprise $[Ni^{2+}Fe^{3+}]$ bridged to $[3Fe\text{-}4S]^{1-}$.[182,215] The $C_{red1}$ state, which is formed upon a one-electron reduction of $C_{ox}$ at potentials below -200 mV [199,202,214] and has an overall electronic spin of ½, corresponds to $[Ni^{2+}Fe^{2+}]$ bridged to $[3Fe\text{-}4S]^{1-}$.[168,198] The $C_{red2}$ state is formed upon further reduction ($E$ = -520 mV at pH 7),[215,216] and the EPR spectrum is altered compared to that of $C_{red1}$. $C_{red2}$ is almost certainly two electrons more reduced than $C_{red1}$, although it is not known where exactly the extra electrons are localised.[199] It is likely that they are spread across the [3Fe-4S] cluster. Formally (and for convenience), the $C_{red2}$ state is represented with the electrons on the nickel atom, as in the catalytic mechanism that is outlined in Figure 15.[183,205]

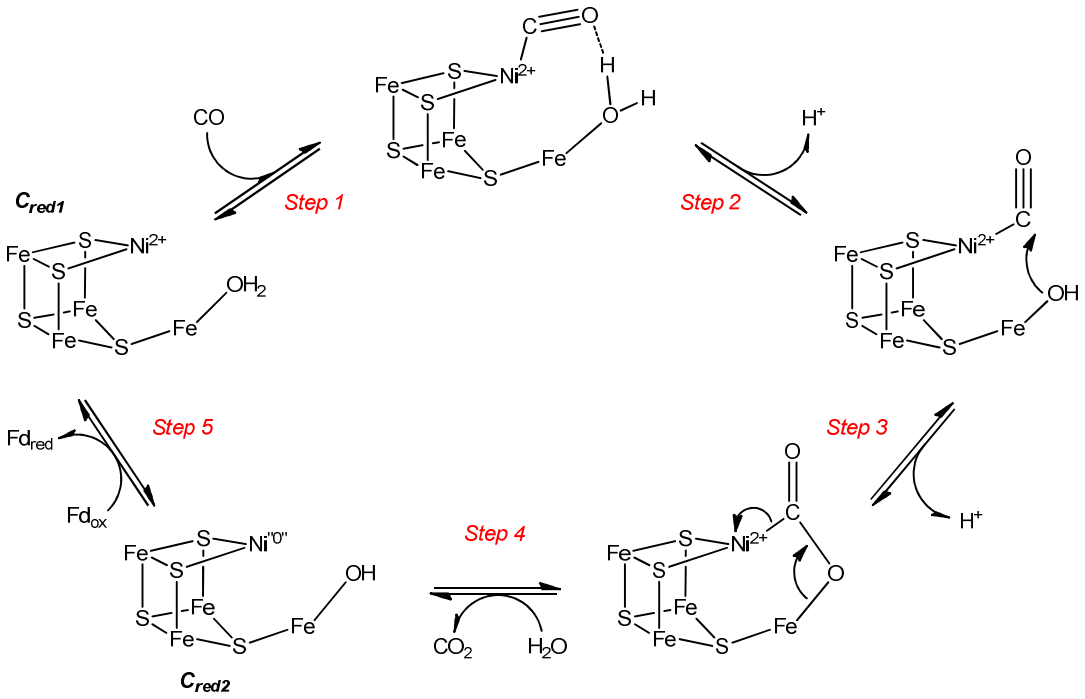


**Figure 15 Proposed mechanism for Ni-CODH-catalysed CO oxidation of CO to $CO_2$ at the C-cluster.** For clarity the residues coordinating the C-cluster are not shown. In particular, it should be noted that the Ni atom is in fact also coordinated by a cysteine ($C_{526}$, such that the $C_{red1}$ state has a distorted T-shaped coordination geometry), and the dangling Fe is also coordinated by a histidine ($H_{261}$) and a cysteine ($C_{295}$) such that when water is bound this Fe is approximately tetrahedrally coordinated. These residues can be seen in Figure 13. Fd = ferredoxin.

The stepwise process, for the direction of CO oxidation, is as follows (for $CO_2$ reduction, the same mechanism operates in the reverse direction):

*Step 1.* CO binds to the $C_{red1}$ state of the C-cluster, with the nickel atom coordinating the carbon atom. Evidence for this being the CO binding site is provided by X-ray crystallography of both CO-bound[217] and $CN^-$-bound states[194,218] (cyanide is a competitive inhibitor of CODH), FTIR[219] and X-ray absorption studies.[203]

*Step 2.* The Fe-bound water molecule is deprotonated. Histidine and lysine residues positioned close to the C-cluster are thought to assist with this step,[191,193] and mutagenesis experiments in which these residues were replaced substantiate this.[220]

*Step 3.* Hydroxide bound to the Fe atom attacks the CO carbon, forming a carboxylate that bridges the Ni and Fe atoms; Ni acts as a Lewis base, Fe as a Lewis acid. A stable seven-membered ring is formed at this point.

*Step 4.* $CO_2$ is eliminated, which is coupled, formally, to the two-electron reduction of $Ni^{2+}$ to $Ni^{"0"}$. In reality, it is likely that the two extra electrons are delocalised into the cluster, as opposed to remaining on the Ni.

*Step 5.* The C-cluster is re-oxidised by two sequential one-electron oxidations (*via* the $C_{int}$ state) by an external redox mediator such as ferredoxin (Fd).

Note the conformations of CO binding that have been drawn. No crystal structure of CO bound at the active site has been obtained for *Ch* CODH, but the structure of CO bound at *Methanosarcina barkeri* CODH shows a bent conformation (as drawn for the product of *Step 1* in the Figure 15 mechanism), with a Ni-C-O bond angle of 103º.[217] Similarly, *cyanide* (an inhibitor of CODH that is isoelectronic with CO) bound at the C-cluster of the enzyme from *Mt* is in a bent conformation.[194] As the product of *Step 1* stands, the distance between the dangling Fe-coordinated water and the carbonyl carbon atom is too great for catalysis. It has therefore been proposed that a 'shift' in coordination of CO must occur, such that the carbon atom moves closer to the water molecule.[195] This is supported by the position of the carbon atom in the crystal structure of the C-cluster with $CO_2$ bound[192] (as drawn in Figure 15 as the

product of *Step 3*), which is significantly different. Following such a shift, the Ni coordination geometry changes from distorted tetrahedral to square planar.

## 1.8 HYDROGEN CYCLING IN BIOLOGY

The emerging role of $H_2$ as an anthropogenic fuel was discussed in section 1.2, but this simplest of molecules has been used by many *microbes* as an energy source for millions of years.[221] Although the overall concentration of $H_2$ in the Earth's lower atmosphere is very low (around 0.5 ppm),[222] it is produced in certain environments through various biological processes and it is in these instances that $H_2$-utilising organisms are able to operate. Examples of $H_2$-producing processes in biology include nitrogenase-catalysed nitrogen fixation ($H_2$ is formed in a side-reaction),[223] and photobiological production in green algae such as *Chlamydomonas reinhardtii*.[224] The enzymes present in microbes that are responsible for the catalytic interconversion of $H_2$ and protons ($H_2 \leftrightarrows 2H^+ + 2e^-$) are called hydrogenases, of which there are three main classes: [NiFe]- and [FeFe]-hydrogenases (the notation indicates the bimetallic structures of the active sites), and mononuclear [Fe]-hydrogenases.[225] Generally, [NiFe]-hydrogenases are catalytically biased towards $H_2$ oxidation, and [FeFe]-hydrogenases towards proton reduction.[226] In microbial hydrogen uptake, the oxidation of $H_2$ is coupled to the reduction of an electron acceptor, *e.g.* reduction of $CO_2$ to $CH_4$ in methanogens,[227] or the reduction of sulphate to sulfide in *Desulfovibrio* and *Desulfomicrobium* species.[228]

Like the Ni-containing CODH described in section 1.7.1, bimetallic hydrogenases isolated from several different species have also been demonstrated to be highly efficient electrocatalysts (that is, only tiny overpotentials are required to drive catalysis in either

direction). Also, catalytic TOFs under mild conditions are very high – of the order of thousands per second.[226] These two reasons, together with the fact that the active sites contain only nickel and/or iron and no precious metals, mean that hydrogenases are the subjects of great interest, both for reasons of scientific curiosity and because they are expected to inspire the design of synthetic $H_2$-cycling catalysts that will be crucial in a future hydrogen economy.

### 1.8.1 STRUCTURE AND ACTIVE SITE OF [NiFe]-HYDROGENASE

Experiments in this Thesis involve a [NiFe]-hydrogenase termed hydrogenase 2 from *Eschericia coli* (*Ec*Hyd2),[229,230] the crystal structure of which has not yet been obtained. The [NiFe]-hydrogenase from *Desulfovibrio gigas* is often taken as a 'standard' model for [NiFe]-hydrogenases, and its crystal structure[231] is shown in Figure 16 together with a representation of the [NiFe] active site. There are two sub-units – the smaller one (32 kDa) contains a chain of iron-sulfur clusters (similar to that found in Ni-CODH), and the larger one (62 kDa) houses the active site. The active site is deeply buried within the protein, which protects the organometallic site from the surrounding aqueous environment. Gas channels[232] and several proton channels[232,233] extend from close to the active site to the surface of the protein to provide substrate access.

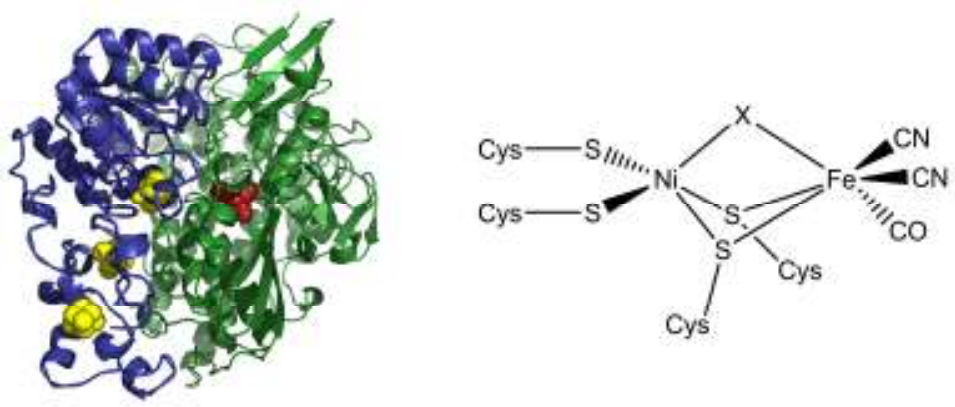


**Figure 16 The crystal structure and active site of the [NiFe]-hydrogenase from *Desulfovibrio gigas* (PDB code: 2FRV)** The crystal structure (left) shows the presence of three iron-sulfur clusters (yellow) that together act as an electron 'wire' to the active site (red). The enzyme is comprised of two subunits, termed 'large' and 'small'. The active site is deeply buried within the large subunit (green), and the iron-sulfur clusters are in the small subunit (blue). In the representation of the active site on the right, the identity of X depends on the state. If X = H, the enzyme is in an active state; if X = $OH^-$, the enzyme is inactive but 'ready'; and if inactive and 'unready', X is thought to be $OOH^-$ (see main text).

The chain of iron-sulfur clusters is a key feature of the architecture of both of the bimetallic classes, and has the purpose of mediating the transport of electrons between the surface of the protein and the active site. In [NiFe]-hydrogenases this chain consists of a [4Fe-4S] cluster closest to the active site, a second [4Fe-4S] cluster furthest away from the active site and closest to the protein surface, and a [3Fe-4S] cluster in between.[232] These are referred to as the proximal, distal and medial clusters, respectively, and the separations between them are typically 12 – 14 Å. It is understood that spacings of this size are short enough such that electron transfer does not limit the rate of enzymatic turnover.[234]

X-ray diffraction crystallographic studies by Volbeda *et al.* on [NiFe]-hydrogenase from *Desulfovibrio gigas* ascertained that the active site contains iron as the second metal, alongside nickel.[235] The Ni atom is coordinated by four cysteines, two of which bridge to the

Fe atom. The Fe atom is also coordinated by one CO and two $CN^-$ ligands.[236,237] The presence of the CO and $CN^-$ ligands – highly unusual in biology - means that the active site is well suited for study by infrared spectroscopy: the stretching modes of both CO and $CN^-$ are of strong intensity, and the force constants are highly sensitive to subtle variation in back donation from metal orbitals of π symmetry. Bagley *et al.* were the first to detect the infrared stretching frequencies of the CO and $CN^-$ ligands in the active site of [NiFe]-hydrogenase from *Allochromatium vinosum*,[238,239] and subsequent reports have made use of these spectroscopic handles to distinguish between different states of the active site.

The active site varies between several catalytically active or inactive states, depending on the identity of the bridging ligand labelled X in Figure 16. There are two main *inactive* states, denoted 'ready' ($X = OH^-$)[238,240] and 'unready' (X is thought to be $OOH^-$).[241] The 'ready' and 'unready' states are often referred to as Ni-B and Ni-A respectively. Conversion from active to inactive states can be caused by the presence of $O_2$, and the 'ready' and 'unready' states can be distinguished by the kinetics of their reductive re-activation: the 'ready' state reactivates much faster than the 'unready' state.[242,243] It has been suggested that in the *active* form of the enzyme, ligand X in Figure 16 is a hydride, in which case the '18-electron rule'[244] holds for both the Ni and Fe (assuming both of these are in the 2+ oxidation state). In the absence of ligand X the metal sites are unsaturated, and [NiFe]-hydrogenases are usually therefore sensitive to attack by small species such as $O_2$, CO and $S^{2-}$.[243] The π back-donation of electrons from transition metals to $O_2$ and CO means that these molecules are particularly potent inhibitors of the enzyme.[243]

### 1.8.2 CATALYTIC MECHANISM OF [NiFe]-HYDROGENASE

The catalytic mechanisms of both bimetallic hydrogenases have been extensively studied by various techniques, of which protein film electrochemistry (see section 2.1.1) has been particularly useful, and several key review papers summarise the current understanding.[226,232,233,243,245-247] In all active site states, the Fe is in the low-spin 2+ state, due to the strong field CO and $CN^-$ ligands.[248] The oxidation state of the Ni varies between 1+, 2+ and 3+, with the states containing $Ni^{1+}$ and $Ni^{3+}$ being characterisable by EPR spectroscopy. Further details of the various states are not directly relevant to this Thesis, but are well documented in the previously mentioned review papers.

The catalytic cycle is still not fully understood, especially in regard to the site of $H_2$ binding.[249] It is known that the inhibitor CO binds to the Ni, and also that the gas channel that transports substrate to the active site ends closer to Ni than Fe; this evidence would suggest, therefore, that $H_2$ binds at Ni. However, it has also been proposed, for example by Hall and co-workers on the basis of density functional theory studies, that $H_2$ actually binds at Fe.[250] Regardless of the identification of the initial binding step, it is accepted that the next step is the base-assisted heterolytic cleavage of $H_2$ to form a hydride that bridges the $Ni^{2+}$ and $Fe^{2+}$. The proton is bound to one of the Ni-coordinating cysteines. Hall and co-workers suggest the following mechanism for the rest of the cycle: the $Ni^{2+}$ is oxidised to $Ni^{3+}$ (the electron is transferred to the iron-sulfur relay), and the cysteine deprotonated. The bridging hydride then shifts to the cysteine as a proton, with the electrons being transferred to $Ni^{3+}$ to form $Ni^{1+}$, before a second electron is injected into the iron-sulfur relay to reform the initial $Ni^{2+}Fe^{2+}$ state.

# 2 METHODS, MATERIALS & ELECTROCHEMICAL THEORY

## 2.1 ELECTROCHEMICAL METHODS

### 2.1.1 PROTEIN FILM ELECTROCHEMISTRY

Protein film electrochemistry (PFE) is a suite of electrochemical techniques that can be used to investigate the catalytic (and non-catalytic) behaviour of redox-active protein molecules.[251-253] The sample is adsorbed onto an electrode surface to provide monolayer or sub-monolayer coverage, which for an electrode having diameter of a few millimetres usually corresponds to less than 1 pmol.[243,252,254] The most commonly used electrodes are graphite (usually edge plane) because of the presence of various oxygen-containing functional groups such as -COOH and -COH, which are understood to be responsible for spontaneous protein adsorption.[253,255,256] The requirement for only tiny amounts of protein makes PFE a particularly attractive technique for the study of enzymes, for which preparation is time-consuming and yields often low.[185,230] Before the discovery and development of PFE, electrochemical investigations of proteins almost exclusively used high concentrations of protein in solution, together with mediators to shuttle electrons to and from the electrode. A second major advantage of PFE, therefore, is that the slow diffusion of mediators is no longer a complicating factor.

When PFE is applied to the study of redox-active enzymes (as is the case in this Thesis), the factors affecting the current can, conceptually, be considered as three resistors connected in series.[257] These are shown in Figure 17, and discussed in section 2.1.1.2.

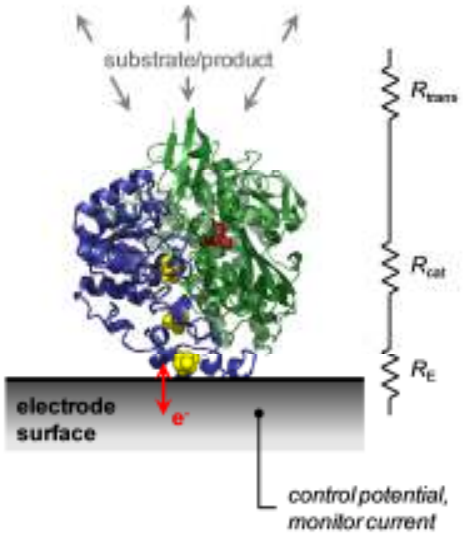


**Figure 17 Cartoon representation of the technique of protein film electrochemistry (PFE) as applied to the study of enzymatic catalysis of redox reactions.** Enzyme molecules are attached directly onto the surface of the electrode, which in this Thesis is either pyrolytic graphite (edge plane) or $TiO_2$. Possible rate determining steps are represented by a series of resistors connected in series: $R_E$ corresponds to interfacial electron transfer between the electrode surface and the entry/exit site into the electronic relay chain (represented here by yellow clusters); $R_{cat}$ corresponds to electron transfer to through the enzyme molecule; $R_{trans}$ corresponds to the transport of substrate and product to or from the electrode. The concept of considering electron transfer as being through a set of in-series resistors is taken from reference [257]. The enzyme used in this cartoon is (arbitrarily) [NiFe]-hydrogenase from *Desulfovibrio gigas* (PDB code: 1FRV).

Two types of PFE experiment are used in this Thesis. In *cyclic voltammetry* experiments, current is recorded whilst the potential of the working electrode (at which the protein sample is adsorbed) is continually swept between two values at a specified rate. In *chronoamperometry* experiments, the electrode is held at a constant value while the current is recorded. Therefore, while cyclic voltammetry experiments suffer from the fact that time and potential are convoluted, this is not the case with chronoamperometry. Since the protein molecules are directly attached to the electrode surface they experience almost exactly the potential that is applied, and assuming that they are attached such that electron transfer is

possible then the electrode acts as an unlimited electron source or sink. The recorded current consists of two components: a non-Faradaic (capacitative) current and a Faradaic (non-capacitative) current. These are now discussed in turn.

#### 2.1.1.1 NON-FARADAIC CURRENTS

As the potential of the working electrode is swept in a cyclic voltammetry experiment, charge builds up on the surface of the electrode. Ions in solution arrange themselves in response to this, accumulating at the surface as the charge on the electrode is increased, thus forming an electrical double layer.[258] The current that is recorded from the charging and de-charging of the double layer is referred to as non-Faradaic current, and the analogy that can be made with the behaviour of a capacitor means that this is also sometimes referred to as 'capacitative' current, the size of which depends on the surface area of the electrode, the scan rate and the solution composition.[258] Figure 18 depicts the principle of a cyclic voltammetry experiment in which the potential of the working electrode is swept between values of $E_1$ and $E_2$, and an example of the resulting non-Faradaic current that is obtained with a 'blank' (*i.e.* unmodified) graphite electrode.

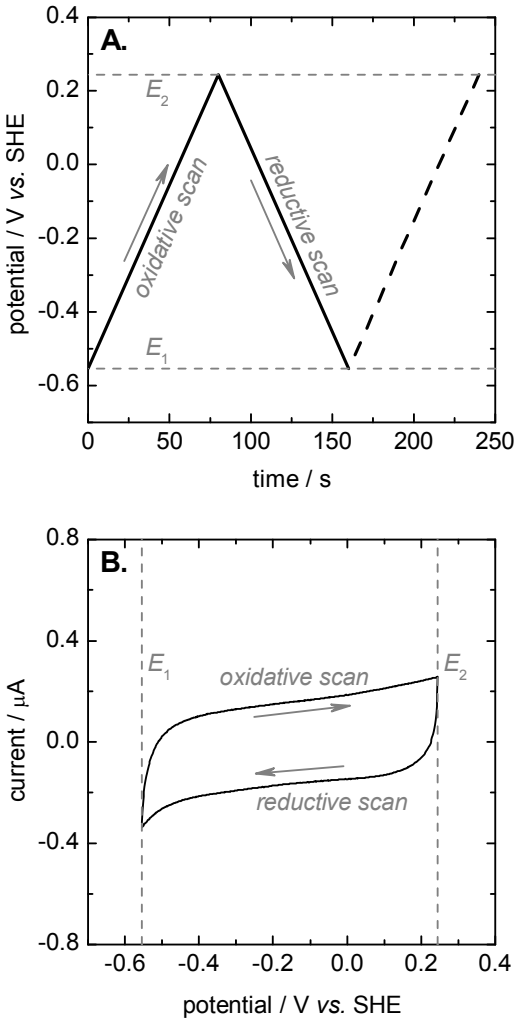


**Figure 18 Principle of a cyclic voltammetry experiment, and the recorded non-Faradaic (capacitative) current response from an experiment using a 'blank' (unmodified) pyrolytic graphite working electrode.** (A) Variation in applied potential with time, between values of $E_1$ and $E_2$ at a scan rate of 10 mV $s^{-1}$ (in this example, $E_1$ = -0.55 V and $E_2$ = 0.24 V). (B) The non-Faradaic (capacitative) current recorded at a pyrolytic graphite electrode when it is swept from $E_1$ to $E_2$, and back to $E_1$. This voltammogram was recorded at 20 ºC with an electrode of surface area 0.03 $cm^2$, in 0.20 M MES (pH 6).

#### 2.1.1.2 FARADAIC CURRENTS

Faradaic currents correspond to redox processes occurring at the working electrode. In principle, both catalytic and non-catalytic currents can be detected by PFE. The latter arise from the transfer of electrons into, or out of, redox sites in the protein molecule, and cyclic voltammograms might therefore be expected to contain a pair of oxidation and reduction peaks for each site, centred at the potential of the couple. These signals (called non-turnover signals) are in practice often difficult to detect, since the electroactive coverage of most proteins is usually very low. In any case, these signals are not of interest in this Thesis. For enzymatic PFE, if there are substrate species present in solution then *catalytic* currents are expected at sufficient overpotentials potentials (driving forces). The currents that are recorded (from the transfer of electrons into or out of the enzyme molecules) are superimposed onto the 'background' non-Faradaic current. By IUPAC convention, anodic (*i.e.* oxidative) currents are plotted in the positive direction, and cathodic (*i.e.* reductive) currents are plotted in the negative direction. Currents recorded during chronoamperometry experiments also include non-Faradaic components, although these decay exponentially after the potential is initially set.[256]

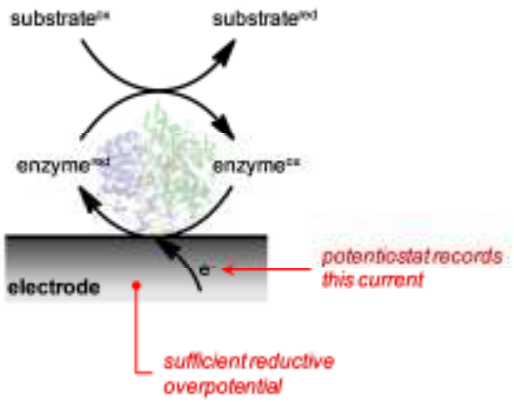


**Figure 19 Scheme representing electrocatalytic reduction in a PFE experiment.** At sufficient overpotential, the electrode transfers electrons into the oxidised form of the enzyme (enzyme$^{ox}$, reducing it to enzyme$^{red}$); enzyme$^{red}$ is then re-oxidised by the oxidised form of substrate, which itself is reduced. The transfer of electrons out of the electrode is recorded as a negative current.

The Faradaic current should ideally be a direct measure of the rate of the redox reaction within the protein. However, as illustrated in Figure 17, the overall current is not only affected by the flow of electrons through the protein but also by the 'resistances' of the interfacial electron transfer with the electrode surface and of the rate of transport of substrate species to the enzyme. In this Thesis, all of the PFE experiments are catalytic (*i.e.* they probe the enzyme-catalysed turnover of substrate, Figure 19). In order for the enzyme active site to be the control centre that determines the potential of catalytic activity, the rate of reaction at the active site must be slower than the rates of the other processes (*i.e.* interfacial electron transfer and mass transport).

#### 2.1.1.2.1 EFFECTS OF INTERFACIAL ELECTRON TRANSFER AND MASS TRANSPORT

The Butler-Volmer equation describes the relationship between Faradaic current (interfacial electron transfer) and electrode potential, assuming that the redox reaction occurs in both

directions. Consider the interconversion of an oxidised species (ox) and a reduced species (red) at an electrode, having the rate constants $k_{red}$ and $k_{ox}$:

$$\mathrm{ox} + n\mathrm{e}^- \underset{k_{ox}}{\overset{k_{red}}{\rightleftharpoons}} \mathrm{red} \qquad \text{Equation 1}$$

The current, $i$, flowing through the electrode is given by the equation :

$$i = jAF \qquad \text{Equation 2}$$

where $j$ is the net flux of electrons (units of moles (unit area)$^{-1}$ s$^{-1}$), $A$ is the surface area of the electrode, and $F$ is the Faraday constant.

The net flux, $j$, is the sum of the oxidative and reductive fluxes ($j_{ox}$ and $j_{red}$), which are given by:

$$j_{ox} = nk_{ox}\Gamma_{red} \qquad \text{Equation 3}$$

$$j_{red} = -nk_{red}\Gamma_{ox} \qquad \text{Equation 4}$$

where $\Gamma_{red}$ and $\Gamma_{ox}$ are the electroactive coverages (per unit area) at the electrode of the reduced and oxidised species, and $n$ is the number of electrons involved in the interconversion of ox and red.

The oxidative and reductive currents, $i_{ox}$ and $i_{red}$, are therefore given by:

$$i_{ox} = nk_{ox}\Gamma_{red}AF \qquad \text{Equation 5}$$

$$i_{red} = -nk_{red}\Gamma_{ox}AF \qquad \text{Equation 6}$$

The standard electron transfer exchange rate constants, $k_{0,ox}$ and $k_{0,red}$, refer to the rates of electron transfer in the absence of any overpotential. $k_{ox}$ and $k_{red}$ differ from $k_{0,ox}$ and $k_{0,red}$ according to the equations:

$$k_{ox} = k_{0,ox}e^{(1-\alpha)nf(E-E^{\theta'})} \quad \text{Equation 7}$$

$$k_{red} = k_{0,red}e^{-\alpha nf(E-E^{\theta'})} \quad \text{Equation 8}$$

where $\alpha$ is known as the transfer coefficient[258] (a value between 0 and 1 that accounts for the symmetry of the barrier to electron transfer),[§] $f = F/RT$, $E$ is the applied electrode potential and $E^{\theta'}$ is the potential of the mixture of ox and red at equilibrium under standard conditions (calculated using the Nernst equation). The total interfacial current at the electrode can now be found:

$$i = i_{ox} + i_{red} \quad \text{Equation 9}$$

$$= nFAk_{ox}\Gamma_{red} - nFAk_{red}\Gamma_{ox} \quad \text{Equation 10}$$

$$= nFA(k_{ox}\Gamma_{red} - k_{red}\Gamma_{ox}) \quad \text{Equation 11}$$

$$= nFA(k_{0,ox}\Gamma_{red}e^{(1-\alpha)nf(E-E^{\theta'})} - k_{0,red}\Gamma_{ox}e^{-\alpha nf(E-E^{\theta'})}) \quad \text{Equation 12}$$

At equilibrium, $k_{0,ox} = k_{0,red} = k_0$, which enables the Butler-Volmer equation to be obtained:[258]

$$i = nFAk_0(\Gamma_{red}e^{(1-\alpha)nf(E-E^{0'})} - \Gamma_{ox}e^{-\alpha nf(E-E^{0'})}) \quad \text{Equation 13}$$

[§] An $\alpha$ value near to 0 implies that the transition state closely resembles the reactants; a value near to 1 implies that it closely resembles the products.

To be able to extract the maximum amount of information on enzymatic catalysis from a PFE experiment, the current that is measured must not be limited by the rate of diffusion of substrate to the electrode surface. In order to eliminate mass transport limitation, electrodes may be rapidly rotated (at several thousand rpm), which induces a laminar flow pattern (forced convection) of solution towards the electrode surface.[259] In cases where the current *is* limited by the rate of substrate mass transport ($i = i_{lim}$), current increases with the square of the rotation rate, as described by the Levich equation:[259]

$$i_{lim}=0.62nF[S]_{bulk}D^{2/3}\nu^{-1/6}\omega^{1/2} \qquad \text{Equation 14}$$

where $[S]_{bulk}$ is the bulk solution substrate concentration, $D$ is the diffusion coefficient of the substrate, $\nu$ is the kinematic viscosity of the solvent and $\omega$ is the electrode rotation rate.

Rotating electrodes were used in this Thesis where appropriate. Sufficiently high rotation rates (≥ 2000 rpm) were used so that catalytic currents were not dependent on this factor (this was checked by stepping to higher rotation rates momentarily), and therefore the electrochemistry reflects the inherent properties of the enzymes rather than mass transport limitation.

#### 2.1.1.2.2 THE CURRENT-POTENTIAL WAVESHAPE FOR AN IDEAL ELECTROCATALYST

In the presence of substrate, catalytic turnover occurs when the enzyme is subjected to sufficient thermodynamic driving force (*i.e.* overpotential). Figure 20 shows the 'waveshape' of catalytic current as a function of potential for an ideal electrocatalyst at an electrode. Arbitrarily, since the current plotted here is positive, this example is for an oxidative process.

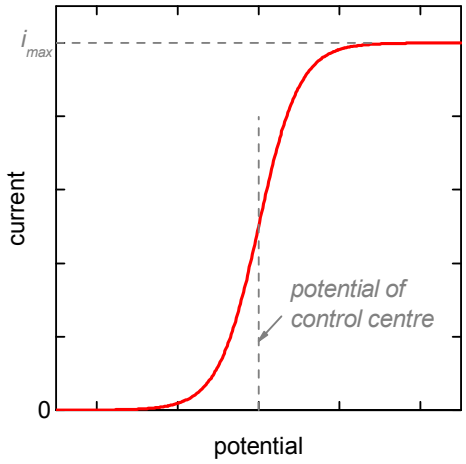


**Figure 20 Catalytic current as a function of potential for an ideal electrocatalyst.** The potential of the control centre (often the active site in the case of an enzyme) is the potential around which the rate of current increase is at its maximum. $i_{max}$ is the current at very high overpotential, at which point the rate of catalysis is no longer limited by the rate of electron transfer.

The current has a sigmoidal dependence on potential. Catalysis occurs at potentials more positive than the thermodynamic potential for the redox reaction under the conditions of the experiment, as determined by the Nernst equation. At small or moderate overpotentials, current increases with driving force, since the rate of catalysis is determined by the rate of electron transfer. At very high overpotential, the current plateaus at a value of $i_{max}$ (Figure 20). Now, the rate of catalysis is not potential-dependent, and instead depends on other factors (the inherent catalytic nature of the enzyme). Assuming that the system is not mass transport-limited (see earlier), this current reflects the maximum TOF of the enzyme, $k_{cat}^{max}$, according to:

$$i_{max}=nFA\Gamma k_{cat}^{max} \qquad \text{Equation 15}$$

This relationship therefore allows the maximum TOF of the enzyme to be calculated, assuming that the electroactive coverage, $\Gamma$, is known. This value may be calculated from non-turnover signals, from which the area under each peak is proportional to $Av\Gamma$.[253] However, as mentioned earlier, such signals are difficult to detect for large enzymes having multiple redox centres.

## 2.1.2 ELECTROCHEMICAL SETUP

### 2.1.2.1 THE THREE-ELECTRODE SYSTEM

For all of the electrochemical experiments in this Thesis, a three-electrode setup, as represented by Figure 21, is used.

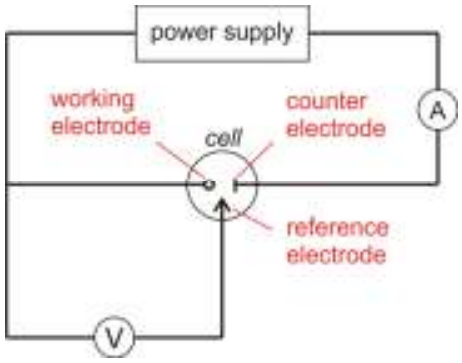


**Figure 21 A schematic circuit diagram of showing the principle of operation of the three-electrode system used in this Thesis.** A = ammeter, V = voltmeter (in practice these are inbuilt into the potentiostat, see section 2.1.2.2).

The voltage, $E$, is applied between the working and reference electrodes. In the absence of a counter electrode, $E$ is given by equation 16:

$$E = (\Phi_w - \Phi_s^w) + iR_s + (\Phi_s^{ref} - \Phi_{ref}) \qquad \text{Equation 16}$$

where $\Phi_w$ and $\Phi_{ref}$ are the electric potentials of the working and reference electrodes, $i$ is the current flowing between them, and $\Phi_s^w$ and $\Phi_s^{ref}$ are the electric potentials of the solution very close to the working and reference electrodes. The term $iR_s$ represents the electrical resistance of the electrolyte solution between the working and reference electrodes. This is sometimes referred to as the 'voltage drop,' and can be significant except for in the case of microelectrode studies. PFE experiments rely on precise control of the potential of the working electrode, and it is therefore essential that the reference electrode (in this Thesis, either a saturated calomel electrode (SCE) or an Ag/AgCl electrode (both BASi)) provides a constant value of ($\Phi_s^{ref}$-$\Phi_{ref}$). In a two-electrode setup, current would necessarily flow through the reference electrode, resulting in changes in the potential difference between the reference electrode and the nearby solution ($\Phi_s^{ref}$-$\Phi_{ref}$). For this reason, a third (counter) electrode is used, which in this Thesis is always Pt wire having as surface area greater than that of the working electrode. The potential of the counter electrode is controlled by the potentiostat such that the current flow balances that at the working electrode, and hence the current flow through the reference electrode is minimal.[258]

#### 2.1.2.2 POTENTIOSTAT EQUIPMENT AND SOFTWARE

All electrochemical experiments are carried out using either an Autolab PG10 with GPES software, or an Autolab PGSTAT101 and NOVA software (all manufactured and supplied by EcoChemie).

#### 2.1.2.3 ELECTROCHEMICAL CELLS

Two types of electrochemical cell (Figure 22) are used in this Thesis, both of which were manufactured from glass and according to custom designs by Terri Adams (University of Oxford).

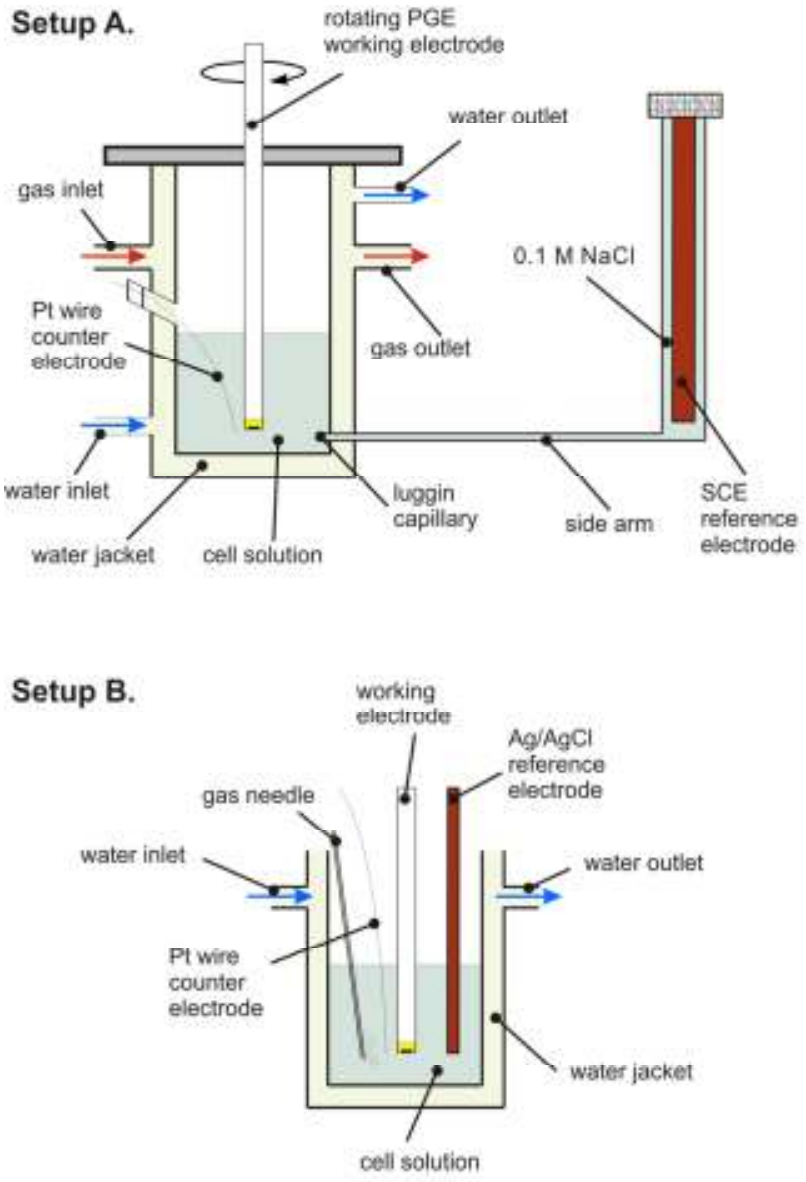


**Figure 22 Electrochemical cell setups for PFE experiments.** Setup A is used for experiments in chapter 3, in which a rotating PGE electrode (see section 2.1.2.4) is used in conjunction with a sealed cell. In this setup, gases are flowed through the headspace, and the reference electrode (SCE) housed in a side arm, separated from the main cell body by a luggin capillary. Setup B (a one-compartment cell, left open to the glove box atmosphere) is used for experiments in chapters 4 and 5, with stationary electrodes (either $TiO_2$ thin film or PGE, section 2.1.2.4). The reference electrode (Ag/AgCl) is positioned in the same cell compartment as the working and counter electrodes; and gases gently bubbled directly into the cell solution. Temperatures of cell solutions are controlled by the water jackets, through which thermostated water is continually flowed. In both setups, the counter electrode is a Pt wire.

Setup A is used for all PFE experiments in chapter 3, with an earthed electrode rotator (EG&G M636, not shown) clamped tightly around the top of the cell with gases purged through an inlet and outlet. The reference electrode is separated from the main cell body, such that it remains at ambient temperature. In chapters 4 and 5 setup B is used, in which the cell is left open to the glove box atmosphere and gases bubbled gently into the electrolyte solution. In both cases, the temperature is controlled by a water jacket through which thermostated water is continually pumped. All potentials are adjusted to the standard hydrogen electrode from SCE according to equation 17,[258] or from Ag/AgCl by equation 18:[260]

$$E_{SHE} = E_{SCE} + 0.242 \text{ V at } 25 \text{ ºC} \qquad \text{Equation 17}$$

$$E_{SHE} = E_{Ag/AgCl} + 0.208 \text{ V at } 25 \text{ ºC} \qquad \text{Equation 18}$$

#### 2.1.2.4 WORKING ELECTRODES

Three kinds of working electrodes are used in this Thesis: rotating disc PGE electrodes, stationary PGE electrodes, and stationary $TiO_2$ thin film electrodes. The PGE electrodes are used for electrochemical studies of enzymes; the $TiO_2$ thin film electrodes are used for electrochemical studies of enzymes, and also of a ruthenium photosensitiser (see section 2.4.2.2).

In PGE electrodes, the graphite is aligned such that the edge plane is exposed and in contact with electrolyte solution. Immediately before electrochemical experiments, the electrode tips are abraded using sandpaper (P800, RS Electronics) to expose a clean and rough surface. *Rotating disc* PGE electrodes are used with a rotator (EG&G) through which the electrical

connection is made; *stationary* PGE electrodes are simply connected into the cell using crocodile clips. Details on the construction of PGE electrodes are given in section 2.1.2.4.1.

The $TiO_2$ thin film working electrodes, having a geometric area of around 5 mm x 5 mm, are (by definition) not suited to sanding and therefore a fresh electrode is used for each new experiment. The method of preparation of $TiO_2$ thin films, and subsequent conversion into electrodes, is described in section 2.1.2.4.2.

#### 2.1.2.4.1 PREPARATION OF PGE WORKING ELECTRODES

*Rotating disc* PGE electrodes (Figure 23A) were prepared by joining a cylindrical piece of pyrolytic graphite (length 10 mm, diameter 2 mm, with the circular face being the edge-plane) onto a steel rod (length ~ 100 mm) with conducting silver epoxy (RS Components). The steel rod is housed inside a Teflon (PTFE) case, and is thus insulated from the electrolyte solution. The protruding graphite section was surrounded by epoxy resin (non-conductive, RS Components), leaving just the edge-plane face exposed. The Teflon case contains an internal steel screw thread, which completes the electrical connection with the electrode rotator when screwed in place.

*Stationary* PGE electrodes (Figure 23B) were prepared in a similar manner, by attaching a cuboid section of pyrolytic graphite to a steel rod (length ~ 100 mm), which is again housed inside a Teflon (PTFE) case. The steel rod in this case protrudes from the opposite end of the casing, such that a crocodile clip can connect to the electrode.

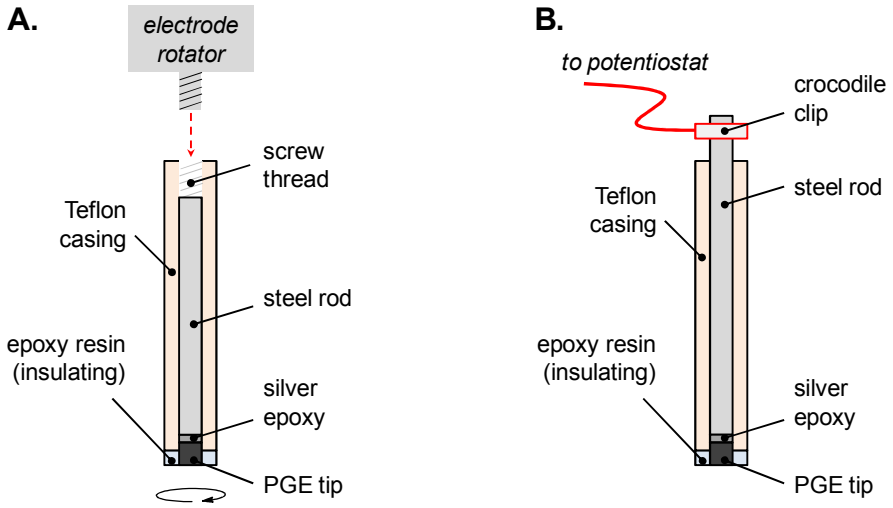


**Figure 23 The construction of PGE electrodes.** (A) rotating disc; (B) stationary.

#### 2.1.2.4.2 PREPARATION OF $TiO_2$ THIN FILM ELECTRODES

The method of preparation of $TiO_2$ thin film electrodes was as follows. To prepare a batch of ten electrodes, 0.2 g P25 $TiO_2$ nanoparticles (section 2.4.2.1) were dispersed by sonication in 0.1 M $HNO_3$ (700 mg $TiO_2$ (mL $HNO_3$)$^{-1}$) for 30 min. Glass slides coated with indium tin oxide (ITO, supplied by SPI) were cut to dimensions of approximately 25 x 10 mm and cleaned by sonication in acetone, ethanol and then water (10 min in each). Once dry, approximately 20 µL of the P25 $TiO_2$ suspension was dropped onto the ITO-coated face of the glass slide. The 'Doctor's Blade' technique[261] was used to create a film of $TiO_2$ suspension covering an area of approximately 10 mm x 10 mm at one end of the slide, with the thickness controlled by a layer of Scotch tape. The electrode was allowed to dry at room temperature for 1 h before calcination in a furnace at 450 ºC (ramped from room temperature at a rate of 5 ºC min$^{-1}$, and allowed to return to room temperature slowly overnight, Figure 24 photograph (a)). Then, an electrical connection was made from the non-coated end of the ITO to a copper wire, using silver epoxy adhesive (photograph (b)). After this was dry (~ 30

min), a small section of glass tubing, attached to the glass slide using epoxy adhesive, was used to encase the copper wire in order to insulate the metal from electrolyte cell solution. Finally, epoxy adhesive was used to insulate excess ITO and $TiO_2$, such that a single area of $TiO_2$ film of dimensions 5 mm x 5 mm remained exposed (photograph (c)). Electrodes were stored in the dark and used within one week of preparation.

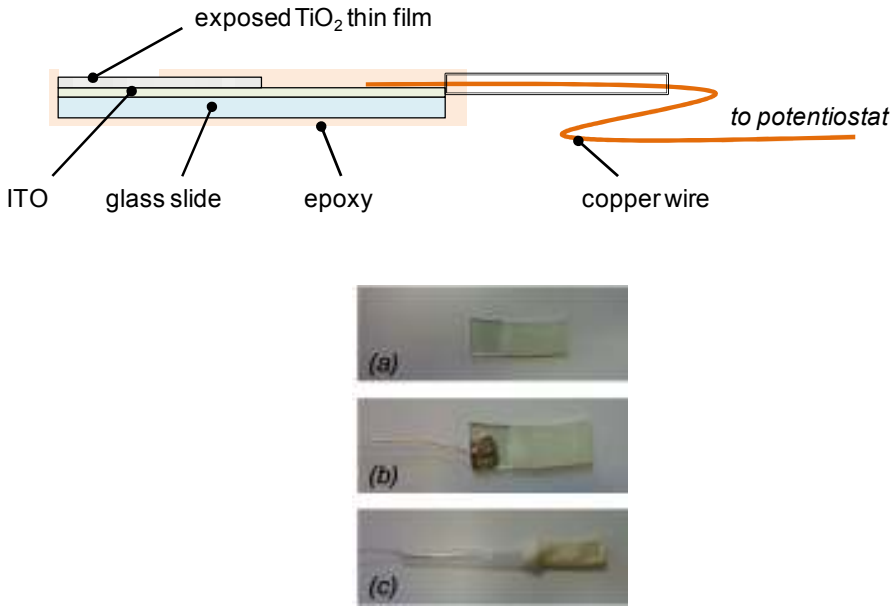


**Figure 24 $TiO_2$ thin film electrode, and photographs at various stages of preparation as described in the main text.**

#### 2.1.2.4.3 MODIFICATION OF WORKING ELECTRODES WITH ELECTROCHEMICALLY ACTIVE SPECIES

PGE electrodes are only used for PFE experiments. For each enzyme (*Ec*Hyd2, $CODH_I$ and $CODH_{II}$; see section 2.4.1), the method of electrode modification is identical. The electrode surface is thoroughly abraded with sandpaper (Tufbak Durite, P800 grade), before sonicating in purified water and rinsing thoroughly. The PGE surface is then carefully dried, before

spotting 2 - 4 μL of enzyme solution on and off the surface for 10 – 20 s. Concentrations of enzyme solutions were: 1.5 μM (*Ec*Hyd2), 0.12 – 0.18 mM ($CODH_I$), 0.14 mM ($CODH_{II}$). The electrodes are then connected into the electrochemical cell.

$TiO_2$ thin film electrodes are used both for PFE experiments (with $CODH_I$ and $CODH_{II}$), and for electrochemical experiments with RuP attached at the surface. The method for modification of these electrodes with enzymes, as optimised by preliminary experiments, is as follows. 2 - 4 μL of enzyme solution (concentration as before) is spotted on and off the dry $TiO_2$ surface for around 1 min. The surface of the electrode is allowed to almost completely dry (~ 2 min), before connecting into the electrochemical cell.

To modify $TiO_2$ thin film electrodes with RuP, the following method is used. The electrode is positioned in a glass vial containing ~ 3 mL of 40 μM RuP in 0.20 M MES (pH 6.0), such that the $TiO_2$ film is leaning against the side of the vial in an almost vertical position. The solution is gently stirred for 1 h to allow attachment of RuP to $TiO_2$. After this time, the electrode (now orange in colour, indicating successful attachment of RuP) is rinsed with purified water, and connected into the electrochemical cell.

For both PGE and $TiO_2$ electrodes, the addition of enzyme solutions into the electrolyte solution (as opposed to spotting directly onto the electrode) yields either no catalytic current, or only trace activity as compared to when the electrode surface is modified.

PGE electrodes are re-used for multiple experiments, with thorough sanding between experiments in order to remove old enzyme films. $TiO_2$ thin film electrodes are used for one experiment each only, since enzyme films, once applied, cannot be removed.

## 2.2 SOLUTION ASSAY FOR $CO_2$ REDUCTION ACTIVITY OF $CODH_I$

Solution assays are performed in an anaerobic glove box ($O_2$ < 3 ppm) in order to determine the $CO_2$ reduction activity of $CODH_I$ under mildly reducing conditions. A 0.2 µmol aliquot (10 µL, 20 mM) of electrochemically reduced methyl viologen ($MV^{\bullet+}$, $\lambda_{max}$ = 604 nm, $E^{o}$ = -0.44 V) is added to 1 mL of $CO_2$ saturated MES buffer solution (pH 6, 20 °C). 66 pmol of $CODH_I$ is injected (giving a final enzyme concentration of 66 nM) and the absorbance at 604 nm monitored over time. The initial rate of $MV^{\bullet+}$ oxidation is used to determine the initial TOF of $CODH_I$-catalysed $CO_2$ reduction.

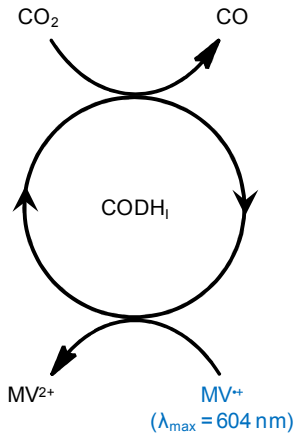


**Figure 25 Scheme showing the principle of the spectroscopic assay for $CO_2$ reduction activity of $CODH_I$.** The rate of oxidation of $MV^{+\bullet}$ to $MV^{2+}$ (a one electron process) is twice the rate of CODH-catalysed $CO_2$ reduction (a two electron process).

## 2.3 OTHER ANALYTICAL TECHNIQUES

### 2.3.1 GAS CHROMATOGRAPHY

Gas chromatography (GC) is used for the separation and detection of $H_2$, CO and $CH_4$ using an Agilent Technologies 7890A GC instrument with a thermal conductivity detector. 10 µL

aliquots of gas are used for analysis, which are extracted from reaction vessel headspaces and injected into the GC using a gas-tight Hamilton syringe.

For the separation and detection of CO and $CH_4$ in chapters 4, 5 and 6, a Restek ShinCarbon ST micropacked column (held isothermally at 31 ºC) is used, with He carrier gas and a constant pressure of 35 psi. An example of a typical set of chromatograms is shown in Figure 26; these are from a photocatalytic experiment carried out over the course of 4 h, in which a [RuP-$TiO_2$-$CODH_I$] system (see chapter 4) reduces $CO_2$ to CO under visible light irradiation.

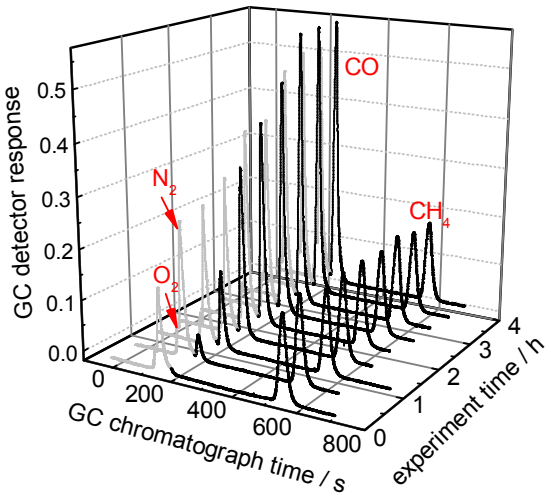


**Figure 26 A typical series of gas chromatograms recorded over the course of 4 h at 30 min intervals, showing production of CO by a photocatalytic [RuP-$TiO_2$-$CODH_I$] system (see chapter 4 for details).** The initial portions of the chromatograms (in grey, so that the CO peaks are not obscured) show $O_2$ and $N_2$ peaks, the presence of which are attributed to trace amounts of air entering the GC inlet or from the reaction vessel headspace.

Amounts of CO are quantified against an internal standard (2% $CH_4$), with reference to calibration plots obtained with various known amounts of CO (an example of which is shown in Figure 27). Chromatogram peak areas are found using Agilent EZChrom Elite software.

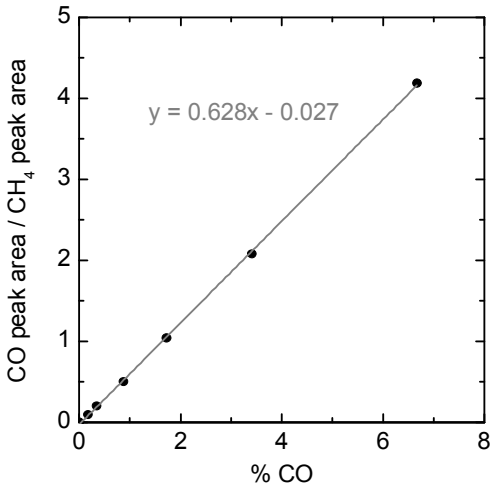


**Figure 27 Typical calibration plot for quantification of CO in chapters 4, 5 and 6, using the CO:$CH_4$ peak area ratio.** To construct this plot, chromatograms are obtained by analysing samples from a reaction vessel containing a 2% $CH_4$ internal standard and known amounts of CO. A Restek ShinCarbon ST micropacked column (held isothermally at 31 ºC) is used, with He carrier gas and a constant pressure of 35 psi.

The conversion factor obtained from the calibration plot in panel A (0.628) allows the amount of headspace CO to be quantified according to the formulae:

% CO = (CO peak area / $CH_4$ peak area) / 0.628

moles CO = (% CO / 100) x ($\alpha$ $dm^3$ / 22.4 $dm^3$ $mol^{-1}$), where $\alpha$ is the headspace volume of the reaction vessel.

For separation and detection of CO, $H_2$ and $CH_4$ in chapter 3, an Agilent 5 Å molecular sieve column (held isothermally at 34 ºC) is used, with $N_2$ carrier gas and a flow rate of 3.5 mL $min^{-1}$. Amounts of $H_2$ and CO are quantified against the internal standard (2% $CH_4$), with reference to calibration plots obtained with various known amounts of $H_2$ or CO (examples of which are shown in Figure 28).

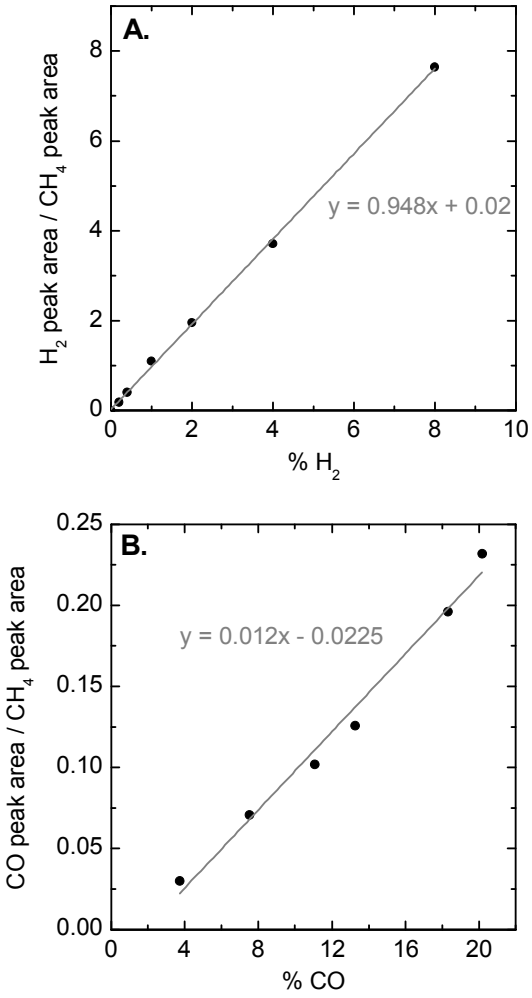


**Figure 28 Typical calibration plot for quantification of (A) $H_2$ and (B) CO in chapter 3, using the $H_2$:$CH_4$ and CO:$CH_4$ peak area.** To construct this plot, chromatograms were obtained by analysing samples from a reaction vessel containing a 2% $CH_4$ internal standard and known amounts of $H_2$ or CO. An Agilent 5 Å molecular sieve column (held isothermally at 34 ºC) was used, with $N_2$ carrier gas and a flow rate of 3.5 mL $min^{-1}$.

The conversion factor obtained from the calibration plot in panel A (0.948) allows the amount of headspace $H_2$ to be quantified according to the formulae:

% $H_2$ = ($H_2$ peak area / $CH_4$ peak area) / 0.948

moles $H_2$ = (% $H_2$ / 100) x ($\alpha$ $dm^3$ / 22.4 $dm^3$ $mol^{-1}$), where $\alpha$ is the headspace volume of the reaction vessel.

The conversion factor obtained from the calibration plot in panel B (0.012) allows the amount of headspace CO to be quantified according to the formulae:

% CO = (CO peak area / $CH_4$ peak area) / 0.012

moles CO = (% CO / 100) x ($\alpha$ $dm^3$ / 22.4 $dm^3$ $mol^{-1}$), where $\alpha$ is the headspace volume of the reaction vessel.

### 2.3.2 UV-VIS SPECTROSCOPY

UV-vis spectroscopy is used to study the attachment of enzymes (*Ec*Hyd2, $CODH_I$ and $CODH_{II}$) and RuP to various particulate materials (pyrolytic graphite, anatase $TiO_2$, rutile $TiO_2$, P25 $TiO_2$, ZnO, $SrTiO_3$ and CdS). Enzymes can be spectroscopically detected in solution because they have a general absorbance centred at 280 nm, arising from the tryptophan and tyrosine content;[262] RuP absorbs strongly in the visible range at 455 nm due to its MLCT transition (from a ruthenium-based d orbital to a bipyridine-based $\pi^*$ orbital, see section 1.6.2).[158,263] All UV-vis spectra in this Thesis are recorded using quartz cuvettes (Fisher Scientific) with a path length of 1 cm, using a Perkin Elmer Lambda 19 spectrometer.

The generalised method for quantification of the uptake of enzymes or RuP to particles is as follows (specific details relevant to particular experiments are given at the relevant points in results sections). The particles are suspended in aqueous buffer solution, and the enzyme/RuP component added as a solution of known concentration. The suspension is stirred for a

measured period of time to allow attachment to the particles, before centrifuging to pellet. The supernatant solution is then filtered to remove any remaining trace of particles, and the UV-vis spectrum of the clear solution is collected. Spectra are also collected for identical enzyme/RuP solutions that have not been exposed to particles, with the difference between the absorbances of the particles-exposed and the non particles-exposed solutions corresponding to the amount of enzyme/RuP that has been taken up.

### 2.3.3 X-RAY DIFFRACTION

X-ray diffraction patterns of CdS materials are collected using a PANalytical X'Pert Diffractometer by Dr Yatendra Chaudhary (University of Oxford), and analysed using X'Pert HighScore Plus software.

### 2.3.4 ELECTRON MICROSCOPY

SEM images of $TiO_2$ thin film electrodes and TEM images (JEOL 4000EX operated at 80 kV) of CdS nanomaterials are collected by Christopher S. Allen and Jamie H. Warner (Department of Materials, University of Oxford). TEM (cryo-EM) images of $TiO_2$ nanoparticles functionalised with $CODH_I$ and RuP are collected with Dr Robert Gilbert (Division of Structural Biology, University of Oxford).

## 2.4 CHEMICALS, SOLUTIONS AND GASES

### 2.4.1 ENZYME SAMPLES

#### 2.4.1.1 *CARBOXYDOTHERMUS HYDROGENOFORMANS* CARBON MONOXIDE DEHYDROGENASE I ($CODH_I$) AND CARBON MONOXIDE DEHYDROGENASE II ($CODH_{II}$)

Samples of $CODH_I$ (0.12 – 0.18 mM) and $CODH_{II}$ (0.14 mM) were purified and supplied by Elizabeth Pierce under the supervision of Professor Stephen Ragsdale at the University of Michigan, U.S.A. The protocol was as follows, which is broadly based on a previously reported procedure.[185] The bacterium *Carboxydothermus hydrogenoformans* was grown in a 10 L fermentor in the medium described[185] except that the CO flow rate during growth was between 1 and 1.5 L $min^{-1}$ and the fermentor medium was supplemented with 9 mM sodium pyruvate. The fermentor was inoculated from a culture grown in 1 L of the same medium, in a sealed 2 L bottle, on 30 mM sodium pyruvate. This medium was saturated with CO before inoculation. For the purification of both $CODH_I$ and $CODH_{II}$ the procedure described was modified as follows: after suspension in lysis buffer, cells were sonicated for 15 min, and the cell lysate was centrifuged for 45 min at 120,000 x g. The Source 15 ISO column was omitted, and instead $CODH_I$ and $CODH_{II}$ were loaded together on butyl sepharose after treatment with ammonium sulfate. $CODH_I$ and $CODH_{II}$ were separated by the butyl sepharose column and were further purified separately. Each protein was loaded on a 75 mL high resolution Q sepharose column and eluted with an 800 mL linear gradient from 0 to 0.5 M NaCl. 1 M ammonium sulfate was added to each protein for a final purification using a 50 mL Source 15 ISO column with an 800 mL linear gradient from 1 to 0.2 M ammonium sulfate.

The purified enzymes (both $CODH_I$ and $CODH_{II}$) were supplied in buffered solutions (pH 8) that contained the following components: tris(hydroxymethyl)aminomethane (50 mM), dithiothreitol (2 mM), sodium dithionite (2 mM), methyl viologen (0.1 mM) and KCl (50 mM). Solutions were stored anaerobically at 4 ºC until use.

#### 2.4.1.2 *ESCHERICHIA COLI* HYDROGENASE 2 (*Ec*Hyd2)

Samples of *Ec*Hyd2 used in chapter 3 were purified exactly as previously reported[230] by Dr Michael Lukey (University of Oxford). The purified enzyme was in buffered solution (pH 7.2) that contained the following components: dithiothreitol (1 mM), tris(hydroxymethyl)aminomethane (20 mM), NaCl (150 mM), 0.02% (w/v) n-dodecyl-β-D-maltoside. Samples were stored under liquid nitrogen until use.

### 2.4.2 LIGHT-SENSITIVE MATERIALS

#### 2.4.2.1 SEMICONDUCTOR NANOMATERIALS

Various semiconductor nanomaterials are used in chapters 4, 5 and 6, and these were either purchased (and used as received) or synthesised. Materials that were obtained from commercial suppliers are detailed in Table 3.

**Table 3** Semiconductor nanoparticles obtained from commercial suppliers for use in this Thesis.

| material | supplier | purity stated by supplier (trace metals basis) |
|---|---|---|
| $TiO_2$ (8:2 anatase:rutile, 'P25'), 21 nm average diameter | Degussa | > 99.5% |
| $TiO_2$ (anatase), < 25 nm | Sigma | 99.7% |
| $TiO_2$ (rutile), < 100 nm | Sigma | 99.5% |
| $SrTiO_3$, < 100 nm | Sigma | 99.5+% |
| ZnO, < 100 nm | Sigma | >99% |

Cadmium sulfide nanocrystals of two different morphologies were prepared by Dr Yatendra Chaudhary (University of Oxford). Quantum dots ('$CdS_{QD}$'), which were roughly spherical in shape and yellow in colour, were synthesised according to a previously published procedure.[264] Briefly, a mixture of cadmium acetate, dodecylamine and sulfur powder was heated in a Teflon-lined pressure vessel at 220 ºC for 10 h. The resulting material was then collected by centrifugation, washed thoroughly with ethanol and carbon disulfide, and allowed to dry at room temperature under ambient conditions. Cadmium sulfide nanorods ('$CdS_{NR}$') were prepared according to a separate reported procedure,[265] and a third CdS material was prepared by subjecting the $CdS_{QD}$ sample to calcination by heating at 450 ºC for 45 min (the sample was heated from room temperature at 5 ºC $min^{-1}$). These materials are discussed in section 6.4.1.

#### 2.4.2.2 $[Ru(bpy)_2(4,4'\text{-}(PO_3H_2)_2bpy)]Br_2$

$[Ru(bpy)_2(4,4'\text{-}(PO_3H_2)_2bpy)]Br_2$ (the chemical structure of the complex is depicted in Figure 29) was prepared according to a previously published procedure[266] from the starting materials $4,4'\text{-}(PO_3Et_2)_2bpy$ (HetCat, Switzerland) and $Ru(bpy)_2Cl_2$ (Sigma). Following replacement of the chlorido ligands of $[RuCl_2(bpy)_2]^{2+}$ by $4,4'\text{-}(PO_3Et_2)_2bpy$, hydrolysis of the phosphonated esters with $Me_3SiBr$ in MeOH gave the final product. $^1$H-NMR, ESI-MS and UV-vis confirmed the composition and purity of the prepared compound.

The doubly charged complex $[Ru(bpy)_2(4,4'\text{-}(PO_3H_2)_2bpy)]^{2+}$ is abbreviated throughout this Thesis as 'RuP'.

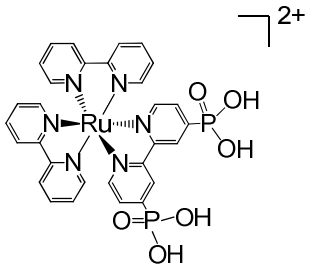


**Figure 29 The chemical structure of $[Ru(bpy)_2(4,4'\text{-}(PO_3H_2)_2bpy)]^{2+}$ (RuP).**

### 2.4.3 GASES AND CONTROL OF GAS MIXTURES

Details of the various gases and gas mixtures that are used in this Thesis (all supplied by BOC) are given in Table 4.

**Table 4** Gases used in this Thesis.

| gas | purity stated by supplier |
|---|---|
| carbon dioxide | 99.995% |
| carbon monoxide | 99.9% |
| hydrogen | 99.995% |
| nitrogen | 99.9999% |
| methane | 99.995% |
| oxygen | 99.9995% |
| 2% $CH_4$ in $CO_2$ | 2 ± 0.1% $CH_4$ |

Gas mixtures other than 2% $CH_4$ in $CO_2$ are made using mass flow controllers (Smart-Trak, Sierra Instruments Inc.).

### 2.4.4 BUFFER SOLUTIONS

Buffer solutions are prepared with purified water (Millipore, resistivity 18 MΩ cm), and titrated to the desired pH using concentrated HCl or NaOH and a pH meter (Accumet 950,

Fisher Scientific). For use with $O_2$-sensitive enzymes, buffer solutions are thoroughly de-oxygenated by bubbling with $N_2$ prior to use. Two types of buffer are used in this Thesis:

**Mixed buffer system, used in chapter 3.** The advantage of a mixed buffer system is that it allows experiments to be carried out over a wide pH range. The buffer comprising the components shown in Table 5 was suitable for all experiments in chapter 3 except for those involving high concentrations of $CO_2$, for which a MES-only buffer (see below) was used.

**Table 5** Components of mixed buffer system used in chapter 3.

| component | supplier | concentration / mM |
|---|---|---|
| NaCl | Fisher Scientific | 100 |
| 2-(*N*-morpholino)ethanesulfonic acid (MES) | Melford | 15 |
| *N*-(2-hydroxyethyl)piperazine-*N'*-(2-ethanesulfonic acid (HEPES) | Fisher Scientific | 15 |
| *N*-(tris(hydroxymethyl)methyl)-3-aminopropanesulfonic acid (TAPS) | Melford | 15 |
| 2-(cyclohexylamino)ethanesulfonic acid (CHES) | Melford | 15 |
| sodium acetate | Fisher Scientific | 15 |

**MES-only $CO_2$-stable buffer (0.20 M MES), used in chapters 3, 4, 5 and 6.** Carbon dioxide is moderately soluble in water, dissolving to form carbonic acid ($H_2CO_3$, a weak acid)[267] according to the equilibrium:

$$CO_2 + H_2O \text{ Ý } H_2CO_3$$

Although the hydration constant, $K_h$, is low ($1.70 \times 10^{-3}$), the presence of $CO_2$ leads to the acidification of aqueous solutions, and a strong buffer is required to maintain the desired pH. For experiments using high concentrations of $CO_2$ (often 1 atm.), and it was found that

0.20 M MES at pH 5.5 – 6.5 had sufficient buffering capacity to maintain the pH under 1 atm. $CO_2$ at 10 ºC – 50 ºC.

For some photocatalytic experiments, additional components (electron donors, including triethanolamine and EDTA) are added to this buffer, and these are detailed in the relevant sections of results chapters.

## 2.5 GLOVE BOXES

All electrochemical experiments are carried out in an anaerobic glove box (Belle or MBraun, $O_2$ < 3 ppm), as are all manipulations involving any of the three enzymes (*Ec*Hyd2, $CODH_I$, $CODH_{II}$).

# 3 THE WATER-GAS SHIFT REACTION CATALYSED BY REDOX ENZYMES ON CONDUCTING GRAPHITE PLATELETS

## ABSTRACT

The water-gas shift reaction ($CO + H_2O$ Ý $H_2 + CO_2$) is of major industrial importance because it is the principal method through which fossil fuel-derived $H_2$ is purified. In order to achieve sufficient conversion rates, the industrial catalysts that are used today are operated at 250 – 450 ºC, but from a thermodynamic perspective these high temperatures are unfavourable because the reaction is exothermic ($\Delta H$ = -41.1 kJ $mol^{-1}$).

This chapter describes the design and construction of a novel heterogeneous catalyst for the water-gas shift reaction. The catalyst, operating in water under mild conditions, comprises two enzymes - a hydrogenase and a carbon monoxide dehydrogenase - which are electrically 'wired' together by a graphite particle. The overall reaction is therefore considered here as the combination of two separate redox processes: electrons released from the oxidation of CO to $CO_2$ at the carbon monoxide dehydrogenase are conducted through the graphite to the hydrogenase, where they are used for the reduction of protons to $H_2$. The performance of the system, which operates at room temperature, is compared to the existing water-gas shift reaction catalysts (both industrial and state-of-the-art, bench-level materials) that require high temperatures.

The experiments are unlikely to have direct relevance for energy technology, as they use tiny amounts of fragile enzymes rather than robust synthetic materials that could be scaled up indefinitely. However, the chapter demonstrates some interesting alternative concepts for catalysis and highlights the wide gap between redox enzymes and synthetic catalysts in terms

of both rates and efficiency. Some of the extraordinary characteristics of these enzymes as electrocatalysts are important in the remainder of this Thesis.

Some of the work in this chapter has been published:

Oliver Lazarus, Thomas W. Woolerton, Alison Parkin, Michael J. Lukey, Erwin Reisner, Javier Seravalli, Elizabeth Pierce, Stephen W. Ragsdale, Frank Sargent, and Fraser A. Armstrong, *J. Am. Chem. Soc.*, **2009**, *131*, 14154-14155.

## 3.1 INTRODUCTION: THE WATER-GAS SHIFT REACTION AND ITS SIGNIFICANCE

The water-gas shift (WGS) reaction is the reaction of CO with water vapour to form $H_2$ and $CO_2$ (equation 19).[268-270]

$$CO + H_2O \rightleftharpoons CO_2 + H_2 \qquad \Delta H = -41.1 \text{ kJ mol}^{-1}, \quad \Delta G = -20 \text{ kJ mol}^{-1}$$

Equation 19

The moderate exothermicity means that the relative concentrations of reactants and products are highly sensitive to changes in temperature: the term 'shift' reflects the ability to adjust the position of the equilibrium by altering the reaction conditions. By enabling control of the relative amounts of $H_2$ and CO (these being the components of 'synthesis gas'), the WGS reaction is of major relevance to industrial processes including the preparation of methanol[75,76,91,271] and hydrocarbons,[28,272] for which the $H_2$:CO molar feedstock ratios are crucial. It also has a prominent role in industrial hydrogen production, particularly within the context of producing fuel cell grade $H_2$. The interest in $H_2$ as a fuel is long-established, and much investment continues to be made into methods for its production as well as storage and deployment in fuel cells. As was discussed in section 1.2, a *clean* hydrogen economy requires the production of $H_2$ from water (not carbonaceous sources), and the energy input must be renewable (*e.g.* solar or wind generated electricity). However, the industrial realisation of this remains a long-term goal, and today most $H_2$ is prepared by the (unsustainable) steam reformation of methane (equation 20), for which the infrastructure is well established and efficiencies moderately high (70-85%).[269]

$$CH_4 + H_2O \rightleftharpoons CO + 3H_2 \qquad \Delta H = 206.3 \text{ kJ mol}^{-1}$$

Equation 20

Some $H_2$ is also prepared by the reaction of coke with steam:

$$C + H_2O \rightleftharpoons CO + H_2 \qquad \Delta H = 131.2 \text{ kJ mol}^{-1}$$

Equation 21

The higher molar ratio of $H_2$ to CO is obtained from steam reformation (equation 20), and on this basis is the preferred method. In either case, however, it is necessary for the CO to be removed, for which the WGS reaction is typically used. The production of high purity $H_2$, containing only very small amounts of CO, is particularly important for fuel cells in which the platinum catalysts are readily poisoned by CO.[273,274] This implications of this end-use on the design of WGS reaction catalysts is discussed later.

From a thermodynamic perspective lower temperatures favour a higher yield of $H_2$, but this is kinetically unfavourable and as such the industrial WGS reaction is carried out in two stages, in separate reactors of different temperatures.[268,270] The high temperature reactor (350 – 450 °C) allows fast kinetics, but gives an unfavourable $H_2$ equilibrium yield in what is referred to as the high temperature shift (HTS). A lower temperature reactor (190 – 250 °C) therefore follows this first step in the low temperature shift (LTS) process. Both steps are usually carried out at high pressure (25-35 bar). Two main families of catalysts have emerged, each tailored to the conditions of either the HTS or the LTS, and these are detailed in section 3.2.1. The overall major route of $H_2$ production in place today is shown in Scheme 3.

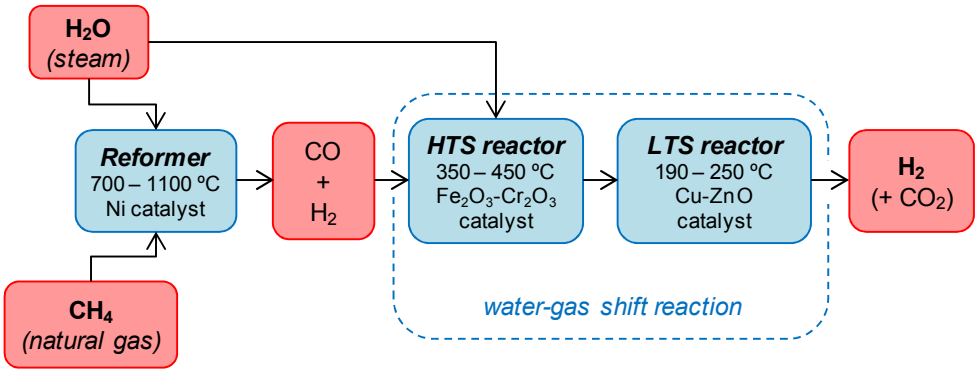


**Scheme 3.** Main route of present day industrial $H_2$ production. Steam and natural gas are fed into a reformer, producing CO and $H_2$ at high temperature over a Ni catalyst. This gas mixture, commonly called 'synthesis gas,' is then fed into two separate reactors along with more steam, whereupon the WGS reaction increases the yield of $H_2$. Details of the $Fe_2O_3$-$Cr_2O_3$ (HTS) and Cu-ZnO (LTS) catalysts are given in section 3.2.1.

## 3.2 EXISTING WATER-GAS SHIFT REACTION CATALYSIS

### 3.2.1 INDUSTRIAL CATALYSTS

The catalysts used in the industrial WGS reaction can be broadly divided into two categories: (1) $Fe_2O_3$-$Cr_2O_3$ for the high temperature shift; and (2) low temperature shift catalysts: Cu-ZnO, and 'sulfided' Co-Mo or Ni-Mo.

#### 3.2.1.1 HIGH TEMPERATURE SHIFT CATALYSIS BY $Fe_2O_3$-$Cr_2O_3$

The classic $Fe_2O_3$-$Cr_2O_3$ HTS catalyst (usually 80 – 90% $Fe_2O_3$) is effective in the temperature range 350 – 450 ºC.[270,275,276] It is typically promoted with $Al_2O_3$, which serves to prevent the sintering of the $Fe_2O_3$ particles.[276] The active catalyst is, in fact, not $Fe_2O_3$ but $Fe_3O_4$, the $Fe_2O_3$ being reduced upon start-up of the reactor by $H_2$ and CO once a temperature of around 300 ºC is reached.[277] Lifetimes are typically around 3-5 years, although this depends heavily on the operating temperature and the $CO_2$:CO and $H_2O$:$H_2$ ratios; if $H_2$ and CO (reductants) are present at too high concentrations then over time $Fe_3O_4$ will be further reduced to metallic Fe, thereby causing deactivation. Small amounts of sulfide ($H_2S$) are often present in the synthesis gas that enters the WGS reactor, and while this is relevant to the operation of other WGS reaction catalysts (see later) it is not of concern here due to the reversibility of equation 22, and in this way $Fe_2O_3$-$Cr_2O_3$ can tolerate up to around 1000 ppm of $H_2S$:[268,278]

$$Fe_3O_4 + 3H_2S + H_2 \rightarrow 3FeS + 4H_2O \qquad \Delta H = -75 \text{ kJ mol}^{-1}$$

Equation 22

Several mechanisms for iron-chromium catalysis have been suggested.[270,277] Oki *et al.* proposed the multistep mechanism shown below in equations 23 - 27,[279,280] in which the redox state of the catalyst remains unchanged throughout catalytic cycles ('a.s.' refers to an adsorption site on the catalyst). The rate determining step in this mechanism was said to be either of the reactions between surface adsorbed species, *i.e.* equation 25 or equation 27, depending on the exact reaction conditions.

$$CO\ (g) + a.s. \rightleftharpoons CO\ (a.s.) \qquad \text{Equation 23}$$

$$H_2O\ (g) + 3a.s. \rightleftharpoons 2H\ (a.s.) + O\ (a.s.) \qquad \text{Equation 24}$$

$$CO\ (a.s.) + O\ (a.s.) \rightleftharpoons CO_2\ (a.s.) + a.s. \qquad \text{Equation 25}$$

$$CO_2\ (a.s.) \rightleftharpoons CO_2\ (g) + a.s. \qquad \text{Equation 26}$$

$$2H\ (a.s.) \rightleftharpoons H_2\ (g) + 2a.s. \qquad \text{Equation 27}$$

However, it is now generally more widely accepted, following kinetic studies,[281,282] that the iron at the surface *does* undergo cycling of its oxidation state: dissociation of $H_2O$ gives $H_2$ and an oxidised iron atom; CO then abstracts the oxygen atom at the oxide surface to become $CO_2$.[283,284] The rate determining step in this scenario is either the adsorption of $H_2O$ or CO from the gas phase onto the catalyst surface, as opposed to the interconversion of reactants and products.

#### 3.2.1.2 LOW TEMPERATURE SHIFT CATALYSIS BY Cu-ZnO AND 'SULFIDED' Co-Mo / Ni-Mo

The Cu-ZnO catalyst is commonly used for the LTS process (190 – 250 ºC),[285-288] under which conditions the iron-chromium catalyst is less active. The Cu-ZnO catalyst, also often promoted by $Al_2O_3$, has the disadvantage of being sensitive to $H_2S$ according to the largely irreversible reaction:[289]

$$2Cu + H_2S \rightarrow Cu_2S + H_2 \qquad \Delta H = -59.4 \text{ kJ mol}^{-1}$$

Equation 28

The accumulation of sulfide on the copper surface therefore blocks active catalytic sites, and having a high surface area of ZnO is favourable in order to sacrificially adsorb $H_2S$ (a highly thermodynamically favoured reaction) to prolong the lifetime of the copper component.[271] Nevertheless, in the presence of sulfur compounds at concentrations above around 0.1 ppm the catalyst is, over time, adversely affected, and this led to the development of a third category of WGS catalyst: Co-Mo or Ni-Mo catalysts supported on alumina.[290-292] These catalysts are sulfur-tolerant – hence they are often referred to as 'sour gas shift catalysts' – and in fact *require* the presence of sulfur above 300 ppm in order to operate efficiently.[268] Although the $Fe_2O_3$-$Cr_2O_3$ catalysts described earlier are also tolerant towards sulfur, the Co-Mo- or Ni-Mo-alumina formulations are able to operate at lower temperatures of 250 - 350 ºC, and are therefore preferable on thermodynamic grounds. Therefore, while they are not operable at temperatures as low as the classic Cu-ZnO catalyst, they provide the advantage of sulfur tolerance in situations in which it is required, but at temperatures lower than those used in the HTS.

### 3.2.2 RESEARCH-LEVEL CATALYSTS: THE STATE OF THE ART

The dawn of $H_2$-fuelled vehicles initiated a renaissance in WGS research activity (Figure 30). The reason for this, as mentioned briefly earlier, is that the fuel cells used in these vehicles require the levels of CO in the fossil fuel-derived $H_2$ to be very low (< 50 - 100 ppm).[275] WGS reactors, housed *on-board* the vehicles, are used in order to achieve this. The requirements here are severe: these reactors must be around one hundred times smaller than

conventional, industrial, ones, and low weights and costs are also critical. The classic catalysts discussed in section 3.2.1, developed long before $H_2$ fuel cells and designed for use in large catalyst beds, are not suitable; instead the replacement of the dual HTS/LTS setup with a single, *medium* temperature reactor (and a compatible catalyst) is necessary. To this end, the past 10–15 years has seen a large number of new WGS reaction catalysts being reported.[293-304] Most of these tend to involve a precious metal (*e.g.* Au, Pt, Rh, Ru or Pd) immobilised on a partially reducible support such as $TiO_2$, $CeO_2$ or $ZrO_2$, and are therefore referred to as 'supported precious metal catalysts.'

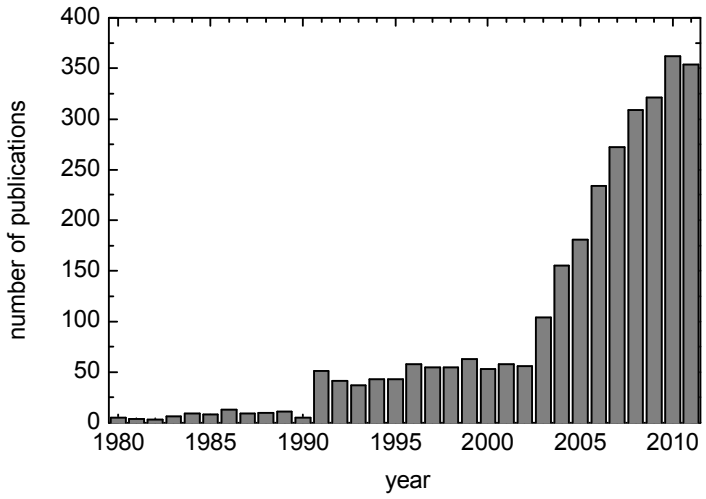


**Figure 30 Scientific publications matching the key words *water gas shift* and *catalyst*, according to the Thomson Reuters Web of Knowledge database (accessed 2 May 2011).** The noticeable increase in research activity coincides with the time of development of vehicles containing hydrogen fuel cells, the catalysts in which require high purity $H_2$. The first prototype hydrogen car (the Honda FCX) was launched in 1999, with the first production model (the Honda FCX Clarity) going on sale in 2007.[305]

Of this new group of catalysts, $Pt/CeO_2/Al_2O_3$[294,299-301] and $Pt/TiO_2$[303] formulations are generally considered to be the most active at high temperatures (high temperatures are required because of the strong adsorption of CO on Pt), with gold being more suitable at low

temperatures.[306] It is interesting to note that the support plays a critical role in catalysis: it has been found that the turnover frequencies for CO conversion do not depend on the level of metal loading, but are influenced by the nature of the metal oxide support.[307,308] The reducibility of the metal oxide is crucial; catalytic rates of Pt or Ru on $Al_2O_3$, MgO and $SiO_2$ (irreducible) supports are 1-2 orders of magnitude slower than when $TiO_2$ or $CeO_2$ (reducible oxides) are used.[307] The reason for this is the redox role of the supporting oxide in the mechanism, which is understood to proceed as follows:[306,309] CO adsorbs at the precious metal site, before being oxidised by $CeO_2$ (or $TiO_2$) to $CO_2$. The reduced metal oxide ($Ce_2O_3$ or $Ti_2O_3$) is then re-oxidised by water, forming $H_2$. In general, gold catalysts are considered to be the most active at the thermodynamically-favourable lower temperatures,[306] under which conditions it is believed that an alternative mechanism (the 'associative' mechanism,[298,309-311] in contrast to the 'redox' mechanism described above) is dominant: bridging OH groups on the reduced ceria react with CO, leading to surface-coordinated formate. Water then attacks and $H_2$ and $CO_2$ are released.

As a ball-park indication of activities, turnover frequencies (defined as moles of CO converted per mole of surface precious metal atom per second) of up to 2 $s^{-1}$ have been achieved using $Pt/CeO_2$ at 280 ºC,[307] and up to 3.9 $s^{-1}$ using $Au/CeO_2$ at 240 ºC.[312] An appreciation of the state of the art is relevant in this chapter in which a new type of WGS reaction catalyst is developed, and the rates of existing catalysts shall be returned to in greater detail later.

## 3.3 DESIGN OF A ENZYME-BASED WATER-GAS SHIFT REACTION CATALYST: CONCEPT AND GENERAL PRINCIPLES

Although discussed indirectly in section 1.7, it is appropriate to underline here that, in effect, the WGS reaction is carried out in nature by hydrogenogenic bacteria.[313-316] These anaerobic organisms, *Carboxydothermus hydrogenoformans* being one such example,[185,190] couple the CODH-catalysed oxidation of CO to $CO_2$ with the hydrogenase-catalysed reduction of protons to $H_2$. The net reaction is therefore chemically identical to the industrial WGS reaction. While the principal industrial use is the production of high purity $H_2$, the bacterial complex exists for the purpose of energy generation. CO is more reducing than $H_2$, so $CO_2$ and $H_2$ production from protons and CO (equation 19) releases energy. In the microbes this is stored in the form of a proton gradient across the cell membrane.

This 'biological WGS' reaction provides a reminder that the WGS reaction can be considered as the combination of two half-reactions - the oxidation of CO (equation 29) and the reduction of $H^+$ (equation 30). One may therefore envisage construction of a WGS reaction catalystby combining two redox catalysts, one specific to each half-reaction.

$$CO + H_2O \rightarrow CO_2 + 2H^+ + 2e^- \qquad \text{Equation 29}$$

$$2H^+ + 2e^- \rightarrow H_2 \qquad \text{Equation 30}$$

$$CO + H_2O \rightarrow CO_2 + H_2 \qquad \text{Equation 31}$$

By electrically 'wiring' a CO oxidation catalyst to a second, $H_2$-producing catalyst, electrons released from the oxidation of CO are made available for proton reduction. As previously discussed in section 1.7.1, *Ch* Ni-$CODH_I$ ('$CODH_I$') is an excellent electrocatalyst for the

reversible oxidation of CO to $CO_2$.[196] Hydrogenase 2 from *E. coli* ('*Ec*Hyd2', section 1.8) is primarily a $H_2$-oxidiser, but it also catalyses $H_2$ production at good rates.[230] Unusually for a hydrogenase – and of crucial importance for the application here - it also retains some activity in the presence of CO. The exploitation of *Ec*Hyd2 and $CODH_I$ as the electrocatalysts in a wired assembly therefore has the potential to form an effective system for overall catalysis of the WGS reaction.

Previous work has demonstrated the principle of electrically connecting two redox enzymes on conducting pyrolytic graphite (PG) particles (referred to here as 'platelets,' in reference to their shape) to catalyse a chemical reaction.[317] This system, in which electrons released from the oxidation of $H_2$ were used for the reduction of nitrate or fumarate, relies on the appropriate enzymes being readily adsorbed onto the PG surface (specifically, attachment is assumed to take place predominantly at the edge plane due to the high concentration of reactive functionalities,[255] which is also commonly used as the electrode surface in PFE experiments).[243] Figure 31 shows a cartoon representation of a graphite platelet-based catalyst for the WGS reaction, this time based on the attachment of $CODH_I$ and *Ec*Hyd2.[**] The illustration of the assembly here emphasises the principle of operation and to highlight the fact that the platelet is decorated by many enzyme molecules. For convenience, while not implying any stoichiometry, the construct shall be referred to hereafter by the short-hand notation '[$CODH_I$-PG-*Ec*Hyd2]'.

[**] The expectation that these two enzymes should spontaneously adsorb onto PG platelets is reasonable, since protein film electrochemistry studies on both of these enzymes using PG electrodes have previously been carried out.[195, 229]

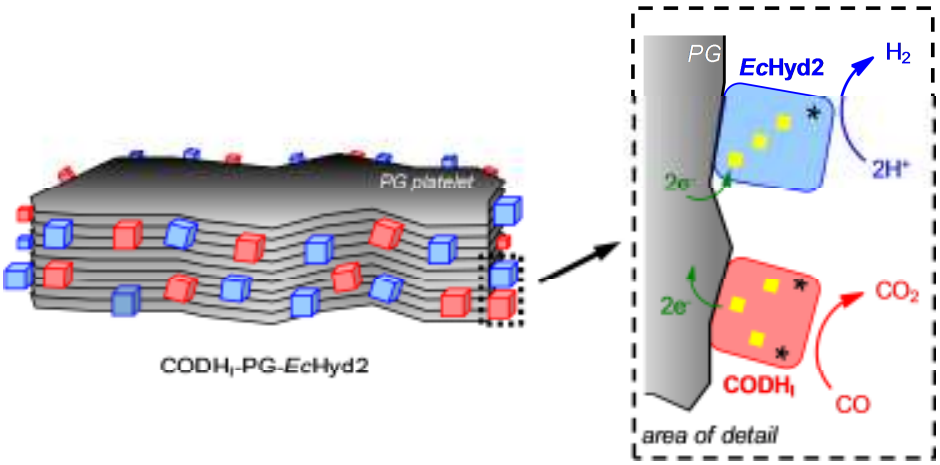


**Figure 31 Cartoon representation of an enzyme-based system for catalysis of the WGS reaction ([CODH$_I$-PG-*Ec*Hyd2]).** Enzymes capable of catalysing the oxidation of CO to $CO_2$ (CODH$_I$) and reduction of protons to $H_2$ (*Ec*Hyd2) are co-attached to graphite platelets. Electrons released from the oxidation of CO at CODH$_I$ are conducted through the platelet to *Ec*Hyd2, whereupon they are used for the reduction of protons to $H_2$. The cartoon is not to scale, and the concentrations of enzymes are arbitrary. In the expansion, yellow squares represent FeS clusters in the enzymes, with the active sites as asterisks. PG = pyrolytic graphite.

An essential requirement for such a function to work is that the two enzymes are *complementary*; that is, there must exist a potential window within which both the oxidative and reductive reactions occur. The concept of complementary electrocatalysis is illustrated in Figure 32, using the sigmoidal current-voltage curves expected for ideal electrocatalysts. The onset potential for oxidation of A to B (marked as a red dot on the catalytic wave of the same colour) is more negative than the onset potential for reduction of C to D (blue dot on the blue catalytic wave), and therefore in the case represented here the oxidatively-released electrons are sufficiently reducing for the reduction reaction. The total driving force for the reaction corresponds to the difference in onset potentials, as marked.

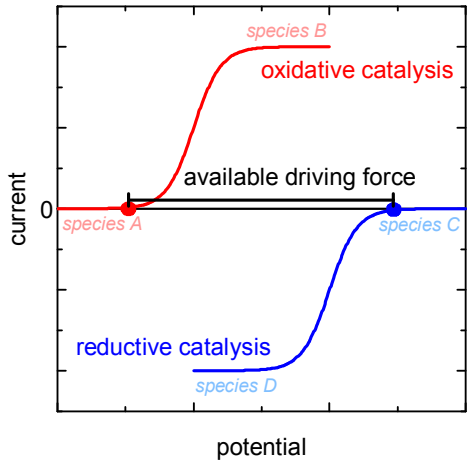


**Figure 32 Sigmoidal current *vs.* potential profiles for idealised oxidative (red) and reductive (blue) electrocatalysts.** These electrocatalysts can be said to the *complementary*, since there exists a potential window in which both the oxidative and reductive processes are catalysed. The difference in the catalytic onset potentials (marked) corresponds to the available driving force for the overall redox reaction.

## 3.4 PROTEIN FILM ELECTROCHEMISTRY AS A TOOL IN THE DESIGN OF AN ENZYME-BASED WATER-GAS SHIFT REACTION CATALYST

### 3.4.1 DETERMINATION OF AN APPROPRIATE pH FOR [CODH$_I$-PG-*Ec*HYD2] $H_2$ PRODUCTION EXPERIMENTS

PFE (the principle of which is described in section 2.1.1) has been previously used in electrochemical studies of both CODH$_I$[196] and *Ec*Hyd2,[230] and the same technique may be used here to inform on appropriate reaction conditions for $H_2$ production experiments using the proposed [CODH$_I$-PG-*Ec*Hyd2] catalyst. Figure 33 shows cyclic voltammograms recorded at 30 ºC and various pH values with CODH$_I$ (panel A) or *Ec*Hyd2 (B) adsorbed onto the surface of a rotating pyrolytic graphite electrode (the electrode is constructed from the same material as the graphite particles as described later in section 3.5.1). For each of the experiments in panel A, CO was continually flushed through the headspace of the

electrochemical cell; the positive current arises due to the transfer of electrons from the enzyme to the electrode as CO is oxidised to $CO_2$ by $CODH_I$. In panel B, $N_2$ was continually flushed through the cell, with the negative current corresponding to the *Ec*Hyd2-catalysed reduction of protons to $H_2$. The grey voltammograms show the current response of the electrode in the absence of enzyme; these were recorded at pH 6, and at the other pH values almost identical results were obtained (not shown). The voltammograms were recorded in the orders of pH 6, pH 7, pH 4, pH 5 (panel A); and pH 6.5, pH 6, pH 7.5, pH 7 (panel B). Following the collection of each set of voltammograms (both sets were recorded using a single enzyme film), a further scan at the initial pH value revealed that the extent of enzyme film loss was insignificant in each case. The electrochemical cell buffer solution was changed quickly in between experiments and the electrode surface was not allowed to dry.

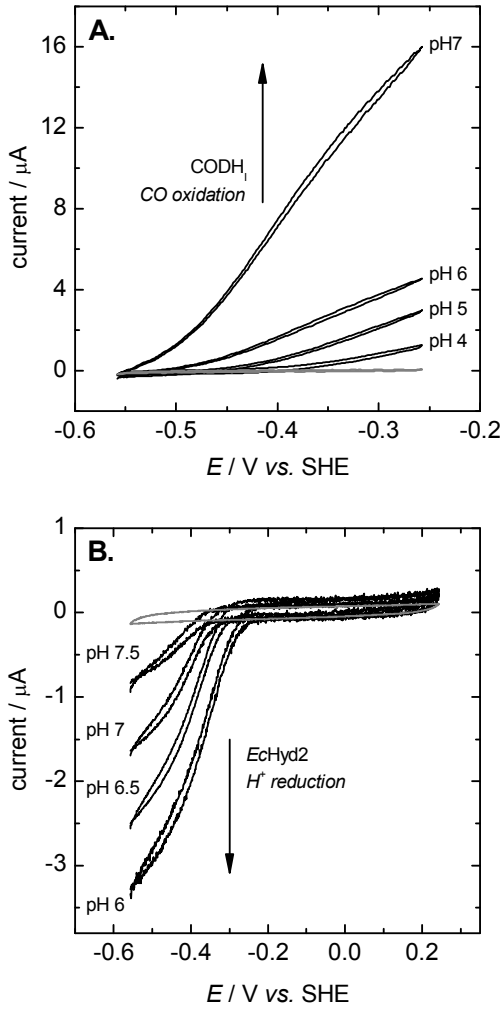


**Figure 33 The effect of pH on CO oxidation by $CODH_I$ (A) and on $H_2$ production by *Ec*Hyd2 (B) adsorbed on rotating PGE electrodes at 30 ºC.** Voltammograms were recorded at 10 mV $s^{-1}$ under 1 atm. CO (A) or 1 atm. $N_2$ (B), with an electrode rotation rate of 4000 rpm. The cell buffer was 0.20 M MES ($CODH_I$) or mixed buffer system (*Ec*Hyd2, see section 2.4.4 for buffer composition). The background currents recorded at unmodified electrodes (pH 6) are shown in grey.

The CO oxidation activity of $CODH_I$ (panel A) increases with pH. While there are many pH-dependent interactions in enzyme catalysis, this result is largely expected because in the oxidation of CO to $CO_2$ protons are removed from water ($CO + H_2O \rightarrow CO_2 + 2e^- + 2H^+$). The opposite trend is observed for the *Ec*Hyd2-catalysed $H_2$ production (panel B), since here

protons themselves are the enzyme substrate. However, the effect of varying the pH on the inherent catalytic activities of either enzyme is not quite as large as may be perceived upon first glance of Figure 33; the onset potentials incur a Nernstian 59 mV shift in the negative direction for each increasing pH unit (as expected), and therefore any one electrochemical potential corresponds to a different catalytic driving force depending on the pH.

The increasing or decreasing of the pH has opposing effects on the rates of catalysis of either enzyme, and therefore a platelet-based WGS reaction experiment (in which both enzymes are necessarily under identical conditions) may be predicted to show little overall pH dependence. That said, rates of WGS reaction catalysis can be expected to be limited by the least active enzyme. Although the technique of PFE suffers from variation in activities between different films of the same enzyme, the voltammograms shown here (recorded with a single film of $CODH_I$ and a single film of *Ec*Hyd2) are representative of the general trend observed across many experiments that $CODH_I$ CO oxidation currents are greater than *Ec*Hyd2 $H_2$ production currents. For this reason it was decided that the experimental conditions for platelet-catalysed $H_2$ production experiments should be suited primarily to the hydrogenase, and forthcoming graphite platelet experiments were thus carried out (except where otherwise stated) at pH 6, under which conditions the CO oxidation activity $CODH_I$ is also reasonable.

### 3.4.2 THERMODYNAMIC FEASIBILITY AND INHERENT SUITABILITY OF $CODH_I$ AND *Ec*Hyd2 AS CO-CATALYSTS

Figure 34 allows assessment of the suitability of $CODH_I$ and *Ec*Hyd2 as co-catalysts in a graphite platelet-based WGS reaction catalyst. In separate experiments for each enzyme,

cyclic voltammograms were recorded in the presence of both the oxidised and reduced substrates ($CO/CO_2$ for $CODH_I$, $H_2$ and $H^+$ for *Ec*Hyd2). $CODH_I$ is a reversible electrocatalyst and the red voltammogram in panel A, recorded under a gas atmosphere of 50% CO and 50% $CO_2$, therefore shows both oxidative and reductive currents. The voltammogram cuts sharply through the line of zero current at the potential predicted by the Nernst equation (Appendix A1), showing that there is almost no electrochemical overpotential necessary to drive catalysis in either direction. Similarly, the blue *Ec*Hyd2 voltammogram, recorded under 50% $H_2$ in $N_2$, also cuts sharply through the line of zero current at the predicted potential (Appendix A1), indicating the remarkable efficiency of $2H^+/H_2$ interconversion. It is clear from the window between onset potentials that the electrocatalysis meets the requirement of *complementarity* that was outlined in section 3.3 so that the overall reaction ($CO + H_2O \rightarrow H_2 + CO_2$) is thermodynamically feasible, albeit only *just*: the difference in intersection potential of 110 mV marks the small Gibbs energy difference under these conditions.

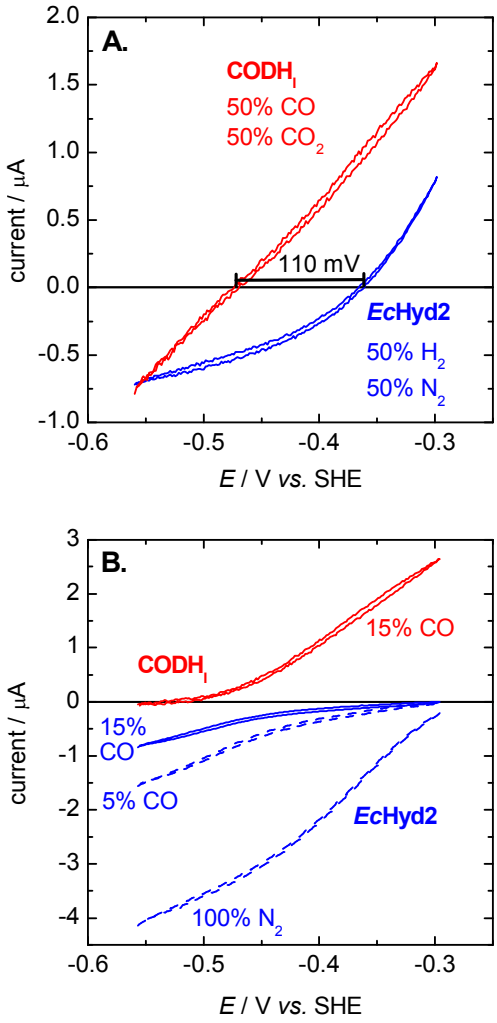


**Figure 34 Cyclic voltammograms of CODH$_I$ (red) and *Ec*Hyd2 (blue) adsorbed on rotating PGE electrodes under various gas atmospheres (always 1 atm. total pressure) at pH 6 and 30 °C.** The cell buffer was 0.20 M MES (CODH$_I$) or mixed buffer system (*Ec*Hyd2, see section 2.4.4 for buffer composition). Voltammograms were recorded at 10 mV s$^{-1}$ with an electrode rotation rate of 4000 rpm.

Panel B shows the electrocatalytic activities of CODH$_I$ and *Ec*Hyd2 under conditions relevant to the graphite platelet experimental conditions. The solid voltammograms are recorded under 15% CO in $N_2$ (far exceeding $K_M^{CO}$ for CODH$_I$ of ~0.2%),[††196] under which

[††] The Michaelis constant, $K_M$, is the substrate concentration at which the rate of reaction is half of the limiting (maximum) rate.

conditions the proton reduction activity of *Ec*Hyd2 has dropped to around 15% of its activity in 100% $N_2$. During catalysis of the WGS reaction, the CO level would decrease over time (assuming a closed system). Therefore, the activity of *Ec*Hyd2 under a lower level of CO (5%) was tested. The voltammogram marked '5% CO', which was recorded after the '15% CO' voltammogram, shows that the decrease in CO concentration is accompanied by the recovery of some $H_2$ production activity. Figure 34 as a whole therefore indicates that not only are $CODH_I$ and *Ec*Hyd2 electrochemically complementary, they are also compatible co-catalysts (that is, they are able to function under a common set of reaction conditions). On this basis, catalysis of the WGS reaction by [$CODH_I$-PG-*Ec*Hyd2] is, at least in principle, shown to be feasible.

## 3.5 [$CODH_I$-PG-*Ec*HYD2] $H_2$ PRODUCTION EXPERIMENTS

### 3.5.1 CATALYST ASSEMBLY

Due to the $O_2$-sensitivity of both $CODH_I$ and *Ec*Hyd2, strict anaerobicity was maintained throughout all stages of preparation of the WGS catalyst. Platelets (15 mg) were freshly ground from pyrolytic graphite using SiC paper and dispersed by sonication in 50 μL mixed buffer system (see section 2.4.4 for buffer composition) in a glass test tube. Platelets produced using an identical method were previously found to have diameters of several microns.[317] Solutions of 40 μL of 117 μM $CODH_I$ and 160 μL of 1.5 μM *Ec*Hyd2 were premixed, then added to the tube.[‡‡] After 30 minutes on ice (to optimise enzyme adsorption), the suspension was diluted with buffer to a total volume of 3 mL, transferred to a gastight ultracentrifuge tube and spun to pellet the graphite platelets. The supernatant was then

[‡‡] This mixture of enzyme solutions was decided following a series of preliminary experiments.

removed and the platelets resuspended in 5 mL of fresh, enzyme-free buffer, and transferred back to the glass tube which was then tightly sealed with a rubber septum. The 3.5 mL headspace of the reaction vessel was flushed with 2% $CH_4$ in $N_2$ and the reaction started by injecting 0.6 mL of CO, with the pressure returned to 1 atm. by the immediate removal of the same volume of gas. This process resulted in the presence of 15% CO in the headspace. The platelet suspensions were continually stirred during experiments, and except where otherwise stated, maintained at 30 ºC by positioning of the reaction vessel in a thermostated water bath. Concentrations of CO and $H_2$ in the headspace were monitored by gas chromatography at regular time intervals throughout the reaction, relative to an internal standard of 2% $CH_4$ (section 2.3.1). Figure 35 shows photographs of a typical system at key stages of preparation.


**Figure 35 Preparation of the [$CODH_I$-PG-*Ec*Hyd2] WGS reaction catalytic system.** Photographs of a typical $CODH_I$-PG-*Ec*Hyd2 system before (a) and after (b) centrifugation, and following buffer exchange and transfer into a reaction vessel (c). The buffer exchange and re-suspension step was carried out in a glove box under an anaerobic ($O_2$ < 2 ppm) atmosphere.

### 3.5.2 THE WATER-GAS SHIFT REACTION CATALYSED BY [CODH$_I$-PG-*Ec*HYD2]

Figure 36 shows the simultaneous $H_2$ production and CO consumption in an initial experiment carried out at room temperature at pH 6, with the system prepared as just described.

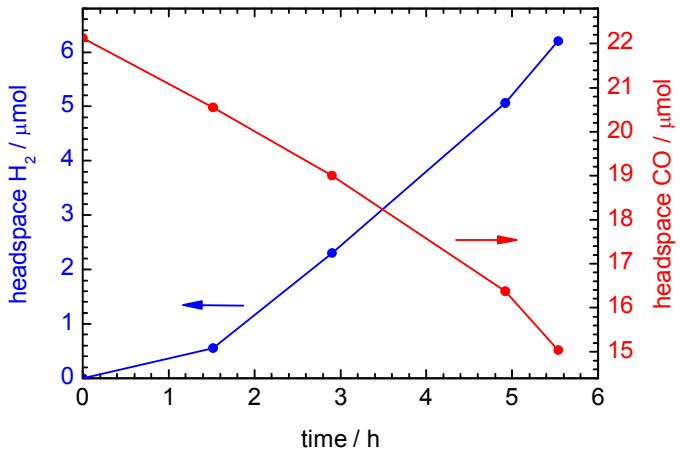


**Figure 36 Initial demonstration of catalysis of the WGS reaction by [CODH$_I$-PG-*Ec*Hyd2] at room temperature, showing $H_2$ production and CO depletion over 5.5 h.** Amounts of $H_2$ and CO are determined from the $H_2$:$CH_4$ and CO:$CH_4$ gas chromatogram peak area ratios, with reference to calibration plots (see section 2.3.1). The amounts of system components were: 4.68 nmol CODH$_I$, 0.24 nmol *Ec*Hyd2, 15 mg PG platelets, 3 mL mixed buffer system (pH 6, see section 2.4.4 for buffer composition).

Over the course of 5.5 h, 6.2 µmol $H_2$ was accumulated in the reaction vessel headspace. As is to be expected from the 1:1 stoichiometry of the WGS reaction (equation 19), there is a roughly equal decrease in the amount of CO, from 22.1 µmol to 15.0 µmol. Since 0.24 nmol of the $H_2$ producing enzyme (*Ec*Hyd2) was used in the assembly, an average TOF of 1.3 mol $H_2$ produced (mol *Ec*Hyd2)$^{-1}$ s$^{-1}$ may be calculated. Similarly, the TOF based on CODH$_I$ is 0.08 mol CO consumed (mol CODH$_I$)$^{-1}$ s$^{-1}$. At this stage these numbers represent *lower limits*, since it is unlikely that all of the enzyme molecules are adsorbed onto the PG platelets,

and also because a proportion of those that are attached will be inactive if they are orientated inappropriately for electron transfer. A detailed consideration of turnover rates, taking into account forthcoming experiments, follows in section 3.6.1.

Panel A of Figure 37 shows amounts of $H_2$ in the vessel headspace accumulated after 2.7 h in experiments using identical systems carried out at different temperatures (pH 6 in all cases). Predictably, lowering the temperature results in less $H_2$ production, with the 10 ºC system retaining around 40% of the activity recorded at 30 ºC. Section 3.6.1 gives an evaluation of rates in the context of existing WGS catalysts.

Panel B uses this temperature-dependence data to construct an Eyring plot. Eyring plots (Appendix A2) can be used to quantify the temperature dependence of the rate of a reaction in terms of $\Delta H^{\ddagger}$, the enthalpy change of reaction for formation of the transition state (also known as the activation enthalpy). Classically, $\ln(k/T)$ is plotted against $1/T$, where $k$ is the rate constant for the reaction, and $\Delta H^{\ddagger}$ is extracted from the gradient of the linear line of best fit by multiplying the gradient by $-R$. Here, $\ln(\mathrm{mol}_{H_2}/T)$ (where $\mathrm{mol}_{H_2}$ is the amount of $H_2$ produced) is plotted against $1/T$ – a valid manipulation since the amount of $H_2$ produced is proportional to $k$. The gradient yields a $\Delta H^{\ddagger}$ value of 31.3 kJ $mol^{-1}$: close to the activation enthalpy for CO oxidation by $CODH_I$ previously reported (30 kJ $mol^{-1}$),[196] and greatly different to that of proton reduction by *Ec*Hyd2 (~ 65 kJ $mol^{-1}$).[318] The significance of this finding is discussed in section 3.6.1.

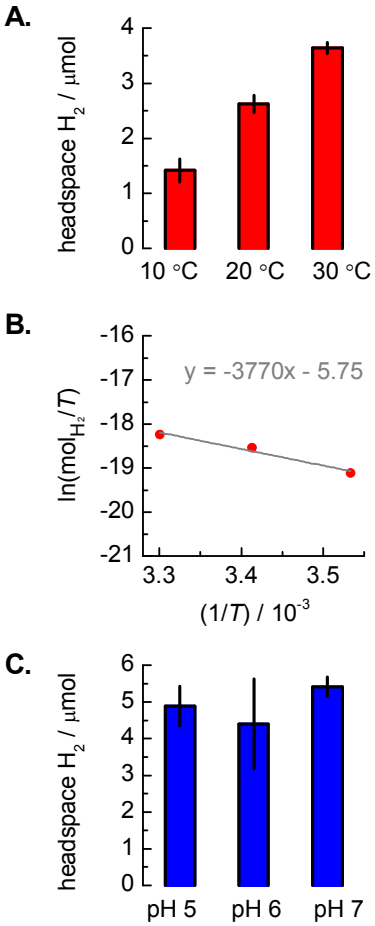


**Figure 37 Effects of reaction conditions on the activities of [$CODH_I$-PG-*Ec*Hyd2] WGS catalytic systems.** (A) Amounts of headspace $H_2$ accumulated over 2.7 h at various temperatures (pH 6); (B) Eyring plot, constructed from the data in panel A; (C) amounts of headspace $H_2$ accumulated at various pHs over 3.3 h (30 ºC). The amounts of system components were: 4.68 nmol $CODH_I$, 0.24 nmol EcHyd2, 15 mg PG platelets, 3 mL mixed buffer system (see section 2.4.4 for buffer composition).

Panel C shows amounts of $H_2$ accumulated after 3.3 h in experiments carried out at different pHs at 30 ºC. There is no significant effect here, which is to be expected because both CO oxidation and $H_2$ production half-reactions are two-proton processes, the former releasing protons and the latter consuming them (equations 29 and 30).

Catalysis over an extended period of time was investigated, and Figure 38 shows $H_2$ production and CO depletion (pH 6, 30 ºC) over the course of 55 h. Following the introduction of CO into the reaction vessel headspace, $H_2$ was produced with the simultaneous depletion of CO at the same rate. After 21 h, 15.2 µmol $H_2$ has been produced and almost the entire initial amount of CO (14.9 µmol) has been consumed. Over this period of time the rate of $H_2$ production decreases, as expected. At 21 h, a second injection of CO (0.6 mL) was made into the reaction vessel headspace, and catalysis immediately re-starts. This 'refuelling' process is repeated at 52 h.

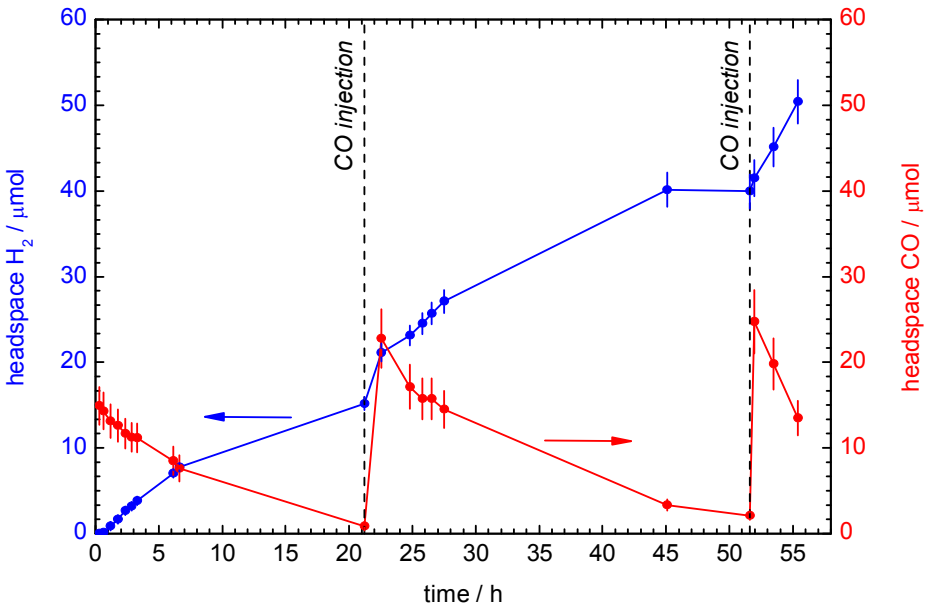


**Figure 38 $H_2$ production and CO depletion by [$CODH_I$-PG-*Ec*Hyd2] at 30 ºC over the course of 55 h.** The reaction was started by injection of 0.6 mL CO into the reaction vessel headspace, with further fresh injections of the same amount of CO made at the times indicated. The amounts of $H_2$ and CO are determined from the $H_2$:$CH_4$ and CO:$CH_4$ gas chromatogram peak area ratios, with reference to calibration plots (see section 2.3.1). The amounts of system components were: 4.68 nmol $CODH_I$, 0.24 nmol *Ec*Hyd2, 15 mg PG platelets, 3 mL mixed buffer system (pH 6, see section 2.4.4 for buffer composition).

Across the entire time course of the experiment, 50.4 μmol $H_2$ was accumulated, and 45.9 μmol CO consumed (14.0 μmol from 0 h to 21 h, 20.7 μmol from 21 h to 52 h, and 11.2 μmol from 52 h to 55 h).

### 3.5.3 RATE CALCULATIONS

As described in section 2.3.2, where a general method was described, UV-vis spectrophotometry can provide information on the amounts of $CODH_I$ and *Ec*Hyd2 attached to PG platelets. In order to determine the amounts of enzyme adsorbed to 15 mg platelets, the precise method was as follows. As described in section 3.5.1, the platelets were dispersed by sonication in 50 μL mixed buffer system in a glass test tube. Then, either 40 μL of 117 μM $CODH_I$ (4.68 nmol) or 160 μL of 1.5 μM *Ec*Hyd2 (0.24 nmol) was added to the tube. After 30 minutes on ice, the suspension was diluted with buffer to a total volume of 3 mL, transferred to an ultracentrifuge tube and spun to pellet the graphite platelets. The supernatant was then removed, and its UV-vis absorbance at 280 nm ($A_{280}$) recorded. $A_{280}$ values were also obtained for enzyme solutions of the same final concentration but which had not been exposed to graphite platelets; the difference in $A_{280}$ of the 'before' and 'after' solutions enables determination of the amount of enzyme taken up by the platelets. $A_{280}$ values, and the corresponding enzyme loadings are given in Table 6:

**Table 6** 280 nm absorbances ($A_{280}$ values) for 3 mL solutions (pH 6, mixed buffer system[a]) of $CODH_I$ and *Ec*Hyd2 before and after adsorption of enzymes onto 15 mg PG platelets.[b]

| enzyme | $A_{280}$ *Before* adsorption to PG platelets | $A_{280}$ *After* adsorption to PG platelets | amount of enzyme adsorbed on PG platelets / nmol |
|---|---|---|---|
| $CODH_I$ (4.68 nmol, 1.56 μM) | 0.952 | 0.22 | 3.60 |
| *Ec*Hyd2 (0.24 nmol, 0.08 μM) | 0.118 | 0.078 | 0.081 |

[a] See section 2.4.4 for buffer composition. [b] Adsorption was carried out by adding enzyme solutions (40 μL of 117 μM $CODH_I$, or 160 μL of 1.5 μM *Ec*Hyd2) to PG platelets, and leaving for 30 min on ice.

These data allow the calculation of catalytic turnover rates, based on actual enzyme loadings (Table 7). It should be noted, however, that rates based on these values are still, in fact, *lower limits*; the adsorption study just described was carried out with each enzyme independently, almost certainly leading to inflated values for adsorption amounts compared to the real [$CODH_I$-PG-*Ec*Hyd2] system prepared using pre-mixed enzymes. Competitive co-adsorption of $CODH_I$ and *Ec*Hyd2 onto the PG platelets is expected to lead to lower loadings than those indicated in Table 6, and therefore faster turnover frequencies than those shown in Table 7.

**Table 7** Turnover frequencies for catalysis of the WGS reaction at pH 6 by [$CODH_I$-PG-*Ec*Hyd2], prepared according to the procedure outlined in section 3.5.1.

| | | *(i.)* TOF [(μmol $H_2$ produced) (g catalyst)$^{-1}$ $s^{-1}$] [a] | *(ii.)* TOF [(mol $H_2$ produced) (mol *Ec*Hyd2)$^{-1}$ $s^{-1}$] [b] | *(iii.)* TOF [(mol CO consumed) (mol $CODH_I$)$^{-1}$ $s^{-1}$] [c] |
|---|---|---|---|---|
| 30 ºC | initial rate (0 – 3.3 h) | 78.8 ± 3.94 | 3.75 ± 0.19 | 0.09 ± 0.013 |
| | average rate, first period before CO replenishment (0 – 21 h) | 47.7 ± 2.39 | 2.36 ± 0.12 | 0.05 ± 0.008 |
| | average rate, entire time course (0 – 55 h) | 60.7 ± 3.04 | 3.00 ± 0.14 | 0.06 ± 0.010 |
| 10 ºC | initial rate (0 – 2.7 h) | 28.6 ± 4.25 | 1.41 ± 0.21 | 0.03 ± 0.005[d] |
| 20 ºC | initial rate (0 – 2.7 h) | 53.0 ± 3.18 | 2.62 ± 0.16 | 0.06 ± 0.004[d] |

[a] The mass of the catalyst is taken to be the mass of graphite platelets (*i.e.* 15 mg), since the enzyme mass is negligible. [b] Calculated from the total amount of $H_2$ in the reaction vessel headspace and the amount of *Ec*Hyd2 determined to have been taken up by PG platelets (Table 6). [c] Except where otherwise stated, calculated from the total amount of CO in the reaction vessel headspace and the amount of $CODH_I$ determined to have been taken up by PG platelets (Table 6). [d] These values are calculated using the amount of $H_2$ in the vessel headspace (assumed to be approximately equal to the amount of CO).

## 3.6 DISCUSSION

### 3.6.1 RATE CONSIDERATIONS AND THE FUNDAMENTAL ROLES OF *Ec*Hyd2 AND $CODH_I$ AS SPECIALIST ELECTROCATALYSTS

The work outlined in this chapter has demonstrated the assembly and operation of a novel system that catalyses the WGS reaction, *i.e.* carries out the overall conversion of CO and water to $H_2$ and $CO_2$. Clearly, there are obvious factors that preclude this system from ever being viable for practical use (scale-up issues and oxygen-sensitivity of the enzymes being two). Nevertheless, the rates achieved with this bench-level system ought to be compared with those of the industrial catalysts (described in section 3.2.1) and also with those of the newer, state-of-the-art catalysts consisting of metal oxide-supported precious metals (section

3.2.2). Since different studies use various reaction conditions and initial reactant ($CO/H_2O$) compositions, several of the precious metal catalysts were recently screened in a study by Thinon *et al*. in order to determine their activities under identical conditions (selected as *300 ºC*, 2:1 $H_2O$:CO initial ratio).[308] Turnover rates in μmol (g cat)$^{-1}$ s$^{-1}$ for some of these catalysts are shown in Table 8:

**Table 8** WGS reaction catalytic activities of several supported precious metal catalysts at 300 ºC (2:1 $H_2O$:CO initial ratio) adapted from reference [308].

| catalyst | activity / μmol (g cat)$^{-1}$ s$^{-1}$ |
|---|---|
| 0.9% $Pt/CeO_2/Al_2O_3$ | 27 |
| 1.5% $Pt/ZrO_2$ | 20 |
| 2% $Pt/CeO_2$ | 15 |
| 1.9% $Pt/TiO_2$ | 39 |
| 1.5% $Pt/Fe_2O_3$ | 6 |
| 1.7% $Pd/CeO_2$ | 8 |
| 5% $Au/CeO_2$ | 27 |
| 1.5% $Au/TiO_2$ | 12 |
| 5% $Au/Fe_2O_3$ | 12 |
| 1.5% $Au/ZrO_2$ | 12 |

Comparison of these rates with the data in column i. of Table 7 reveals that, assessed on a *per gram catalyst* basis, the catalytic rates of the [$CODH_I$-PG-*Ec*Hyd2] system (~ 30 – 80 μmol g$^{-1}$ s$^{-1}$, calculated using the mass of graphite and ignoring the negligible mass of enzyme, at temperatures ranging from 10 – 30 ºC), are at least comparable to those of the precious metal class. Note, however, that the turnover frequencies given in Table 8 are from experiments carried out at 300 ºC; whereas the enzyme-based system delivers similar rates at ambient temperatures. The classic $Fe_3O_4$-$Cr_2O_3$ catalysts that are routinely used in industrial

HTS reactors have been reported to afford activities as high as 120 - 150 μmol $g^{-1}$ $s^{-1}$ at 450 ºC[319,320] – not significantly faster than the platelet system, but again at a drastically elevated temperature. The enzyme-containing system presented here thus serves as a benchmark for catalysis of the WGS reaction, indicating the rates that can be achieved at ambient temperatures and mild pHs without the involvement of any expensive precious metals.

Turnover rates *per mole* of catalyst are less frequently reported in the literature, probably due to the difficulty in defining what the discrete catalytic unit of a solid state catalyst is and determining how many of these units are present, and the uncertainty over the mechanistic pathway (see section 3.2.2). Molar turnover frequencies have, nonetheless, been reported in some instances - two of the very best being those mentioned in section 3.2.2: 2 $s^{-1}$ using $Pt/CeO_2$ at 280 ºC[307] and 3.9 $s^{-1}$ using $Au/CeO_2$ at 240 ºC.[312] These rates are calculated using the number of moles of surface precious metal atom. This is not necessarily a perfect basis - the metal oxide is understood to have mechanistic significance as well as the precious metal, as discussed in section 3.2.2 - but it at least allows comparisons to be made with other catalysts in the same precious metal family. Determination of molar turnover frequencies for [$CODH_I$-PG-*Ec*Hyd2] is also not clear-cut for a similar reason: what is the discrete catalytic unit? Since each enzyme catalyses a two electron process, it initially seems sensible to define each $CODH_I$/*Ec*Hyd2 *pair* as a catalytic unit. Since the loading of the *minority* enzyme defines the number of $CODH_I$/*Ec*Hyd2 pairs, the turnover frequencies per mole of attached *Ec*Hyd2 (1.4 – 3.8 $s^{-1}$, column ii. of Table 7) are, by definition, equal to the rates per mole of enzyme pair.

It is arguable, however, that this approach ignores the very essence of the design of the system, in which the surface concentration of each half-reaction catalyst can, in principle, be controlled so as to effect maximum efficiency. Calculating turnover frequencies based on the loading of the *majority* enzyme ($CODH_I$ in this case), thereby giving lower rates, might in fact be fairer (*Ec*Hyd2 turnover to produce $H_2$ is, after all, dependent upon electron supply from $CODH_I$-catalysed CO oxidation). These more conservative, $CODH_I$-based turnover frequencies (0.03 – 0.09 $s^{-1}$) are shown in column iii. of Table 7. Physically, however, these are somewhat nonsensical because on such a basis one unit of catalyst is now, by default, defined as one $CODH_I$ molecule wired to "0.023" *Ec*Hyd2 molecules (3.60 nmol $CODH_I$ is co-attached with 0.081 nmol *Ec*Hyd2). It is instructive at this point to turn to the information gained from the temperature dependence of $H_2$ production (Figure 37). From the Eyring plot in panel B, an activation enthalpy for the system of 31.3 kJ $mol^{-1}$ was extracted. It was noted that this value is very close to the activation enthalpy for CO oxidation by $CODH_I$ (reported previously to be 30 kJ $mol^{-1}$),[318] and this therefore strongly implies that, overall, the system is limited by the rate of electron supply from $CODH_I$ as opposed to the rate of *Ec*Hyd2-catalysed $H_2$ production. In light of this, it is arguably more appropriate to accept the rates calculated from the $CODH_I$ loadings, despite the slightly odd physical description that is imposed by doing so.

Whichever approach is taken, it is clear that the enzyme-based turnover frequencies are much lower than the solution assay-determined rates that have been reported for both enzymes (200 $s^{-1}$ for $H_2$ production by *Ec*Hyd2;[229] 30,000 $s^{-1}$ for CO oxidation by $CODH_I$[185]). In addition to the possibility that only a fraction of the adsorbed enzymes are electrochemically

active (a likely, albeit unproven scenario), a major factor here is the very small thermodynamic driving force. This was highlighted by the voltammetry in section 3.4.2; there exists a driving force for the WGS reaction of only around 100 mV. The fact that the device operates at all is, of course, due to each half-reaction being catalysed by a substrate-specific enzyme that has been perfected for the purpose through evolutionary pressure, and that the enzymes are compatible co-catalysts. Both enzymes display only very small overpotential requirements, and the high activities mean than despite the small Gibbs energy difference for the reaction, $H_2$ is still produced at reasonable rate. Also, [NiFe]-hydrogenases are normally poor $H_2$ producers (in biology they are 'uptake' hydrogenases),[243] and are strongly inhibited by $H_2$.[321] *Ec*Hyd2 is unusual in that it is a proficient $H_2$ producer even in the presence of $H_2$. This variation in sensitivity is quantified by the difference in $K_I^{app}(H_2)$ inhibition constants:[§§] 210 μM in the case of *Ec*Hyd2 at pH 6 and 30 ºC ,[230] compared to values of 7.1 μM (*Ralstonia eutropha* membrane bound hydrogenase) and 10.8 μM (*Ralstonia metallidurans* membrane bound hydrogenase),[321] the *Ralstonia* hydrogenases being regarded as more typical of [NiFe]-hydrogenases in this respect.

Carbon monoxide is a classic inhibitor of hydrogenases,[322-325] but the ability of *Ec*Hyd2 to retain appreciable activity under reasonably high CO concentrations here is vital. The 'biological WGS reaction' was discussed earlier (section 3.3); clearly, the hydrogenases involved in such complexes are able to function, but the CO concentrations involved are much lower so this does not actually infer any significant CO tolerance. In fact, to the contrary, a study of the CODH-linked hydrogenase in *Rubrivivax gelatinosus* found that the

[§§] The inhibition constant, $K_I^{app}$, is the concentration of an inhibitor that is required to produce half of the maximum inhibition. Lower values of $K_I^{app}$ are therefore indicative of more potent inhibition.

hydrogenase activity was halved by the introduction of just 3.9 μM (0.4% CO).[326] As a final point to note, platinum metal is the only alternative to hydrogenase as a candidate to meet the necessary requirement here of being a low-overpotential $H_2$ production catalyst. It would not be suitable in this application, however, because it is irreversibly poisoned by CO, and the exceptional catalytic properties of *Ec*Hyd2 are therefore further underlined.

### 3.6.2 BROADER IMPLICATIONS FOR CATALYSIS AND RELEVANCE TO THE REMAINDER OF THIS THESIS

Clearly, the system described in this chapter is not presented as a practical WGS reaction catalyst. Rather, it is a vehicle to highlight key catalytic properties of the enzymes (as discussed above), but secondly it serves as a model that may inspire the design of robust, synthetic catalysts for various redox reactions. In respect of the latter purpose, there are two key features. The first point to note is that, in some situations, the approach of wiring together two electrocatalysts, each being a highly effective catalyst for a single half-reaction, can be advantageous. Of course, this comes at the expense of having the simplicity of a single catalyst for an entire reaction, and in many cases (including the WGS reaction), execution of this strategy demands the use of catalysts that are highly efficient, *i.e.* able to provide high rates of catalysis with minimal overpotential. This is highlighted here, because the [$CODH_I$-PG-*Ec*Hyd2] assembly would not function if either of the enzymes required even 0.1 V to activate oxidation or reduction.

Secondly, there is an important advantage in co-attaching oxidation and reduction catalysts *to a central, conducting particle*. In doing so, differences in the activities of either catalyst can be compensated for by adjusting their relative quantities. This kind of activity ‘matching’

would not be possible in a system in which two redox catalysts are directly connected, and even in biology 1:1 complexes may not always be the optimum configuration in terms of harvesting the maximum capabilities of the enzymes. While this principle was not formally exploited for the purposes of this chapter (though various mixtures of $CODH_I$ and *Ec*Hyd2 were trialled in the preliminary experiments), the idea is highly relevant to the forthcoming chapters in which CODHs are used in light-driven systems for photocatalytic $CO_2$ reduction. Here, electrons are not sourced from an oxidisable 'fuel', but from photoexcitable moieties.

# 4 $CO_2$ PHOTOREDUCTION AT FUNCTIONALISED $TiO_2$ NANOPARTICLES (1)

## ABSTRACT

This chapter presents a prototype, enzyme-based device for the conversion of $CO_2$ to a single reduction product (CO), with the energy input supplied by visible light. The enzymes $CODH_I$ and $CODH_{II}$ from the organism *Carboxydothermus hydrogenoformans*[185] are used as catalysts, thereby affording a two-electron reduction pathway that avoids single electron reductions *via* the high energy intermediate $CO_2^{\bullet-}$.[81,105] The formation of a *clean* product (as opposed to mixtures of CO, $CH_4$, $CH_3OH$ *etc*. that are commonly produced by existing $CO_2$ photoreduction systems)[129] is also ensured. The design is based around the co-attachment of enzymes and a ruthenium bipyridyl dye complex to a common $TiO_2$ nanoparticle. Inspired by the light harvesting mechanism of Grätzel-type photovoltaic cells,[12,13] where electrons are injected from photoexcited dye complexes into mesoporous metal oxide electrodes before entering an external circuit, in the fuel-producing system described here, which takes the form of an aqueous suspension under mild conditions, the high-energy electrons are injected into the conduction bands of separate, CODH-functionalised $TiO_2$ nanoparticles. These electrons are at sufficiently high energy for enzyme-catalysed $CO_2$ reduction to CO and the overall result, therefore, is photochemical $CO_2$ reduction.

This chapter describes the step-wise development of this system from conception through to initial demonstration. The first step is attachment of $CODH_I$ and $CODH_{II}$ to $TiO_2$ nanoparticles, and subsequently, through the use of electrochemical techniques, investigation of the catalytic behaviours of these enzymes when they are immobilised on this semiconducting surface. Proof-of-concept of $CO_2$ photoreduction is then presented, followed

by an initial exploration of the characteristics of the system in terms of its durability, sensitivity to temperature and pH, and demonstration of its operation in real sunlight.

Some of the work in this chapter has been published:

Thomas W. Woolerton, Sally Sheard, Erwin Reisner, Elizabeth Pierce, Stephen W. Ragsdale and Fraser A. Armstrong, *J. Am. Chem. Soc.*, **2010**, *132*, 2132-2133.

Thomas W. Woolerton, Sally Sheard, Elizabeth Pierce, Stephen W. Ragsdale and Fraser A. Armstrong, *Energy Environ. Sci.*, **2011**, *4*, 2393-2399.

## 4.1 INTRODUCTION

Section 1.4 described the chemical challenges of reductive activation of $CO_2$ and electrocatalysts that have been developed for this purpose, most of which suffer from one or more inadequacies. The same chapter (section 1.7) also introduced anaerobic carbon monoxide dehydrogenases (Ni-CODHs) as biological catalysts that achieve high CO oxidation turnover rates for energy generation purposes in certain bacteria. Two Ni-CODHs from *Carboxydothermus hydrogenoformans*, $CODH_I$ and $CODH_{II}$, have been characterised as *reversible* electrocatalysts for the interconversion of CO and $CO_2$ when they are immobilised on PGE electrodes.[196,197] Furthermore, the catalysis in either direction is highly efficient, requiring only a very small energy input requirement (overpotential) to drive catalysis, and turnover occurs at rates (thousands per second)[185] that far exceed those recorded with synthetic $CO_2$ reduction electrocatalysts. It follows, therefore, that the coupling of this enzyme with light harvesters - moieties capable of absorbing photons to generate high energy electrons - has the possibility of forming a high-performance $CO_2$ photoreduction catalyst.

As earlier described, Ni-CODHs are, to highlight just three shortcomings, highly sensitive to $O_2$, fragile, and labour-intensive to purify. Clearly, therefore, the intent here is not to assemble a CODH-containing photocatalyst and present it as a robust and practical solution to solar fuel generation. Rather, the drive at this stage is chiefly one of intellectual curiosity: with an exceptionally effective $CO_2$ reduction electrocatalyst, is it possible to construct an outstanding $CO_2$ photoreduction device?

### 4.1.1 RATIONAL DESIGN AND PRINCIPLE OF OPERATION OF A CODH-BASED CATALYTIC SYSTEM FOR $CO_2$ PHOTOREDUCTION

Figure 39 illustrates the conceptual design of a CODH-based $CO_2$ photoreduction system. The design comprises the transition metal dye complex RuP (sections 1.6.2 and 2.4.2.2) and a CODH co-attached to a $TiO_2$ (anatase) nanoparticle, and in shorthand such an assembly will be represented by the notation '[RuP-$TiO_2$-CODH]'. It should be stressed that Figure 39 is a cartoon representation for the purpose of illustrating the principle of operation only; the components are not to scale, and the composition that is shown (one nanoparticle binding a single metal complex and a single enzyme molecule) is arbitrary.

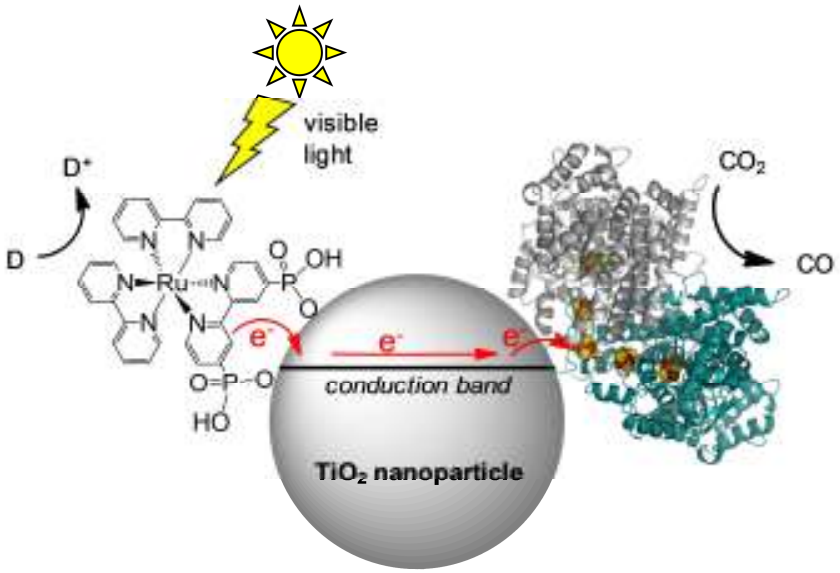


**Figure 39 Design of an enzyme-based system for $CO_2$ photoreduction to CO.** Cartoon representation of $CO_2$ reduction at a $TiO_2$ (anatase) nanoparticle functionalised with a carbon monoxide dehydrogenase enzyme ($CODH_{II}$, PDB code 1SU7, is shown here) and the ruthenium photosensitiser RuP. The anatase nanoparticles used in this Thesis are 20-25 nm in size. Photons of sufficient energy are absorbed by the ruthenium complex in an MCLT process ($\lambda_{max}$ = 455 nm).[263] The resulting excited state ($RuP^{II*}$) is sufficiently reducing to inject an electron into the conduction band of the $TiO_2$ nanoparticle. Electrons in the conduction band migrate to the enzyme where they are used in the reduction of $CO_2$ to CO according to the mechanism previously described in section 1.7.1.2. This cartoon illustration is not to scale, and is not intended to imply any stoichiometry. Systems of this kind will be represented by the shorthand notation [RuP-$TiO_2$-CODH] throughout this Thesis.

The role of RuP here is analogous to that in DSSCs as described in section 1.6.2. To recap briefly: in such a photovoltaic cell, a mesoporous photoanode comprising a thin film of sintered $TiO_2$ particles is sensitised to visible light by a transition metal complex (a 'photosensitiser'), such as RuP. Absorption of a photon of sufficient energy excites an electron in RuP from a ruthenium-based d orbital to a bipyridine-based $\pi^*$ orbital in an MLCT process. In the case of RuP, this absorbance is centred at $\lambda_{max}$ = 455 nm.[263] The metal complex, now in a high energy excited-state ('$RuP^{II*}$'), is now capable of injecting an electron into the anatase conduction band, which lies at lower energy (see section 4.1.2 later for a more detailed discussion on mechanistic routes and thermodynamic feasibility). The electrons migrate to the back contact of the electrode and flow around an external circuit as an electrical current. However, if the external circuit is removed and the $TiO_2$ particles are not the constituent parts of an electrode but instead exist as discrete units in suspension, it is possible to conceive of a different purpose for photoinjected electrons: after migration to a suitable catalyst (or, at least, a trapping site such as a metallic cluster at the $TiO_2$ surface), they can be used to carry out useful reduction reactions. This is the basis for the system proposed in Figure 39 here.

With a large number of RuP complexes attached to each $TiO_2$ nanoparticle unit, continuous visible light irradiation will establish a store of electrons in the semiconductor; these electrons, ideally, migrate through the conduction band to the surface-immobilised CODH molecules. Assuming there to be enzyme molecules attached to the semiconductor in orientations that permit electron transfer into the D-cluster (the iron-sulfur cluster closest to the protein surface; see section 1.7.1.1), reduction of $CO_2$ to CO is achieved by the catalytic mechanism already described in section 1.7.1.2.

On injecting an electron, $RuP^{II*}$ is oxidised to $RuP^{III}$. In order for the system to be truly catalytic (*i.e.* for there to be continual CO production, with many turnovers per catalyst), the ruthenium complex must be regenerated following each photoinjection. An electron donor is therefore required to reduce $RuP^{III}$ to $RuP^{II}$ (in the related DSSC system, a redox couple – usually $I^-/I_3^-$ - cycles between a cathode counter electrode and the oxidised dye, effectively acting as an electron shuttle to regenerate the reduced form).[12,13] As discussed in section 1.2.2, the ideal 'sacrificial' electron donor in a fuel producing system is water, but in the absence of a capable water oxidation catalyst – or, for the purpose of allowing focus on the fuel forming process, as is the case here - a more readily oxidisable sacrificial donor species (represented by D in Figure 39) may be used.

A ruthenium bipyridyl dye is chosen here for primarily the same reasons that this family of photosensitiser is widely used in DSSCs:[158] these complexes offer strong absorbance in the visible range,[158] photoexcited states are long-lived and highly reducing (see 4.1.2),[158] and rates of electron injection from photoexcited states to $TiO_2$ are fast ($10^{10} – 10^{12}$ $s^{-1}$).[165,327] The specific choice of RuP – having phosphonic acid groups at both of the *para* positions of one of the bipyridyl ligands – is due to its strong binding to the Lewis acidic $Ti^{IV}$ centres at the $TiO_2$ surface.[266,328,329] Adduct formation constants in water for sensitisers with phosphonic acid groups have been found to be an order of magnitude greater than for those with carboxylic acid groups, because the Ti-phosphonate linkage is less vulnerable to hydrolytic cleavage than the Ti-carboxylate linkage.[329,330]

All of the $TiO_2$-based systems in this chapter use Degussa P25 $TiO_2$, a readily available mixture of anatase and rutile (8:2) with a BET-determined surface area of 50 $m^2$ $g^{-1}$ and a

mean particle size of 21 nm.[331] Specific reference is made to anatase, even when referring to P25 $TiO_2$ in general, and the reason for this is discussed in section 4.1.2.

### 4.1.2 MECHANISTIC DETAIL AND THERMODYNAMIC FEASIBILITY

Figure 40 shows the main reduction potentials (at pH 6) involved in the system. The $CO_2$ reduction potential value used here is the standard reduction potential corrected to 20 ºC at this pH.[81] The anatase conduction band potential at the same pH (-0.52 V)[332] is around 60 mV more negative than that of the $CO_2$/CO couple, and so there is a thermodynamic driving force (albeit slim) for CO production. The conduction band potential of rutile (present at 20% in P25 $TiO_2$) is 0.2 V more positive than that of anatase.[333] For this reason it is expected that only the anatase form is useful here, since rutile conduction band electrons are not reducing enough to be useful for $CO_2$ reduction to CO. The reduction potential of the photoexcited state of RuP (*i.e.* $E(RuP^{III}/RuP^{II*})$) is -0.95 V,[334] and thus an electronic 'cascade' is in place such that the overall process – photoreduction of $CO_2$ to CO by visible light – is thermodynamically feasible.

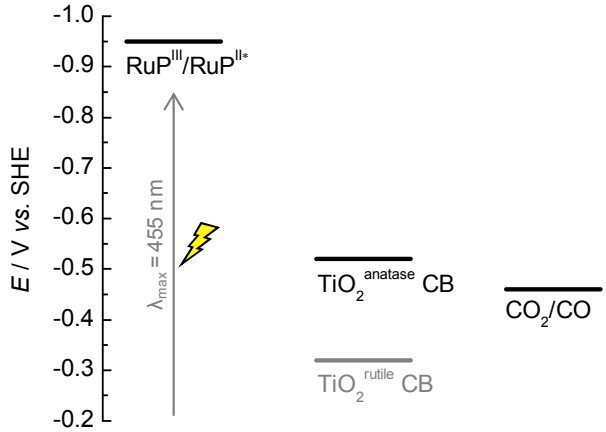


**Figure 40** The reduction potentials involved in overall photoreduction of $CO_2$ in this system, at pH 6. Values are taken from references [81,332-334].

Reduction potentials in aqueous solution for two ruthenium bipyridyl complexes – $[Ru(bpy)_3]^{2+}$ (having no functional groups on the bipyridyl ligands) and RuP – are shown in Table 9.[263,334,335] The $RuP^{II*}/RuP^{I}$ value is unknown. However, on comparison of the other RuP redox potentials with those of $[Ru(bpy)_3]^{2+}$ (Table 9), it may be predicted with reasonable confidence that the $RuP^{II*}/RuP^{I}$ potential is fairly similar to the $[Ru(bpy)_3]^{II*}/[Ru(bpy)_3]^{I}$ value of 0.83 V.

**Table 9** Reduction potentials (V *vs.* SHE) for ruthenium bipyridyl complexes, measured in water.[263,334,335]

| | *E*(III/II) | *E*(III/II*) | *E*(II/I) | *E*(II*/I) |
|---|---|---|---|---|
| $[Ru(bpy)_3]^{2+}$ | 1.27 | -0.87 | –1.32 | 0.83 |
| $[Ru(bpy)_2(4,4'\text{-}(PO_3H_2)_2bpy)]^{2+}$ (RuP) | 1.26 | -0.95 | –1.21 | *unknown* |

Although only one mechanism of electron photoinjection from RuP into $TiO_2$ has been mentioned so far, there is an alternative, and both of these are shown in Figure 41. In what is defined here as Mechanism 1, MLCT photoexcitation of RuP forms the excited state $RuP^{II*}$, and this is immediately followed by injection of an electron into the $TiO_2$ conduction band. The resulting oxidised dye, $RuP^{III}$, is then reduced back to $RuP^{II}$ by the sacrificial electron donor, and another cycle of photoinjection and regeneration can occur. This is the route that has already been described. The alternative route is shown as Mechanism 2. Here, photoexcitation occurs as before, but instead of immediate electron injection into the $TiO_2$ conduction band, the excited state dye is firstly reduced by the sacrificial electron donor, forming $RuP^{I}$. Electron injection from *this* species reforms the original state of the dye ($RuP^{II}$), and the electrons in the $TiO_2$ conduction band migrate to the CODH catalytic centre for $CO_2$ reduction, as before.

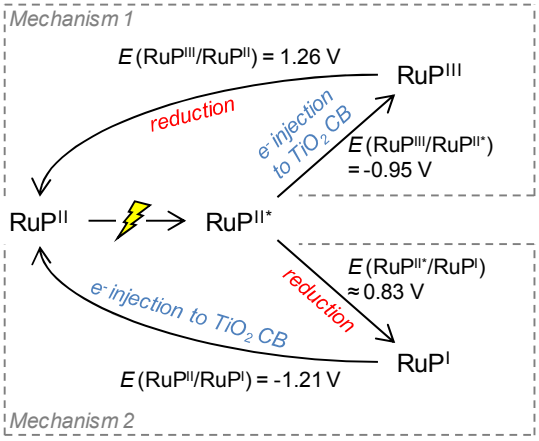


**Figure 41 Possible mechanisms for continuous photoinjection from RuP into $TiO_2$.** In Mechanism 1, photoexcitation of $RuP^{II}$ to $RuP^{II*}$ is immediately followed by electron injection (into the conduction band of $TiO_2$), before $RuP^{II}$ is regenerated through reduction by a sacrificial electron donor. In Mechanism 2, the photoexcited state ($RuP^{II*}$) is firstly reduced to $RuP^{I}$ by the sacrificial electron donor, before electron injection from this reduced species into $TiO_2$. In the presence of a high concentration of a sufficiently reducing electron donor, both mechanisms are cyclical and therefore allow continuous photoinjection to occur. Reduction potentials are those shown in Table 9, taken from references [263,334].

Operation of Mechanism 2 may be preferable, because $RuP^{I}$ is more reducing than $RuP^{II*}$ by around 0.26 V. However, it can be assumed that in practice the dominant mechanism is Mechanism 1. While the *thermodynamics* of Mechanism 2 are sound, this route will be suppressed on *kinetic* grounds. Electron injection from excited states of ruthenium bipyridyl complexes into $TiO_2$ has been extensively studied, and is known to occur on picosecond timescales.[160-165] Quenching of $RuP^{II*}$ by a solution species to form $RuP^{I}$ (the Mechanism 2 route) is therefore kinetically disfavoured compared to the ultrafast electron transfer into $TiO_2$ from $RuP^{II*}$ (Mechanism 1).

It should be noted that the schemes above represent the desired (productive) processes for $CO_2$ photoreduction. There exist, however, a number of undesirable (waste) processes. The most obvious are back electron transfers; that is, recombinations of photoinjected electrons

with oxidised photosensitiser species. These reactions can be written as shown below, where $TiO_2(e^-)$ represents an electron in the conduction band of $TiO_2$:

$TiO_2(e^-)–RuP^{III} \rightarrow TiO_2–RuP^{II}$ (Back electron transfer applicable to Mechanism 1)

$TiO_2(e^-)–RuP^{II} \rightarrow TiO_2–RuP^{I}$ (Back electron transfer applicable to Mechanism 2)

In terms of avoiding unwanted back electron transfers, Mechanism 2 again offers an advantage, because $RuP^I$ is highly reducing ($E(RuP^{II}/RuP^I) = -1.21$ V). Electron transfer from the $TiO_2$ conduction band (-0.52 V) to $RuP^{II}$ is therefore highly disfavoured thermodynamically and unlikely to occur. Nonetheless, in the event that such a recombination does take place, the ruthenium product is $RuP^I$; that is to say the photoinjecting species is simply reformed. The back electron transfer applicable to Mechanism 1 is of greater concern. Here, recombination forms not the photoinjecting species ($RuP^{II*}$), but the reduced (ground) state of the dye, $RuP^{II}$. Competition of the rate of this waste process with reductive regeneration of $RuP^{II}$ by the sacrificial electron donor is therefore critical (experiments in Chapter 5 will investigate the effect of concentration and identity of the sacrificial electron donor). In the initial experiments presented in this chapter, MES is the suspension buffer and it is also capable of providing electrons as the sacrificial electron donor.[336-338]

To date, PFE experiments on *Ch* CODHs have only been carried out using graphite electrodes, at which it was established that both $CODH_I$[196,197] and $CODH_{II}$[197] adsorb readily and that electronic interaction between the electrode surface and the enzyme molecules is facile, even if current responses are unstable over time. For both enzymes, a cationic co-adsorbate (polymyxin B sulfate) was required to achieve enzyme films that were sufficiently

stable on the electrodes to allow experiments to be carried out. The interaction between CODHs and $TiO_2$ surfaces is thus far unknown – both the surface functionalities as well as the electronic character of $TiO_2$ are different to graphite – and so the starting point of this chapter is to establish whether these enzymes are able to attach to this semiconducting material to form electrocatalysts preserving the characteristics established at graphite electrodes. Motivation to carry out electrochemical experiments of CODHs on $TiO_2$ electrodes also comes from previous studies of other proteins such as cytochrome *c* and haemoglobin at this (and other semiconductor) electrode surfaces. In these reports[339-348] it was, in general, found that $TiO_2$ offers numerous attractions as an electrode surface for the study of proteins: it has a high biocompatibility, can enable specific binding with protein molecules, and the mesoporosity of the electrodes (see later) provide a large surface area for high protein loading.

## 4.2 RESULTS AND DISCUSSION

### 4.2.1 ATTACHMENT OF $CODH_I$ AND $CODH_{II}$ TO $TiO_2$ NANOPARTICLES

The solar fuel system outlined in section 4.1.1 relies upon successful attachment of enzyme molecules to the $TiO_2$ surface, and furthermore, the binding must be such that the D-cluster of CODH (the FeS cluster closest to the protein surface) is within electronic contact of the semiconductor. The isoelectric point of both $CODH_I$ and $CODH_{II}$ is 5.5,[185] and that of P25 $TiO_2$ is 6.2.[349] Therefore, envisioning the prominent adsorption interaction to be electrostatic, one would predict pH 6.0 (a value between the isoelectric points of the enzymes and $TiO_2$) to be a suitable condition for attachment: at this pH, the net surface charges of the enzyme and $TiO_2$ will be negative and positive, respectively.

UV-vis spectroscopy was used to detect the attachment of $CODH_I$ and $CODH_{II}$ (separately) onto P25 $TiO_2$ nanoparticles in suspension in aqueous solution (Figure 42). The adsorption procedure used here matches the protocol that will later be followed for the assembly of [RuP-$TiO_2$-CODH] $CO_2$ photoreduction systems. This procedure, carried out in an anaerobic glovebox (Belle, $O_2$ < 3 ppm) was as follows: 5 mg of nanoparticles were suspended in 5 mL of 0.20 M MES buffer solution (pH 6.0) by sonication at room temperature for 20 min. Then, 2.56 nmol of $CODH_I$ or $CODH_{II}$ was added (as a solution of typical stock concentration of 0.12 – 0.18 mM), and the suspension was stirred for 20 min to allow adsorption to the nanoparticles. The reaction vessel was then removed from the glovebox and centrifuged and filtered through a PTFE filter to remove the nanoparticles, before measuring the UV-vis absorption of the clear solution (grey spectrum in Figure 42). A spectrum (black) was also recorded of an enzyme solution that had not been exposed to nanoparticles, but had otherwise been treated identically.

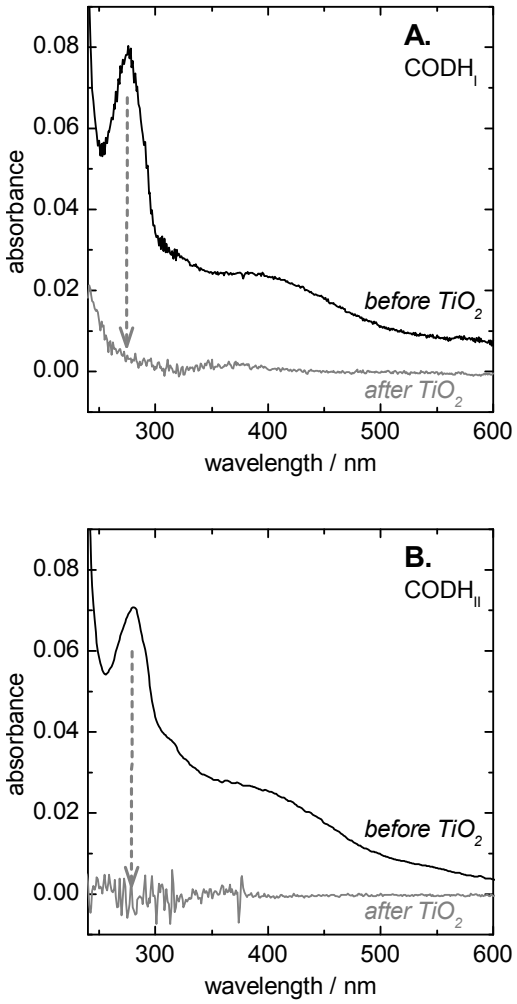


**Figure 42** UV-vis absorbance spectra of 2.56 nmol $CODH_I$ (A) or $CODH_{II}$ (B) in 5 mL 0.20 M MES buffer (pH 6.0) before (black) and after (grey) adsorption onto 5 mg P25 $TiO_2$ nanoparticles in suspension. Before collecting the grey spectrum, the nanoparticles were separated from the solution by centrifugation and filtration.

The spectra in Figure 42A indicates almost complete adsorption, under the conditions of this procedure, of the 2.56 nmol $CODH_I$ onto 5 mg P25 $TiO_2$ nanoparticles (from several repeats, an average attachment of 2.40 ± 0.03 nmol to 5 mg nanoparticles was calculated). The spectra in panel B indicate *complete* uptake of the 2.56 nmol $CODH_{II}$ onto the same amount of nanoparticles. From the total surface area of the $TiO_2$ sample and the average size of the

nanoparticles, it is possible to calculate an approximate loading of around 5-10 enzyme molecules per nanoparticle (Appendix A3).

## 4.2.2 ELECTROCATALYTIC ACTIVITY OF CODHs ATTACHED TO $TiO_2$ THIN FILM ELECTRODES

### 4.2.2.1 CHARACTERISATION OF P25 $TiO_2$ THIN FILM ELECTRODES

The cartoon representation of the $CO_2$ photoreduction system proposed in Figure 39 shows that there are two separate active species that must interact with the semiconductor: the ruthenium-based dye species RuP and the CODH (either $CODH_I$ or $CODH_{II}$). In order to assess and study the behaviour of these components at the surface of P25 $TiO_2$ in aqueous solution, thin-film electrodes comprised of the same material were prepared according to the 'Doctor's Blade' method[261] described in section 2.1.2.4.2. The electrodes, having the form of a mesoporous, thin (< 10 μm) film of $TiO_2$ sintered onto a conducting (indium tin oxide, ITO)-glass substrate, were stationary - as opposed to rotating - both for practical reasons associated with the method of construction and also to ensure the validity of the electrochemical response in view of the proposed solar fuel system: $TiO_2$ particles in suspension are non-rotating (in an electrochemical sense), and therefore PFE experiments using a rotating electrode would be less relevant here.

Scanning electron micrograph (SEM) images of a P25 $TiO_2$ thin film electrode are shown in Figure 43. The film is observed to be highly porous (as expected). The images also reveal the presence of cracks of widths of around 0.1 – 0.5 μm extending across the surface of the film that arose during the calcination process, although these are not of significant concern.

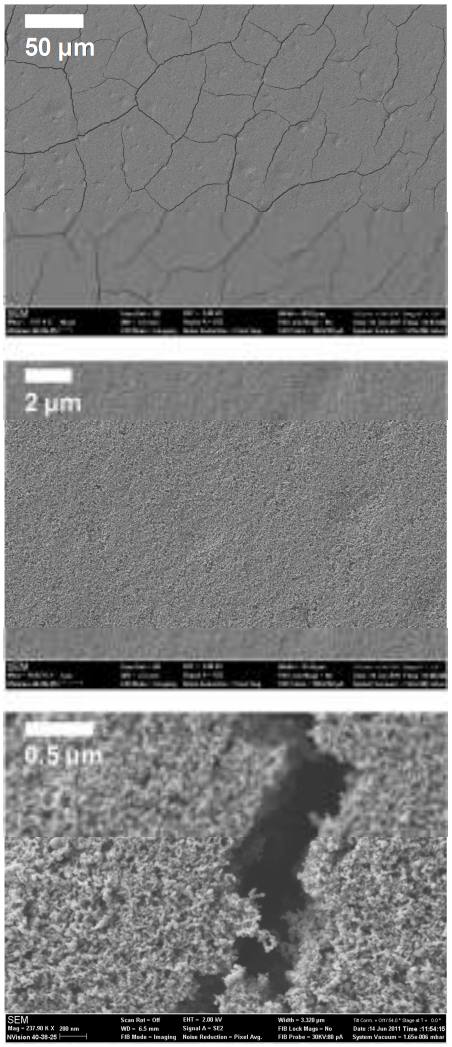


**Figure 43** SEM images of a P25 $TiO_2$ thin film electrode. The method of preparation is described in section 2.1.2.4.2. The bottom image is a magnification of one of the cracks in the film that are visible in the top image.

The porosity of the thin film means that the *electrochemically active* area of the electrode is significantly greater than the *geometric* area (studies of electrodes produced in a very similar manner, also from P25 $TiO_2$, were found to have an active surface area around 150 times greater than the geometric area).[345] This porosity also means that the magnitude of the electrochemical response of the unmodified electrode (the 'background' current) is sensitive to the film thickness. Due to the simple 'Doctor's Blade' method by which the electrodes are

prepared, there is no strict control over the film thickness, and hence the size of the background current. Figure 44 shows cyclic voltammograms of two unmodified P25 $TiO_2$ thin film electrodes of the same geometric area; we can infer from the relative magnitudes of the voltammetric responses that the grey voltammogram was recorded at an electrode of greater film thickness. While this is of no immediate concern (catalytic voltammograms can always be compared to the background current recorded at that particular electrode, and when appropriate can be processed by subtraction of the background), large background currents may mask the electrochemical response of interest. For this reason, electrodes providing background current responses exceeding ±8 μA when scanned within the potential range of Figure 44 (-0.6 V – 0 V *vs.* SHE) were discarded.

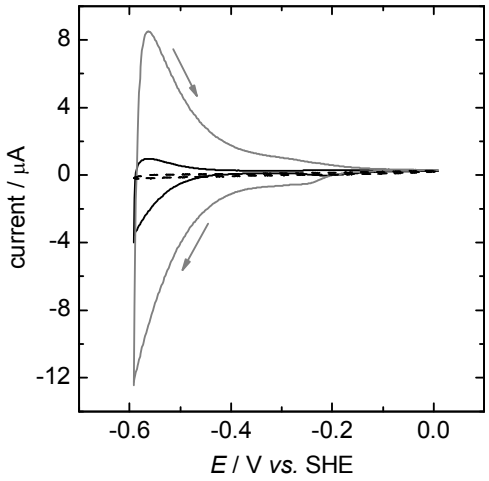


**Figure 44** Cyclic voltammograms of unmodified $TiO_2$ thin film electrodes (solid lines) recorded at 10 mV $s^{-1}$ in 0.20 M MES (pH 6.0) buffer solution at 20 ºC. The variation in magnitude of the current results from the difference in the thickness of the $TiO_2$ films, which are highly porous (the grey voltammogram is recorded using a thicker film). The dotted grey line is the response of the conducting (ITO-coated) glass substrate alone, in the absence of a $TiO_2$ film. Arrows indicate the scan direction.

The characteristic 'trumpet' shape of these voltammograms is attributable to the reversible reduction of surface Ti atoms ($Ti^{4+} + e^- \acute{Y} Ti^{3+}$), with electrons being injected into (or extracted from) sub-band gap states.[350,351] As the current is swept in the negative direction from around -0.4 V (note the direction of the arrows in Figure 44), electrons start to occupy conduction band states and the accumulating charge is compensated for by adsorption of a proton. The overall process is best represented by the equation:

$$Ti^{IV}O_2 + e^- + H^+ \rightarrow Ti^{III}O(OH)$$

#### 4.2.2.2 DIRECT ELECTROCHEMISTRY OF CODH ATTACHED TO P25 $TiO_2$ THIN FILM ELECTRODES

Figure 42 indicates that $CODH_I$ and $CODH_{II}$ adsorb to the surface of P25 $TiO_2$, but provides no information on whether the enzyme molecules are attached *electroactively* (that is, such that electron transfer between enzyme and $TiO_2$ is viable). $CODH_I$ and $CODH_{II}$ are known to display rapid and efficient interconversion of CO and $CO_2$ when adsorbed onto PGE electrodes,[196,197] and electrochemical experiments are now described that were carried out to, firstly, ascertain the ability of these enzymes to demonstrate catalytic activity when attached to a $TiO_2$ electrode, and secondly, to allow a critical comparison to the behaviours at graphite. In all cases, electrodes were modified by spotting a 4 μL aliquot of enzyme solution (concentration 0.12 – 0.18 mM) onto and off the electrode surface repeatedly for around 1 min, then leaving the electrode surface to partially dry (~ 2 min) before connecting it into the electrochemical cell.

Cyclic voltammograms recorded using these electrodes with CO or $CO_2$ gently bubbling through the electrochemical cell solution are shown in Figure 45. It is clear from panels A –

D that both $CODH_I$ and $CODH_{II}$ are indeed active in terms of catalysis of CO oxidation and $CO_2$ reduction on both PGE and $TiO_2$ thin film electrodes (as mentioned earlier, it was already known that $CODH_I$ exhibits excellent catalysis at graphite). In the absence of substrate (CO or $CO_2$), no catalytic current was observed at any of the electrodes, nor was there any response if the same amount of enzyme solution that was spotted onto the electrodes was instead simply added to the electrochemical cell solution. Also, control experiments using bare ITO electrodes (*i.e.* without a $TiO_2$ thin film) onto which enzyme had been added, exhibited no catalytic current. Crucially (in view of assembly of a CODH-$TiO_2$ based $CO_2$ photoreduction system), the sharp reductive waves at CODH-modified $TiO_2$ electrodes in the presence of $CO_2$ (panels C and D) indicate excellent reductive catalysis, with the onset potentials matching those at graphite (~ -0.4 V).

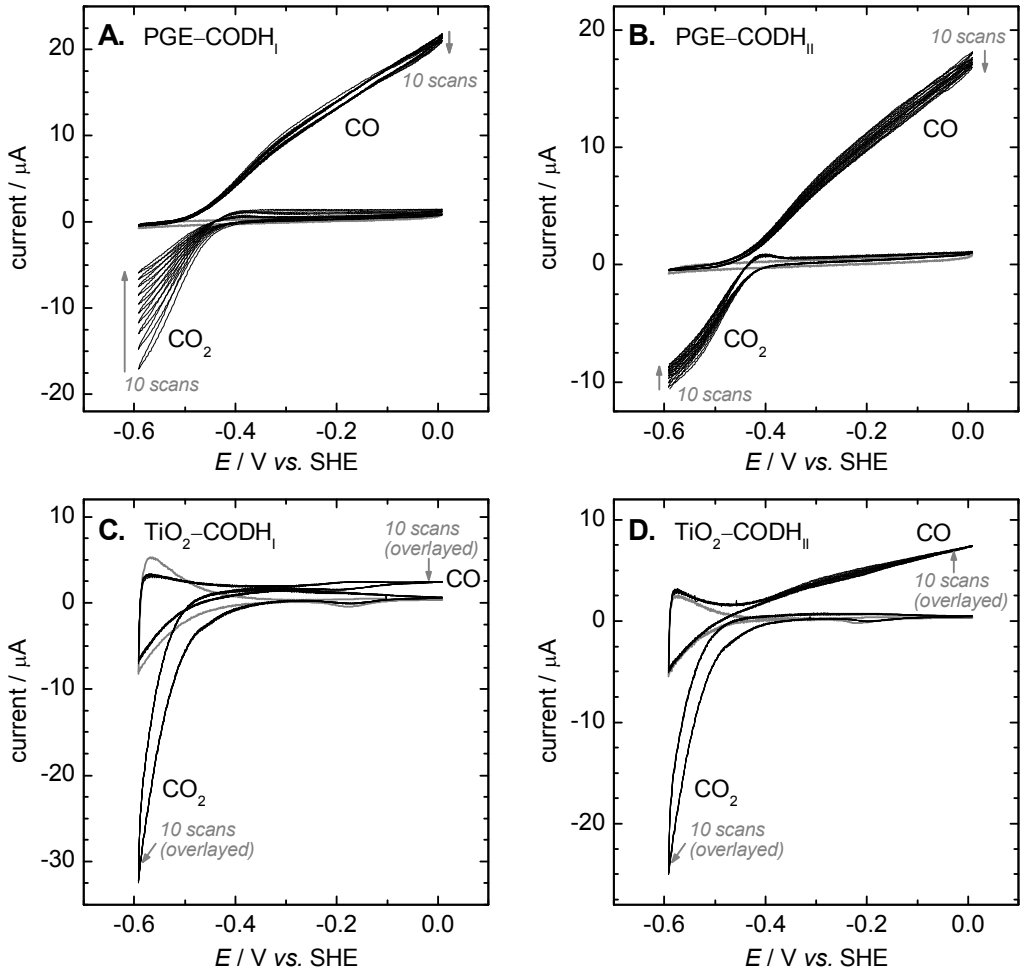


**Figure 45 Catalytic cyclic voltammetry of $CODH_I$ or $CODH_{II}$ immobilised on stationary PGE and P25 $TiO_2$ thin film electrodes.** Shown in black are sets of ten immediately successive voltammograms (10 mV $s^{-1}$) recorded at electrodes modified with either $CODH_I$ or $CODH_{II}$ (as indicated), with CO and $CO_2$ (in separate experiments) bubbling through the cell solution. Each set of scans was recorded as soon as the electrode had been modified with enzyme. The background currents recorded at unmodified electrodes with CO bubbling though the cell solution are shown in grey. In all experiments (10 mV $s^{-1}$), the cell solution was 0.20 M MES (pH 6.0) and the temperature was maintained at 20 ºC.

Although the presence of catalytic activity in all of the enzyme-electrode permutations is clear, there are subtle differences in the electrochemistry at the different surfaces. Firstly, it is apparent from a comparison of panels A and C that $CODH_I$ is considerably more stable -

under the conditions of these experiments, at least - on $TiO_2$ than on PGE. This is particularly the case during reductive catalysis when $CO_2$ is bubbled through the cell: over the course of ten cycles (at a scan rate of 10 mV $s^{-1}$, corresponding to a total time of around 20 min) the activity of $CODH_I$ on PGE has more than halved, whereas the voltammograms recorded using $TiO_2$ completely overlay, indicating no loss of activity. A very small amount of activity loss is observed under CO at PGE, but this is negligible in comparison to the loss under $CO_2$. Panels B and D show similar trends: $CODH_{II}$ is more stable on $TiO_2$ than PGE.

Figure 46 shows chronoamperometry experiments intended to investigate the differences in stability of CODH-catalysed $CO_2$ reduction over a longer time period of 4 h (most interest is in $CO_2$ reduction here, as opposed to CO oxidation). In these experiments, the electrode was poised at -0.52 V (sufficiently reducing to drive $CO_2$ reduction) while $CO_2$ was bubbled through the cell solution. In agreement with the experiments in Figure 45, CODH-modified $TiO_2$ electrodes displayed superior stability, although there was some loss of activity over 4 h for both $CODH_I$-modified $TiO_2$ and $CODH_{II}$-modified $TiO_2$. Average activity losses, calculated from several repeats, are shown in Table 10 which follows.

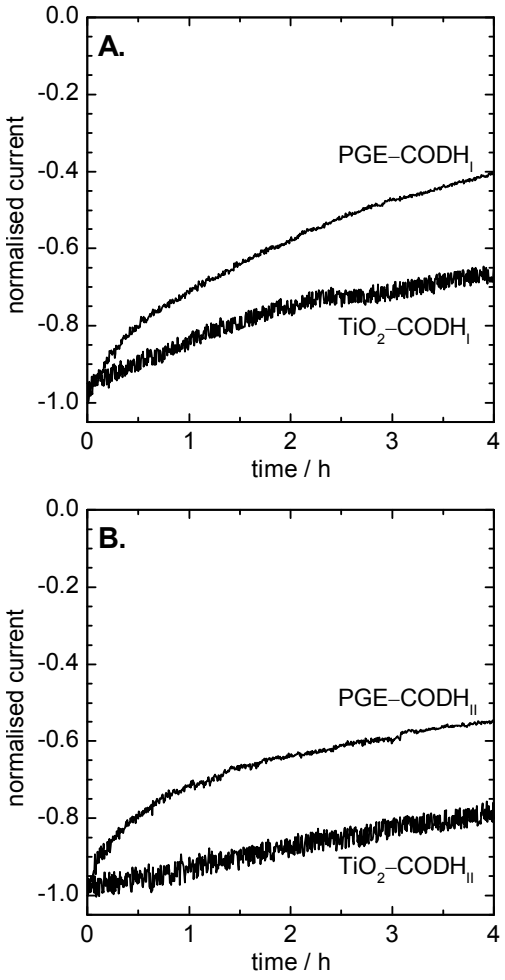


**Figure 46 Stability of $CODH_I$ and $CODH_{II}$ on PGE and P25 $TiO_2$ thin film electrodes at 20 ºC.** Typical chronoamperometry experiments (normalised to the current at 0 h) using PGE and P25 $TiO_2$ electrodes modified with either $CODH_I$ (A) or $CODH_{II}$ (B). $CO_2$ was bubbled through the cell solution (0.20 M MES, pH 6.0) with the electrode potential held at -0.52 V. Average activity losses are shown in Table 10.

**Table 10** Average $CO_2$ reduction activity losses suffered over 4 h at electrodes modified with either $CODH_I$ or $CODH_{II}$, under the conditions of Figure 46 (-0.52 V, pH 6.0, 20 ºC).

| electrode material | enzyme | % $CO_2$ reduction activity lost over 4 h |
|---|---|---|
| PGE | $CODH_I$ | 69 ± 9.8 |
| PGE | $CODH_{II}$ | 53 ± 7.6 |
| P25 $TiO_2$ | $CODH_I$ | 34 ± 5.8 |
| P25 $TiO_2$ | $CODH_{II}$ | 23 ± 7.0 |

The second major difference between the electrochemistry at PGE compared to $TiO_2$ is that, for both $CODH_I$ and $CODH_{II}$, the relative activities of CO oxidation and $CO_2$ reduction appear to depend upon the underlying electrode material – on PGE electrodes the magnitudes of oxidative and reductive currents are approximately equal (in panel A, the first $CO_2$ reductive wave is considered), whereas at the $TiO_2$ thin film electrodes $CO_2$ reduction is clearly favoured over CO oxidation. In order to examine this more precisely – specifically, to remove any complication of activity loss between sets of voltammograms under 100% CO and 100% $CO_2$ – experiments were carried out in the presence of mixed substrate (50% CO, 50% $CO_2$, Figure 47). Now, both oxidation and reduction activities are observable in the same voltammogram, and the observed biases of each of the enzymes on the two electrode materials is quantifiable.

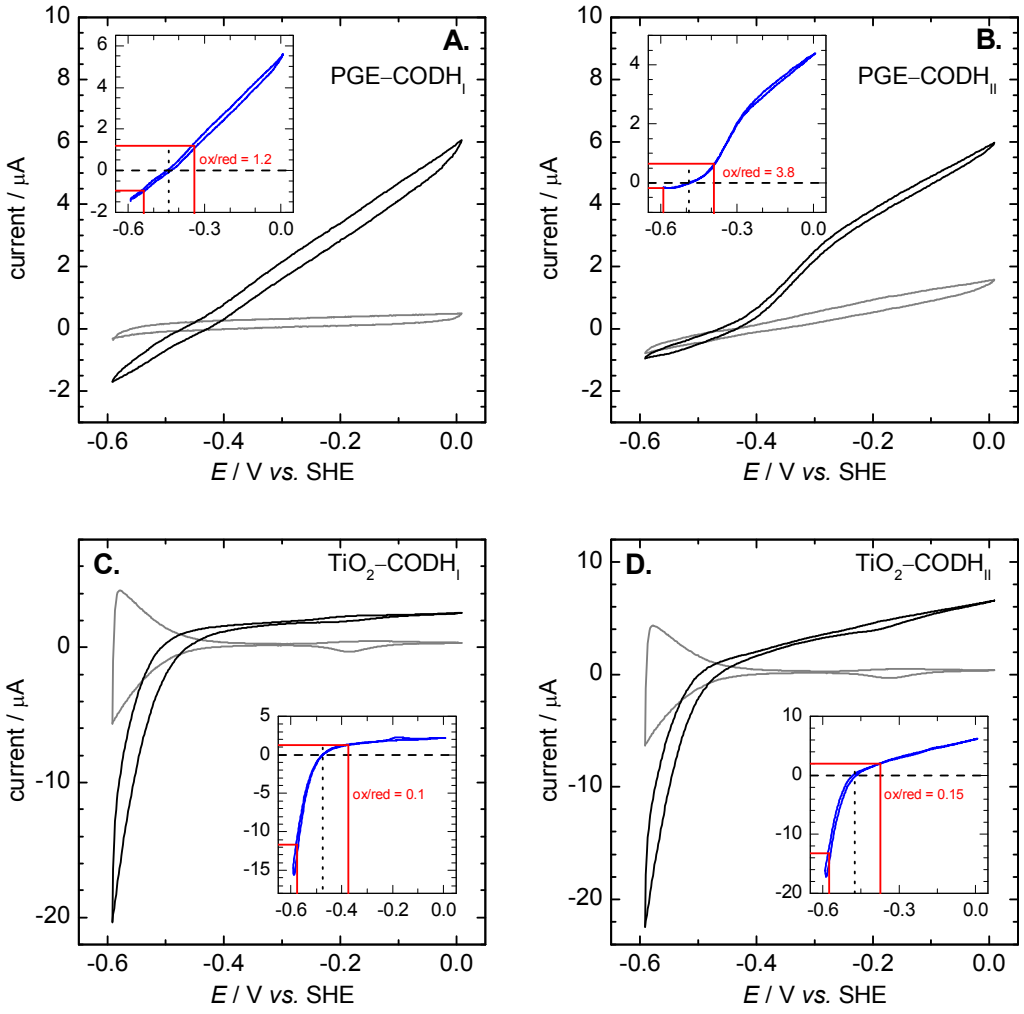


**Figure 47** Cyclic voltammograms recorded at 10 mV $s^{-1}$ using stationary PGE (A and B) and P25 $TiO_2$ thin film (C and D) electrodes, with a gas mixture of 50% CO, 50% $CO_2$ bubbling through the cell solution. The black voltammograms were recorded at electrodes modified with either $CODH_I$ or $CODH_{II}$ (as indicated), and the grey voltammograms show the responses of unmodified electrodes. The insets show the currents recorded at the enzyme-modified electrodes following subtraction of the background current (*i.e.* black minus grey). The vertical dotted lines mark the potential of the interception of the background-subtracted voltammograms with the zero current line. The horizontal red lines mark the current recorded 100 mV either side of the zero current potential, from which the ratio of oxidation current to reduction current ('ox/red') is calculated. In all experiments, the cell solution was 0.20 M MES (pH 6.0) and the temperature was maintained at 20 ºC.

Let us first consider the catalytic behaviour of the enzymes on PGE electrodes. Referring back to panels A and B of Figure 45, in which in any one set of experiments the gas being bubbled through the cell solution was either 100% CO (equivalent to an aqueous solution concentration of 0.95 mM) or 100% $CO_2$ (34 mM), $CODH_I$ and $CODH_{II}$ appeared to be very similar in terms of their abilities to catalyse oxidation and reduction at similar rates (that is, neither enzyme displayed a noticeable 'catalytic bias'). However, the voltammograms in panels A and B of Figure 47 – in which CO and $CO_2$ are *both* present at the same time - reveal a marked difference between the enzymes in terms of this property. $CODH_I$ (panel A) catalyses both directions of interconversion at roughly equal rates (as might be expected from the behaviour observed in Figure 45A), but $CODH_{II}$ (panel B) shows very little $CO_2$ reduction activity under these mixed-substrate conditions. Combining information from Figure 45B and Figure 47B, it is possible to infer that the presence of CO at the concentration used here (50% gas atmosphere, equivalent to 0.48 mM solution concentration) leads to almost complete suppression of $CO_2$ reduction activity. This phenomenon, termed 'product inhibition,' has been observed in a number of redox enzymes, including [FeFe]-hydrogenases.[352] A full investigation of the extent $CODH_{II}$ to product inhibition of $CO_2$ reduction is outside the scope of this Thesis, and is currently under investigation.[353]

Turning to panel C of Figure 47, it is clear that under mixed substrate conditions, $CODH_I$ attached to a $TiO_2$ electrode remains a much more effective catalyst for $CO_2$ reduction than for CO oxidation (more quantitatively, the ratio of oxidative current to reductive current - 'ox/red' - when driving forces of 100 mV are applied, is 0.1). A similar bias is observed for $CODH_{II}$ at $TiO_2$ (panel D), with an ox/red ratio of 0.15, but at first this seems to be in conflict with the inhibitory effect observed at PGE-$CODH_{II}$ under the same conditions (just

mentioned). In order to try to explain the reasons for the catalytic biases (from now on, termed *apparent* catalytic biases) the electronic structures of the electrode materials must be considered.

#### 4.2.2.3 ELECTRONIC STRUCTURES OF PGE AND $TiO_2$: EFFECT ON APPARENT CATALYTIC BIASES OF $CODH_I$ AND $CODH_{II}$

The electrode surface-dependent differences in the catalytic voltammetry of both CODHs may be accounted for by considering the electronic structures of the electrode materials. It is most appropriate to discuss electronic structure here in terms of energy bands; conduction is possible when bands are partially filled. In graphite the valence and conduction bands overlap, so essentially the electronic structure comprises one partially filled band and electronic conduction is facile. In the case of semiconductors such as $TiO_2$, in order for conduction to be possible electrons must be promoted into the conduction band from the valence band (this may be achieved either thermally or photochemically by irradiation of photons of sufficient energy), or alternatively electrons can be introduced artificially (*i.e.* from an external source such as a potentiostat).[354]

The 'Fermi level' is defined as the potential at which the probability of occupation by an electron is ½ (note, however, that this is not to say that an electronic state must exist at that potential). For $TiO_2$ – a 'natural' n-type semiconductor, the Fermi level is slightly more positive than the conduction band potential. At a certain applied potential, no space-charge layer will exist within the semiconductor, and there is no band bending (that is to say, the energy levels of the conduction and valence bands do not vary depending on the distance from the semiconductor-solution interface). This potential is termed the 'flatband potential'. At pH 6 (the pH of the voltammetry experiments in this chapter) the flatband potential of

anatase is at around -0.52 V;[355] when an external potential more *negative* than this is applied to a $TiO_2$ thin film electrode ($E < E_{flatband}$), electrons will start to fill sub-band gap defect states (either oxygen vacancies in the bulk, or surface Ti atoms that are coordinated to water molecules).[355] An accumulation layer is formed in the surface layers of the semiconductor close to the solution interface, and as a result the bands bend downwards towards the solution interface (Figure 48, left). Conversely, when the $TiO_2$ thin film is under the influence of an externally-applied potential that is more *positive* than the flatband potential ($E > E_{flatband}$, right-hand diagram), its conductivity is low because the bands now bend upwards and the Fermi level lies in between the conduction and valence bands.

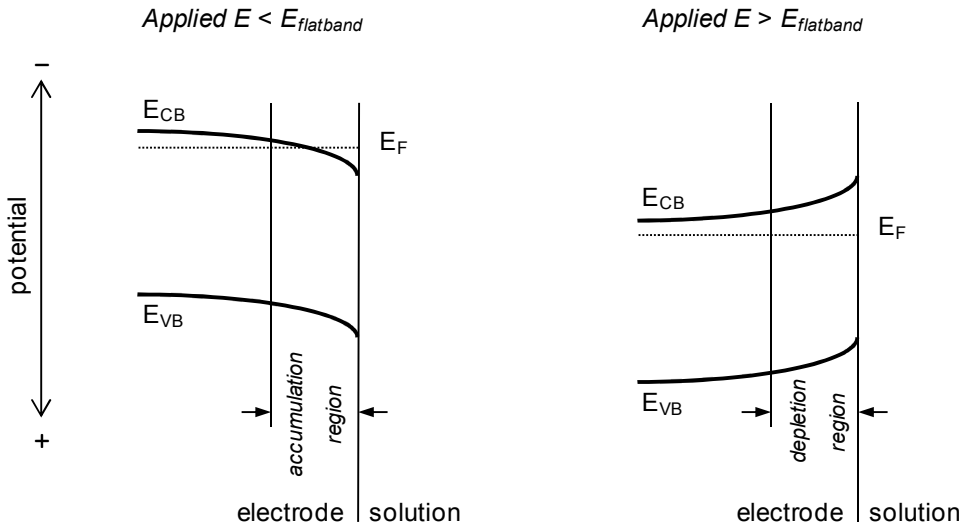


**Figure 48 The effect of external applied potential on the band edges in $TiO_2$ (an n-type semiconductor).** On the left, the applied potential is more negative than the flatband potential ($E < E_{flatband}$); electrons fill sub-band gap states and an accumulation layer is formed. On the right, the applied potential is more positive than the flatband potential ($E > E_{flatband}$) and a depletion layer is formed. Due to the direction of band bending, electronic conduction is only possible in the left-hand scenario (equivalently, conduction is not possible in the right-hand scenario because the Fermi level lies well within the band gap).

It should be noted at this point that for materials on the nanoscale or smaller (such as the anatase nanoparticles used later in this thesis), a space-charge region cannot be supported because the dimensions of such particles is smaller than the depth of the potential gradient.[356,357] Therefore the band bending behaviour illustrated above does not occur in such instances, and applies only to larger semiconductor materials approaching a 'bulk' regime.

An elegant pair of spectroelectrochemical experiments by Topoglidis *et al.*[347] serve to illustrate the fact that $TiO_2$ thin film electrodes are only conductive at low potentials. The onset potential for conductance was determined by taking advantage of the colour change of the film that occurs on account of the one electron reduction of $Ti^{IV}$ to $Ti^{III}$. At potentials more negative than -0.3 V *vs.* Ag/AgCl, the $TiO_2$ films develop an absorption centred at 750 nm that is attributable to intra- and interband transitions of electrons accumulated in conduction band states ($Ti^{III}$). This absorption does not appear when the electrode is poised at more positive potentials (> -0.3 V *vs.* Ag/AgCl) that are not sufficiently reducing to inject electrons. The behaviour of cytochrome-*c* immobilised on the $TiO_2$ electrodes was consistent with the conductivity probe experiment: reduction of the protein (monitored by the 550 nm optical absorbance of the reduced heme centre) was only effected below -0.3 V *vs.* Ag/AgCl despite the fact that its redox potential in solution is much more positive (+0.38 mV). This is attributed to the $TiO_2$ not having sufficient conductivity at higher potentials; by the same notion, oxidation of the protein is not possible because the $TiO_2$ film is not conductive at the necessary potential.

The same conductivity characteristic has implications here at CODH-modified electrodes: at more positive potentials the Fermi level lies well within the band gap of the $TiO_2$ film, and so

the conductivity is very low. Under the conditions of the experiments in Figure 47 (a gas atmosphere of 50% CO, 50% $CO_2$ at pH 6.0), the PGE-$CODH_I$ voltammogram (Panel A) cuts the line of zero current at around -0.45 V; below this potential $CO_2$ reduction is catalysed, and above this potential CO oxidation is catalysed. Here, the observed catalytic currents are not affected by the electronic properties of the electrode, since graphite is an excellent conductor regardless of the applied potential. As discussed earlier, almost no catalytic bias is observed. In the case of $TiO_2$-$CODH_I$ (panel C), however, the oxidation current (present in a potential range corresponding to poor electronic conductivity) is suppressed compared with the $CO_2$ reduction current, which occurs at the more negative potentials at which $TiO_2$ is conductive.

The $TiO_2$-$CODH_{II}$ case (panel D in Figure 47) is more complex, because, as described earlier, the PGE-$CODH_{II}$ electrochemistry (panel B) – assuming this electrode to provide a truer report on the inherent characteristics of the enzyme - indicates that the enzyme displays product inhibition of $CO_2$ reduction. At first glance, it is therefore remarkable that the $TiO_2$-$CODH_{II}$ voltammogram (panel D) shows such a strong $CO_2$ reduction wave under these mixed substrate conditions, but on further consideration this actually serves to highlight the insulating nature of the $TiO_2$ film further and emphasises the high activity of the enzyme immobilised on $TiO_2$: assuming the result in panel B to be a true reflection of the inherent characteristic of the enzyme, the large reduction current of -20 μA in panel D represents the remaining activity of an enzyme that has been greatly inhibited by the presence of a high product (CO) concentration.

In light of the earlier discussion on the varying, potential-dependent conductivity of $TiO_2$, the fact that a small amount of CODH-catalysed CO oxidation is detected in these electrochemical experiments (panels C and D of Figure 45 and Figure 47) is also interesting. This may be attributed to direct electronic contact between some of the enzyme molecules and the ITO-coated glass, a scenario made possible by the aforementioned porosity of the $TiO_2$ films. Control experiments in which CODH was spotted onto bare ITO electrodes yielded no catalytic current response, but it is readily conceivable for enzyme molecules that are anchored by $TiO_2$ particles deep within the film to exchange electrons directly with the ITO. Being a good conductor, ITO suffers no potential-dependent conductivity attenuation, and a component of CO oxidation current can therefore arise.

Subtleties aside, the most important conclusion from the point of view of construction of a $CO_2$-reducing solar fuel system is that both $CODH_I$ and $CODH_{II}$ are electrochemically active for $CO_2$ reduction at this semiconducting surface. Fast rates (at least as high as those at PGE electrodes) are achieved, and, critically, since only slim thermodynamics are available (section 4.1.2), efficiencies are preserved which means that as is the case at graphite electrons, minimal overpotentials are required to drive reduction. In addition, $CO_2$ reduction activity stabilities are reasonably good over time periods of several hours. The next step, therefore, is to drive reduction with electrons provided not from an external potentiostat, but through photochemical routes.

### 4.2.3 DEMONSTRATION OF ELECTROCATALYTIC ACTIVITY DRIVEN BY NEAR-UV LIGHT

P25 $TiO_2$ is predominantly (80%) anatase[331] - a wide band gap semiconductor ($E_g$ = 3.2 eV) requiring light of wavelength < 390 nm to excite electrons from the valence band into the conduction band. Therefore, the formation of [$CODH_I$-$TiO_2$] units *via* the procedure outlined in section 4.2.1, although not resulting in a *visible* light-driven system, can be expected to catalyse the reduction of $CO_2$ to CO using energy provided from near-UV light. Under such conditions, there is no requirement for RuP; electrons are excited into the conduction band directly from the valence band, with the resulting holes being quenched by electron donation from the sacrificial electron donor.

To prepare such a system, the nanoparticles were suspended and functionalised with enzyme as described in section 4.2.1, using a quartz pressure vessel (transparent to UV and visible light), as the reaction vessel. This was sealed tightly with a rubber septum, before flushing the headspace with 2% $CH_4$ in $CO_2$ for 20 min while stirring the suspension. After this, the system was exposed to near-UV light (UVL-28 EL Series UV lamp, 2 mW $cm^{-2}$, $\lambda$ = 365 nm) for 4 h, with GC analysis of the reaction vessel headspace at 0.5, 1, 1.5, 2, 3 and 4 h. The amount of CO in the headspace was quantified against the 2% $CH_4$ internal standard, with reference to calibration plots using known amounts of CO (as described in section 2.3.1). Figure 49 shows the evolution of CO over time, with 1.63 ± 0.17 μmol produced after 4 h, corresponding to a TON of 679 ± 71, and an average TOF over this time period of 0.047 ± 0.005 $s^{-1}$.

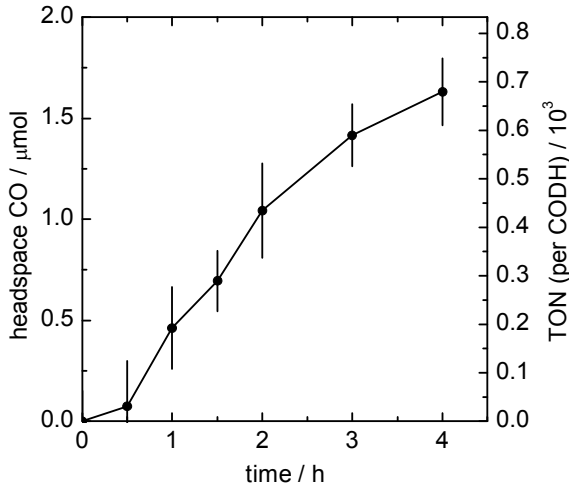


**Figure 49 CO production by [$CODH_I$-$TiO_2$] at room temperature driven by 365 nm (near-UV) light.** The amounts of system components were: 2.56 nmol $CODH_I$, 5 mg P25 $TiO_2$, 5 mL 0.20 M MES buffer solution (pH 6.0). The amounts of CO are determined from the CO peak area:$CH_4$ gas chromatogram peak area ratios, with reference to calibration plots.

A marked decrease in activity over time is observed, the reasons for which will be investigated later in chapter 5. Control systems, in which CODH, $TiO_2$ or $CO_2$ were omitted, failed to produce any detectable amount of CO after 4 h; nor did samples that were protected from light.

### 4.2.4 SENSITISATION OF P25 $TiO_2$ TO VISIBLE LIGHT: TOWARDS VISIBLE LIGHT-DRIVEN $CO_2$ PHOTOREDUCTION

The experiment shown in Figure 49 demonstrates that $TiO_2$ (presumably anatase) conduction band electrons are capable of migrating to surface-immobilised $CODH_I$ molecules for $CO_2$ reduction to CO. The next step is to establish electron supply from visible light-driven electron injection using the ruthenium dye RuP, as opposed to direct band gap excitation that requires near-UV light.

Experiments were firstly carried out in order to verify the ability of RuP to attach to P25 $TiO_2$ nanoparticles under the proposed conditions for $CO_2$ photoreduction experiments (0.20 M MES, pH 6.0, room temperature), and to quantify the amount of dye corresponding to complete coverage of 5 mg nanoparticles. Figure 50A shows UV-vis spectra indicating the attachment of RuP from a 112 μM solution to a 1 mg $mL^{-1}$ suspension of P25 $TiO_2$ nanoparticles. The following method was used: 5 mg of nanoparticles were suspended in 5 mL of 0.20 M MES buffer solution (pH 6.0) by sonication at room temperature for 20 min. Then, RuP was added to the suspension to a final concentration of 112 μM, and stirred gently overnight to allow adsorption to the nanoparticles. The suspension was taken out of the glovebox and centrifuged and filtered using a PTFE filter to remove the nanoparticles, before recording a UV-vis absorption spectrum of the clear solution. The spectra in Figure 50A show absorbance of the RuP solutions before (a) and after (b) overnight exposure to the $TiO_2$ suspension (the solutions were diluted 15-fold before collecting the UV-vis spectra). The band at 455 nm corresponds to the visible ($d \rightarrow \pi^*$) transition of RuP, and the difference in intensities of this absorption between spectra (a) and (b) – 38.0% ± 1.5%, corresponding to 213 ± 8 nmol for 5 mg $TiO_2$ - indicates the maximum possible adsorption of dye to this amount of nanoparticles (it is presumed that this loading represents *complete coverage*, since allowing several days for dye attachment led to no further attachment). On this basis, it was decided to assemble (initially, at least) [RuP-$TiO_2$-CODH] systems for $CO_2$ photoreduction experiments using 10% (*i.e.* 56 nmol) of the amount of RuP used in this experiment, such that sufficient surface remains for attachment of CODH to the nanoparticles. Since 213 nmol RuP is required for complete coverage of the surface of 5 mg nanoparticles, 56 nmol is expected to cover approximately 25%.

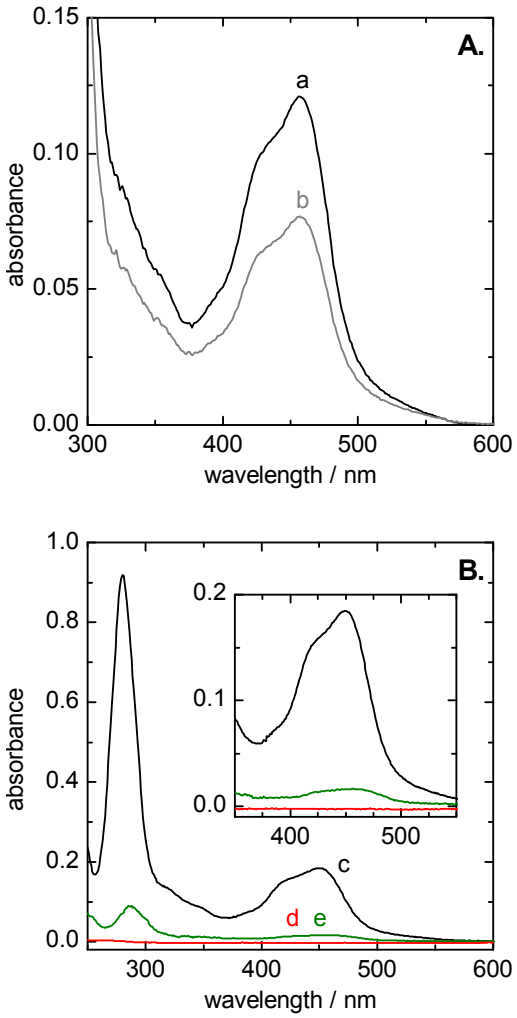


**Figure 50 UV-vis absorbance spectra to detect attachment of RuP to P25 $TiO_2$ nanoparticles in aqueous suspension.** (A) Spectra for quantification of maximum coverage of RuP on 5 mg P25 $TiO_2$: 0.56 µmol (112 µM) RuP in 5 mL 0.20 M MES (pH 6.0) before (a) and after (b) overnight exposure to a suspension of 5 mg (1 mg $mL^{-1}$) P25 $TiO_2$ nanoparticles. Both of these solutions were diluted 15-fold before collecting spectra. (B) Attachment of RuP to P25 $TiO_2$ following the method and conditions proposed for preparation of [CODH-$TiO_2$-RuP] $CO_2$ photoreduction systems: 56 nmol (11 µM) RuP in 0.20 M MES (pH 6.0) buffer before (c) and after (d) exposure to a suspension of 5 mg (1 mg $mL^{-1}$) nanoparticles, and (e) after exposure to a suspension of nanoparticles that had already been functionalised with $CODH_I$ by the procedure described in section 4.2.1.

Figure 50B shows the adsorption of this amount (56 nmol) of RuP onto 5 mg P25 $TiO_2$ nanoparticles. The same method as just described to obtain the spectra in panel A was used,

except that RuP was added to a final concentration of 11 μM (56 nmol in 5 mL), and 20 min was allowed for attachment while stirring. Spectrum (d) shows the absorbance of the clear supernatant solution. A spectrum was also recorded of a solution that had not been exposed to nanoparticles, but had otherwise been treated identically (spectrum c). As expected from the result in Figure 50A, complete adsorption of this quantity of dye is observed.

It was decided that in preparation of [RuP-$TiO_2$-CODH] photoreduction systems, the nanoparticles would firstly be modified with enzyme, and secondly with dye (the reason being the relative sizes of the molecules, although the importance of modification in this order is investigated later). In light of this, the effect of *pre-adsorbed* $CODH_I$ on subsequent attachment of RuP was investigated by collecting a UV-vis spectrum (e) of the RuP solution described above following exposure to nanoparticles that had been functionalised immediately before by $CODH_I$ (according to the method described in section 4.2.1). In this case, RuP adsorption to $TiO_2$ was slightly less than complete (84.8% ± 2.1%), with the difference in spectra (d) and (e) attributed to the surface being partially occupied by adsorbed enzyme molecules.

Table 11 summarises the RuP and CODH adsorption data presented thus far:

**Table 11** Spectrophotometrically-determined uptake of RuP, $CODH_I$ and $CODH_{II}$ to 5 mL (1 mg $mL^{-1}$) P25 $TiO_2$ nanoparticle suspensions[a]

| adsorbate | amount added to 5 mg P25 $TiO_2$ / nmol | amount taken up[b] / nmol |
|---|---|---|
| RuP | 560 | 213 ± 8 |
| | 56 (*without* prior attachment of $CODH_I$ to $TiO_2$) | 56 (complete uptake) |
| | 56 (*with* prior attachment of $CODH_I$ to $TiO_2$) | 47.5 ± 1.2 |
| $CODH_I$ | 2.56 | 2.40 ± 0.03 |
| $CODH_{II}$ | 2.56 | 2.56 (complete uptake) |

[a] Suspensions were prepared with 0.20 M MES buffer solution (pH 6.0). [b] Adsorption amounts were calculated as detailed in the main text, using UV-vis absorption data from solutions of RuP/$CODH_I$/$CODH_{II}$ before and after incubation with nanoparticles.

### 4.2.5 DEMONSTRATION OF SUSTAINED ELECTRON INJECTION FROM PHOTOEXCITED RuP TO $TiO_2$

Figure 51 below provides confirmation of successful electron injection from RuP to $TiO_2$ under conditions that were shown in section 4.2.2.2 to be suitable for CODH-catalysed $CO_2$ reduction. In these experiments, RuP was adsorbed to P25 $TiO_2$ thin film electrodes (to form [RuP-$TiO_2$]) by soaking the electrode in a dilute (40 μM) solution of RuP in 0.20 M MES (pH 6.0) for 1 hour while gently stirring. The electrode (now orange in colour, indicating successful attachment of RuP) was then rinsed with water, and connected into an electrochemical cell. The cell solution was 0.20 M MES (pH 6.0), and this was gently bubbled with inert gas (Ar) throughout the experiments in order to stir the solution.

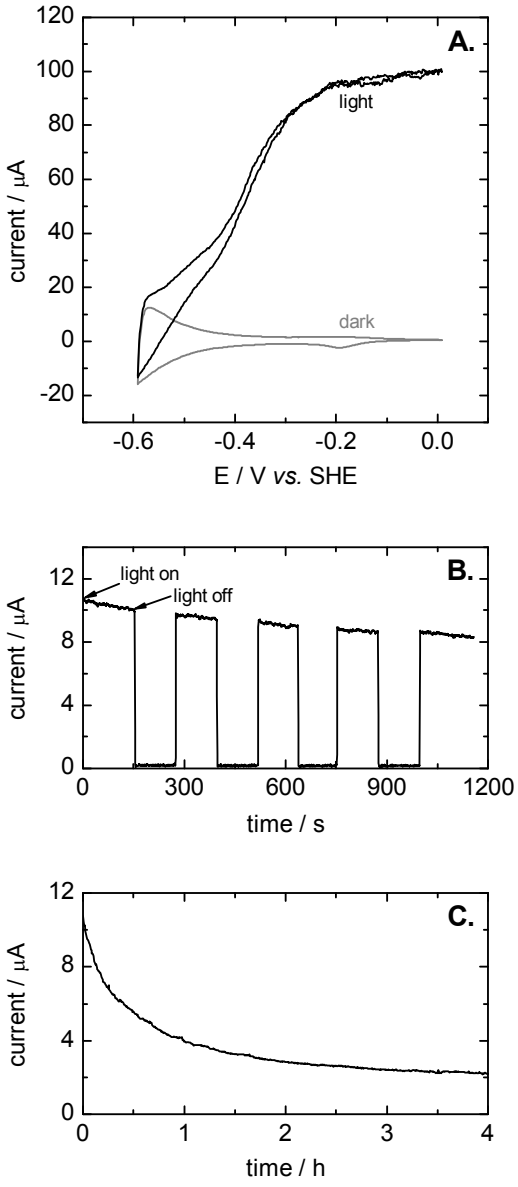


**Figure 51 Photocurrents at P25 $TiO_2$ thin film electrodes modified with RuP ([RuP-$TiO_2$]).** (A) Cyclic voltammograms recorded with [$TiO_2$-RuP] electrodes in the dark (grey) and under visible light irradiation (black, $\lambda > 420$ nm). (B) Photocurrents are toggled on/off by switching the light source on/off repeatedly, with the electrode held at -0.52 V *vs.* SHE. (C) Continuous photocurrent at a [$TiO_2$-RuP] electrode under constant irradiation by the same light source. In all experiments, the cell solution was 0.20 mM MES (pH 6.0), maintained at 20 ºC.

Panel A shows cyclic voltammograms recorded with this electrode under dark conditions, and when the electrode was irradiated with visible light ($\lambda > 420$ nm). As the electrode is swept to more oxidising potentials, the photocurrent increases until it reaches a plateau at around -0.2 V. The photocurrent is registered as a positive current: electrons are injected from the photoexcited state of RuP (see section 4.1.2) into the $TiO_2$ conduction band, thus giving rise to an oxidative current. Following electron injection, the RuP ground state is regenerated by electron donation from MES, acting as sacrificial electron donor.

Panel B shows the toggling on and off of the photocurrent when the light source is switched on and off (the photocurrent response is immediate). In control experiments, using $TiO_2$ electrodes that had not been modified with dye, almost no photocurrent was detected. Panel C shows the continuous photocurrent at a fresh [RuP-$TiO_2$] electrode that is under constant irradiation (note the longer time period of this experiment compared to panel A). The photocurrent is clearly unstable, with a decrease in photocurrent over 4 h of 88 ± 3%, averaged over several repeats using different electrodes.

### 4.2.6 VISIBLE LIGHT-DRIVEN $CO_2$ REDUCTION AT FUNCTIONALISED $TiO_2$ NANOPARTICLES

Both of the active components of the proposed $CO_2$ photoreduction system (RuP and $CODH_{I/II}$) have been shown to successfully attach to P25 $TiO_2$ nanoparticles, and their activities at thin film electrodes have been demonstrated. The aim is now to assemble a functional [RuP-$TiO_2$-CODH] system that is able to reduce $CO_2$ to CO when exposed to visible light.

#### 4.2.6.1 [RuP-$TiO_2$-$CODH_I$] SYSTEM PREPARATION, TERMINOLOGY, AND PHOTOCHEMICAL EXPERIMENTS

Based on the results of initial experiments, a standard protocol (to be called the *standard procedure*) was established for the preparation of [RuP-$TiO_2$-$CODH_I$] $CO_2$ photoreduction systems. Except where otherwise stated, each system was prepared according to this procedure, and the resulting assembly shall be referred to as the *standard system*. The methods for adsorption of $CODH_I$ and RuP to nanoparticles matches those described previously in sections 4.2.1 and 4.2.4. The protocol, in entirety, was as follows. In an anaerobic glovebox, 5 mg of nanoparticles was suspended in 5 mL of 0.20 M MES buffer solution (pH 6.0) by sonication in a pyrex pressure vessel (total volume 9 mL) at room temperature for 20 min. Then, 2.56 nmol of CODH (either $CODH_I$ or $CODH_{II}$, as a solution of concentration 0.12 – 0.18 mM) was added to the nanoparticles to give a final concentration of 11 μM CODH, and the suspension was stirred for 20 min to allow adsorption. Next, attachment of RuP was carried out by adding 100 μL of 0.56 mM RuP (56 nmol) in 0.20 M MES (pH 6.0) to the suspension (to give a final concentration of 11 μM RuP), and stirring for 20 min. The pressure vessel was tightly sealed with a rubber septum and removed from the glovebox, before the headspace was flushed with 2% $CH_4$ in $CO_2$ for 20 min while gently stirring. The vessel was then clamped in a water bath connected to a thermostated water circulator with the temperature maintained at 20 ºC, and exposed to visible light ($\lambda > 420$ nm) provided by a Kodak Carousel S-AV 1010 projector fitted with a 250 W (24 V) tungsten-halogen bulb and a 420 nm long-pass filter. At the position of the reaction vessel, the light intensity was 45 mW $cm^{-2}$. These experimental conditions are referred to throughout this Thesis as *standard conditions.*

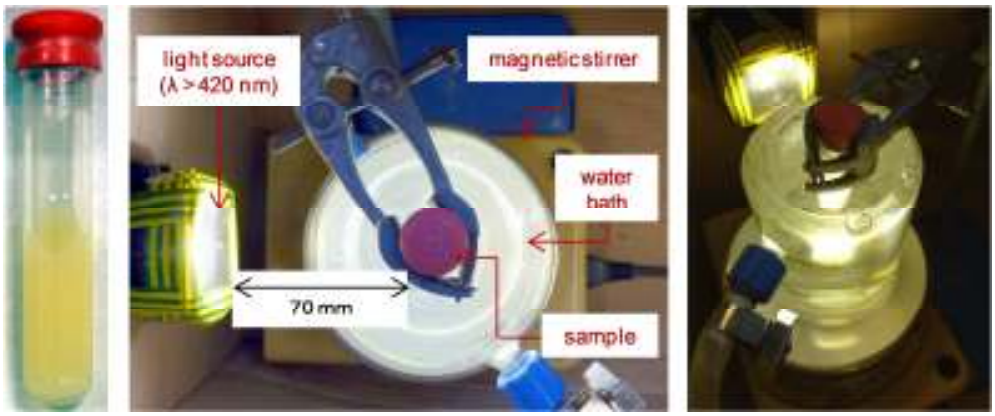


**Figure 52 Photographs of a typical particulate [RuP-$TiO_2$-CODH] system (the reaction vessel contains 5 mL of a 1 mg $mL^{-1}$ suspension), and the experimental setup used to carry out $CO_2$ photoreduction experiments.** The experimental setup was housed inside a box in order to exclude ambient light. Throughout experiments, the suspension was gently stirred, and thermostated water pumped through the water bath to control the temperature of the sample. Except where otherwise stated, the reaction vessel was positioned at a distance of 70 mm from the light source, resulting in a light intensity of 45 mW $cm^{-2}$.

#### 4.2.6.2 INITIAL DEMONSTRATION OF $CO_2$ PHOTOREDUCTION AT FUNCTIONALISED $TiO_2$ NANOPARTICLES

Figure 53 shows CO production by [RuP-$TiO_2$-$CODH_I$] and [RuP-$TiO_2$-$CODH_{II}$] systems, prepared as described in section 4.2.6.1, over the course of 4 h under visible light at 20 ºC. The gas headspace was periodically monitored by gas chromatography, with the amount of CO quantified by reference to the internal $CH_4$ as described in section 2.3.1 and used previously for the UV-driven system in section 4.2.3.

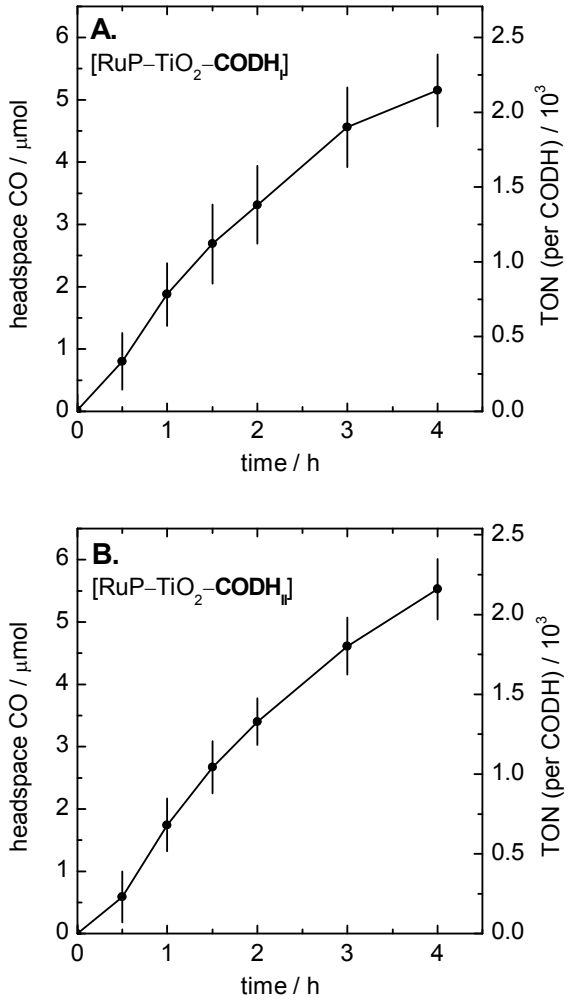


**Figure 53 CO production by [RuP-$TiO_2$-$CODH_I$] (A) and [RuP-$TiO_2$-$CODH_{II}$] (B).** Plots indicate the amounts of CO in the reaction vessel headspace against time, for systems prepared according to the *standard procedure* and run under *standard conditions*. The amounts of system components used in preparation were: 5 mg P25 $TiO_2$, 2.56 nmol $CODH_I$ or $CODH_{II}$, 56 nmol RuP, 5 mL 0.20 M MES (pH 6.0); and the reaction vessels were maintained at 20 ºC while irradiated with visible light ($\lambda > 420$ nm, 45 mW $cm^{-2}$). The amounts of CO are determined from the CO peak area:$CH_4$ gas chromatogram peak area ratios, with reference to calibration plots.

Light-driven CO production is successful with both systems, and this is catalytic: TONs after 4 h, calculated per attached CODH molecule, are 2145 ± 242 ([RuP-$TiO_2$-$CODH_I$]) and 2160

± 191 ([RuP-$TiO_2$-$CODH_{II}$]). The average turnover *frequency* over this time, also calculated based on the amount of CODH, is 0.15 $s^{-1}$ for both systems. A detailed discussion and evaluation of these, and other, performance metrics is given in section 4.3. The rate of CO production over the time period of these experiments is observed to be unstable, and this is the subject of later investigation in this Thesis.

Control experiments, in which either RuP, CODH, $TiO_2$ or $CO_2$ was excluded from the system yielded either no detectable CO at all after 4 h, or only tiny, trace amounts. The exclusion of light led to no CO production, and an experiment in which after 1 h the irradiation was halted for a period of 3 h resulted in CO production ceasing for this time, before continuing upon the recommencement of irradiation (Figure 54). These important control experiments support the operation of the mechanism proposed in section 4.1.1.

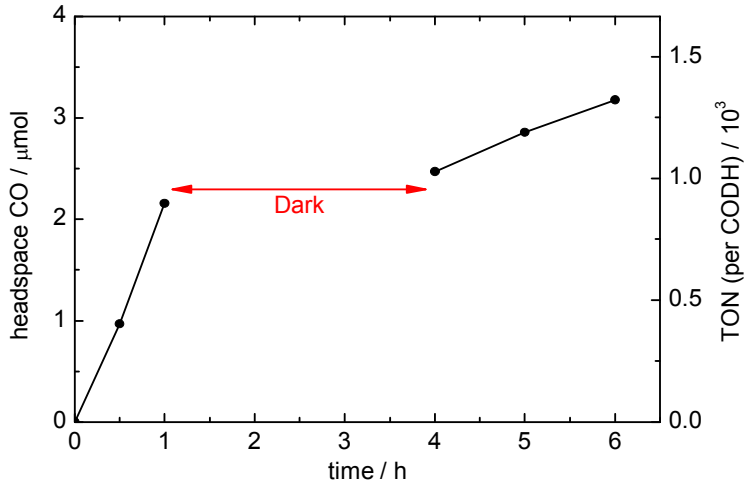


**Figure 54 CO production by [RuP-$TiO_2$-$CODH_I$] in which after 1 h, irradiation was halted for 3 h and then restarted.** The system was prepared according to the *standard procedure*, and the amounts of system components used in preparation were: 5 mg P25 $TiO_2$, 2.56 nmol $CODH_I$, 56 nmol RuP, 5 mL 0.20 M MES (pH 6.0). The reaction vessel was maintained at 20 ºC both during periods of visible light irradiation ($\lambda > 420$ nm, 45 mW $cm^{-2}$), and during the period of light exclusion.

The order of functionalisation of $TiO_2$ (*i.e.* whether the nanoparticles were modified with CODH followed by RuP, or RuP followed by CODH) was investigated, but not found to have any significant effect on the activity of the system (Appendix A4).

#### 4.2.6.3 TEMPERATURE AND pH DEPENDENCE

Figure 55 shows the effects of temperature and pH on $CO_2$ photoreduction at [RuP-$TiO_2$-$CODH_I$]. Systems were prepared exactly as described in section 4.2.6.1, except for alteration of the temperature regulation during photoreduction experiments (panel A), or of the pH of the 0.20 M MES solution in which the functionalised nanoparticles were dispersed (panel B). As expected, higher temperature leads to faster rates of CO production, even up to 50 ºC (as described in Chapter 1, *Carboxydothermus hydrogenoformans* is a thermophilic organism with a growth optimum of 70 – 72 ºC).[189] The effect of pH is small, although the range of pH that could be investigated was restricted due to the narrow range of pH (5.5 – 6.5) within which MES is able to buffer the high concentration of $CO_2$.

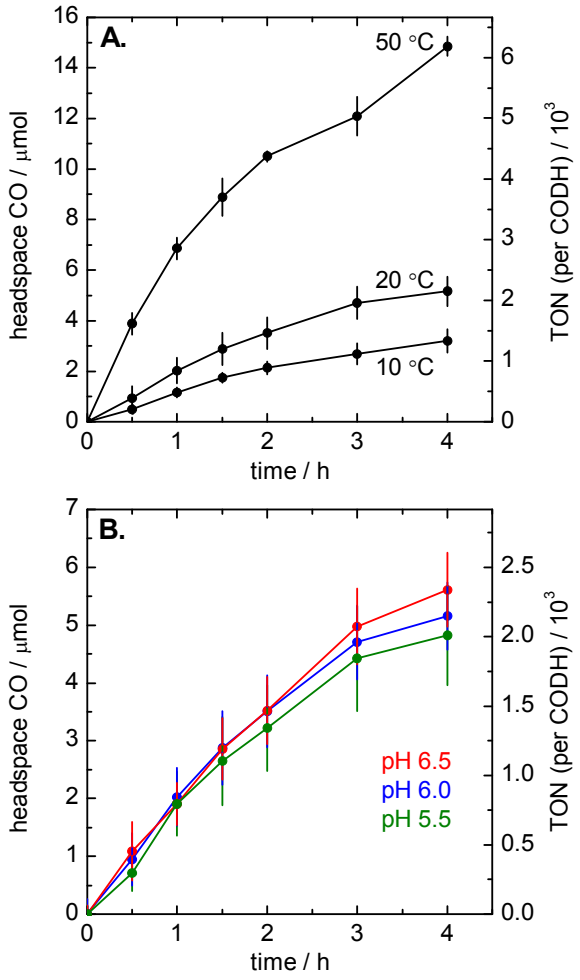


**Figure 55 Temperature (A) and pH (B) dependences of $CO_2$ photoreduction at [RuP-$TiO_2$-$CODH_I$].** The amounts of system components were: 5 mg P25 $TiO_2$, 2.56 nmol $CODH_I$, 56 nmol RuP, 5 mL 0.20 M MES. Systems were prepared according to the *standard procedure*, except for in the pH of the MES buffer solutions used in (B). Experiments were run under *standard conditions*, except for the variation of temperature in (A). In the temperature dependence experiments the pH was 6.0, and in the pH dependence experiments the temperature was 20 ºC. All systems were irradiated with visible light ($\lambda > 420$ nm, 45 mW $cm^{-2}$).

## 4.2.7 DURABILITY

### 4.2.7.1 TOLERANCE TO AIR AND $O_2$

As described in section 1.7, Ni-CODHs, which are responsible for $CO/CO_2$ interconversion in anaerobic organisms, are completely inactivated by exposure to $O_2$.[185,187,188] Figure 56 shows experiments in which [RuP-$TiO_2$-$CODH_I$] systems are subjected to brief exposure to air or $O_2$. Functionalised nanoparticles were prepared according to the *standard procedure*, and irradiated with visible light for 1.5 h under *standard conditions* with GC analysis of the headspace at 0, 0.5, 1 and 1.5 h (black plot). After this, irradiation was stopped, and the reaction vessel was flushed for 20 min with either $N_2$ (a), air (b) or $O_2$ (c) while the suspension was gently stirred. Then, the system was re-flushed with 2% $CH_4$ in $CO_2$ for 20 min while gently stirring, and irradiation continued for 2 h. The green, red and blue plots show the production of CO for the systems following exposure to $N_2$, air or $O_2$, respectively.

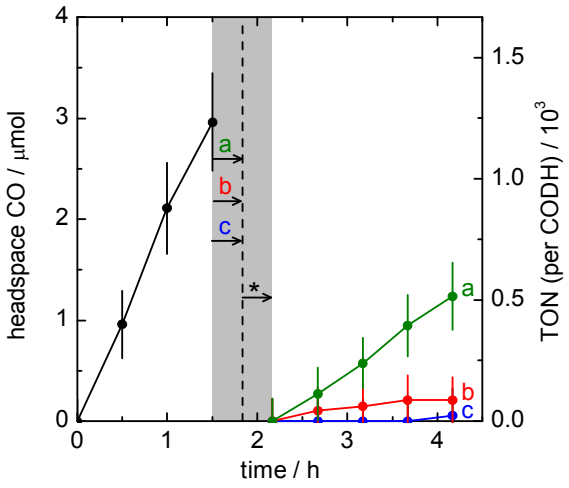


**Figure 56 Effect of exposure to air or $O_2$ on the CO production activity of [RuP-$TiO_2$-$CODH_I$].** The black plot shows the production of CO by the system prepared according to the *standard procedure* and run according to *standard conditions*. After 1.5 h, the reaction vessel was flushed with either $N_2$ (control, a) air (b) or $O_2$ (c) for 20 min while gently stirring, before being re-flushed with 2% $CH_4$ in $CO_2$ for 20 min (marked *). Irradiation was then restarted, with the vessel headspace monitored by GC analysis every 30 min. The amounts of system components were: 5 mg P25 $TiO_2$, 2.56 nmol $CODH_I$, 56 nmol RuP, 5 mL 0.20 M MES (pH 6.0); and the reaction vessels were maintained at 20 ºC under visible light irradiation ($\lambda > 420$ nm, 45 mW $cm^{-2}$) except for the period shown in grey, during which light was excluded.

#### 4.2.7.2 STORAGE OF FUNCTIONALISED NANOPARTICLES FOR 'ON-DEMAND' USE

An attractive proposition is a catalyst taking the form of a powder, which can be stored and re-dispersed in water as and when required for 'on-demand' catalysis. To this end, the possibility of centrifuging the functionalised $TiO_2$ nanoparticles, removing the supernatant and re-suspending in fresh buffer solution was explored. Figure 57 shows the effect of centrifugation and buffer exchange. Plot (a) shows the performance of [RuP-$TiO_2$-$CODH_I$] prepared according to the *standard procedure* and run according to *standard conditions* for 3 h; and plot (b) is the result of an experiment in which an identical system was assembled before transferring the suspension into a gas-tight tube and centrifuging to pellet the nanoparticles. The supernatant was then removed, replaced with fresh buffer solution, and the

nanoparticles re-suspended by gentle shaking. The suspension was then transferred back into a pressure vessel, sealed tightly, and flushed with 2% $CH_4$ in $CO_2$ before being exposed to visible light ($\lambda > 420$ nm). With the exception of centrifugation and gas flushing, all steps were performed in an anaerobic glove box.

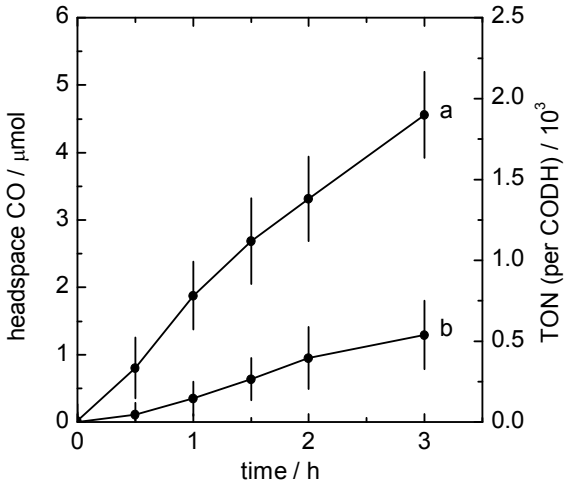


**Figure 57 Effect of centrifugation and buffer exchange on the activity of [RuP-$TiO_2$-$CODH_I$].** Plot (a) shows CO production by the system prepared according to the *standard procedure* and run according to *standard conditions.* Plot (b) shows CO production by an identically prepared system, which had been treated as follows: after preparation (and while still in an anaerobic glove box), the suspension was transferred into gas-tight tubes and centrifuged to pellet the nanoparticles. The supernatant was then removed, replaced with fresh buffer solution, and the nanoparticles re-suspended by gently shaking. The suspension was then transferred to a reaction vessel, sealed tightly and flushed with 2% $CH_4$ in $CO_2$ before being irradiated with visible light ($\lambda > 420$ nm, 45 mW $cm^{-2}$). The amounts of system components were: 5 mg P25 $TiO_2$, 2.56 nmol $CODH_I$, 56 nmol RuP, 5 mL 0.20 M MES (pH 6.0); and the reaction vessels were maintained at 20 ºC.

Activity is notably suppressed by the action of centrifugation and buffer exchange. An obvious explanation for this would be weak attachment of enzyme molecules and/or RuP to the nanoparticles, but the spectrophotometry experiments in sections 4.2.1 and 4.2.4 indicate that this is not the case. It is possible that leakage of small amounts of air into the centrifuge tubes partially deactivates the enzyme. Many attempts at pelletting and resuspending the

nanoparticles consistently resulted in inactive systems, and for this reason $CO_2$ photoreduction experiments were run immediately following assembly. While the particles clearly cannot be re-suspended for storage, later experiments (section 5.3) will investigate the possibility of storing systems in suspension form.

## 4.3 CONCLUSIONS AND PERSPECTIVES

This chapter described the design of an enzyme-based catalytic system for photoreduction of $CO_2$ to a single product (CO), and initial demonstration of its successful operation under irradiation by an artificial visible light source. The design involved three core components, the presence of each of which was essential for the activity of the system: a ruthenium photosensitiser dye (RuP), a $TiO_2$ nanoparticle, and a CODH enzyme for $CO_2$ reduction. Turnover frequencies can therefore be calculated based on the amount of any one of these constituent parts. Table 12 shows this data, based on the total amounts of CODH and RuP adsorbed by the nanoparticles and the amounts of CO produced, for the [RuP-$TiO_2$-$CODH_I$] and [RuP-$TiO_2$-$CODH_{II}$] *standard systems* shown in Figure 53. This table also provides the 'initial' (defined as 0 – 1 h), and final (3 – 4 h) rates, quantifying the decrease in rate over time that was mentioned in section 4.2.6.2.

**Table 12** Turnover frequencies for [RuP-$TiO_2$-$CODH_I$] and [RuP-$TiO_2$-$CODH_{II}$] *standard systems* prepared according to the *standard procedure* and run under *standard conditions*, as defined in section 4.2.6.1.

| | TOF[a] [(mol CO) (mol $CODH_I$)$^{-1}$ $s^{-1}$] | TOF[b] [(mol CO) (mol RuP)$^{-1}$ $s^{-1}$] | TOF [(µmol CO) (g $TiO_2$)$^{-1}$ $h^{-1}$] |
|---|---|---|---|
| **[RuP-$TiO_2$-$CODH_I$]** | | | |
| initial rate (0 – 1 h) | 0.22 ± 0.06 | 0.0110 ± 0.0029 | 375 ± 100 |
| final rate (3 – 4 h) | 0.07 ± 0.02 | 0.0033 ± 0.0010 | 113 ± 36 |
| average rate (0 – 4 h) | 0.15 ± 0.02 | 0.0075 ± 0.0008 | 258 ± 29 |
| **[RuP-$TiO_2$-$CODH_{II}$]** | | | |
| initial rate (0 – 1 h) | 0.19 ± 0.05 | 0.0102 ± 0.0025 | 349 ± 85 |
| final rate (3 – 4 h) | 0.10 ± 0.03 | 0.0053 ± 0.0016 | 182 ± 56 |
| average rate (0 – 4 h) | 0.15 ± 0.01 | 0.0081 ± 0.0007 | 276 ± 24 |

[a] Calculated from the total amount of CO in the reaction vessel headspace and the amount of CODH determined to have been taken up by nanoparticles (section 4.2.1, *i.e.* 2.40 nmol $CODH_I$, 2.56 nmol $CODH_{II}$). [b] Calculated from the total amount of CO in the reaction vessel headspace and the amount of RuP determined to have been taken up by nanoparticles after prior functionalisation with CODH (section 4.2.4, *i.e.* 47.5 nmol). It was assumed that the amount of RuP bound to $TiO_2$-$CODH_{II}$ is the same as the amount bound to $TiO_2$-$CODH_I$).

From experiments shown in Figure 53, turnover *numbers* achieved in 4 h based on CODH or RuP loadings (*i.e.* the total number of moles of CO produced per mole of enzyme or per mole of RuP) were calculated. It should be noted that these are not *maximum* TONs, since both the $CODH_I$ and the $CODH_{II}$ systems were still active after 4 h. The 4 h TON values of 2145 ± 242 (per $CODH_I$) and 108 ± 12 (per RuP) (for [RuP-$TiO_2$-$CODH_I$]), and 2160 ± 191 (per $CODH_{II}$) and 116 ± 10 (per RuP) (for [RuP-$TiO_2$-$CODH_{II}$]) indicate that the systems are truly catalytic. The mechanism proposed in section 4.1.1 – or at least, at this stage, the aspects of CODH turnover and photosensitiser regeneration – can therefore be confirmed.

It should be noted that the rates in Table 12 should be considered as *lower limits*, since the calculations assume that all of the photosensitiser and enzyme molecules are attached to the nanoparticles in *electroactive* configurations. On a *per CODH* basis (column 1), the rates seem very low in view of previously reported turnover frequencies of Ni-CODHs (thousands per second). The following chapter addresses the challenge of optimising the system in terms

of its absolute rate, and also of improving the stability: it is clear that rates decrease over time (the 3 – 4 h rates are 50 – 70% slower than the 0 – 1 h rates, Table 12). In more positive light, calculation of rates in terms of mass of $TiO_2$ (column 3) yields values of 375 μmol CO produced (g $TiO_2$)$^{-1}$ $h^{-1}$ initially, and 113 μmol CO produced (g $TiO_2$)$^{-1}$ $h^{-1}$ after 3 h for [RuP-$TiO_2$-$CODH_I$], and 349 μmol CO produced (g $TiO_2$)$^{-1}$ $h^{-1}$ falling to 276 μmol CO produced (g $TiO_2$)$^{-1}$ $h^{-1}$ for [RuP-$TiO_2$-$CODH_{II}$]. These are usually the rate units of choice for $TiO_2$ powder-based photocatalytic systems, and by this measure the initially presented [RuP-$TiO_2$-$CODH_I$] system compares very favourably with other $TiO_2$ powder-based $CO_2$ photoreduction systems in which typical rates of conversion are less than 30 μmol (g $TiO_2$)$^{-1}$ $h^{-1}$.[129] Further discussion in this respect follows at the end of the next chapter.

The initial design of the system (section 4.1.1) depicted the nanoparticles as operating in a greater capacity than simply as a scaffold for RuP and CODH (the term 'scaffold' referring to a scenario in which the semiconductor surface simply holds pairs of RuP and $CODH_I$ in sufficiently close proximity of one another for direct electron transfer). Rather, the intention, as shown schematically in Figure 39, is for electrons to be transferred from the dye complex into the conduction band of $TiO_2$, and from here into the enzyme. This has the potential to be developed into a much more effective system, since electrons can be 'pooled' into the semiconductor unit before being fed into CODHs; in the former system, any dye molecules that were adsorbed in positions too far away from a co-adsorbed CODH would be wasted (and vice versa). A parallel can be drawn here with the $H_2$-producing device in chapter 3 that catalysed the water-gas shift reaction: using a central particle provides the opportunity for activities of electron-donating and electron-accepting species to be finely balanced, and this

immediately gives rise to an advantage over constructs assembled by Golbeck and co-workers,[358-360] for solar fuel ($H_2$) production. Here, a hydrogenase is covalently wired to photosystem I. While elegant, the 1:1 configuration in such a system is restrictive. In the next chapter, the effects of varying the RuP:CODH ratio are investigated.

What is the evidence for operation of a $TiO_2$-mediated pathway over direct electron transfer from RuP to CODH? Firstly, control systems in which RuP and $CODH_I$ were in solution in the absence of $TiO_2$ nanoparticles failed to show any CO production after 4 h, although this only proves the requirement for $TiO_2$ *in some capacity*. Firmer evidence is provided by the experiment in Figure 49. Here, RuP was excluded, but electrons were provided by near-UV light inducing direct semiconductor band gap excitation. Electrons are promoted from valence band to conduction band, and the successful production of CO in this system therefore indicates that the mechanism of electron injection from $TiO_2$ conduction band into the enzyme must be possible. Evidence opposing the direct transfer of electrons from RuP to CODH (without passing through $TiO_2$) stems from experiments using pure *rutile* nanoparticles. In these experiments, not even trace amounts of CO were detected. The conduction band potential of rutile is around 0.2 V more positive than that of anatase[333] and it is therefore not sufficiently reducing to be able to inject electrons into CODH, but the *complete* lack of activity strongly indicates that a mechanism involving direct electron transfer to CODH from a nearby co-attached photosensitiser does not operate to any significant extent.

Finally, a key aim for any photocatalytic fuel-producing system is, naturally, to be able to operate with the sun as the light source. With this in mind, Figure 58 shows CO production

by the [RuP-$TiO_2$-$CODH_I$] system driven by sunlight in Oxford, UK, on an October day. The amount of CO produced after 3 h, 2.21 µmol, is respectable compared to the productivity recorded under controlled laboratory conditions with a steady, artificial light source.

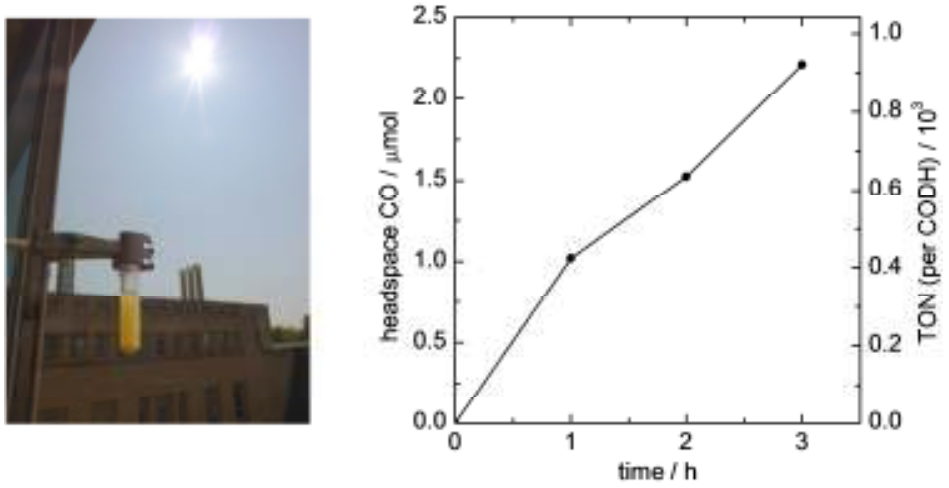


**Figure 58 CO production by [RuP-$TiO_2$-$CODH_I$] in real sunlight (Oxford, UK in October).** The system was prepared according to the *standard procedure* (the amounts of system components were: 5 mg P25 $TiO_2$, 2.56 nmol $CODH_I$, 56 nmol RuP, 5 mL 0.20 M MES (pH 6.0)). The air temperature varied from 17 – 22 ºC during the course of the experiment.

# 5 $CO_2$ PHOTOREDUCTION AT FUNCTIONALISED $TiO_2$ NANOPARTICLES (2)

## ABSTRACT

This chapter follows on directly from the initial proof-of-concept $CO_2$ photoreduction system presented in chapter 4, in which $TiO_2$ nanoparticles modified with an efficient $CO_2$-reducing enzyme (carbon monoxide dehydrogenase) and a ruthenium photosensitiser were able to reduce $CO_2$ to CO under the action of visible light. The turnover rates achieved by this system compared very favourably with those reported for other $TiO_2$ particle-based systems, but were much lower than rates of inherent CODH turnover that have previously been reported.[185] A detailed characterisation is therefore now carried out in order to understand which factor (or factors) affect the $CO_2$ photoreduction rate. The design of the system – with the same nanoparticle carrying both the catalytic and light harvesting moieties – allows control over their relative concentrations, and the study here of systems of varying configuration is revealing in terms of rate limitation. The effects of light intensity and attenuation, and the variation of electron donor (both species and concentration) are probed. A rational attempt at controlling the orientation of enzyme binding at the $TiO_2$ surface is also outlined.

It was also apparent in the initial demonstration of the photocatalyst (chapter 4) that the system is moderately unstable (the rate of CO production is roughly halved after 3 h). The second part of this chapter addresses this issue, which is crucial to the relevance of the system as a model for a robust, scalable solar fuel solution. Factors such as the effect of diminishing thermodynamic driving force, product inhibition, trace $O_2$ damage, and photodamage to individual device components are investigated.

Some of the work in this chapter has been published:

Thomas W. Woolerton, Sally Sheard, Erwin Reisner, Elizabeth Pierce, Stephen W. Ragsdale and Fraser A. Armstrong, *J. Am. Chem. Soc.*, **2010**, *132*, 2132-2133.

Thomas W. Woolerton, Sally Sheard, Elizabeth Pierce, Stephen W. Ragsdale and Fraser A. Armstrong, *Energy Environ. Sci.*, **2011**, *4*, 2393-2399.

## 5.1 INTRODUCTION: OBJECTIVES OF THIS CHAPTER

By using solution assays with electron acceptors, very fast turnover frequencies for both $CODH_I$ (39,000 $s^{-1}$) and $CODH_{II}$ (31,000 $s^{-1}$) have been reported[185] – several orders of magnitude beyond the rates achieved in the previous chapter by [RuP-$TiO_2$-CODH] photoreduction systems (0.15 – 0.22 mol CO (mol $CODH_I)^{-1}$ $s^{-1}$). It should be noted, however, that these incredibly high values were measured for catalysis in the direction of CO oxidation (the predominant direction of *in vivo* catalysis),[185] and at high temperature (70 ºC). Therefore, although both of these enzymes are reversible electrocatalysts that are also capable of fast rates of $CO_2$ reduction,[196] these turnover frequencies are not accurate indications of the $CO_2$ reduction rates to be expected under the conditions of the photoreduction experiments presented thus far (20 ºC, pH 6). For this reason it is instructive to establish a more representative turnover rate for CODH-catalysed $CO_2$ reduction under these mild conditions. Furthermore, section 4.1.2 highlighted the fact that the potential difference between anatase conduction band electrons and the $CO_2$/CO reduction potential is small (around 60 mV), and therefore a large overpotential to facilitate fast rates is unavailable. Therefore, in order to maximise the relevance to the photocatalyst, an assay to determine a realistically achievable TOF should not only be at the appropriate conditions; it should also only use a mildly reducing thermodynamic driving force. Once this rate is established, the discrepancy with the rates of CODH-catalysed CO production by [RuP-$TiO_2$-CODH] can be addressed.

Previously reported semiconductor-based $CO_2$ photoreduction systems often display a decrease in catalytic activity over time,[131,133,137,167,361-365] and in many of these cases no explanation, or only speculative suggestions, are provided. From the plots of headspace CO

*vs.* time in the previous chapter it is clear that the [RuP-$TiO_2$-CODH] system also suffers from noticeable instability over the course of several hours, and the second part of this chapter investigates factors that contribute to this behaviour.

## 5.2 INVESTIGATING THE PHOTOCATALYTIC TURNOVER RATE

### 5.2.1 ASSAY FOR THE INHERENT TURNOVER FREQUENCY OF CODH-CATALYSED $CO_2$ REDUCTION

Figure 59 shows an assay for $CODH_I$-catalysed $CO_2$ reduction with reduced methyl viologen ($MV^{+\bullet}$) as the electron donor, using the method described in section 2.2. An average TOF of $102 \pm 35\ s^{-1}$ was calculated. This value can be considered to be an approximate indication of the rate of $CO_2$ reduction attainable using mildly reducing anatase conduction band electrons, because the $MV^{2+}/MV^{+\bullet}$ reduction potential (-0.44 V)[366] is not vastly different to the anatase conduction band potential at pH 6 (-0.52 V).[332]

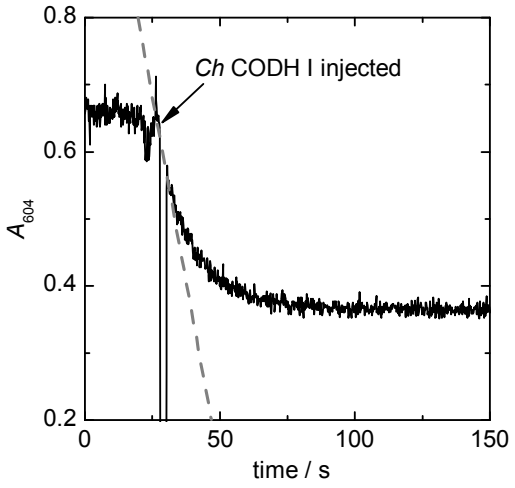


**Figure 59 A spectroscopic assay, using electrons provided from the reduced form of methyl viologen, to determine the rate of $CODH_I$-catalysed $CO_2$ reduction in 0.20 M MES at 20 ºC, pH 6.0.** The enzyme TOF is calculated from the initial rate of oxidation of reduced methyl viologen (*i.e.* $MV^{+\bullet} \rightarrow MV^{2+} + e^-$), which is followed spectroscopically by following the decrease in concentration of $MV^{+\bullet}$, for which $\lambda_{max}$ = 604 nm. The detailed experimental method is described in section 2.2.

### 5.2.2 VARIATION IN LIGHT INTENSITY, AND LIGHT ATTENUATION EFFECTS

The focus in this chapter lies on chemical aspects of the photoreduction system, but it is appropriate also to consider the broader 'engineering' aspects of any solar fuel system, and in particular those that impact the harvesting of light. Figure 60A shows the effect on activity of increasing the intensity of the light source. These experiments were carried out using the [RuP-$TiO_2$-$CODH_{II}$] photocatalyst, and show that a decrease in light intensity from 45 mW $cm^{-2}$ (that used according to *standard conditions*) to 19 mW $cm^{-2}$ leads to a loss in overall activity of around 20% (total CO production after 4 h falls from 5.53 μmol to 4.41 μmol), but that an increase in intensity to 63 mW $cm^{-2}$ does not impact the rate. That the overall activity is affected by light intensity only up to a certain point is expected: at low photon flux, the rate of photoexcitation of RuP is rate limiting, but once a certain light intensity is reached, another factor (of which there are several possibilities, *vide infra*) becomes the limitation.

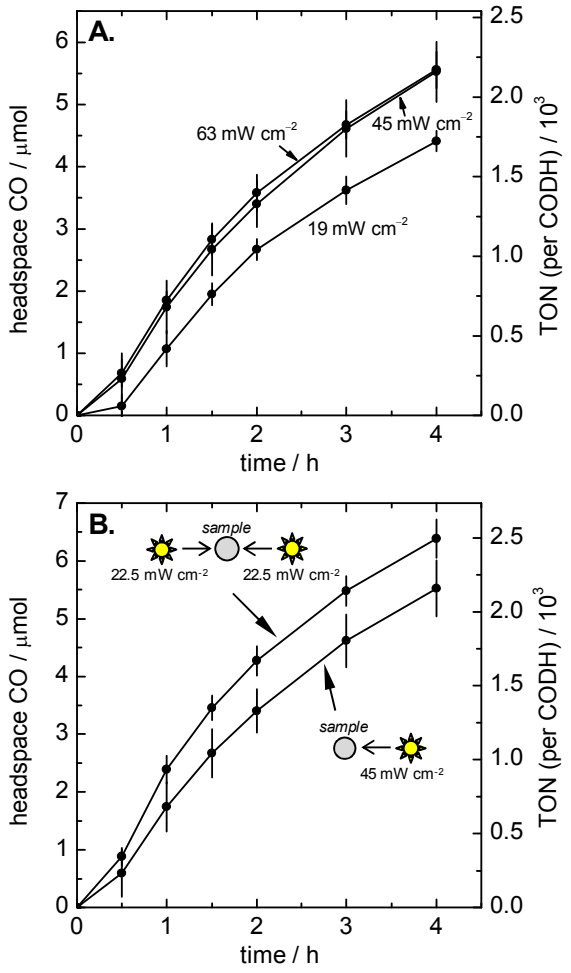


**Figure 60 $CO_2$ photoreduction at [RuP-$TiO_2$-$CODH_{II}$] under different irradiation setups.** Experiments investigating the effects of light intensity (A), and of splitting the irradiation between two diametrically opposed sources, each providing half of the intensity (22.5 mW $cm^{-2}$) of a single light source (45 mW $cm^{-2}$). (B). All systems were prepared according to the *standard procedure* and run under *standard conditions* except for in the nature of irradiation. The amounts of system components were: 5 mg P25 $TiO_2$, 2.56 nmol $CODH_I$, 56 nmol RuP, 5 mL 0.20 M MES buffer (pH 6.0) and the reaction vessels (initially under a gas atmosphere of 2% $CH_4$ in $CO_2$) were maintained at 20 ºC while under visible light ($\lambda > 420$ nm).

Figure 60B shows the advantage that is gained from using the same total light intensity but with the irradiation split such that the sample is irradiated from two (diametrically opposed) angles. The difference in the CO production plots is attributable to the effect of light

scattering (attenuation) by $TiO_2$ nanoparticles, which prevents the same intensity of light from reaching all of the photocatalytic units. To investigate this attenuation effect further, Figure 61A shows the effect on activity of doubling (plot b) or halving (c) the number of [RuP-$TiO_2$-$CODH_{II}$] units in the system compared to the number of units present in the *standard system* (a).

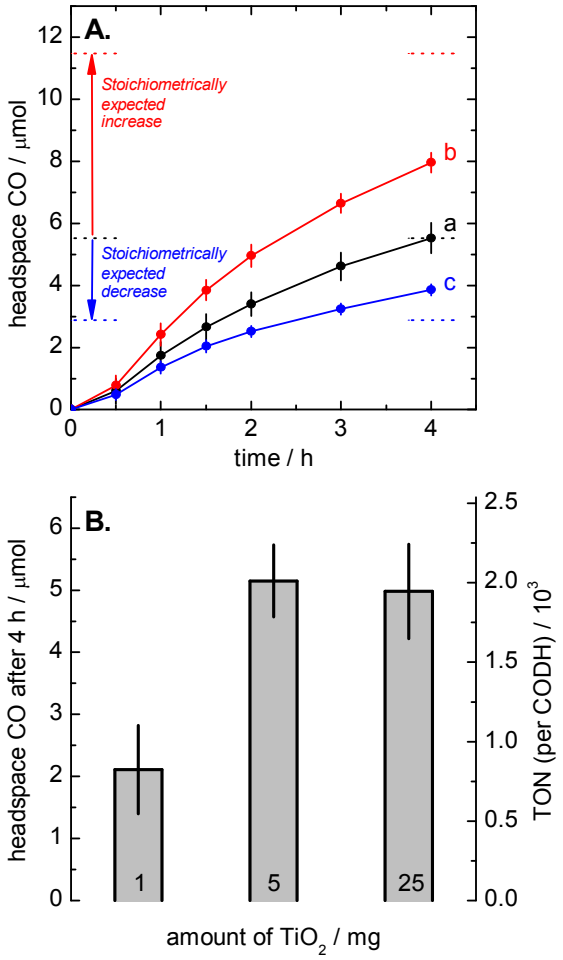


**Figure 61** (A) $CO_2$ photoreduction by systems in which the total number of [RuP-$TiO_2$-$CODH_{II}$] units were either doubled (b) or halved (c) compared to the amounts used in preparation of the *standard system* (a). (Amounts used in the *standard system* are: 5 mg P25 $TiO_2$, 56 nmol RuP, 2.56 nmol $CODH_{II}$). (B) Amounts of headspace CO produced after 4 h irradiation of [RuP-$TiO_2$-$CODH_I$] systems in which the amounts of RuP (56 nmol) and $CODH_I$ (2.56 nmol) were kept constant, but the mass of $TiO_2$ was 1 mg, 5 mg (*standard system*) or 25 mg. For all experiments, the reaction vessels (initially under a gas atmosphere of 2% $CH_4$ in $CO_2$) were maintained at 20 ºC while irradiated with visible light ($\lambda$ > 420 nm, 45 mW $cm^{-2}$), and the suspension buffer was 5 mL 0.20 M MES (pH 6.0).

Although increasing the amount of [RuP-$TiO_2$-$CODH_{II}$] units leads to greater absolute CO production (Table 13, column (i.)), it is also clear that the overall activity is not directly proportional to the number of units – doubling the number of photocatalytic units only leads

to an increase in CO production over 4 h from 5.53 μmol to 7.96 μmol, and halving only decreases activity from 5.53 μmol to 3.86 μmol. Previously, it has been found that for solid suspension systems the light attenuation coefficient, *A'*, is proportional to the square root of the particle concentration, *c*:[367,368] $A' \propto c^{1/2}$. Therefore, doubling the concentration of catalytic units can be expected to increase activity by a factor of $2^{1/2}$, and halving the concentration to decrease activity by a factor of $2^{1/2}$. The results here (Figure 61A and column i. of Table 13) are consistent with this predicted behaviour (7.96 μmol ≈ $2^{1/2}$ x 5.53 μmol; 3.86 μmol ≈ 5.53 μmol / $2^{1/2}$).

**Table 13** Total CO production and turnover frequencies for [RuP-$TiO_2$-$CODH_{II}$] systems prepared according to the *standard procedure*, except for in the amounts of $TiO_2$, $CODH_{II}$ and RuP used in assembly. The systems were run under *standard conditions* (20 ºC, pH 6.0, irradiated with visible light (λ > 420 nm, 45 mW $cm^{-2}$).

| | *(i.)* CO produced after 4 h / μmol | *(ii.)* TOF[a, b] [(mol CO) (mol $CODH_{II}$)$^{-1}$ $s^{-1}$] | *(iii.)* TOF[a, c] [(mol CO) (mol RuP)$^{-1}$ $s^{-1}$] | *(iv.)* TOF[a] [(μmol CO) (g $TiO_2$)$^{-1}$ $h^{-1}$] | *(v.)* TOF[a] [(μmol CO) $mL^{-1}$ $h^{-1}$] |
|---|---|---|---|---|---|
| **2 x** [$TiO_2$, $CODH_{II}$, RuP][d] (Fig. 61A, plot (b)) | 7.96 ± 0.32 | 0.11 ± 0.01 | 0.0058 ± 0.0002 | 199 ± 8 | 0.40 ± 0.02 |
| **1 x** [$TiO_2$, $CODH_{II}$, RuP][d] *(Standard system)* (Fig. 61A, plot (a)) | 5.53 ± 0.49 | 0.15 ± 0.01 | 0.0081 ± 0.0007 | 276 ± 24 | 0.28 ± 0.02 |
| **0.5 x** [$TiO_2$, $CODH_{II}$, RuP] [d] (Fig. 61A, plot (c)) | 3.86 ± 0.18 | 0.21 ± 0.01 | 0.0113 ± 0.0005 | 386 ± 18 | 0.19 ± 0.01 |

[a] Turnover frequencies are calculated from the total amount of CO in the reaction vessel headspace after 4 h, and therefore represent average rates over this time. [b] Based on the amount of $CODH_{II}$ determined to have been taken up by nanoparticles (section 4.2.1). [c] Based on the amount of RuP determined to have been taken up by nanoparticles after prior functionalisation with CODH, *i.e.* 47.5 nmol (section 4.2.4). [d] The notation '1 x [$TiO_2$, $CODH_{II}$, RuP]' refers to the amounts of these components used in assembly of the *standard system*, *i.e.* 5 mg $TiO_2$, 2.56 nmol $CODH_{II}$, 56 nmol RuP. '2 x' and '0.5 x' indicate twice or half of each of these amounts.

Due to the impact of light attenuation, less concentrated suspensions offer an advantage in terms of maximising turnover frequencies (either calculated per CODH, per RuP, or per gram of $TiO_2$) (columns (ii.) – (iv.)). An alternative perspective, however, and from the point of view of the technological application of such a suspension-type system where volume and weight are important considerations, higher concentration systems are favourable on a *per unit of total system volume* measure (column (v.)).

Figure 61B shows the total amount of headspace CO produced after 4 h by [RuP-$TiO_2$-$CODH_I$] systems in which the amounts of RuP (56 nmol) and $CODH_{II}$ (2.56 nmol) are constant across all experiments, but the mass of $TiO_2$ nanoparticles is altered between 1 mg, 5 mg (this system corresponding to the *standard system*) and 25 mg. Switching from 5 mg $TiO_2$ nanoparticles to 1 mg $TiO_2$ results in significantly lower activity. This can be explained using the UV-vis absorbance study in section 4.2.4: 213 nmol RuP was shown to correspond to complete coverage of 5 mg P25 $TiO_2$, and so coverage of 1 mg nanoparticles is achieved with 43 nmol RuP (213 nmol x (1 mg / 5)). The 56 nmol RuP used here is therefore excessive for 1 mg $TiO_2$ because it is capable of blocking all adsorption sites.[***]

There is little variation in activity between 5 and 25 mg. It is likely that there are several factors involved here; as well as the light attenuation effect already discussed, a greater

[***] Although the assembly method for the nanoparticles involves pre-modification with $CODH_{II}$ before RuP is added, in a scenario in which adsorption sites are limited the photosensitiser can be expected to displace the enzyme because of the high affinity of the phosphonate groups for titanium.[266, 328, 329]

number of nanoparticles means that it is more likely for enzyme molecules to be wasted by their attachment to particles carrying no photosensitiser (and vice versa), but a greater amount of $TiO_2$ may also provide advantages that counterbalance this effect.

## 5.2.3 LOADINGS OF ACTIVE COMPONENTS ON $TiO_2$: EFFECT ON CO PRODUCTION RATE

### 5.2.3.1 THE *STANDARD SYSTEM* REGIME

The *standard system* described earlier is prepared by functionalising 5 mg $TiO_2$ nanoparticles with 2.56 nmol CODH and 56 nmol RuP. This section considers the effect of independently varying the loadings of these components. Figure 62 shows the amounts of CO in the reaction vessel headspace after 4 h irradiation (black data points) for a range of [RuP-$TiO_2$-$CODH_I$] systems prepared with varying amounts of $CODH_I$ and the amount of RuP photosensitiser held constant (panel A), or with varying amounts of RuP and the amount of $CODH_I$ held constant (panel B). Also shown (red data points) are the corresponding amounts of photosensitiser or enzyme actually taken up by the nanoparticles, as determined by the UV-vis spectrophotometric method using the method described in section 2.3.2. The data points highlighted in yellow correspond to the activity of the *standard system*.

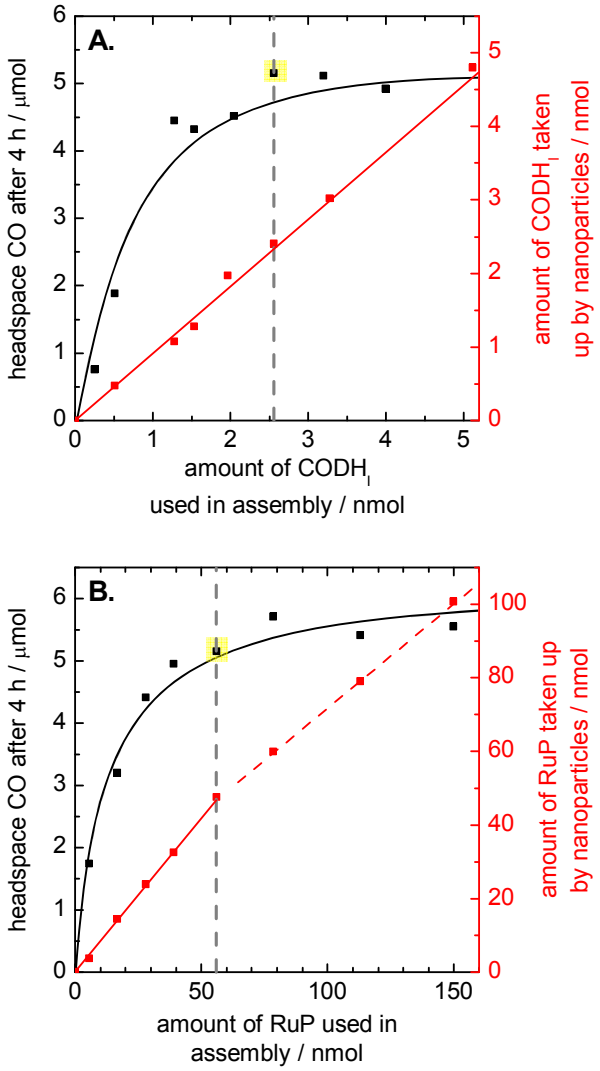


**Figure 62 Effect of varied RuP/CODH$_I$ loading on CO production at [RuP-TiO$_2$-CODH$_I$] in the *standard system* regime.** Black data points: amounts of headspace CO accumulated after 4 h irradiation of [RuP-TiO$_2$-CODH$_I$] systems in which the amount of RuP (56 nmol) used was constant across all experiments, but the amount of CODH$_I$ was varied (A); or in which the amount of CODH$_I$ (2.56 nmol) used was constant across all experiments, but the amount of RuP was varied (B). The *standard procedure* for system preparation was followed in all cases, except for in the amounts of CODH$_I$ or RuP used. Red data points: amounts of CODH$_I$ or RuP actually taken up by the P25 TiO$_2$ nanoparticles, as determined by the UV-vis spectrophotometry method described in section 2.3.2. The dotted grey lines passing through the highlighted data point indicate the amount of CODH$_I$ (panel A) or RuP (panel B) corresponding to *standard conditions*. For all experiments, 5 mg TiO$_2$ nanoparticles were used, the reaction vessels (initially under a gas atmosphere of 2% CH$_4$ in CO$_2$) were maintained at 20 ºC while irradiated with visible light ($\lambda > 420$ nm, 45 mW cm$^{-2}$), and the suspension buffer was 5 mL 0.20 M MES (pH 6.0).

The plots show that photocatalytic activity cannot be continually improved by using increasing amounts of photosensitiser or enzyme. In both cases, saturation of the nanoparticles can be immediately discounted as the reason for CO production reaching a limit: the UV-vis spectrophotometry data (red) indicate that attachment of $CODH_I$ to the nanoparticles is proportional to the amount used in system preparation (in fact, uptake of the enzyme is almost exhaustive), and that attachment of RuP to the nanoparticles is also roughly proportional to the amount added in preparation (there is a slight decrease in gradient, indicated by the dashed red line, above 50 nmol RuP). At low amounts of $CODH_I$ (less than around 1 nmol, panel A) or low amounts of RuP (less than around 50 nmol, panel B), the system behaves predictably, with total turnover being dependent on (and limited by) the component that is in short supply. Although the possibility of additional enzyme molecules beyond 1 nmol not being able to adsorb to the nanoparticles is ruled out by the spectrophotometry data, they do not provide information on whether the $CODH_I$ molecules are in electronic contact with $TiO_2$, so that photoinjected electrons can be readily transferred from semiconductor to D-cluster. TEM (cryo-EM) images of [RuP-$TiO_2$-$CODH_I$] units (Appendix A5) were collected, but these are not of high enough resolution to reveal bound enzyme molecules and hence their orientations with respect to the nanoparticle surfaces (the enzyme has a distinctive shape).[191]

As an alternative suggestion for the relative insensitivity to enzyme loadings in excess of 1 nmol, Appendix A6 uses the footprint dimensions of CODH (roughly 88 Å x 60 Å, from the crystal structure)[191] and the P25 $TiO_2$ BET surface area[331] of 50 $m^2\ g^{-1}$ to determine the approximate amount of enzyme required for complete monolayer coverage of the

nanoparticles. The calculated value of 8 nmol is larger than the amounts of enzyme used in Figure 62A (up to 5 nmol), but the calculation assumes a close-packing arrangement of enzyme molecules. Since 'monolayer coverage' of giant, irregularly shaped enzyme molecules is, in practice, unlikely to consist of close-packing, one may reasonably speculate that within this study's 1 – 5 nmol range, 'monolayer saturation' *may* occur, with excess enzyme molecules initiating multi-layer formation. In a multi-layer scenario, the extra distance between second (and subsequent) layer enzyme molecules would hinder electron transfer, given the large dimensions of CODH.

In Figure 62B, in which each system has been functionalised with 2.56 nmol $CODH_I$, total CO production is observed to be proportional to the amount of photosensitiser within the range of 0 - ~50 nmol RuP, but additional photosensitiser beyond this is not useful, despite the fact that, as previously stated, it continues to bind. The *standard system* is therefore finely balanced in terms of its rate-limiting component. However, the experiment in Figure 63 provides further information. Here, photocatalysis by the *standard system* is revealed to be affected by the electron donor concentration, and therefore the system is clearly sensitive to the rate of electron supply. Section 5.2.4 will investigate further the effect of altering the electron donor species.

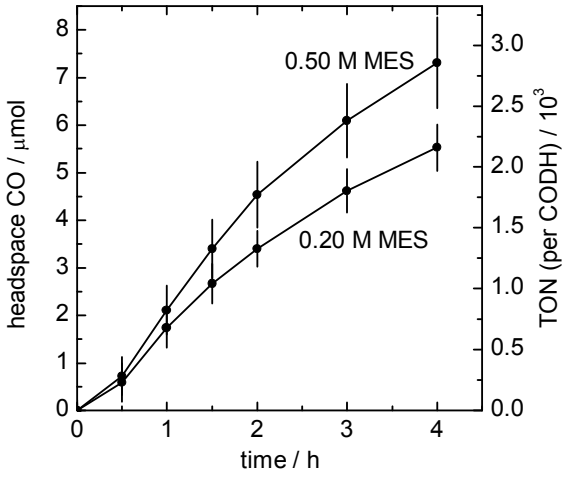


**Figure 63 Influence of the concentration of MES electron donor on $CO_2$ photoreduction at [RuP-$TiO_2$-$CODH_I$].** Both systems were prepared according to the *standard procedure* except for in the MES concentration and run under *standard conditions*. The amounts of system components were: 5 mg P25 $TiO_2$, 2.56 nmol $CODH_I$, 56 nmol RuP, 5 mL MES buffer (pH 6.0, and 0.20 M or 0.50 M, as indicated); and the reaction vessels (initially under a gas atmosphere of 2% $CH_4$ in $CO_2$) were maintained at 20 ºC while under visible light ($\lambda > 420$ nm, 45 mW $cm^{-2}$).

#### 5.2.3.2 THE *LOW-[RuP] STANDARD SYSTEM* REGIME

Figure 64 describes photocatalysis by the [RuP-$TiO_2$-$CODH_I$] system in which *standard conditions* have been re-defined, with the nanoparticles now being modified with ten times less RuP (5.6 nmol instead of 56 nmol). The assembly prepared by modifying 5 mg P25 $TiO_2$ with 5.6 nmol RuP and 2.56 nmol $CODH_I$ (highlighted in green) is termed the *low-[RuP] standard system*, and the configuration of this system is such that electron donation from the photosensitiser is now clearly rate limiting.

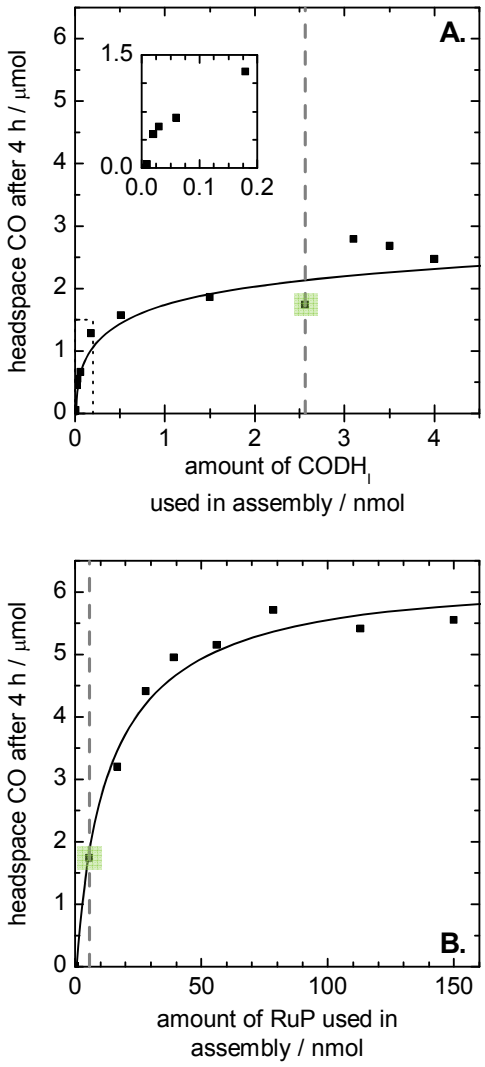


**Figure 64 Effect of varied RuP/CODH$_I$ loading on CO production at [RuP-TiO$_2$-CODH$_I$] in the *low-[RuP] standard system* regime.** Data points indicate the amounts of headspace CO accumulated after 4 h irradiation of [RuP-TiO$_2$-CODH$_I$] systems in which (A) the amount of RuP (5.6 nmol) used was constant across all experiments, but the amount of CODH$_I$ was varied; or in which (B) the amount of CODH$_I$ (2.56 nmol) used was constant across all experiments, but the amount of RuP was varied. The *standard procedure* for system preparation was followed in all cases, except for in the amounts of CODH$_I$ or RuP used in functionalisation of the nanoparticles. The dotted grey lines passing through the highlighted data point indicate the amount of CODH$_I$ (panel A) or RuP (panel B) corresponding to *low-[RuP] standard conditions.* For all experiments, 5 mg P25 TiO$_2$ nanoparticles were used, the reaction vessels (initially under a gas atmosphere of 2% CH$_4$ in CO$_2$) were maintained at 20 ºC while irradiated with visible light ($\lambda$ > 420 nm, 45 mW cm$^{-2}$), and the suspension buffer was 5 mL 0.20 M MES (pH 6.0).

The dashed grey lines indicate the experiments corresponding to *low-[RuP] standard conditions*. If the electron donor is rate limiting, then a clear dependence on RuP is expected, and this is indeed the case: the steep gradient of the best fit line in panel B shows that the rate is now highly sensitive to photosensitiser loading around the point of *low-[RuP] standard conditions*, and panel A indicates no significant dependence on enzyme loading around 2.56 nmol $CODH_I$. At *very* low amounts of $CODH_I$ (below around 0.2 nmol, shown in greater detail in the inset of panel A), the system now becomes limited by enzyme loading, and this is, of course, expected.

## 5.2.4 VARIATION OF SACRIFICIAL ELECTRON DONOR

### 5.2.4.1 PHOTOSENSITISER REGENERATION PROBED BY ELECTROCHEMISTRY

Section 5.2.3.1 revealed the sensitivity of the *standard system* to MES (electron donor) concentration, despite the fact that this sacrificial species was present in vast excess over RuP (56 nmol RuP in 5 mL suspension equates to a concentration of 11 μM; MES is present in the *standard system* at 0.20 M). This section uses RuP-sensitised $TiO_2$ thin film electrodes to study the suitabilities and efficiencies of triethanolamine (TEOA) and ethylenediaminetetraacetic acid (EDTA) as alternative candidates for the sacrificial electron donor.

For these experiments (Figure 65), P25 $TiO_2$ thin film electrodes were prepared as described in section 2.1.2.4.2, and modified with RuP (section 2.1.2.4.3). Each electrode was then connected as the working electrode into the electrochemical cell, and poised at a potential of -0.52 V under ambient light. The ambient light was dim, and in the context of these experiments may be considered as ‘dark’ conditions. No significant photocurrent was

detected during this period. After around 200 s, the $TiO_2$-RuP electrodes were irradiated with visible light ($\lambda > 420$ nm) with the potential remaining at -0.52 V, and photocurrents were induced as described previously (section 4.2.5). This current can be repeatedly toggled on and off, as shown here between 0 and 750 s, and during these initial periods the cell solution was 0.20 M MES (5 mL, pH 6.0). Then, at the points indicated (during periods of continued irradiation) an additional electron donor species - TEOA (panel A), or EDTA (panel B) - was introduced by injecting 1 mL of a 0.15 M TEOA/EDTA (in 0.20 M MES, pH 6.0) solution. The final concentration of the newly introduced compound was therefore 25 mM. Similarly, after approximately a further 250 s, a second 1 mL injection of the TEOA/EDTA solution was made, followed by a third after another 250 s. Finally, after a total time of ~ 1400 s, the electrode was returned to dark conditions.

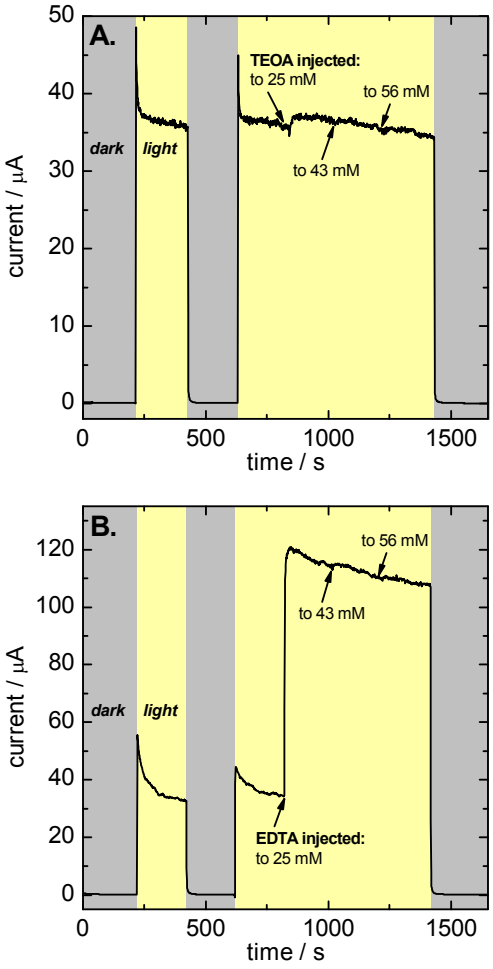


**Figure 65 Chronoamperometry experiments to assess the effects of different electron donors on photocurrents at RuP-sensitised P25 $TiO_2$ thin film electrodes.** The electrodes were poised at -0.52 V throughout, with visible light ($\lambda > 420$ nm) irradiation toggled off/on as indicated by grey/yellow highlighting. In each case, the cell buffer was initially 0.20 M MES (pH 6.0), before TEOA (A) or EDTA (B) was injected to final concentrations of 25, 43 and 56 mM as indicated. All experiments were carried out in an anaerobic glove box ($O_2 < 3$ ppm), and the cell buffer solution was maintained at 20 ºC throughout.

The photocurrents are detected as positive (oxidation) currents, because electrons are injected into the electrode from the photoexcited ruthenium species. Furthermore, the size of the current is proportional to the rate of electron injection; therefore, these electrochemical experiments report on the effects of different electron donors on the rates of photoinjection.

Panel B shows that the additional presence of 25 mM TEOA has only a very slight effect on the photocurrent (an average increase of 3.5 ± 0.7% was recorded across several repeats), and further additions of TEOA (to 43 mM then 56 mM) make no difference. The introduction of 25 mM EDTA, however, significantly enhances the photocurrent (average increase of 195 ± 41%), although further additions beyond 25 mM lead to no additional increase. It was earlier established (section 5.2.3) that the [RuP-$TiO_2$-$CODH_I$] $CO_2$ photoreduction system, at least in its *standard system* composition, is limited by dye regeneration from the sacrificial electron donor (photocatalysis was faster when the concentration of MES was raised from 0.20 to 0.50 M). These electrochemical experiments suggest that the presence of EDTA in the suspension buffer of $CO_2$ photoreduction systems can be expected to lead to an increase in overall CO production, with the inclusion of TEOA anticipated to have little effect. This hypothesis is tested in section 5.2.4.2.

#### 5.2.4.2 EFFECT OF ELECTRON DONOR ON $CO_2$ PHOTOREDUCTION BY [RuP-$TiO_2$-CODH]

Figure 66 shows the results of $CO_2$ photoreduction experiments in which the sacrificial electron donor system is altered; activities (defined here as the amount of CO accumulated after 4 h irradiation) of the various [RuP-$TiO_2$-CODH] systems are plotted relative to the normalised activity of the *standard system* in which the functionalised nanoparticles were suspended in 0.20 M MES without any additional electron donor. The blue bars show the effect of including TEOA in addition to 0.20 M MES; in agreement with the electrochemical experiment in Figure 65B the presence of 25 mM TEOA does not increase CO production to any noticeable degree, although upon stepping to 500 mM TEOA there is an enhancement of around 30%.

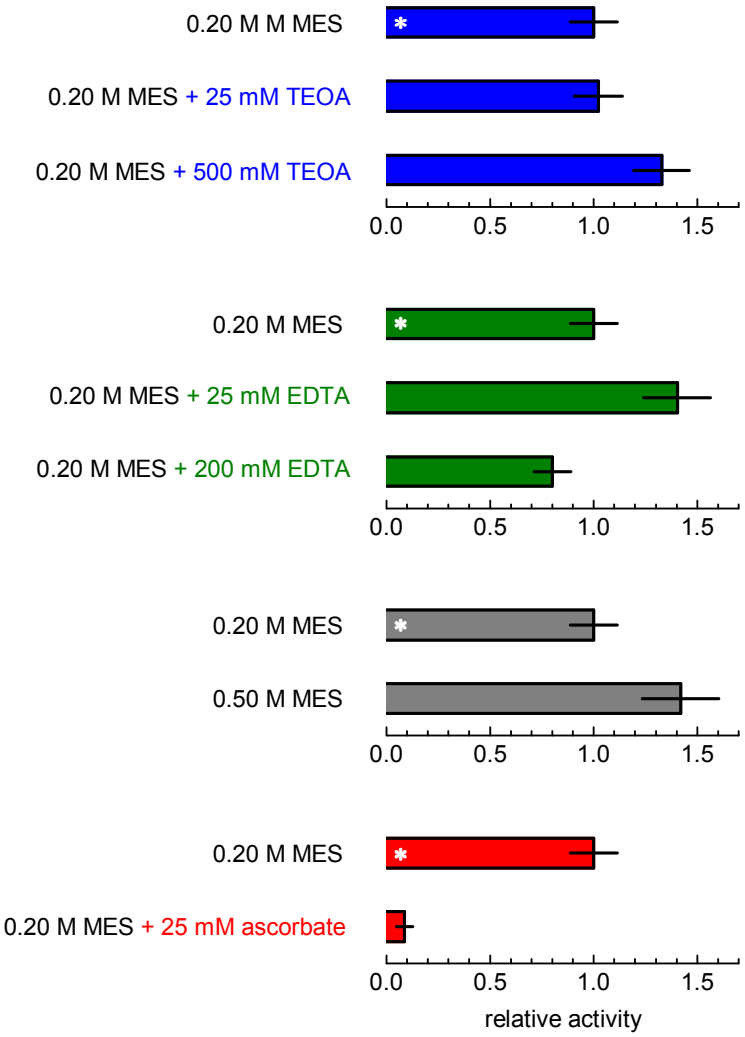


**Figure 66 Effects of various sacrificial electron donor systems on $CO_2$ photoreduction at [RuP-$TiO_2$-CODH] systems.** Activities, defined as the total amounts of CO accumulated in reaction vessel headspaces after 4 h irradiation ($\lambda > 420$ nm, 45 mW $cm^{-2}$), are plotted relative to the amount of CO produced by *standard systems* (which is normalised to 1.0, and indicated by white asterisks). For all experiments, systems were prepared according to the *standard procedure*, except for in the electron donor systems used. The amounts of system components were: 5 mg P25 $TiO_2$, 2.56 nmol CODH ($CODH_I$ was used in all cases, except for experiments represented by red bars, in which $CODH_{II}$ was used), 56 nmol RuP, 5 mL electron donor/buffer solution (pH 6.0); and the reaction vessels (initially under a gas atmosphere of 2% $CH_4$ in $CO_2$) were maintained at 20 ºC.

The effect of EDTA (green bars) is also in agreement with the electrochemical finding: inclusion of 25 mM EDTA leads to significant enhancement of the average $CO_2$ photoreduction rate. That the extent of increase in activity of the photocatalyst (around 40% over the *standard system*) does not match the enhancement of photocurrent in Figure 65B is not surprising, because while the RuP-$TiO_2$ electrode is relevant to the photocatalytic system, the chronoamperometry does not provide a *direct* probe. The potential at which the electrodes in Figure 65 were poised (-0.52 V) was chosen because it is approximately the potential of the $TiO_2$ conduction band, but there are important physical differences between the photocatalytic and electrochemical systems. For example, the electrodes are prepared from thin films of $TiO_2$ nanoparticles that have been calcined – and the sintering of particles effected through this process creates an almost continuous network of $TiO_2$ that is different to clusters of individual particles in suspension. The upshot is that while the results from the electrochemical experiments are *qualitatively* relevant to the photoreduction suspension systems, they should not be expected to predict *quantitative* activity enhancements.

For completeness, Figure 66 also shows the previously established effect (section 5.2.3.1) of increasing the MES concentration from 0.20 M to 0.50 M (grey bars). Also, ascorbate is another commonly used sacrificial electron donor in solar fuel systems, but it is incompatible with [RuP-$TiO_2$-CODH] because ascorbate binds strongly to the $TiO_2$ surface.[369] This is visible on suspending bare P25 $TiO_2$ nanoparticles in 25 mM sodium ascorbate: a light yellow colour appears, arising from the charge transfer of electrons from ascorbate into the $TiO_2$ conduction band. Presumably, the binding of ascorbate hinders the attachment of RuP and CODH, hence the poor rate of $CO_2$ photoreduction (Figure 66, red bars).

### 5.2.5 SURFACE MODIFICATION OF $TiO_2$ TO PROMOTE FAVOURABLE CODH ATTACHMENT

It has been established that $CODH_I$ adsorbs onto the surface of P25 $TiO_2$, and, from electrochemistry and $CO_2$ photoreduction experiments results it must be true that at least some – even if not all - of the enzyme molecules attach such that there is electronic contact with the semiconductor. What is *not* known is the proportion of enzyme molecules for which this is the case, and as previously mentioned, TEM images (Appendix A5) were not able to reveal the orientation of enzyme attachment. On the assumption that the simple adsorption of CODH leads to a range of enzyme orientations at the $TiO_2$ surface (most of which do not allow electron transfer) a strategy was devised with the aim of influencing the point of attachment of CODH to $TiO_2$. The ideal attachment would have the D-cluster of the enzyme positioned as close as possible to the $TiO_2$ surface in order to facilitate rapid electron transfer. Inspection of a surface charge distribution model (Figure 67B, generated using PyMOL software) reveals three highly negatively charged patches of protein surface (indicated by arrows) surrounding the D-cluster of $CODH_{II}$. Figure 67C shows a cartoon representation of a strategy that makes use of these charged regions to exert some control over the orientation of $CODH_{II}$ molecules at $TiO_2$. Since it contains a phosphonate group, *o*-phosphorylethanol amine (OPEA) has been previously used as a $TiO_2$ surface modifying group.[370] At the opposite end to the phosphonate group is a primary amine group, the p*K*a of which is 10.39. At pH 6.0 this group will be protonated to $–NH_3^+$, which now provides an electrostatic 'anchor' for $CODH_{II}$ through one of the negatively charged protein patches, and the small size of the OPEA molecule provides a short path for electron transfer.

The three patches identified in Figure 67B are not the only negatively charged areas on the surface of the protein – there are around 12 similarly sized patches in total – so this approach is not expected to provide complete control over attachment orientation. Nevertheless, reducing the total number of attachment orientations to just a few options – one of which is the preferred orientation - may offer an advantage in terms of the total number of electrochemically active enzymes per $TiO_2$ unit and was therefore deemed to be worth pursuing.

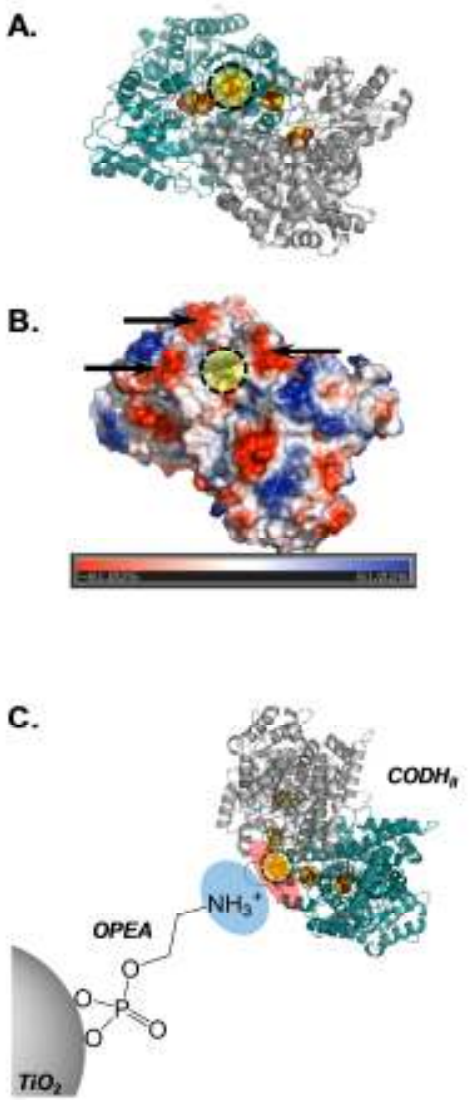


**Figure 67 Strategy for directed attachment of $CODH_{II}$ to P25 $TiO_2$ nanoparticles.** (A) The structure of $CODH_{II}$ from *Carboxydothermus hydrogenoformans* (PDB code 1SUF) highlighting the D-cluster. (B) Surface charge distribution of the same enzyme, in the same orientation as (A), generated using PyMOL software. Positive charges are blue, negative charges are red. Arrows indicate three patches of the protein surface close to the D-cluster that have a particularly high negative charge. (C) Cartoon representation of directed attachment of $CODH_{II}$ to P25 $TiO_2$, using the electrostatic interaction between the protonated amine group of OPEA (positively charged, blue) and the identified 'negative-rich' patch around the D-cluster of the enzyme.

$CO_2$ photoreduction systems were prepared as described in section 4.2.6.1, except that the order of functionalisation with $CODH_{II}$ and RuP was switched, so that in this instance the

dye was pre-attached.[†††] After pre-adsorbing RuP, 3 mg (21 μmol) OPEA (as 100 μL of a 30 mg $mL^{-1}$ solution) was added to the RuP-$TiO_2$ suspension and stirred for 20 min, before adding 2.56 nmol $CODH_{II}$ and stirring for a further 20 min. The reaction vessel was then sealed tightly, flushed with 2% $CH_4$ in $CO_2$ and irradiated with visible light (λ > 420 nm, 45 mW $cm^{-2}$) as described in section 4.2.6.1. Figure 68 shows CO production by the OPEA-modified system ([RuP-$TiO_2$-OPEA-$CODH_{II}$]) in comparison to the un-modified [RuP-$TiO_2$-$CODH_{II}$] *standard system.*

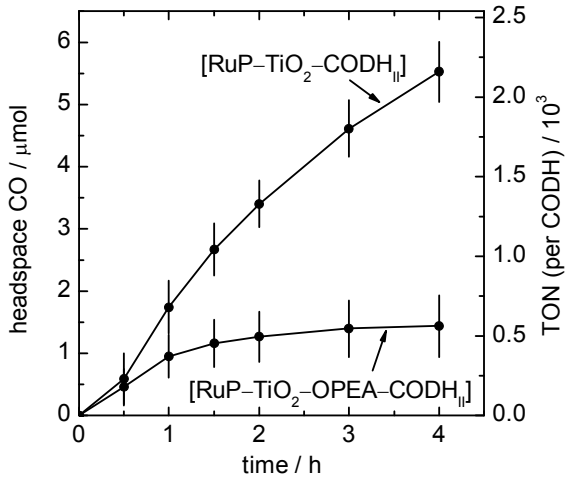


**Figure 68 $CO_2$ photoreduction by the [RuP-$TiO_2$-$CODH_{II}$] *standard system* and by [RuP-$TiO_2$-OPEA-$CODH_{II}$].** The *standard system* was prepared according to the *standard procedure*; the OPEA-linked system was prepared by firstly adsorbing RuP to the nanoparticles, followed by addition of OPEA (3 mg, 21 μmol) and then $CODH_{II}$. The amounts of components used in both systems are: 5 mg P25 $TiO_2$, 56 nmol RuP, 2.56 nmol $CODH_{II}$, 5 mL 0.20 M MES (pH 6.0). The reaction vessels (initially under a gas atmosphere of 2% $CH_4$ in $CO_2$) were maintained at 20 ºC while irradiated with visible light (λ > 420 nm, 45 mW $cm^{-2}$).

[†††] The reason for this was to eliminate the risk of OPEA completely covering the $TiO_2$ surface, thereby preventing RuP attachment. Adding RuP as a *first* step (and in the quantity established in section 4.2.4) is known to provide coverage of around 25% of the surface of 5 mg nanoparticles, and therefore it is certain that sites will remain available for OPEA and $CODH_{II}$ attachment.

It is clear that the OPEA-modification step leads to a significant decrease in overall system activity, and subsequent UV-vis spectrophotometry (data not shown) revealed that total enzyme attachment was reduced compared to the *standard system* in which CODH was adsorbed directly onto the $TiO_2$ surface. Like previous UV-vis data, there is no information on whether the enzyme molecules that are taken up are oriented 'correctly' (it is entirely possible that fewer $CODH_{II}$ molecules are attached in the OPEA-modified system, but that it contains more active units), but nevertheless low overall enzyme attachment is a discouraging indicator. A significant factor may be the size of the OPEA linker. Assuming OPEA to have an approximate length of 1 nm, a significant decrease in the rate of electron transfer from $TiO_2$ into the CODH D-cluster can be expected. Rate of electron transfer is proportional to $e^{-\beta R}$, where R is the distance and β is proportional to the tunnelling barrier height.[371] For proteins, a β value of 1.4 $Å^{-1}$ is typical,[234] and thus increasing the electron transfer distance by 1 nm has a large effect on rate. Further discussion of controlled CODH attachment is given in section 4.3.

## 5.3 INVESTIGATING THE SOURCE OF INSTABILITY

### 5.3.1 PHOTOCATALYSIS BY [RuP-$TiO_2$-CODH] SYSTEMS ACROSS EXTENDED TIME PERIODS

Figure 69 shows CO production by the [RuP-$TiO_2$-$CODH_{II}$] *standard system*, over a longer period of time than experiments discussed so far. The photocatalyst was prepared according to the *standard procedure* and initially run under *standard conditions* for 8 h (first section of Figure 69), over which period the decrease in activity over time is very clear.

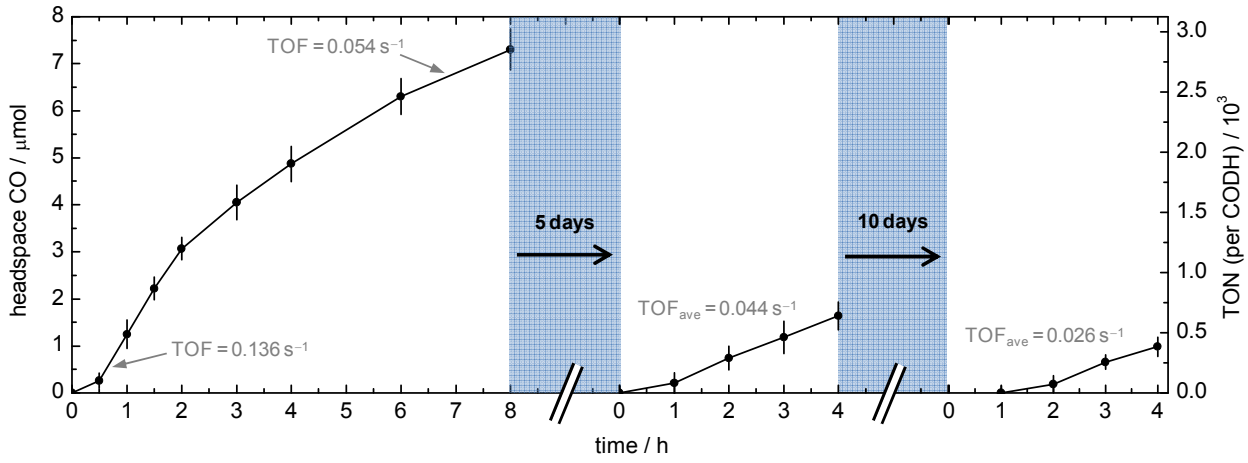


**Figure 69 Long-term $CO_2$ photoreduction activity of [RuP-$TiO_2$-$CODH_{II}$].** The *standard system* was prepared and run under *standard conditions* (starting from a gas atmosphere of 2% $CH_4$ in $CO_2$) for 8 h. After this time, the reaction vessel was well sealed, protected from ambient light and stored undisturbed at 4 ºC for 5 days; it was then re-flushed with 2% $CH_4$ in $CO_2$ and irradiation re-started with regular gas headspace monitoring for 4 h. After this time the pressure vessel was again well sealed, protected from ambient light and stored undisturbed at 4 ºC for a further 10 days; re-flushed with 2% $CH_4$ in $CO_2$ and irradiation re-started with regular gas headspace monitoring for 4 h. The amounts of system components were: 5 mg $TiO_2$, 2.56 nmol $CODH_{II}$, 56 nmol RuP, 5 mL buffer solution (0.2 M MES, pH 6.0). The reaction vessels were maintained at 20 ºC while irradiated with visible light ($\lambda > 420$ nm, 45 mW $cm^{-2}$).

Over 8 h, the TOF - on a *per mol $CODH_{II}$* basis - falls by around 60%, from 0.136 mol CO (mol $CODH_{II}$)$^{-1}$ $s^{-1}$ (average rate for 0 – 1 h) to 0.054 mol CO (mol $CODH_{II}$)$^{-1}$ $s^{-1}$ (average rate for 6 – 8 h). This is consistent with the experiments in section 4.2.6.2, where over shorter experiments lasting 4 h, activity was measured to decrease over the course of experiments by around 70% ([RuP-$TiO_2$-$CODH_I$]) and 50% ([RuP-$TiO_2$-$CODH_{II}$]). UV-vis spectrophotometry experiments (Appendix A7 and summarised in Table 14) indicate that this deactivation cannot be accounted for by desorption of RuP and/or CODH molecules over time, because the decreases in photocatalytic activity are far greater than the extents of desorption.

**Table 14** Spectrophotometrically-determined uptake of RuP, $CODH_I$ and $CODH_{II}$ to 5 mL (1 mg $mL^{-1}$) P25 $TiO_2$ nanoparticle suspensions,[a] and amounts remaining attached after 4 h stirring at 20 ºC

| adsorbate | amount added to 5 mg P25 $TiO_2$ / nmol | amount taken up[b] / nmol | amount remaining attached after 4h[b] / nmol | % desorbed over 4 h |
|---|---|---|---|---|
| RuP | 56 | 56 (complete uptake) | 54.9 ± 0.3 | 2 ± 0.5 |
| $CODH_I$ | 2.56 | 2.40 ± 0.03 | 2.05 ± 0.13 | 15 ± 5 |
| $CODH_{II}$ | 2.56 | 2.56 (complete uptake) | 2.10 ± 0.03 | 18 ± 1 |

[a] Suspension were prepared with 0.20 M MES buffer solution (pH 6.0). [b] Adsorption amounts were calculated as detailed in the main text, using UV-vis absorption data from solutions of RuP/$CODH_I$/$CODH_{II}$ before and after incubation with nanoparticles, and after 20 min stirring.

After the first 8 h period of the experiment in Figure 69, the reaction vessel was well sealed, protected from ambient light by aluminium foil, and stored at 4 ºC for 5 days. Then, the headspace was re-flushed with 2% $CH_4$ in $CO_2$ and irradiation continued for 4 h. This process was then repeated, but with a longer rest period of 10 days. Looking closely at Figure 69, it is interesting to note the amount of activity that remains after long periods (days) of storage. After the first storage period (5 days), the rate at which CO production occurs (0.044 mol CO (mol $CODH_{II}$)$^{-1}$ $s^{-1}$) is not much slower than the rate measured during the final 2 h period of the initial 8 h run (0.054 mol CO (mol $CODH_{II}$)$^{-1}$ $s^{-1}$); and even after a further 10 days the rate has only fallen to 0.026 mol CO (mol $CODH_{II}$)$^{-1}$ $s^{-1}$. Extrapolation of the 8 h plot (note the time axis is broken in Figure 69 is broken) would forecast extremely low rates after 5 and 15 days, and this result therefore implies that the loss of activity over time is not a simple time-dependent effect. The experiments in Figure 70 provide confirmation of this. Here, the [RuP-$TiO_2$-$CODH_{II}$] *standard system* (plot a) is compared to two systems that have both been stored for 5 days before undergoing $CO_2$ photoreduction experiments (plots b and c). Although both have remained under the same conditions (4 ºC, protected from ambient light) during this period, systems (b) and (c) differ in their handling

prior to photocatalysis: immediately following its preparation, system (c) was used in a $CO_2$ photoreduction experiment for 8 h (data not shown) before being stored as described; whereas system (b) was immediately put into storage *without* being used for $CO_2$ photoreduction.

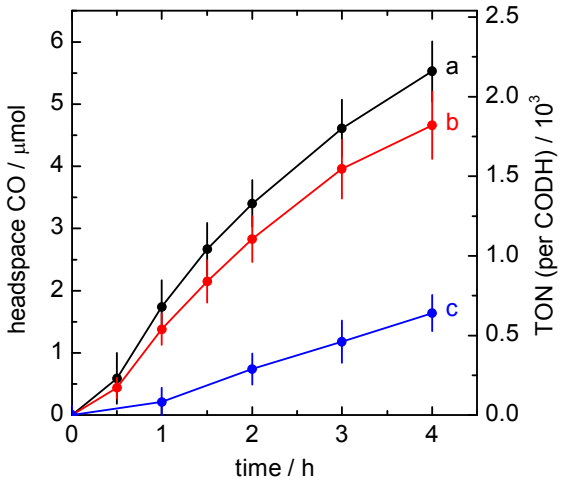


**Figure 70 Effect of 5-day storage on $CO_2$ photoreduction by [RuP-$TiO_2$-$CODH_{II}$].** System (a): *standard system*, prepared according to the *standard procedure*. System (b): *standard system*, prepared according to the *standard procedure* but not used immediately for photocatalysis; instead, the reaction vessel was well sealed and stored at 4 ºC for 5 days while protected from ambient light. After this time, the system was flushed with 2% $CH_4$ in $CO_2$ and run as normal under visible light irradiation. System (c): *standard system* that was prepared and used immediately in a photocatalytic experiment under visible light irradiation for 8 h (data not shown), before being stored for 5 days at 4 ºC while protected from ambient light. After this time, the reaction vessel was flushed with 2% $CH_4$ in $CO_2$ and run once again under visible light (shown here, blue plot). The amounts of system components were: 5 mg $TiO_2$, 2.56 nmol $CODH_{II}$, 56 nmol RuP, 5 mL buffer solution (0.2 M MES, pH 6.0). The reaction vessels (initially under a gas atmosphere of 2% $CH_4$ in $CO_2$) were maintained at 20 ºC while irradiated with visible light ($\lambda > 420$ nm, 45 mW $cm^{-2}$).

Compared to the system in plot (a), the diminished activity of plot (c) contrasts sharply with the relatively unaffected activity of plot (b). This is consistent with the suggestion made previously: the deactivation of the photocatalyst is not a simple time-dependent effect. This is, perhaps, to be expected – one may predict the main effect of an extended lag period to be

the desorption of the active components (CODH and RuP) over time – but the data in Table 14 showed this not to be a significant effect. The result in Figure 70 also illustrates the potential for storage of the photocatalyst for on-demand use.

#### 5.3.1.1 TRACE $O_2$ DAMAGE

As previously described, and as demonstrated in Figure 56, CODHs from the anaerobic organism *Carboxydothermus hydrogenoformans* are highly sensitive to $O_2$. This, of course, is the reason for preparation of [RuP-$TiO_2$-CODH] $CO_2$ photoreduction requiring anaerobic conditions, and for running experiments under $O_2$-free conditions. Rubber septa are used to seal the reaction vessels, because they allow headspace gas samples to be removed for GC gas analysis but they are also 're-sealing'. Ideally, the septa should completely prevent the leakage of air into the system (and stop headspace gas leakage out of the vessel), but in practice it is highly unlikely that such a seal can provide a perfect barrier.[‡‡‡] For this reason, and assuming that a trace amount of $O_2$ must infiltrate the reaction vessel (even if it is a vanishingly small amount), the experiment in Figure 71 was designed to test for the significance of this effect.

[‡‡‡] The GC chromatograms in Figure 26 show peaks attributed to both $O_2$ and $N_2$. This may be due to traces of these gases inside the reaction vessel, or due to air entering the needle tip immediately before injection into the GC inlet, or a combination of these factors.

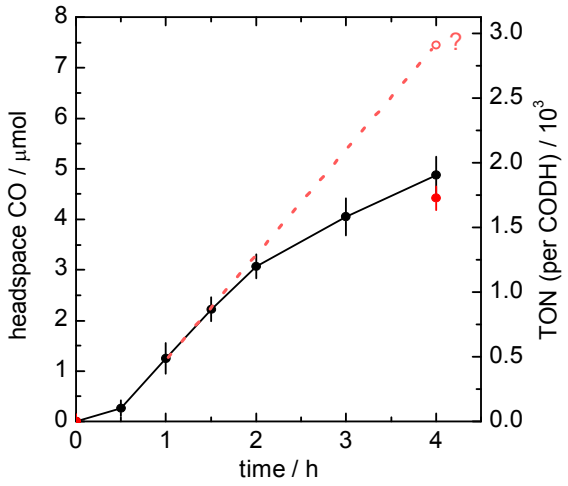


**Figure 71 Testing for the effect of trace $O_2$ damage to $CODH_{II}$ on the instability of [RuP-$TiO_2$-$CODH_{II}$].** The black plot shows CO production by the *standard system*, with regular GC quantification of the amount of headspace CO at 0, 0.5, 1, 1.5, 2, 3 and 4 h. At each of these sampling times, the rubber septum used to seal the reaction vessel gains an extra needle piercing. The solid red data point indicates the amount of headspace CO produced after 4 h by an identically prepared system, but which had undergone no headspace sampling until this time. The rubber septum in this system therefore remained immaculately intact throughout the experiment. The hollow red point indicates the expected amount of headspace CO at 4 h if the reaction rate from the initial part of the experiment (indicated by the dotted red line) were sustained. The amounts of system components were: 5 mg $TiO_2$, 2.56 nmol $CODH_{II}$, 56 nmnol RuP, 5 mL buffer solution (0.2 M MES, pH 6.0). The reaction vessels (initially under a gas atmosphere of 2% $CH_4$ in $CO_2$) were maintained at 20 ºC while irradiated with visible light ($\lambda > 420$ nm, 45 mW $cm^{-2}$).

The black plot in Figure 71 shows CO production by the [RuP-$TiO_2$-$CODH_{II}$] *standard system* over 4 h, with samples of the reaction vessel headspace injected into the GC for analysis at the usual time points (0, 0.5, 1, 1.5, 2, 3 and 4 h). The solid red data point shows the amount of CO produced by an identically prepared [RuP-$TiO_2$-$CODH_{II}$] system that had been run under identical conditions, but in which no headspace gas samples had been taken before the end of the experiment (4 h). In this way, the rubber septum remained *immaculately intact* throughout the course of the experiment, removing the possibility of air leaking into the reaction vessel. Clearly, the avoidance of septa piercings does not eradicate the instability

(the hollow red point shows the amount of headspace CO that would be accumulated after 4 h if there was no decrease in rate over time). The effect of $O_2$ leakage as a side-effect of the regular monitoring of the progression of photoreduction experiments – if this does occur at all – is therefore of no concern and cannot be responsible for deactivation.

#### 5.3.1.2 THERMODYNAMIC EFFECTS: DIMINISHING DRIVING FORCE FOR $CO_2$ REDUCTION

The thermodynamics of $CO_2$ photoreduction by [RuP-$TiO_2$-CODH] was described earlier (section 4.1.2), where it was established that due to the small difference in potential between the $TiO_2$ (anatase) conduction band edge and the $CO_2$/CO redox potential there is only a narrow driving force available for CO production. Furthermore, as $CO_2$ photoreduction continues, the concentration of $CO_2$ decreases as it is converted into CO (the *standard systems*, using either $CODH_I$ or $CODH_{II}$, start under an atmosphere of 98% $CO_2$ / 2% $CH_4$; and after 4 h have reached a composition of around 95% $CO_2$ / 3% (5 μmol) CO / 2% $CH_4$). As the gas composition of the reaction vessel shifts over the course of experiments, the Nernst equation dictates that the reduction potential of the $CO_2$/CO couple will also shift, as shown in Figure 72.

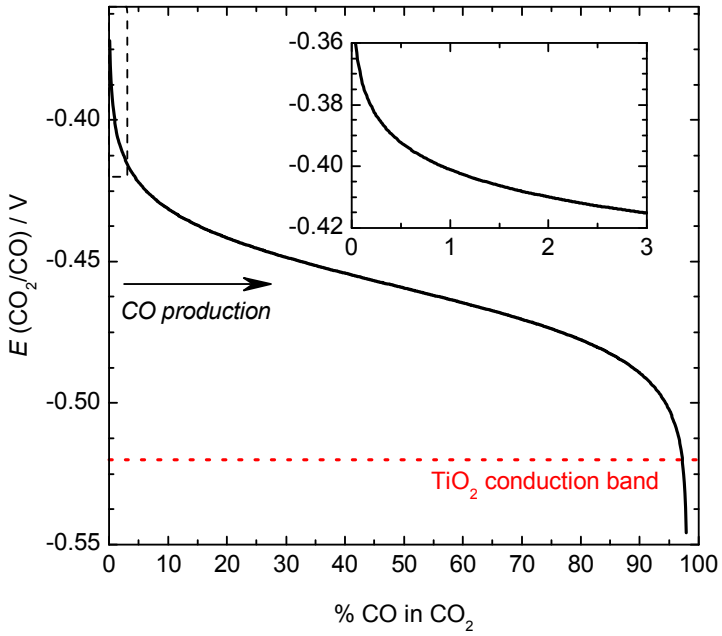


**Figure 72 Reduction potential for the $CO_2$/CO couple at pH 6.0 at 20 °C, plotted against % CO.** *E* is calculated based on the rest of the gas composition being 2% $CH_4$, and the remainder as $CO_2$. The dotted red line indicates the approximate position of the $TiO_2$ (anatase) conduction band potential.

The insets indicate that over the course of a typical (*standard system*) $CO_2$ photoreduction experiment, the ($CO_2$/CO) reduction potential will become more negative as a result of the CO:$CO_2$ ratio increasing, and after 4 h (at which time ~3% CO has accumulated) *E*($CO_2$/CO) is around 60 mV more negative. In relation to the margins with the $TiO_2$ (anatase) conduction band potential, the $CO_2$/CO Nernstian shifts over the courses of experiments are significant, and the $TiO_2$ conduction band electrons become considerably less reducing relative to *E*($CO_2$/CO). The experiments in Figure 73 were designed to test whether this effect is the root cause of the consistently observed decrease in activity over time of $CO_2$ photoreduction experiments. In panel A, the [RuP-$TiO_2$-$CODH_I$] *standard system* was prepared and run under *standard conditions* for 4 h – at which time around 5 µmol (~3%) CO has accumulated

- before pausing the experiment and re-flushing the reaction vessel headspace with 2% $CH_4$ in $CO_2$. After this, irradiation is re-started: CO production continues, but *at the same rate observed at the end of the initial 4 h period* (dotted line), and not at the initially recorded rate (0 – 1 h).

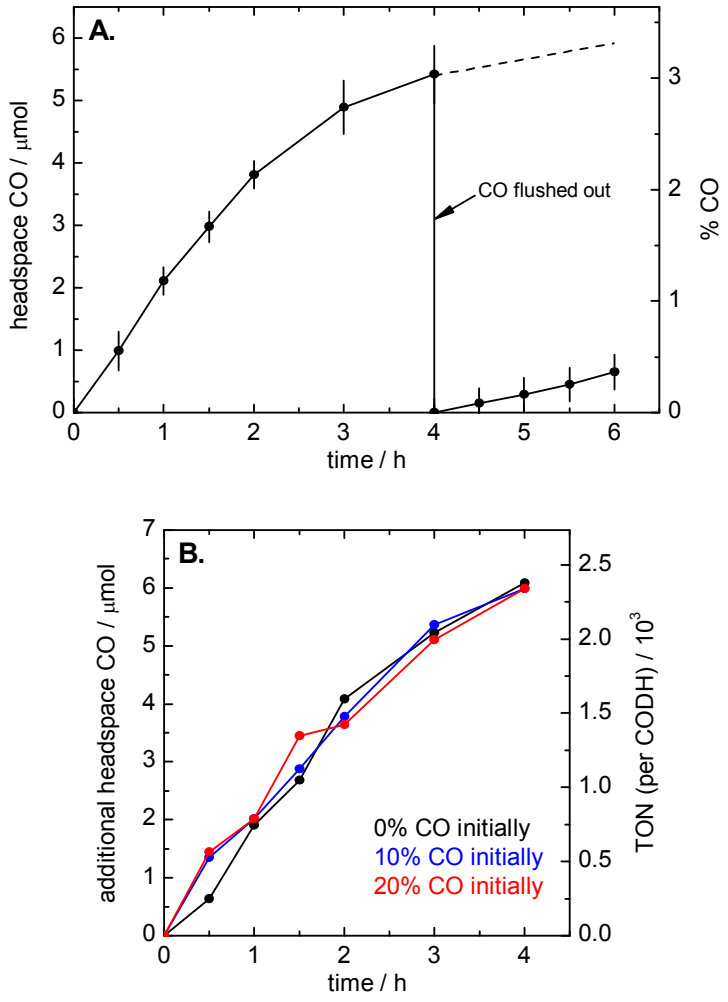


**Figure 73 Testing for product inhibition and substrate depletion as rate-affecting factors in $CO_2$ photoreduction at [RuP-$TiO_2$-CODH$_I$].** In panel (A) the system was prepared according to the *standard procedure* and run (initially under a gas atmosphere of 2% $CH_4$ in $CO_2$) under *standard conditions* for 4 h, before stopping irradiation, re-flushing the reaction vessel headspace with 2% $CH_4$ in $CO_2$, and re-starting the experiment. Panel (B) shows systems that were run under *standard conditions* and prepared according to the *standard procedure* except that before starting irradiation the reaction vessel headspaces were flushed with

either: 1.4% $CH_4$ / 68.6% $CO_2$ / 0% CO, 30% He (black); 1.4% $CH_4$ / 68.6% $CO_2$ / 10% CO, 20% He (blue); or 1.4% $CH_4$ / 68.6% $CO_2$ / 20% CO, 10% He (red). In all experiments the amounts of system components were: 5 mg P25 $TiO_2$, 2.56 nmol $CODH_I$, 56 nmol RuP, 5 mL 0.20 M MES (pH 6.0); and the reaction vessels were maintained at 20 ºC while under visible light ($\lambda > 420$ nm, 45 mW $cm^{-2}$).

The experiments in panel B test for the effect on rate of even slimmer thermodynamics. Here, the composition of the reaction vessel headspace is varied at the start of the experiment so that CO is either absent at the start, or present at a high headspace concentration of 10% or 20%. The initial $CO_2$ concentrations in each of these experiments was the same (68.6%), with a 1.4% $CH_4$ internal standard, and the remaining volume comprising He. When CO is present at these concentrations (and $CO_2$ is at 68.6%), $E(CO_2/CO)$ is shifted considerably in the negative direction[§§§], to around -0.43 for 10% CO and -0.44 V for 20% CO. Despite the driving force for $CO_2$ reduction being considerably smaller when there is a high initial concentration of product (CO), there is no difference between the three plots, and therefore, on the basis of these experiments it is possible to rule out the effect of narrowing thermodynamics for the observed decreases in CO production rate.

#### 5.3.1.3 PHOTO-INDUCED DAMAGE OF CODH AND RuP

Having eliminated extrinsic factors including RuP and CODH desorption, trace $O_2$ enzyme damage and diminishing thermodynamic driving force as contributors to performance instability, attention now turns to intrinsic factors. Figure 74 shows experiments investigating the possibility of prolonged exposure to visible light resulting in degradation of one or more components of the photoreduction system. The black plot (a) shows CO production over the course of 8 h by the [RuP-$TiO_2$-$CODH_{II}$] *standard system*. Plots (b), (c) and (d) relate to

[§§§] The Nernstian potential in the complete absence of CO is, of course, undefined, but at 0.01% CO / 68.6% $CO_2$ $E(CO_2/CO)$ = -0.35 V.

systems that were also subjected to visible light irradiation from 0 h, but that, *from 0 – 8 h*, had the following compositions: (b) [$TiO_2$-$CODH_{II}$] (*i.e.* RuP was omitted); (c) [RuP-$TiO_2$] (*i.e.* $CODH_{II}$ was omitted); (d) [RuP-$TiO_2$-$CODH_{II}$] (*i.e.* complete system). At 8 h, the [$TiO_2$-$CODH_{II}$] and [RuP-$TiO_2$] systems (b and c) had not produced any detectable amount of CO (as expected); and the complete, but thus-far unsampled, full system (d) had produced a similar amount of CO to the black plot (again, as expected). At this point (8 h), all three reaction vessels (b, c and d) were taken into an anaerobic glove box, whereupon the systems were made complete: 56 nmol RuP was added to (b), 2.56 nmol $CODH_{II}$ was added to (c) (in each case, the functionalisation was performed as described in section 4.2.6.1). For (d), no addition was necessary since the system was already complete, but this suspension was nevertheless stirred in its current condition for 20 min. After this time, the reaction vessels were removed from the glove box and re-flushed with 2% $CH_4$ in $CO_2$, before once again being subjected to visible light for a further 4 h.

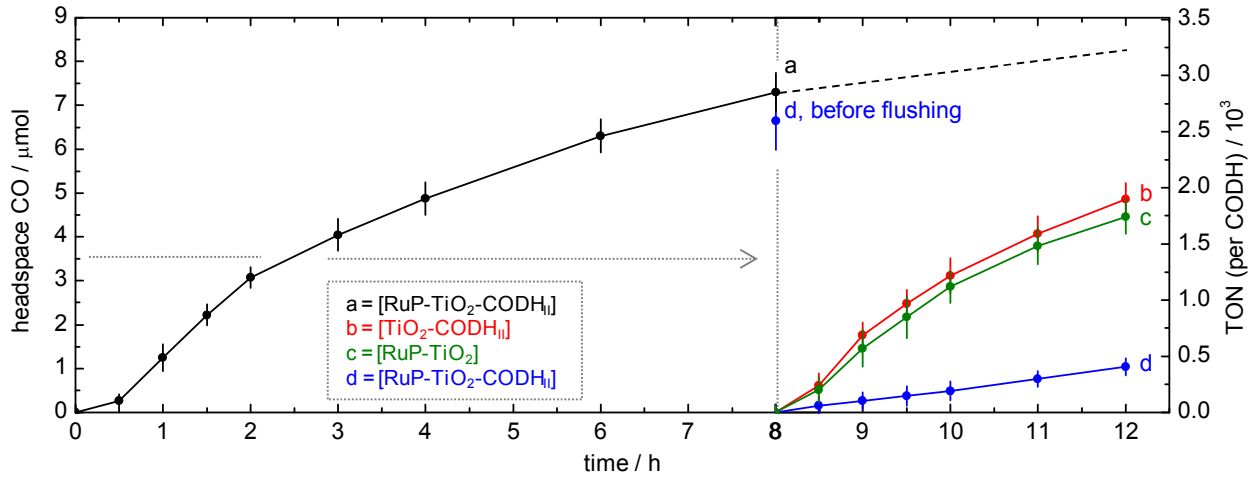


**Figure 74 Investigating the detrimental effect of light on components of the [RuP-$TiO_2$-$CODH_{II}$] $CO_2$ photoreduction system.** Plot (a) shows CO production by the [RuP-$TiO_2$-$CODH_{II}$] *standard system* under *standard conditions* (starting under a gas atmosphere of 2% $CH_4$ in $CO_2$) for 8 h. Plots (b), (c) and (d) relate to the following systems: (b) [$TiO_2$-$CODH_{II}$] (*i.e.* RuP was omitted); (c) [RuP-$TiO_2$] (*i.e.* $CODH_{II}$ was omitted); (d) [RuP-$TiO_2$-$CODH_{II}$] (*i.e.* complete system). These systems were subjected to visible light irradiation for 8 h, during which time the gas headspace was not sampled. After 8 h, the samples were taken into the glove box, whereupon the systems were made complete (RuP was added to system (b); $CODH_{II}$ was added to system (c); no addition was made to system (d)). The reaction vessels were then re-flushed with 2% $CH_4$ in $CO_2$, and irradiation re-started with regular sampling of the gas headspaces. In all experiments the amounts of system components (when present) were: 5 mg P25 $TiO_2$, 2.56 nmol $CODH_I$, 56 nmol RuP, 5 mL 0.20 M MES (pH 6.0); and the reaction vessels were maintained at 20 ºC while under visible light ($\lambda$ > 420 nm, 45 mW $cm^{-2}$).

After being 'made complete' at 8 h, systems (b) (initially lacking RuP) and (c) (initially lacking $CODH_{II}$) both show very similar initial activity to the *standard system* that was run without delay (plot a, 0 – 4 h). In contrast, however, re-setting a complete system after 8 h that has previously been used for $CO_2$ photoreduction (plot d) results in much poorer activity, with the new CO production rate being less than 25% of (b) and (c). The new rate of this system matches the rate observed at the end of the plot of CO production by the *standard system* (a) (dotted black line).

What this indicates is that the cause of decreasing activity over time for any of the previously presented [RuP-$TiO_2$-$CODH_{II}$] $CO_2$ photoreduction systems is not a simple photoinstability of $CODH_{II}$ or RuP – in system (b), $CODH_{II}$ has been exposed to irradiation for 8 h before being used for $CO_2$ photoreduction and yet the overall performance has not suffered; similarly, in system (c), the performance has not suffered on account of RuP being exposed to light for a prolonged period of time.

Why, then, does system (d) not re-start at 8 h at the same rate as (b) and (c)? Here, RuP and $CODH_{II}$ have been under the same conditions from 0 – 8 h as they have in experiments (b) and (c), but the key difference must be that system (d) – being 'complete' – has been turning over in this time; indeed, the blue data point indicates 6.6 μmol CO has been produced in the first 8 h period. In system (b), the $TiO_2$ nanoparticles were not initially sensitised to light, and therefore no electrons were supplied to $CODH_{II}$ to enable turnover (and reduction of $CO_2$ to CO). Similarly, in system (c), the omission of enzyme molecules means that there is no electron acceptor for electrons injected from RuP, so presumably continuous cycling of RuP through ground, photoexcited, and oxidised states does not occur and instead photoinjection is followed by recombination. System (d) differs because both the photosensitiser and enzyme units are continuously cycling (with the oxidised photosensitiser being quenched by the sacrificial electron donor), and it appears that the cycling of this mechanism deactivates the system as a whole.

The experiments in Figure 74 do not provide information on which component (RuP or $CODH_{II}$) is responsible for the instability, although the data in Figure 75 are revealing. Here, chronoamperometry experiments using $TiO_2$ thin film electrodes modified with either RuP,

$CODH_I$ or $CODH_{II}$ are used to assess the stability of each of these active species over a period of 4 h of continual turnover.[****] The experiments were designed to provide results that are as applicable as possible to the [RuP-$TiO_2$-CODH] photocatalyst: the electrode-RuP and electrode-CODH interactions must be relevant proxies to the interactions in the particulate systems. For the chronoamperometry experiments, modified $TiO_2$ electrodes were connected into electrochemical cells containing 0.20 M MES (pH 6.0), and poised at -0.52 V (the approximate position of the $TiO_2$ conduction band). Currents were continuously monitored for 4 h while $CO_2$ was bubbled through the cell solution.

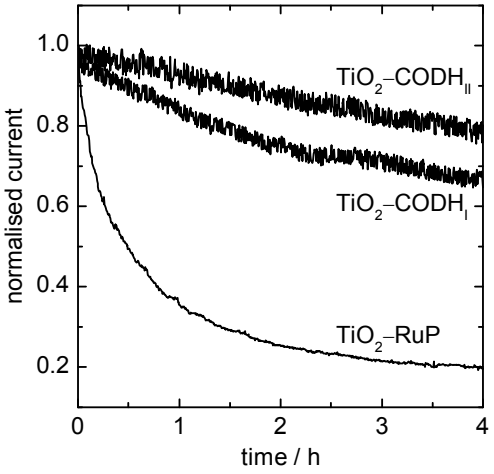


**Figure 75 Normalised currents at $TiO_2$-CODH and $TiO_2$-RuP electrodes (in separate experiments) held at a constant potential of -0.52 V at 20 °C for 4 h.** Throughout the experiments $CO_2$ was bubbled through the cell solution (0.20 M MES, pH 6.0). For ease of comparison both data sets are normalised to +1 (actual $TiO_2$-CODH $CO_2$ reduction currents were negative). Average activity losses from several repeat experiments are shown in Table 15.

[****] The term 'turnover' here refers either to the continuous cycles of photoinjection from RuP, or to CODH-catalysed $CO_2$ reduction.

As described in section 2.1.1, the current at $TiO_2$-CODH electrodes is a direct measure of the rate of $CO_2$ reduction by the enzyme; similarly, the $TiO_2$-RuP current (when the electrode is irradiated) is proportional to the rate at which electrons are injected into the $TiO_2$ conduction band from the photoexcited state of the dye. The typical chronoamperometry traces in Figure 75 show that the activities of CODH-modified electrodes are much more stable than RuP-modified electrodes (average losses are shown in Table 15).

**Table 15** Average activity losses after 4 h at $TiO_2$ thin film electrodes modified with either RuP or $CODH_{II}$, under the conditions of Figure 75.

| electrode | % activity loss after 4 h |
|---|---|
| $TiO_2$-RuP | 88 ± 3.0 |
| $TiO_2$-$CODH_I$ | 34 ± 5.8 |
| $TiO_2$-$CODH_{II}$ | 23 ± 7.0 |

It does not necessarily follow, however, that the instability of RuP photoinjection means that *all* [RuP-$TiO_2$-CODH] $CO_2$ photoreduction systems are unstable. This is only expected to be the case if electron supply is rate-limiting. The Figure 75 chronoamperometry studies only demonstrate that the inherent stability of photoinjection from RuP to $TiO_2$ is lower than the stability of $CO_2$ turnover at $TiO_2$-immobilised CODH (and, indeed, this is only necessarily true under these experimental conditions). However, let us now reconsider the *low-[RuP] standard system* (comprising 5 mg $TiO_2$ modified with 2.56 nmol $CODH_I$ and 5.6 nmol RuP) from section 5.2.3.2, for which it was established that the rate of CO production was limited by the low RuP loading. Figure 64A (reproduced and adapted below as Figure 76A), which plotted the total CO accumulated after 4 h by systems modified with this amount (5.6 nmol) of RuP, indicated that this '*low-[RuP]*' *standard system* (corresponding to the dotted grey

line) was insensitive to $CODH_I$ loading. To recap the essence of section 5.2.3.2: the system here is limited by its RuP deficiency, so extra loading of $CODH_I$ (*i.e.* moving to the right of the dotted grey line) is ineffective. By the same token, lowering the $CODH_I$ loading (*i.e.* moving to the *left* of the dotted grey line) also has little effect, although this only applies for reasonable $CODH_I$ concentrations, and extremely low $CODH_I$ loadings (less than 0.2 nmol, inset plot) create a situation in which the limiting factor is now $CODH_I$, rather than RuP. With this in mind, highlighted in Figure 76A are the CO-production (headspace CO *vs.* time) plots corresponding to systems that are clearly $CODH_I$-limited (a, b, c; blue), and data CO-production plots corresponding to systems that are RuP-limited (d, e, f; red). Panel B shows plots of CO production by these six systems. On close inspection, it is apparent that the red plots – corresponding to an RuP-limited scenario – all exhibit the familiar instability (the rate of CO production decreases over time). In contrast, the *CODH-limited* systems (blue) show no obvious instability – the plots are linear. Although it should be further substantiated, this observation finding neatly ties in with what is predictable from the relative stabilities of the $TiO_2$-RuP and $TiO_2$-CODH interactions that were deduced from the electrochemical experiments in Figure 75.

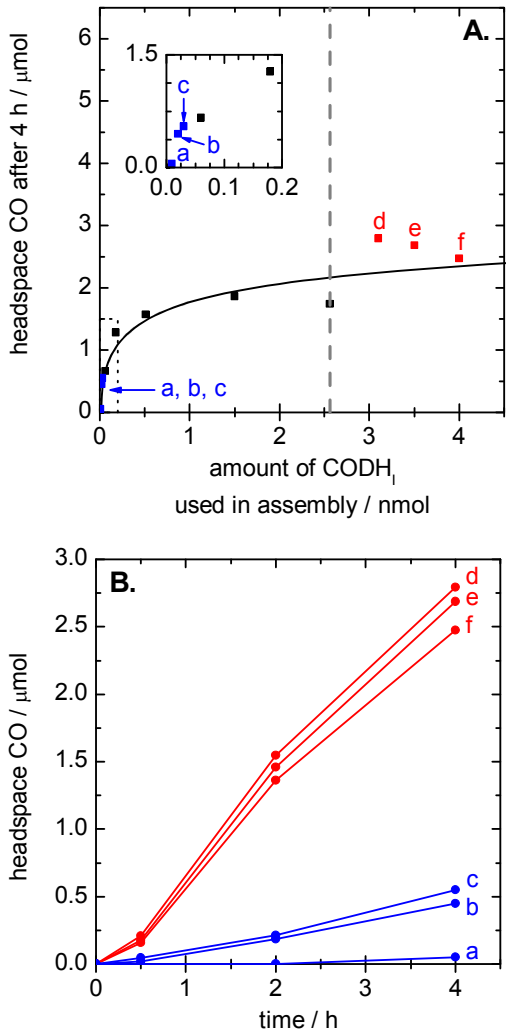


**Figure 76 Observation that [RuP-$TiO_2$-CODH] $CO_2$ photoreduction stability depends on the identity of the rate-limiting component.** (A) Effect of varied $CODH_I$ loading on CO production at [RuP-$TiO_2$-$CODH_I$] in the *low-[RuP]* regime (adapted from Figure 64A). Data points indicate the amounts of headspace CO accumulated after 4 h irradiation of [RuP-$TiO_2$-$CODH_I$] systems in which the amount of RuP used (5.6 nmol) was constant across all experiments, but in which the amount of $CODH_I$ was varied. The *standard procedure* for system preparation was followed in all cases, except for in the amounts of $CODH_I$ used in functionalisation of the nanoparticles. The dotted grey line indicates the amount of $CODH_I$ corresponding to *low-[RuP] standard conditions*. For all experiments, 5 mg P25 $TiO_2$ nanoparticles were used, the reaction vessels (initially under a gas atmosphere of 2% $CH_4$ in $CO_2$) were maintained at 20 ºC while irradiated with visible light ($\lambda > 420$ nm, 45 mW $cm^{-2}$), and the suspension buffer was 5 mL 0.20 M MES (pH 6.0). The blue data points correspond to systems that are clearly limited by low loadings of $CODH_I$; red data points indicate systems that are limited by insufficient RuP. (B) Plots of CO production by the identified blue ($CODH_I$-limited) and red (RuP-limited) systems in panel A. The letters in panel B correspond to the data points marked by the same letters in panel A.

## 5.4 CONCLUSIONS AND PERSPECTIVES

This chapter has investigated a range of factors that affect photocatalysis by the [RuP-$TiO_2$-CODH] assembly. The experiments in section 5.2.2 serve to highlight that for heterogeneous systems such as that described here, effects of light attenuation mean that full optimisation of solar fuel systems require consideration of 'engineering' factors in addition to orchestration of the chemistry. Unavoidable light scattering led to the finding that catalytic rates here do not scale directly with the density of catalytic units, and in fact follow a square root relationship with the particle concentration. This behaviour also draws attention to the issue of how to measure the activities of these catalytic systems. Using the light intensity and the illuminated facial area of the reaction vessel, it is possible to estimate a quantum yield of approximately 0.07% for the [RuP-$TiO_2$-$CODH_I$] *standard system* (Appendix A8). However, the experiments have not been designed to optimise quantum efficiency, but to focus on the reproducible effects of enzyme and RuP loading. Enzymologists will be most interested in rates assessed in terms of moles of CO produced per mole of enzyme; and here the system is found to operate far more slowly (0.15 – 0.22 $s^{-1}$) than the maximum rate that should be attainable (the solution assay in section 5.2.1, under identical conditions to those used in photocatalytic experiments and with appropriately weak driving force for $CO_2$ reduction, yielded a realistic maximum enzyme TOF of around 100 $s^{-1}$). One reason for the slow enzymatic rate is that the attachment of CODH to $TiO_2$ is not directed or controlled in any way, and it must therefore be assumed that the enzyme is bound in a range of orientations, the majority of which are electrochemically inactive. A straightforward approach to control the surface orientation, using a small molecule (OPEA) as a surface modifier, was unsuccessful; and a future approach may require the intricate engineering of a covalent

linkage between enzyme and nanoparticle. One method would be to apply site-directed mutagenesis to incorporate an unnatural amino acid[372] containing a phosphonic acid group into the protein backbone close to the D-cluster of the enzyme, leading to a strong attachment at a point close to where electrons must enter the enzyme.

On a positive note, rates of $TiO_2$ powder-based $CO_2$ reduction photocatalysts are typically measured in units of μmol CO produced (g catalyst) $h^{-1}$, and on this basis the systems described so far in this Thesis excel. By this measure, the best photocatalyst in this chapter (comprising 2.5 mg $TiO_2$ nanoparticles functionalised with 1.28 nmol $CODH_{II}$ and 28 nmol RuP) had a 4 h-averaged activity of 386 ± 18 μmol CO produced (g catalyst) $h^{-1}$ at 20 ºC (Table 13), which is around an order of magnitude faster than rates typically achieved by non-enzyme containing systems as summarised by a 2009 review article by Indrakanti *et al.*[129] (Figure 77).

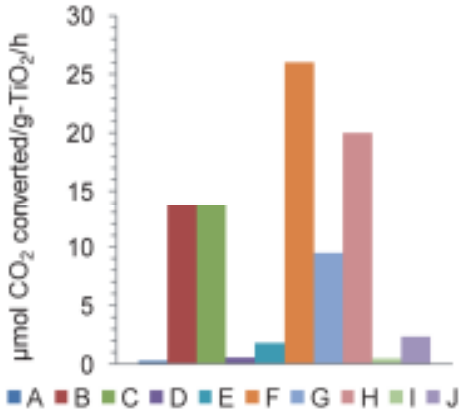


**Figure 77 The highest specific rates of $CO_2$ photoreduction in units of µmol $CO_2$ converted (g $TiO_2$)$^{-1}$ h$^{-1}$ obtained using various $TiO_2$-based catalysts in selected recent articles.** The values are presented here to illustrate typical rates of $CO_2$ photoreduction, and are dependent upon many variables such as metal doping, $CO_2$:$H_2O$ ratios, dispersion of Ti, coordination of Ti species, light intensity, type of lamp used etc. (A): Yamashita *et al.*,[373] (B): Anpo *et al.*,[374] (C): Yamashita *et al.*,[140] (D): Kaneco *et al.*,[363] (E): Kaneco *et al.*,[362] (F): Ikeue *et al.*,[375] (G): Ikeue *et al.*,[376] (H): Tseng *et al.*,[133] (I): Wu *et al.*,[377] (J): Nguyen *et al.*[378] Figure reproduced from Indrakanti *et al.*[129]

One exceptional report not include in Figure 77 claims a rate of 627 µmol (g catalyst) h$^{-1}$ for the reduction of $CO_2$ to methanol using P25 $TiO_2$ loaded onto mesoporous silica under UV light;[365] the same paper, however, reports (for comparison) an average rate at *bare* P25 $TiO_2$ of 140 µmol (g catalyst)$^{-1}$ h$^{-1}$, which is orders of magnitude faster than what has been reported elsewhere for the same catalyst. Also, a very recent report by Li *et al.*, using $TiO_2$ nanotubes modified with $Bi_2S_3$[379] and published after the Indrakanti review, has also slightly bettered the rates shown in Figure 77, producing methanol under visible light at a rate of 45 µmol (g catalyst)$^{-1}$ h$^{-1}$. Nevertheless, co-attachment of RuP and CODH to $TiO_2$ nanoparticles forms a highly effective photocatalyst that operates at near-neutral pH and at ambient temperatures.

The rate of CO production by the *standard system* (defined as 5 mg $TiO_2$ nanoparticles functionalised with 56 nmol RuP and 2.56 nmol CODH) is limited by the rate of photoinjection of electrons. Evidence for this is provided by the observations that: 1) photocatalytic rates increase according to the square root of particle concentration, as predicted by the effect of light attenuation (section 5.2.2); and 2) the system is affected by the identity and concentration of sacrificial electron donor (section 5.2.4.2). This *standard* configuration however, for which a calculation based on spectrophotometric data (Appendix A3) estimates a composition of around 5-10 CODH molecules and around 200 RuP photosensitisers per $TiO_2$ nanoparticle, is clearly very finely balanced because a moderate decrease in the CODH loading leads to a drastic decline in activity (section 5.2.3.1). Electrochemical studies of RuP and CODH attached to $TiO_2$ thin film electrodes support the general principle that photoinjection rates are considerably less stable than enzyme-catalysed $CO_2$ reduction rates. The reason for the instability of photoinjection from RuP remains unclear; no photobleaching over the course of 4 h, nor photosensitiser desorption, was observed. The use of a central nanoparticle as a scaffold for coupling an electron donor with a fuel producing catalyst offers a great advantage in terms of being able to balance activities (a parallel can be drawn here with the [$CODH_I$-PG-*Ec*Hyd2] water-gas shift reaction catalyst that was detailed in chapter 3). The alteration of photosensitiser and enzyme loadings delivered further insight in terms of the instability, because systems using very low loadings of CODH (resulting in an enzyme-limited configuration) were more stable (albeit less active overall) photocatalysts.

While not a technology, this sensitised hybrid enzyme-nanoparticle system (even before further refinements such as covalent attachment are made) serves as a benchmark for what

must be achievable using synthetic catalysts. In particular, the results provide a strong case for $CO_2$ activation catalysts to focus on a two-electron pathway that avoids the thermodynamically uphill step involved in one-electron activations.

# 6 ALTERNATIVE STRATEGIES FOR CODH-CATALYSED $CO_2$ PHOTOREDUCTION USING VISIBLE LIGHT

## ABSTRACT

The advantages of a $CO_2$ photoreduction system based on Degussa P25 $TiO_2$ are numerous: it is readily available, cheap, and easy to disperse in aqueous solutions. However, systems of alternative design, or based around different semiconductor materials, may offer advantages in terms of photocatalytic performance. Enhancements might be achieved through exploring alternative designs, including photogeneration cells and powder based systems with semiconductors that are themselves inherently sensitive to visible lights without the requirement for any kind of modification. Also, the driving force for $CO_2$ reduction can be raised by using materials with lower potential (higher energy) conduction bands. This chapter therefore presents new types of light-sensitive systems in which CODH is used as the CO-producing catalyst: firstly, a photogeneration cell using a dye-sensitised, mesoporous, $TiO_2$ photoanode and a CODH-modified cathode; secondly, powder-based systems using semiconducting metal oxides other than P25 $TiO_2$; and thirdly, constructs formed from the co-attachment of enzyme molecules with cadmium sulfide nanomaterials.

The main focus is on CdS, and the interest in this material stems from its narrow band gap (around 2.3 - 2.4 eV in the bulk form). CdS is therefore able to harvest most of the visible spectrum without the need for an additional photosensitiser moiety, since photons of wavelengths lower than 520 nm have sufficient energy to excite electrons from the valence band to the conduction band. Following this photoexcitation step, the conduction band electrons (which also have the advantage of being around 300 mV more reducing than those in the conduction band of anatase) migrate to CODH for the reduction of $CO_2$ to CO. Systems using three different morphologies of CdS nanomaterials are investigated: quantum

dots of around 6 nm in size, nanorods (~ 40 x 10 nm), and larger aggregates formed upon heat treatment (calcination) of the quantum dots. Rates of $CO_2$ photoreduction at [CdS-CODH] constructs are found to be superior to those achievable with metal oxide nanoparticles (improvements of up to an order of magnitude are measured), and performance is found to be highly influenced by the morphology of the CdS nanomaterial.

Some of the work in this chapter has been published:

Yatendra S. Chaudhary, Thomas W. Woolerton, Christopher S. Allen, Jamie H. Warner, , Elizabeth Pierce, Stephen W. Ragsdale and Fraser A. Armstrong, *Chem. Commun.*, **2012**, *48*, 58-60.

# 6.1 INTRODUCTION

## 6.1.1 PHOTOGENERATION CELLS

Photoelectrochemical cells for fuel formation (referred to from now on as *photogeneration cells*)[12,44,380] involve one or more light sensitive electrodes. In terms of the principle of operation there are parallels with *photovoltaic* cells, but in photogeneration cells the electrons are used not as electricity, but for fuel-forming reactions. Typically, an n-type semiconductor (such as $TiO_2$, and often modified with a photosensitiser) is used as a photoanode, with a metal (commonly Pt in the case of $H_2$-producing cells) as the cathode. Figure 78 shows the principle of operation of a photogeneration cell using an n-type photoanode. The concept of dye-sensitisation is exactly as in DSSCs:[13] electrons are injected into the conduction band from an adsorbed dye species (usually a ruthenium bipyridyl complex), with the illustrated band bending assisting charge separation. The electrons are conducted through the external circuit to a cathode, at which the fuel forming reaction (typically $H^+$ or $CO_2$ reduction) occurs.

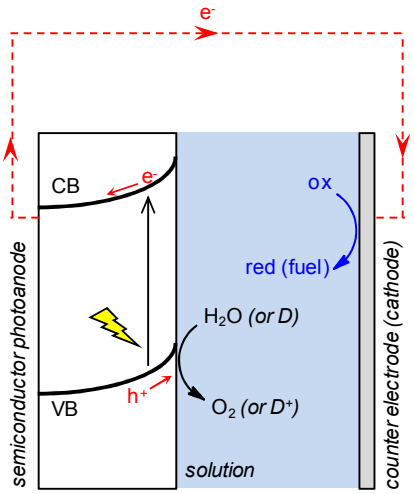


**Figure 78 Principle of operation of a photogeneration cell based on an n-type semiconductor, using band gap irradiation.** 'ox' represents a feedstock (protons or $CO_2$) that can be reduced at the counter electrode (cathode) to form a fuel ('red': $H_2$, or reduced carbon molecules). D represents a sacrificial electron donor.

In work that is relevant to enzyme-catalysed solar fuel formation, Hambourger and co-workers constructed a visible light-driven photogeneration cell for $H_2$ production that uses a porphyrin-sensitised thin film of nanoparticulate $TiO_2$ as a photoanode, and an [FeFe]-hydrogenase-modified carbon felt as the cathode, producing $H_2$ at a rate of 23.4 nmol $H_2$ $min^{-1}$.[381] Holes in the photoanode are filled by electrons liberated from the oxidation of a biofuel (*e.g.* methanol, ethanol or glucose); $H_2$ production here is therefore sustainable and does not rely on a non-renewable sacrificial electron donor. The ideal electron donor would, of course, be water. An alternative configuration is to have a photo*cathode* (typically a p-type material) at which photoexcited electrons drive the fuel-forming reduction reaction, and a metal as the anode. There are a handful of examples of systems that have used such an approach to reduce $CO_2$ to fuels. Early reports in 1978 and 1983 described the production of mixtures of formic acid, formaldehyde and methanol under

visible irradiation of p-type GaP electrodes,[382,383] but cathodic biases were also required in both of these cases. More recently, the discovery of pyridinium as a highly efficient electrocatalyst for $CO_2$ reduction[120,121] (section 1.5.2.4) was followed by the demonstration of a cell which again employed p-GaP as the photocathode to selectively form methanol.[123] This system required no external bias, and it therefore represents a major development as a result of the low overpotential requirement of the pyridinium catalyst, even if the chemistry of the catalytic mechanism is still not fully understood.[122] It is also possible to have a photogeneration cell in which both anode and cathode are light sensitive, and this is often the approach that is used in order to avoid the requirement for an applied bias, because light energy can now be harvested at both electrodes. A very recent example of this used a high surface area $TiO_2$ nanotube array in contact with silicon nanowires (a p-n junction cell) to form hydrocarbons, CO and $H_2$.[384]

### 6.1.2 USE OF ALTERNATIVE METAL OXIDE NANOPARTICLES

Up to this point, only $TiO_2$ has been investigated, but other semiconductors that differ in the key properties of conduction band potential and isoelectronic point are now considered. Selected properties of various metal oxides ($MO_x$), which shall be referred to later, are detailed in Table 16, and the conduction band positions relative to the $RuP^{III}/RuP^{II*}$ couple and the $CO_2/CO$ reduction potential are shown diagrammatically in Figure 79.

**Table 16** Selected properties of nanoparticles used in [RuP-$MO_x$-$CODH_I$] systems for $CO_2$ photoreduction

| $MO_x$ | supplier | $E_g$ / eV | $E_{CB}$ (pH 6) / eV | IEP | particle size[a] / nm | References |
|---|---|---|---|---|---|---|
| P25 $TiO_2$ | Degussa | 3.0, 3.2 | -0.32, -0.52 | 6.2 | 21 | 333, 332,349 |
| anatase $TiO_2$ | Sigma | 3.2 | -0.52 | 5.9 | < 25 | 333, [332,385] |
| ZnO | Sigma | 3.2 | ~ -0.6 | 8.8 | < 100 | [386, 387] |
| $SrTiO_3$ | Sigma | 3.4 | -0.75 | 8.6 | < 100 | [388, 387] |

$E_g$ = band gap energy; $E_{CB}$ = conduction band potential; IEP = isoelectronic point. [a] As stated by the supplier.

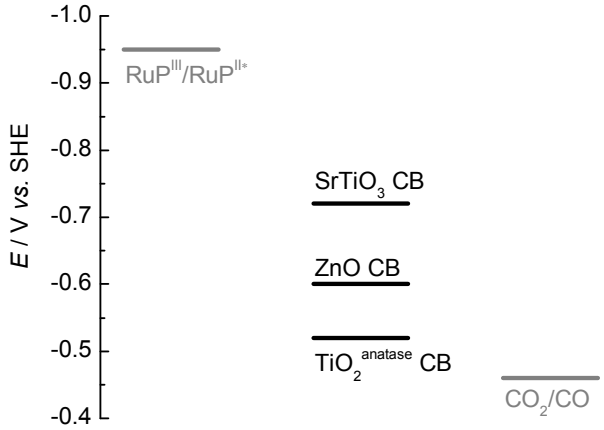


**Figure 79 Conduction band energies of various metal oxide semiconductors at pH 6, relative to reduction potentials of $RuP^{III}/RuP^{II*}$ and the $CO_2$/CO couple.** $E(CO_2/CO)$ is the standard reduction potential for the couple, corrected to pH 6 and 20 ºC.

Each of these metal oxides is a wide band gap semiconductor, and so sensitisation using RuP is required in each case in order for photocatalysis to be driven by visible light.

### 6.1.3 CADMIUM SULFIDE AS A NARROW BAND GAP SEMICONDUCTOR FOR VISIBLE LIGHT HARVESTING, CdS NANOMATERIALS, AND APPLICATIONS WITH BIOMOLECULES

Another alternative to the three-component [RuP-$TiO_2$-CODH] powder systems that were the focus of the previous two chapters is a solar fuel producer comprising only *two* components: a visible light harvesting unit directly attached to the enzyme. A $H_2$-producing device using photosystem I covalently wired to a hydrogenase has been reported,[360] and an analogous $CO_2$-reducing construct using CODH could be envisaged. Similarly, a ruthenium bipyridyl complex, if directly attached to the enzyme close to the D-cluster, could form a highly active photocatalyst. However, to pursue this route would be to forgo one of the advantages of using catalysts attached to *particles* – that rates of substrate turnover can be matched to rates of light harvesting by controlling the relative quantities of each component, and therefore efficiencies can be maximised. A third option for the chromophore, therefore, is a semiconductor in which electrons are excited from the valence band to the conduction band by light of visible wavelengths in direct, 'band gap' excitation. One such candidate is cadmium sulfide (CdS), which has a band gap of 2.4 eV[389] - corresponding to a wavelength of around 520 nm - and the latter part of this chapter investigates [CdS-$CODH_I$] constructs for visible light-driven $CO_2$ reduction.

Like $TiO_2$, CdS is an n-type semiconductor, and the ability of CdS to absorb visible light without the need for sensitisation has led to its application in solar cells in combination with p-CdTe.[390-393] There is major interest in the synthesis, characterisation and application of very small particles of CdS (and, indeed, of other materials), because once very small dimensions are reached many of the properties of the material - including electronic and

optical properties - undergo significant changes.[394,395] At sizes at which the chemical and physical behaviours change from those of the 'bulk' material to being 'molecular', the particles are referred to as quantum dots. The 'quantum confinement' effect of fewer orbital interactions leads to the electronic energy bands found in the bulk material becoming more discrete;[356] one effect is that a space-charge region can no longer be supported, and the band-bending that occurs for bulk materials at the semiconductor-electrolyte interface no longer exists. A second major upshot is that the smaller size of the particle means that the distances that photoinduced charges must travel are reduced compared to larger particles or clusters, and therefore the possibility of wasteful electron-hole recombinations occurring is minimised. A handful of previous reports have described the use of CdS quantum dots and nanoparticles in bioelectrochemical studies, suggesting at least a degree of biocompatibility. Applications have included use in biosensors,[396,397] and combination with graphite electrodes leading to the (not fully understood) enhancement of electrochemical signals from glucose oxidase[398] and haemoglobin.[399]

## 6.2 A WIRED CO PHOTOGENERATION CELL: AN ALTERNATIVE APPROACH FOR FURTHER DEVELOPMENT

Figure 80 shows the design of a CO photogeneration cell using RuP-photosensitised $TiO_2$ as a photoanode, and $CODH_I$ as the $CO_2$-reducing catalyst at the cathode (also $TiO_2$).

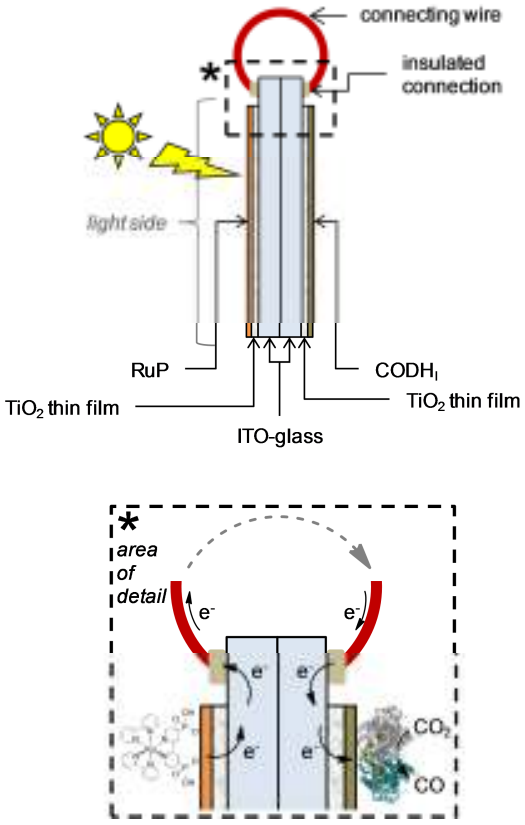


**Figure 80 A wired device for visible light-driven $CO_2$ photoreduction to CO.** Two thin films of $TiO_2$ on ITO-glass, one functionalised with RuP, the other with $CODH_I$, are wired together to form a CO photogeneration cell. Photoinjected electrons at the RuP-modified anode (orange) are conducted through the external wire to the $CODH_I$-modified cathode (brown), whereupon they are used for reduction of $CO_2$ to CO.

One $TiO_2$ film, functionalised with RuP, is joined 'back-to-back' to a second, $CODH_I$-modified film, with an electrical connection made by a wire. The operating principle is that photoinjected electrons flow through the wire to the $CODH_I$-modified $TiO_2$ thin film,

whereupon they are used for $CO_2$ reduction to CO. As in the particulate systems of the previous two chapters (and in the electrochemical experiments using RuP-$TiO_2$ electrodes), the reduced state of RuP is regenerated by electrons provided by MES acting as a sacrificial electron donor.

In general, 'wired' solar fuel devices are considered to be inferior to 'wireless' devices – they are less elegant, but more importantly they involve a greater number of components, leading to more opportunities for efficiency losses. The interest in creating a wired device in this instance, however, is two-fold. Firstly, the separation of sensitiser and enzyme – such that an increase in loading of RuP or CODH on $TiO_2$ is not at the expense of the other component – has the potential to simplify the system conceptually. Secondly, the dimensions of the pores in the thin films are of approximately the same magnitude as the dimensions of CODH,[††††] and as such the probability of a randomly-oriented enzyme molecule being in electronic contact with $TiO_2$ is expected to be greater than the probability of an enzyme molecule on a solid (non-porous) surface being electronically connected.

The $TiO_2$ thin films used in the Figure 80 device, prepared by calcining a dispersion of nanoparticles onto ITO-coated glass slides, are identical to those described in section 2.1.2.4.2. Two of the $TiO_2$-ITO-glass slides, each of dimensions 25 x 10 mm, were glued 'back-to-back' with an insulated copper wire electrically connecting the two ITO surfaces (the contacts were made to areas of ITO that were intentionally left uncoated with $TiO_2$, as illustrated). One of the $TiO_2$ thin films was modified by adsorption of RuP according to the method described in section 2.1.2.4.3. Collection of UV-vis spectra of the RuP solution

[††††] Observable from the SEM images in Figure 43; and expected from the dimensions of the P25 $TiO_2$ nanoparticles (~ 20 nm) from which the thin films are prepared and CODH dimensions (88 Å x 60 Å x 63 Å).

before and after incubation with the $TiO_2$ film indicates that around 50 nmol RuP was attached to the $TiO_2$ film (Appendix A9). The second film was modified with 2.56 nmol $CODH_I$ (the same amount of enzyme used in the powder-based [RuP-$TiO_2$-$CODH_I$] *standard system*) according to the method described in section 2.1.2.4.3. The cell was suspended in 5 mL 0.20 M MES (pH 6) in a sealed reaction vessel and flushed with 2% $CH_4$ in $CO_2$ before irradiating with visible light ($\lambda > 420$ nm, 45 mW $cm^{-2}$) for 6 h.

Figure 81 shows an initial experiment using this CO photogeneration cell. Around 3 μmol CO is produced over 6 h; based on the 2.56 nmol $CODH_I$ that was spotted onto the cathode this corresponds to a TOF of 0.05 mol CO (mol $CODH_I)^{-1}$ $s^{-1}$.

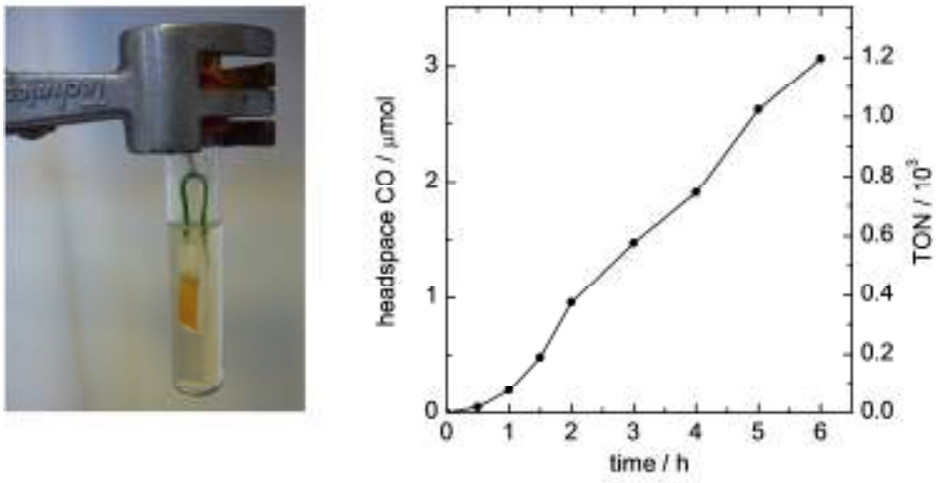


**Figure 81 $CO_2$ photoreduction at the prototype CO photogeneration cell.** The device is suspended in a sealed reaction vessel, as photographed, in order to allow the solution to be stirred. The amounts of system components were: 2.56 nmol $CODH_I$, ~50 nmol RuP, 5 mL 0.20 M MES (pH 6.0); and the reaction vessel was maintained at 20 ºC while illuminated with visible light ($\lambda > 420$ nm, 45 mW $cm^{-2}$).

This result is purely a proof-of-concept operation of a CO photogeneration cell using a photoanode wired to a CODH-functionalised cathode. Although not pursued here, there is

undoubtedly scope for its development. In particular, the depths of the $TiO_2$ thin films is a key area of focus: thicker networks will allow higher loadings of RuP and CODH, but electronic contact must be maintained throughout the film and modification techniques must allow enzyme molecules to permeate throughout the films.

## 6.3 USE OF ALTERNATIVE METAL OXIDE NANOMATERIALS

### 6.3.1 ATTACHMENT OF RuP AND $CODH_I$ TO $MO_X$ NANOPARTICLES

Table 17 shows the extents of adsorption of RuP and $CODH_I$ to aqueous suspensions (0.20 M MES, pH 6.0) of the various semiconductor nanoparticles that were detailed in section 6.1.2. The attachment methods are identical to those that were detailed in sections 4.2.4 (RuP) and 4.2.1 ($CODH_I$) and the extent of uptake of each component was calculated by UV-vis spectrophotometry using the method outlined in section 2.3.2 (Appendix A10).

**Table 17** Spectrophotometrically-determined uptake of RuP and $CODH_I$ to various semiconductor nanoparticle suspensions[a]

| | RuP adsorbed[b] / nmol | $CODH_I$ adsorbed[c] / nmol |
|---|---|---|
| P25 $TiO_2$ | 54.9 ± 1.13 | 2.40 ± 0.03 |
| anatase $TiO_2$ | 54.1 ± 1.77 | 2.13 ± 0.15 |
| ZnO | 35.7 ± 0.43 | 1.99 ± 0.37 |
| $SrTiO_3$ | 48.2 ± 6.87 | 2.49 ± 0.02 |

[a] Suspension concentrations were 5 mg nanoparticles / 5 mL 0.20 M MES buffer solution (pH 6.0), except for ZnO (20 mg nanoparticles / 5 mL buffer solution). [b] Out of a maximum of 56 nmol added. [c] Out of a maximum of 2.56 nmol added. Adsorption amounts were calculated using UV-vis absorption data from separate solutions of $CODH_I$ (0.51 μM) and RuP (11.2 μM) before and after exposure to nanoparticles (see Appendix A10). The concentration of nanoparticles matches those used in the $CO_2$ photoreduction experiments shown in Figure 82. The amount of RuP or $CODH_I$ adsorbed on nanoparticles was calculated from the relative intensities of the peaks at 455 nm (RuP) or 280 nm ($CODH_I$), before and after stirring with nanoparticles for 20 min.

It was previously established that P25 $TiO_2$ adsorbs both RuP (section 4.2.4) and $CODH_I$ (section 4.2.1) extensively. The slightly lower uptake of $CODH_I$ to anatase $TiO_2$ compared to P25 $TiO_2$ may be explainable by referring to the isoelectronic point (IEP) values provided in Table 16 (P25 $TiO_2$ IEP = 6.2;[349] anatase IEP = 5.9).[385] The adsorption studies were carried out at pH 6, and therefore the overall net charge on P25 $TiO_2$ will be slightly positive, and on anatase $TiO_2$ it will be slightly negative. $CODH_I$ has an IEP of 5.5,[185] so will be net negative, and as such it is reasonable to expect stronger (electrostatic) attachment to P25 $TiO_2$. $SrTiO_3$ shows almost complete adsorption of the total amount of $CODH_I$ added, and the IEP of $SrTiO_3$ (8.6)[387] may again be used to explain this: a strong net positive surface charge on the nanoparticle interacts favourably with the slightly negative charge on the enzyme molecule. ZnO shows reasonable uptake of $CODH_I$, and while the IEP of ZnO is also high, the lower uptake compared to $SrTiO_3$ may be accounted for by the slight solubility of ZnO under the conditions of the study.[‡‡‡‡] The same reason applies to the slightly lower attachment of RuP to ZnO, while attachment of RuP to the other materials is almost quantitative.

### 6.3.2 $CO_2$ PHOTOREDUCTION AT [RuP-$MO_X$-$CODH_I$] SUSPENSIONS

Following functionalisation of the nanoparticles to form [RuP-$MO_x$-$CODH_I$] systems ($MO_x$ = P25 $TiO_2$, anatase $TiO_2$, ZnO, $SrTiO_3$) $CO_2$ photoreduction experiments were carried out. Figure 82 shows the amount of CO produced by each system under visible light over 4 h (panel A) and the corresponding numbers of turnovers (panel B). The TONs are based on the amounts of $CODH_I$ attached to the nanoparticles, as indicated in Table 17.

[‡‡‡‡] ZnO was found to be partially soluble in a pH 6 solution of 0.20 M MES, and so the concentration of nanoparticles used in this case was 4 mg $mL^{-1}$ (other semiconductor nanoparticles were used at 1 mg $mL^{-1}$).

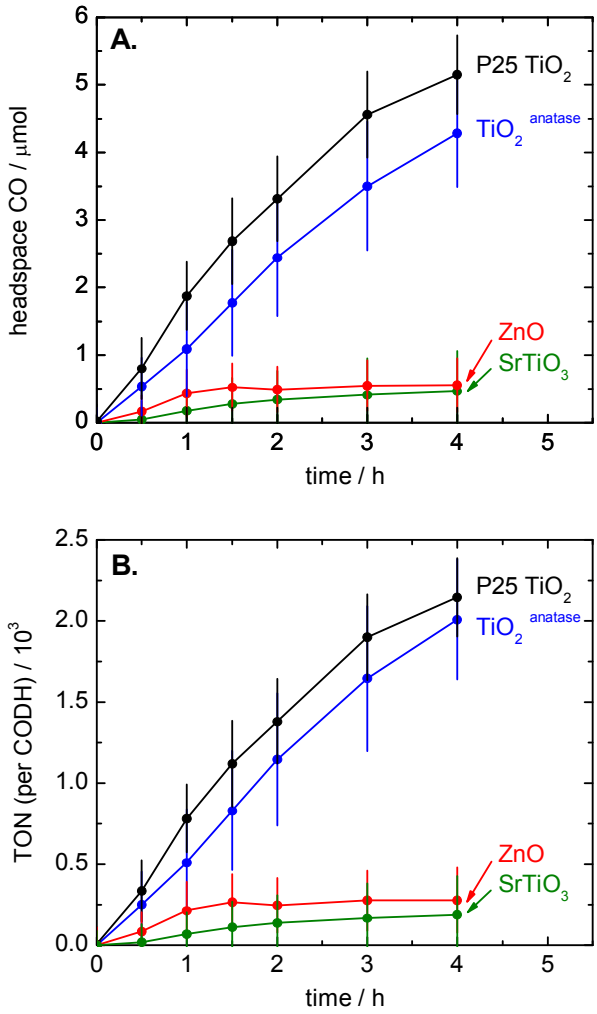


**Figure 82 $CO_2$ photoreduction at various [RuP-$MO_x$-$CODH_I$] systems.** The TONs in panel B are based on the amounts of $CODH_I$ attached to the nanoparticles, as indicated in Table 17. The amounts of components used are: 5 mg $MO_x$ nanoparticles (except for ZnO, 20 mg), 5 mL 0.20 M MES (pH 6.0). Amounts of $CODH_I$ and RuP are as indicated in Table 17. The *standard procedure* was followed for preparation of all systems, except for in the identity of nanoparticles. The reaction vessels (initially under a gas atmosphere of 2% $CH_4$ in $CO_2$) were maintained at 20 ºC while irradiated with visible light ($\lambda > 420$ nm, 45 mW $cm^{-2}$).

The activity using pure anatase nanoparticles (average diameter < 25 nm) is close to that of the P25 $TiO_2$ system (especially when assessed in terms of total turnovers per attached CODH, panel B), and this is expected because P25 $TiO_2$ is mainly anatase. The interest in

ZnO stems from its IEP of 8.8, which is markedly different to that of P25 $TiO_2$ (6.2). The upshot is that at pH 6.0 ZnO will have a net positive charge, compared to the roughly net neutral charge on $TiO_2$, and the orientation of enzyme attachment may therefore be expected to be altered. In the [RuP-ZnO-$CODH_I$] system, only around 0.5 μmol CO was produced after 4 h: 10% of the activity of the P25 $TiO_2$ system. Also, CO production appears to stop after 1 h – possibly attributable to surface layers of ZnO dissolving over time (ZnO nanoparticles were found to be slightly soluble in 0.20 M pH 6 MES, as mentioned earlier). Some of the difference in activity may also be due to poorer binding of RuP to ZnO: only around 60% of the 56 nmol dye (35.7 nmol) is bound after the 20 min modification period, compared to almost complete attachment to P25 $TiO_2$ (Table 17).

$SrTiO_3$ is an attractive candidate because its conduction band lies around 0.2 V more negative than that of anatase.[388] However, the rate of CO production is poor, with around 0.5 μmol CO accumulated after 4 h. This cannot be due to poor adsorption of RuP or $CODH_I$, since uptake of each component is almost complete (Table 17). One possible explanation is that the potential difference between the conduction band and the excited state of the dye is too small to drive rapid electron injection into the semiconductor (Figure 80). Another factor could be the larger size of the $SrTiO_3$ particles (up to 100 nm) compared to the 20 nm $TiO_2$ particles: the requirement for longer electron migration distances increases the opportunities for recombinations and wasteful trapping processes.

## 6.4 $CO_2$ PHOTOREDUCTION SYSTEMS BASED ON CdS NANOMATERIALS

Figure 39 shows the principle of visible light-driven $CO_2$ reduction by [CdS-CODH]. Now, instead of electrons being injected into the semiconductor conduction band from the excited state of a bound dye complex, direct band gap excitation ($E_g$ = 2.3 - 2.4 eV in bulk CdS) promotes electrons from the valence band, and these electrons can then migrate to the enzyme for $CO_2$ reduction. The resulting holes in the valence band are filled by donation of electrons from a sacrificial electron donor (D), and in this way the system is similar to [RuP-$MO_x$-CODH] systems. Not only does a CdS-based system allow direct band gap excitation to be used, the potential of the conduction band (in *bulk* CdS) at pH 6 is around -0.87 V (Figure 83B). CdS conduction band electrons are therefore around 0.3 V more reducing than anatase $TiO_2$ electrons, and for this reason switching to CdS offers an advantage in terms of thermodynamic driving force for CO production. In addition to this, for the reasons outlined in section 6.1.3, the possibility of coupling readily synthesisable CdS nanomaterials ('quantum dots', measuring just a few nm across) with enzyme molecules of a similar size is intriguing.

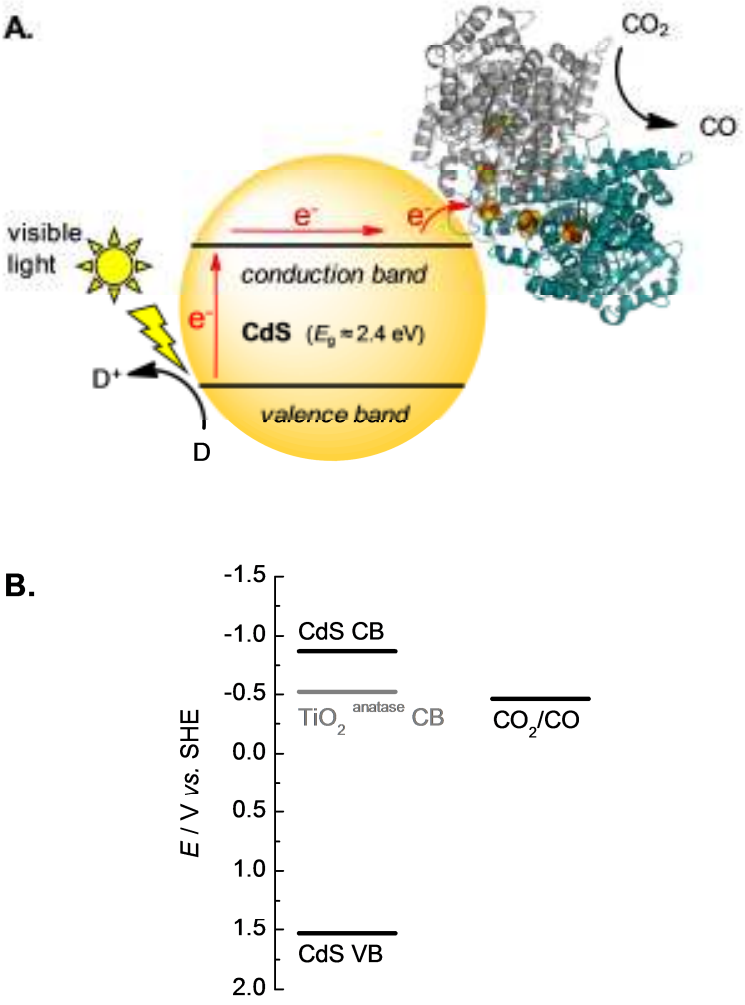


**Figure 83 Design of a [CdS-CODH] construct for $CO_2$ photoreduction to CO.** (A) Cartoon representation of $CO_2$ reduction at a CdS nanoparticle functionalised with a carbon monoxide dehydrogenase enzyme ($CODH_{II}$, PDB code 1SU7, is shown here). Photons of sufficient energy are absorbed by the CdS nanoparticle, inducing promotion of electrons from valence band to conduction band. This cartoon illustration is not to scale, and is not intended to imply any stoichiometry. (B) The reduction potentials involved in overall photoreduction of $CO_2$ in this system, at pH 6. The CdS conduction band is of sufficiently low potential to inject electrons into the enzyme for $CO_2$ reduction to CO. The conduction band potential of anatase $TiO_2$ is also shown in grey, in order to highlight the additional driving force for $CO_2$ reduction available from CdS. $E(CO_2/CO)$ is the standard reduction potential for the couple, corrected to pH 6 and 20 ºC.

### 6.4.1 CdS NANOMATERIALS FOR $CODH_I$-CATALYSED $CO_2$ PHOTOREDUCTION

CdS nanocrystals of two different morphologies were prepared and supplied by Dr Yatendra Chaudhary. Quantum dots ('$CdS_{QD}$'), which were roughly spherical in shape and yellow in colour, were synthesised according to a previously published procedure.[264] Briefly, a mixture of cadmium acetate, dodecylamine and sulfur powder was heated in a Teflon-lined pressure vessel at 220 ºC for 10 h. The resulting material was then collected by centrifugation, washed thoroughly with ethanol and carbon disulfide, and allowed to dry at room temperature under ambient conditions. The X-ray diffraction pattern (Appendix A11) has broad peaks that suggest the formation of ultra-small particles, and indexing of the peaks [(111), (220), (311)] indicates the formation of cubic phase. TEM (Figure 84, top) established that the particles are mainly spherical in shape, with dimensions 5.8 ± 1.8 nm.

In addition, CdS nanorods ('$CdS_{NR}$') were prepared according to a separate reported procedure,[265] and the TEM image of this sample (Figure 84, bottom) reveals average dimensions of 42 ± 10 nm (length) and 10 ± 1 nm (width). A third material was prepared by subjecting the $CdS_{QD}$ sample to calcination by heating at 450 ºC for 45 min (the sample was heated from room temperature at 5 ºC $min^{-1}$). Upon this treatment, the quantum dots converted into larger clusters ('$CdS_{calc.}$') of irregular shape (Figure 84, middle).

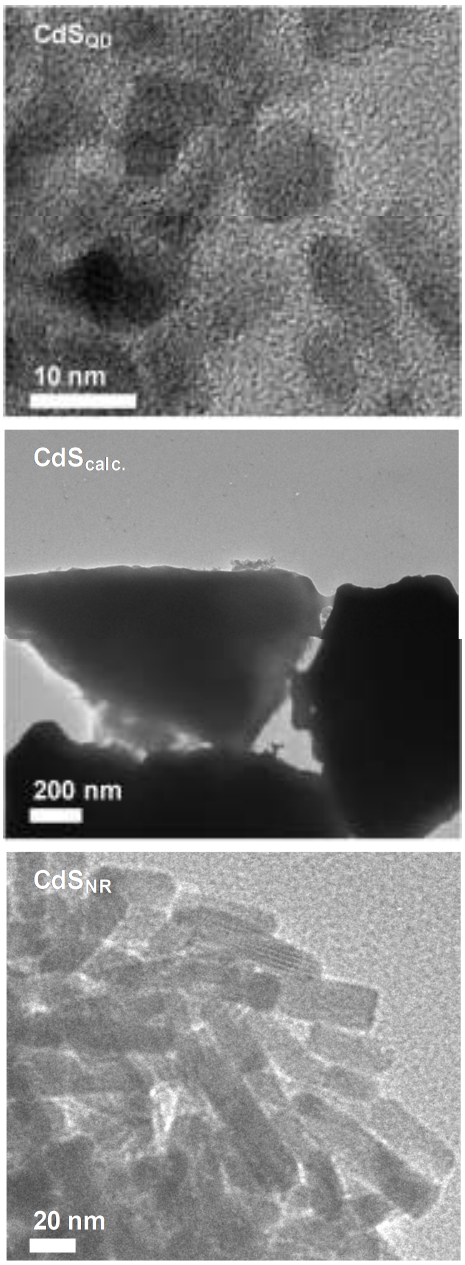


**Figure 84 TEM images of $CdS_{QD}$, $CdS_{calc.}$ and $CdS_{NR}$.** Synthetic procedures are provided in references [264] ($CdS_{QD}$) and [265] ($CdS_{NR}$). $CdS_{calc.}$ was prepared by heating $CdS_{QD}$ at 450 ºC for 45 min.

UV-vis spectroscopy carried out on the $CdS_{QD}$ sample (Figure 85) indicates absorption of wavelengths lower than 545 nm, corresponding to a band gap of around 2.3 eV.

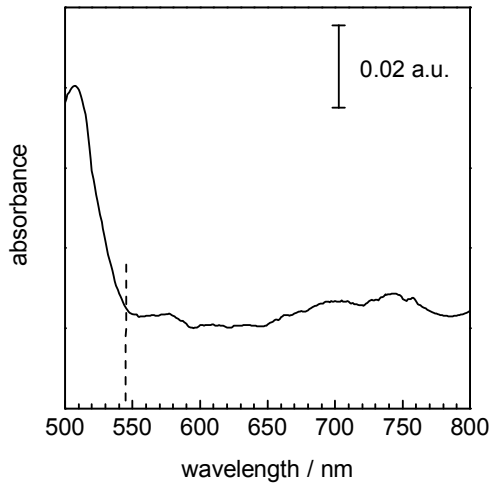


**Figure 85** UV-vis absorbance spectrum for $CdS_{QD}$, collected using a very dilute (< 0.05 mg $mL^{-1}$) aqueous suspension.

### 6.4.2 CO-ATTACHMENT OF CdS NANOMATERIALS WITH $CODH_I$

Previously, discussions around preparation of $CO_2$ photoreduction devices have involved references to the attachment of enzyme molecules *to* nanoparticles (as opposed to the decoration of enzyme molecules with nanoparticles). This is appropriate, since the dimensions of the enzyme molecules (8.8 x 6.3 x 6.0 nm, for $CODH_{II}$)[191] are smaller than the nanoparticles that were used (diameters between 20 – 100 nm). In the case of CdS quantum dots and nanorods, however, the dimensions of the two components are more closely matched, and for this reason it is more sensible for the terminology here to be *co-attachment of CODH with CdS nanomaterials*. In the case of the material produced upon heat treatment of CdS quantum dots ($CdS_{calc.}$), the particles are once again considerably larger than the enzyme molecules, but to avoid confusion the word 'co-attachment' shall be used throughout.

Table 18 indicates the amounts of $CODH_I$ co-attached with CdS nanomaterials ($CdS_{QD}$, $CdS_{NR}$ or $CdS_{calc.}$). Co-attachment was achieved by sonication of the nanomaterial in 5 mL 0.35 M MES solution (pH 6.0) at room temperature for 20 min to form a dispersion, followed by adding $CODH_I$ (2.56 nmol) to the suspension and stirring gently for 20 min. This method of functionalisation of CdS with enzyme is referred to as the *standard procedure*. To determine the amount of enzyme co-attached with CdS, the same spectrophotometric technique applied in section 4.2.1 was used.

**Table 18** Spectrophotometrically-determined uptake of $CODH_I$ to $CdS_{QD}$ or $CdS_{NR}$ suspensions[a]

| | $CODH_I$ adsorbed[b] / nmol |
|---|---|
| $CdS_{QD}$ (10 mg in 5 mL) | 0.59 ± 0.32 |
| $CdS_{QD}$ (20 mg in 5 mL) | 0.95 ± 0.10 |
| $CdS_{calc.}$ (10 mg in 5 mL) | 0.23 ± 0.11 |
| $CdS_{NR}$ (10 mg in 5 mL) | < 0.1 |

[a] Suspensions were prepared in 0.35 M MES buffer solution (pH 6.0)). [b] Out of a maximum of 2.56 nmol (5 mL suspension)$^{-1}$ added. Adsorption amounts were calculated using UV-vis absorption data from solutions of $CODH_I$ (0.51 μM) before and after exposure to nanomaterial. The concentration of nanoparticles matches those used in the $CO_2$ photoreduction experiments shown in Figure 86, Figure 87 and Figure 88 (see later). The amount of $CODH_I$ co-attached with nanomaterial was calculated from the relative intensities of the peaks at 280 nm before and after stirring for 20 min.

Since 2.56 nmol $CODH_I$ is added to each of the suspensions in Table 18, the data indicate relatively poor co-attachment of enzyme to the nanomaterials, especially compared to attachment of the same enzyme to $TiO_2$, in which adsorption of 2.56 nmol enzyme to 5 mg nanoparticles is almost complete (section 4.2.1). Comparing the first and second rows of Table 18, it is apparent that 10 mg $CdS_{QD}$ is insufficient for complete co-attachment with 2.56 nmol enzyme. Doubling the amount of $CdS_{QD}$ roughly doubles the amount of co-attached $CODH_I$, which suggests that the quantum dots are surrounding ('decorating') the

enzyme molecules. Co-attachment of $CODH_I$ with $CdS_{calc.}$ is less extensive than with $CdS_{QD}$. The $CdS_{calc.}$ is formed from $CdS_{QD}$ by simple heat treatment and retains the same phase (*i.e.* cubic), and the obvious contributing factor affecting the adsorption here is the large increase in size on calcination (as indicated in Figure 84) and the associated lower surface area of 10 mg $CdS_{calc.}$ particles compared to 10 mg $CdS_{QD}$ particles.

Co-attachment of enzyme with $CdS_{NR}$ is very poor. However, since the nanorods are synthesised through a completely separate chemical route, the surface groups can be expected to differ from those at $CdS_{QD}$, and it is therefore to be assumed that interactions with the protein surface are different (or, at least, the concentration of surface groups on the particles will not be the same).

It should be noted that due to the synthetic procedures through which the CdS nanomaterials were prepared (dodecylamine was used as a stabilising agent), amine functionalities are present on the surfaces of the nanoparticles.[264,265] The presence of such groups is expected to play a significant role in the attachment of enzyme molecules at the CdS surface, and indeed, a study of the effects of various capping agents on the attachment of enzyme molecules would be an interesting approach in further development of the systems described here.

### 6.4.3 $CO_2$ PHOTOREDUCTION BY [$CdS_{QD}$-$CODH_I$]

To assess the ability of [$CdS_{QD}$-$CODH_I$] to reduce $CO_2$ to CO under visible light irradiation, 5 mL suspensions of the functionalised quantum dots were sealed in reaction vessels, and the headspaces purged with 2% $CH_4$ in $CO_2$ for 20 min. Then, the samples were subjected to visible light irradiation while the suspension was gently stirred. As before for photocatalytic

experiments, reaction vessels were secured in a thermostated water bath in order to control the temperature, and regular analysis of the headspace by gas chromatography was used to follow the reaction.

Figure 86 shows $CO_2$ photoreduction by [$CdS_{QD}$-$CODH_I$] suspensions (5 mL) under visible light ($\lambda > 420$ nm, 45 mW $cm^{-2}$) for 5 h, using either 10 mg $CdS_{QD}$ (*i.e.* 2 mg $mL^{-1}$) or 20 mg $CdS_{QD}$ (*i.e.* 4 mg $mL^{-1}$). Control experiments, in which either $CdS_{QD}$, $CODH_I$, or light was excluded yielded no CO production after 5 h. In each of the systems in Figure 86, the amount of $CODH_I$ used in preparation of the system was the same (2.56 nmol), and the amounts of enzyme actually taken up were given in Table 18 (0.59 ± 0.32 nmol to 10 mg $CdS_{QD}$, 0.95 ± 0.10 nmol to $CdS_{QD}$). Note that *two* TON scales (right-hand axis) are required in Figure 86, due to the different amounts of $CODH_I$ co-attached with 10 mg or 20 mg $CdS_{QD}$. The left-hand axis (absolute amount of CO in the reaction vessel headspace) is common to both plots.

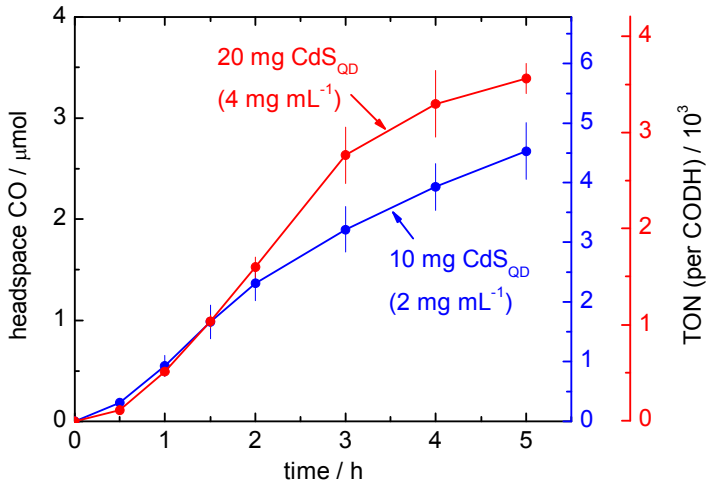


**Figure 86 $CO_2$ photoreduction at [$CdS_{QD}$-$CODH_I$] systems in which 2.56 nmol $CODH_I$ is co-attached with either 10 or 20 mg $CdS_{QD}$.** The electron donor system in each case is 5 mL 0.35 M MES and the *standard procedure* was followed for preparation (except in the mass of $CdS_{QD}$ used). The reaction vessels (initially under a gas atmosphere of 2% $CH_4$ in $CO_2$) were maintained at 20 ºC while irradiated with visible light

($\lambda > 420$ nm, 45 mW $cm^{-2}$). Note that the left-hand axis is common to both data sets; and the right-hand axes are colour coded to match the plots to which they refer.

Up until 2 h there is very little difference in the activities of the systems, although the reason for this is unclear. After 5 h irradiation, however, the system using 20 mg $CdS_{QD}$ has produced more CO than the 10 mg system. At this time, the amount of headspace CO in the 20 mg system at 5 h (3.39 μmol) is 1.3 times greater than the amount produced by the 10 mg system (2.67 μmol), and this increase is close to what would be predicted upon doubling the concentration of a heterogeneous photocatalyst (this is for reasons of light attenuation; see section 5.2.2: doubling the concentration is expected to increase activity by a factor of $2^{1/2}$, ≈ 1.41). The slight discrepancy here with the expected increase is accounted for by the spectrophotometry results in Table 18, which indicate that the amount of $CODH_I$ co-attached with 20 mg $CdS_{QD}$ (0.95 nmol) is not quite twice the amount co-attached with 10 mg $CdS_{QD}$. Table 19 gives rates achieved by these [$CdS_{QD}$-$CODH_I$] systems, based on the amounts of CO in the reaction vessel headspaces after 5 h.

**Table 19** Total CO production and turnover frequencies for [$CdS_{QD}$-$CODH_I$] systems using either 10 or 20 mg $CdS_{QD}$. The systems were run at 20 ºC, irradiated with visible light ($\lambda > 420$ nm, 45 mW $cm^{-2}$).

| | *(i.)* CO produced after 5 h / μmol | *(ii.)* TOF[a] [(mol CO) (mol $CODH_I$)$^{-1}$ $s^{-1}$] | *(iii.)* TOF[a] [(μmol CO) (g $CdS_{QD}$)$^{-1}$ $h^{-1}$] | *(iv.)* TOF[a] [(μmol CO) $mL^{-1}$ $h^{-1}$] |
|---|---|---|---|---|
| [$CdS_{QD}$-$CODH_I$] (10 mg $CdS_{QD}$) | 2.67 ± 0.28 | 0.25 ± 0.03 | 53.4 ± 5.6 | 0.11 ± 0.01 |
| [$CdS_{QD}$-$CODH_I$] (20 mg $CdS_{QD}$) | 3.39 ± 0.15 | 0.20 ± 0.01 | 33.9 ± 1.5 | 0.14 ± 0.01 |

[a] Turnover frequencies are based on the total amount of CO in the reaction vessel headspace after 5 h (and therefore represent average rates over this time), and are calculated using the amounts of co-attached $CODH_I$ as indicated in Table 18.

Figure 87 shows CO production by [$CdS_{QD}$-$CODH_I$] systems (each using 10 mg $CdS_{QD}$ in 5 mL buffer solution), in which the electron donor system is varied from 0.35 M MES (plot

a), to 0.35 M MES with additional components of 0.20 M EDTA (b), 0.20 M TEOA (c), or 0.20 M sodium ascorbate (d). The presence of EDTA has an insignificant effect on activity, and other components have detrimental effects: TEOA lowered activity by around 80%, and ascorbate suppresses all detectable activity. Although comparisons between [RuP-$TiO_2$-$CODH_I$] and [$CdS_{QD}$-$CODH_I$] must be made with caution (the mechanisms of electron supply are completely different), it is interesting to note the contrast of the lack of influence of EDTA here with the significant (rate enhancing) effect it had in the dye-sensitised $TiO_2$ system (section 5.2.4.2). The implication of these results, when combined with the outcome of the experiments in Figure 86, is that the rate of CO production at the $CdS_{QD}$ system is not limited by electron donation into valence band holes, but rather is limited by the amount of co-attached enzyme.

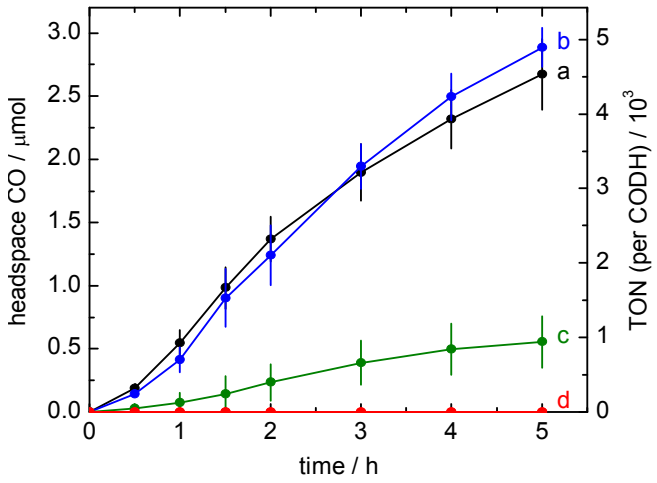


**Figure 87 $CO_2$ photoreduction at [$CdS_{QD}$-$CODH_I$] systems in which the electron donor system is varied.** The amounts of components used are: 10 mg $CdS_{QD}$ particles, 2.56 nmol $CODH_I$. The electron donor systems are 5 mL 0.35 M MES (a), or 0.35 M MES with additional components of 0.20 M EDTA (b), 0.20 M TEOA (c), or 0.20 M sodium ascorbate (d). All suspensions were pH 6.0. The *standard procedure* was followed for preparation of all systems. The reaction vessels (initially under a gas atmosphere of 2% $CH_4$ in $CO_2$) were maintained at 20 ºC while irradiated with visible light ($\lambda > 420$ nm, 45 mW $cm^{-2}$).

High affinities of $–NH_2$ and –COOH groups for CdS are well established.[264,400] TEOA and ascorbate are therefore expected to displace $CODH_I$ from the quantum dot surface (either partially or entirely), thereby suppressing CO production activity. Average rates of these systems (calculated from headspace CO after 5 h) are given in Table 20.

**Table 20** Total CO production and turnover frequencies for [$CdS_{QD}$-$CODH_I$] systems prepared using 10 mg $CdS_{QD}$, with different electron donor systems (pH 6.0). The systems were run at 20 ºC, irradiated with visible light ($\lambda > 420$ nm, 45 mW $cm^{-2}$).

| | *(i.)* CO produced after 5 h / μmol | *(ii.)* TOF[a] [(mol CO) (mol $CODH_I$)$^{-1}$ $s^{-1}$] | *(iii.)* TOF[a] [(μmol CO) (g $CdS_{QD}$)$^{-1}$ $h^{-1}$] | *(iv.)* TOF[a] [(μmol CO) $mL^{-1}$ $h^{-1}$] |
|---|---|---|---|---|
| 0.35 M MES *(Figure 87, plot a)* | 2.67 ± 0.28 | 0.25 ± 0.03 | 53.4 ± 5.6 | 0.11 ± 0.01 |
| 0.35 M MES + 0.20 M EDTA *(b)* | 2.89 ± 0.16 | 0.27 ± 0.02 | 57.8 ± 3.2 | 0.12 ± 0.01 |
| 0.35 M MES + 0.20 M TEOA *(c)* | 0.56 ± 0.21 | 0.05 ± 0.02 | 11.2 ± 4.2 | 0.02 ± 0.01 |
| 0.35 M MES + 0.20 M sodium ascorbate *(d)* | *none detected* | - | - | - |

[a] Turnover frequencies are based on the total amount of CO in the reaction vessel headspace after 5 h (and therefore represent average rates over this time), and are calculated using the amounts of co-attached $CODH_I$ as indicated in Table 18.

Figure 88 compares the photocatalytic performance of [$CdS_{QD}$-$CODH_I$] to [$CdS_{calc.}$-$CODH_I$] and [$CdS_{NR}$-$CODH_I$]. All systems were prepared by stirring 2.56 nmol $CODH_I$ with 10 mg CdS particles for 20 min to allow co-attachment, and the amounts of enzyme taken up by this method were given earlier in Table 18 (0.59 nmol to $CdS_{QD}$, 0.23 nmol to $CdS_{calc.}$, < 0.1 nmol to $CdS_{NR}$). Panel A of Figure 88 shows the increase in headspace CO over time, and panel B shows TONs calculated from the amounts of attached $CODH_I$. As shown by the red data points, no detectable amounts of CO were produced in experiments using $CdS_{calc.}$, despite the fact that enzyme was attached to the particles (albeit less than half the amount co-attached with $CdS_{QD}$). The XRD pattern (Appendix A11) shows no change in phase from $CdS_{QD}$ (it remains cubic after heat treatment). The lack of detectable activity must therefore relate to particle size, and more specifically (and most likely) the large number of grain

boundaries that can be expected to be present in large particles formed from the coalescence of smaller quantum dots. Grain boundaries act as recombination sites for photo-generated electrons and holes.

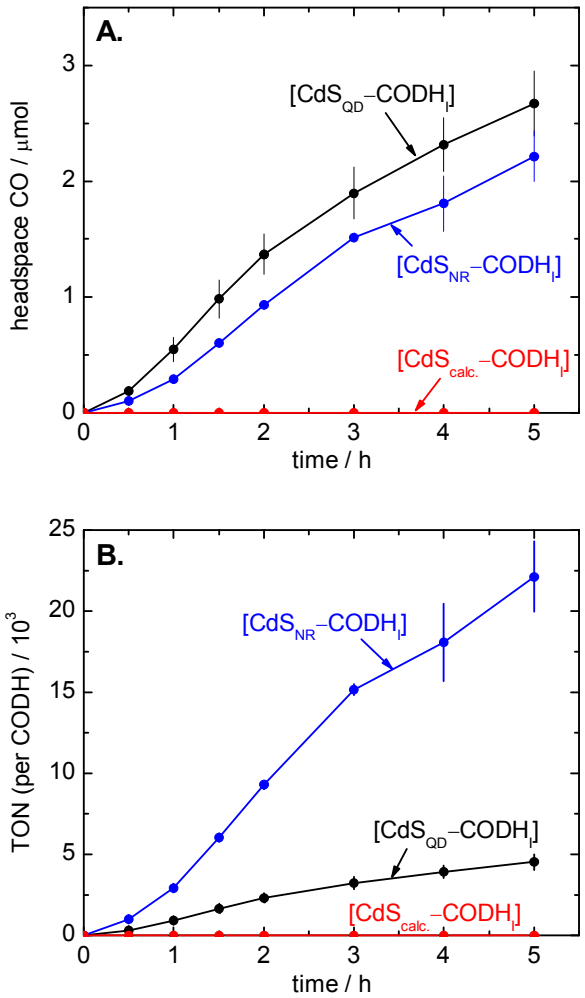


**Figure 88 $CO_2$ photoreduction at various [CdS-CODH$_I$] systems in which the CdS morphology is varied.** (A) The amounts of CO in the reaction vessel headspaces; and (B) TONs calculated from the amounts of CODH$_I$ co-attached with CdS$_{QD}$, CdS$_{calc.}$ or CdS$_{NR}$ (Table 18). The amounts of system components are: 10 mg CdS particles, 2.56 nmol CODH$_I$, 5 mL 0.35 M MES (pH 6.0); and the reaction vessels (initially under a gas atmosphere of 2% $CH_4$ in $CO_2$) were maintained at 20 ºC under visible light ($\lambda > 420$ nm, 45 mW cm$^{-2}$). It should be noted that the TONs for [CdS$_{NR}$-CODH$_I$] in (B) are *lower limits*, since the amount of co-attached enzyme is stated as *less than* 0.1 nmol (Table 18).

The plots in panel A indicate that the rate of CO production is faster at [$CdS_{QD}$-$CODH_I$] than [$CdS_{NR}$-$CODH_I$], but taking into account the amounts of enzyme attached to calculate TONs (panel B) reveals a different picture because very little $CODH_I$ (< 0.1 nmol) is co-attached with $CdS_{NR}$. The TOF (per $CODH_I$) of [$CdS_{NR}$-$CODH_I$], 1.23 ± 0.12 $s^{-1}$, is around 5 times faster than that of [$CdS_{QD}$-$CODH_I$]. Rates are summarised in Table 21.

**Table 21** Total CO production and turnover frequencies for [CdS-$CODH_I$] systems (pH 6.0) prepared using CdS particles of various morphology. The systems were run at 20 ºC, irradiated with visible light ($\lambda > 420$ nm, 45 mW $cm^{-2}$).

| | *(i.)* CO produced after 5 h / μmol | *(ii.)* TOF[a] [(mol CO) (mol $CODH_I$)$^{-1}$ $s^{-1}$] | *(iii.)* TOF[a] [(μmol CO) (g $CdS_{QD}$)$^{-1}$ $h^{-1}$] | *(iv.)* TOF[a] [(μmol CO) $mL^{-1}$ $h^{-1}$] |
|---|---|---|---|---|
| [$CdS_{QD}$-$CODH_I$] | 2.67 ± 0.28 | 0.25 ± 0.03 | 53.4 ± 5.6 | 0.11 ± 0.01 |
| [$CdS_{calc.}$-$CODH_I$] | *none detected* | - | - | - |
| [$CdS_{NR}$-$CODH_I$][b] | 2.21 ±0.22 | 1.23 ± 0.12 | 44.2 ± 4.4 | 0.09 ± 0.01 |

[a] Turnover frequencies are based on the total amount of CO in the reaction vessel headspace after 5 h (and therefore represent average rates over this time), and are calculated using the amounts of co-attached $CODH_I$ as indicated in Table 18. [b] The rates for [$CdS_{NR}$-$CODH_I$] are *lower limits*, since the amount of co-attached enzyme is stated as *less than* 0.1 nmol (Table 18).

## 6.5 CONCLUSIONS AND PERSPECTIVES

Returning to the original powder-based system, switching the nanoparticle material from P25 $TiO_2$ to pure anatase, ZnO, or $SrTiO_3$ (the latter two offer a significantly different surface charge compared to $TiO_2$, and $SrTiO_3$ also provides a greater thermodynamic driving force) led to no increase in the rate of photocatalysis. However, the use of CdS offers an immediate advantage in that it eliminates the requirement for a photosensitiser, and the system therefore becomes two-component instead of three-component. The investigation of systems using three different morphologies of CdS coupled to CODH was highly revealing, because the photocatalytic activities vary drastically. The nanorods couple with the enzyme to form a system offering a TOF of 1.23 mol CO (mol $CODH_I)^{-1}$ $s^{-1}$ at 20 ºC, which is an order of magnitude improvement on the photosensitised $TiO_2$ systems (even though this nanorod system was not as extensively optimised) and is the fastest rate achieved for photocatalytic $CO_2$ reduction in this Thesis. It is impossible to comment on the possibility of a different enzyme orientation (leading to faster electron transfer rates) being responsible, but the lower potential of the CdS conduction band (-0.87 V at pH 6) compared to anatase (-0.52 V) is likely to be important. An alternative reason might stem from the very small sizes of the CdS materials (having dimensions of just a few nm, in contrast to the larger $TiO_2$ particles of around 20 nm diameter), and associated improvements in electron transfer. The photoexcited electrons can transfer to the particle surface (whereupon they are trapped in enzyme molecules) more rapidly in smaller particles, thereby minimising the number of wasteful recombinations. The one-dimensional nature of the nanorods is also known to enable directed (vectorial) electron transport, reducing the possibilities of recombination events and facilitating more efficient charge transport.[401,402] There are also fewer grain boundaries in

smaller particles which can act as recombination sites, and this may be one of the reasons that the larger CdS units formed upon calcination of the quantum dots are inactive, even though CODH was found to adsorb on the surface. Such large particles (measuring hundreds of nm across) are also able to support a space-charge region, with the direction of bend bending channelling electrons away from the n-CdS surface.

The first part of this chapter took advantage of the efficiency – and *stability* – of catalysis that was observed at the $TiO_2$-CODH electrodes (section 4.2.2) in the demonstration of a simple photogeneration cell. The cell uses the $TiO_2$-$CODH_I$ electrode as a cathode and a dye-sensitised $TiO_2$ film as a photoanode, the result being an alternative configuration to the powder suspension approach so far described. This is not the first example of an enzyme being used in a photogeneration cell for $CO_2$ reduction: formate dehydrogenase has been used in a cell for selective $CO_2$ reduction using a p-InP photocathode, producing formate.[384] Methyl viologen was used as a mediator in this system: photoexcited electrons in the conduction band of InP reduced $MV^{2+}$ to $MV^{+\bullet}$, which shuttled electrons to formate dehydrogenase in the cell solution. The report indicates neither the duration of the photocatalytic experiment nor the TOF (although a turnover *number* of 21,000 is given), but replacing diffusion-controlled, mediated catalysis with direct electron transfer to enzyme molecules attached to the cathode surface must offer an advantage.

# REFERENCES

(1) Hoffert, M. I.; Caldeira, K.; Jain, A. K.; Haites, E. F.; Harvey, L. D. D.; Potter, S. D.; Schlesinger, M. E.; Schneider, S. H.; Watts, R. G.; Wigley, T. M. L.; Wuebbles, D. J. *Nature* **1998**, *395*, 881.

(2) *Key World Energy Statistics*; International Energy Agency, 2011.

(3) Lewis, N. S.; Crabtree, G.; Nozik, A. J.; Wasielewski, M. R.; Alivisatos, P. *Basic Research Needs for Solar Energy Utilization*; U.S. Department of Energy, 2005.

(4) Field, C. B.; Campbell, J. E.; Lobell, D. B. *Trends in Ecology & Evolution* **2008**, *23*, 65.

(5) Bertani, R. *Geothermics* **2012**, *41*, 1.

(6) Wiser, R.; Bolinger, M. *2010 Wind Technologies Market Report*; US Department of Energy, 2010.

(7) Jelle, B. P.; Breivik, C.; Rokenes, H. D. *Solar Energy Materials and Solar Cells* **2012**, *100*, 69.

(8) Razykov, T. M.; Ferekides, C. S.; Morel, D.; Stefanakos, E.; Ullal, H. S.; Upadhyaya, H. M. *Solar Energy* **2011**, *85*, 1580.

(9) *Best Research-Cell Efficiencies; http://www.nrel.gov/ncpv/images/efficiency_chart.jpg;* National Renewable Energy Laboratory, USA, accessed April 2012.

(10) *Clean Energy Trends 2012*; Clean Edge, 2012.

(11) *Global Market Outlook for Photovoltaics Until 2014*; European Photovoltaic Industry Association, 2010.

(12) Gratzel, M. *Nature* **2001**, *414*, 338.

(13) Gratzel, M. *Journal of Photochemistry and Photobiology, C: Photochemistry Reviews* **2003**, *4*, 145.

(14) Oregan, B.; Gratzel, M. *Nature* **1991**, *353*, 737.

(15) Kroon, R.; Lenes, M.; Hummelen, J. C.; Blom, P. W. M.; De Boer, B. *Polymer Reviews* **2008**, *48*, 531.

(16) Mayer, A. C.; Scully, S. R.; Hardin, B. E.; Rowell, M. W.; McGehee, M. D. *Materials Today* **2007**, *10*, 28.

(17) Yanmin, W.; Wei, W.; Xin, L.; Yijie, G. *Solar Energy Materials and Solar Cells* **2012**, *98*.

(18) Guenes, S.; Neugebauer, H.; Sariciftci, N. S. *Chemical Reviews* **2007**, *107*, 1324.

(19) Amjad, S.; Neelakrishnan, S.; Rudramoorthy, R. *Renewable & Sustainable Energy Reviews* **2010**, *14*, 1104.

(20) Bakhtiari, A. M. S. *Oil & Gas Journal* **2004**, *102*, 18.

(21) Duncan, R. C. *Oil & Gas Journal* **2003**, *101*, 18.

(22) Aleklett, K.; Hook, M.; Jakobsson, K.; Lardelli, M.; Snowden, S.; Soderbergh, B. *Energy Policy* **2010**, *38*, 1398.

(23) Abanades, J. C. *Chemical Engineering Journal* **2002**, *90*, 303.

(24) de Diego, L. F.; Garcia-Labiano, F.; Adanez, J.; Gayan, P.; Abad, A.; Corbella, B. M.; Palacios, J. M. *Fuel* **2004**, *83*, 1749.

(25) Gupta, H.; Fan, L. S. *Industrial & Engineering Chemistry Research* **2002**, *41*, 4035.

(26) Lackner, K. S. *Science* **2003**, *300*, 1677.

(27) Nikulshina, V.; Galvez, M. E.; Steinfeld, A. *Chemical Engineering Journal* **2007**, *129*, 75.

(28) Elschenbroich, C.; Salzer, A. *Organometallics, A Concise Introduction*; Second ed.; Wiley VCH.

(29) Waugh, K. C. *Catalysis Today* **1992**, *15*, 51.

(30) Steinfeld, A.; Meier, A. In *Encyclopedia of Energy* 2004; Vol. 5, p 623.

(31) Kodama, T. *Progress in Energy and Combustion Science* **2003**, *29*, 567.

(32) Kodama, T.; Gokon, N. *Chemical Reviews* **2007**, *107*, 4048.

(33) Licht, S. *Chemical Communications* **2005**, 4635.

(34) Galvez, M. E.; Loutzenhiser, P. G.; Hischier, I.; Steinfeld, A. *Energy & Fuels* **2008**, *22*, 3544.

(35) Loutzenhiser, P. G.; Galvez, M. E.; Hischier, I.; Stamatiou, A.; Frei, A.; Steinfeld, A. *Energy & Fuels* **2009**, *23*, 2832.

(36) http://www.abengoasolar.com/corp/web/en/nuestras_plantas/plantas_en_operacion/espana/PS10_la_primera_torre_comercial_del_mundo.html, accessed April 2012.

(37) http://www.acciona-na.com/About-Us/Our-Projects/U-S-/Nevada-Solar-One, accessed April 2012.

(38) Steinfeld, A.; Weimer, A. W. *Optics Express* **2010**, *18*, A100.

(39) Roeb, M.; Saeck, J. P.; Rietbrock, P.; Prahl, C.; Schreiber, H.; Neises, M.; de Oliveira, L.; Graf, D.; Ebert, M.; Reinalter, W.; Meyer-Gruenefeldt, M.; Sattler, C.; Lopez, A.; Vidal, A.; Elsberg, A.; Stobbe, P.; Jones, D.; Steele, A.; Lorentzou, S.; Pagkoura, C.; Zygogianni, A.; Agrafiotis, C.; Konstandopoulos, A. G. *Solar Energy* **2011**, *85*, 634.

(40) Stamatiou, A.; Loutzenhiser, P. G.; Steinfeld, A. *Chemistry of Materials* **2010**, *22*, 851.

(41) Furler, P.; Scheffe, J. R.; Steinfeld, A. *Energy & Environmental Science* **2012**, *5*, 6098.

(42) Amao, Y. *Chemcatchem* **2011**, *3*, 458.

(43) Li, X.; Fan, T. *Progress in Chemistry* **2011**, *23*, 1841.

(44) Gust, D.; Moore, T. A.; Moore, A. L. *Accounts of Chemical Research* **2009**, *42*, 1890.

(45) Balzani, V.; Credi, A.; Venturi, M. *Chemsuschem* **2008**, *1*, 26.

(46) Fukuzumi, S. *Physical Chemistry Chemical Physics* **2008**, *10*, 2283.

(47) Kalyanasundaram, K.; Graetzel, M. *Current Opinion in Biotechnology* **2010**, *21*, 298.

(48) Barber, J. *Chemical Society Reviews* **2009**, *38*, 185.

(49) Renger, G. *Primary Processes of Photosynthesis: Principles and Apparatus*; Cambridge: RSC Publishing, 2008.

(50) Pessarakli, M. *Handbook of Photosynthesis*; 2nd edition ed.; Taylor & Francis, 2005.

(51) Blankenship, R. E. *Molecular Mechanisms of Photosynthesis*; Oxford: Blackwell Science, 2002.

(52) Raines, C. A. *Photosynthesis Research* **2003**, *75*, 1.

(53) Kruse, O.; Rupprecht, J.; Mussgnug, J. H.; Dismukes, G. C.; Hankamer, B. *Photochemical & Photobiological Sciences* **2005**, *4*, 957.

(54) Ferreira, K. N.; Iverson, T. M.; Maghlaoui, K.; Barber, J.; Iwata, S. *Science* **2004**, *303*, 1831.

(55) Umena, Y.; Kawakami, K.; Shen, J.-R.; Kamiya, N. *Nature* **2011**, *473*, 55.

(56) Lewis, N. S.; Nocera, D. G. *Proceedings of the National Academy of Sciences of the United States of America* **2006**, *103*, 15729.

(57) Huynh, M. H. V.; Meyer, T. J. *Chemical Reviews* **2007**, *107*, 5004.

(58) Yamazaki, H.; Shouji, A.; Kajita, M.; Yagi, M. *Coordination Chemistry Reviews* **2010**, *254*, 2483.

(59) Hou, H. J. M. *Journal of Integrative Plant Biology* **2010**, *52*, 704.

(60) Crabtree, G. W.; Lewis, N. S. *Physics Today* **2007**, *60*, 37.

(61) Kanady, J. S.; Tsui, E. Y.; Day, M. W.; Agapie, T. *Science* **2011**, *333*, 733.

(62) Ruettinger, W.; Yagi, M.; Wolf, K.; Bernasek, S.; Dismukes, G. C. *Journal of the American Chemical Society* **2000**, *122*, 10353.

(63) Ruettinger, W. F.; Campana, C.; Dismukes, G. C. *Journal of the American Chemical Society* **1997**, *119*, 6670.

(64) Kanan, M. W.; Nocera, D. G. *Science* **2008**, *321*, 1072.

(65) Jones, J. H. *Platinum Metals Review* **2000**, *44*, 94.

(66) Sunley, G. J.; Watson, D. J. *Catalysis Today* **2000**, *58*, 293.

(67) Dekleva, T. W.; Forster, D. *Advances in Catalysis* **1986**, *34*, 81.

(68) Orchin, M.; Rupilius, W. *Catalysis Reviews* **1972**, *6*, 85.

(69) Roberts-Austen, W. C. *Nature* **1898**, *59*, 63.

(70) Mignard, D.; Sahibzada, M.; Duthie, J. M.; Whittington, H. W. *International Journal of Hydrogen Energy* **2003**, *28*, 455.

(71) Specht, M.; Staiss, F.; Bandi, A.; Weimer, T. *International Journal of Hydrogen Energy* **1998**, *23*, 387.

(72) Weimer, T.; Schaber, K.; Specht, M.; Bandi, A. *Energy Conversion and Management* **1996**, *37*, 1351.

(73) Hashimoto, K.; Habazaki, H.; Yamasaki, M.; Meguro, S.; Sasaki, T.; Katagiri, H.; Matsui, T.; Fujimura, K.; Izumiya, K.; Kumagai, N.; Akiyama, E. *Materials Science and Engineering a-Structural Materials Properties Microstructure and Processing* **2001**, *304*, 88.

(74) Olah, G. A.; Goeppert, A.; Prakash, G. K. S. *Journal of Organic Chemistry* **2009**, *74*, 487.

(75) An, X.; Li, J.; Zuo, Y.; Zhang, Q.; Wang, D.; Wang, J. *Catalysis Letters* **2007**, *118*, 264.

(76) Saito, M.; Murata, K. *Catalysis Surveys from Asia* **2004**, *8*, 285.

(77) Saito, M.; Takeuchi, M.; Fujitani, T.; Toyir, J.; Luo, S. C.; Wu, J. G.; Mabuse, H.; Ushikoshi, K.; Mori, K.; Watanabe, T. *Applied Organometallic Chemistry* **2000**, *14*, 763.

(78) Behr, A. *Chemical Engineering & Technology* **1987**, *10*, 16.

(79) Bard, A. J.; Parsons, R.; Jordan, J. *Standard Potentials in Aqueous Solution*; Mercel-Dekker (New York), 1985.

(80) Latimer, W. L. *The Oxidation States of the Elements and Their Potentials in Aqueous Solutions*; 2nd ed.; Prentice-Hall (USA), 1952.

(81) Benson, E. E.; Kubiak, C. P.; Sathrum, A. J.; Smieja, J. M. *Chemical Society Reviews* **2009**, *38*, 89.

(82) Dubois, D. L. In *Encyclopedia of Electrochemistry*; Wiley-VCH: 2006, p 202.

(83) Lilie, J.; Beck, G.; Henglein, A. *Berichte Der Bunsen-Gesellschaft Fur Physikalische Chemie* **1971**, *75*, 458.

(84) Amatore, C.; Nadjo, L.; Saveant, J. M. *Nouveau Journal De Chimie-New Journal of Chemistry* **1984**, *8*, 565.

(85) Amatore, C.; Saveant, J. M. *Journal of the American Chemical Society* **1981**, *103*, 5021.

(86) Hori, Y. In *Handbook of Fuel Cells*; Wiley-VCH: 2010; Vol. 2.

(87) Aulice Scibioh, M.; Viswanathan, B. *PINSA-A (Proceedings of the Indian National Science Academy) Part A (Physical Sciences)* **2004**, *70*.

(88) Hori, Y.; Wakebe, H.; Tsukamoto, T.; Koga, O. *Electrochimica Acta* **1994**, *39*, 1833.

(89) Hori, Y.; Kikuchi, K.; Murata, A.; Suzuki, S. *Chemistry Letters* **1986**, 897.

(90) Hori, Y.; Kikuchi, K.; Suzuki, S. *Chemistry Letters* **1985**, 1695.

(91) Hansen, J. B.; Hojlund Nielsen, P. E. In *Handbook of Heterogeneous Catalysis* 2008; Vol. 13, p 2920.

(92) Peterson, A. A.; Abild-Pedersen, F.; Studt, F.; Rossmeisl, J.; Norskov, J. K. *Energy & Environmental Science* **2010**, *3*, 1311.

(93) Jitaru, M. *Journal of the University of Chemical Technology and Metallurgy* **2007**, *42*, 333.

(94) Hawecker, J.; Lehn, J. M.; Ziessel, R. *Journal of the Chemical Society-Chemical Communications* **1984**, 328.

(95) Johnson, F. P. A.; George, M. W.; Hartl, F.; Turner, J. J. *Organometallics* **1996**, *15*, 3374.

(96) Christensen, P.; Hamnett, A.; Muir, A. V. G.; Timney, J. A.; Higgins, S. *Journal of the Chemical Society-Faraday Transactions* **1994**, *90*, 459.

(97) Ishida, H.; Tanaka, K.; Tanaka, T. *Organometallics* **1987**, *6*, 181.

(98) Collombdunandsauthier, M. N.; Deronzier, A.; Ziessel, R. *Inorganic Chemistry* **1994**, *33*, 2961.

(99) Haukka, M.; Kiviaho, J.; Ahlgren, M.; Pakkanen, T. A. *Organometallics* **1995**, *14*, 825.

(100) Chardonnoblat, S.; Collombdunandsauthier, M. N.; Deronzier, A.; Ziessel, R.; Zsoldos, D. *Inorganic Chemistry* **1994**, *33*, 4410.

(101) Tanaka, H.; Tzeng, B. C.; Nagao, H.; Peng, S. M.; Tanaka, K. *Inorganic Chemistry* **1993**, *32*, 1508.

(102) Bolinger, C. M.; Sullivan, B. P.; Conrad, D.; Gilbert, J. A.; Story, N.; Meyer, T. J. *Journal of the Chemical Society-Chemical Communications* **1985**, 796.

(103) Bruce, M. R. M.; Megehee, E.; Sullivan, B. P.; Thorp, H. H.; Otoole, T. R.; Downard, A.; Pugh, J. R.; Meyer, T. J. *Inorganic Chemistry* **1992**, *31*, 4864.

(104) Bruce, M. R. M.; Megehee, E.; Sullivan, B. P.; Thorp, H.; Otoole, T. R.; Downard, A.; Meyer, T. J. *Organometallics* **1988**, *7*, 238.

(105) Morris, A. J.; Meyer, G. J.; Fujita, E. *Accounts of Chemical Research* **2009**, *42*, 1983.

(106) Slater, S.; Wagenknecht, J. H. *Journal of the American Chemical Society* **1984**, *106*, 5367.

(107) Dubois, D. L.; Miedaner, A.; Haltiwanger, R. C. *Journal of the American Chemical Society* **1991**, *113*, 8753.

(108) Dubois, D. L. *Comments on Inorganic Chemistry* **1997**, *19*, 307.

(109) Miedaner, A.; Noll, B. C.; DuBois, D. L. *Organometallics* **1997**, *16*, 5779.

(110) Bernatis, P. R.; Miedaner, A.; Haltiwanger, R. C.; Dubois, D. L. *Organometallics* **1994**, *13*, 4835.

(111) Rakowski DuBois, M.; DuBois, D. L. *Accounts of Chemical Research* **2009**, *42*, 1974.

(112) Steffey, B. D.; Curtis, C. J.; Dubois, D. L. *Organometallics* **1995**, *14*, 4937.

(113) Fisher, B.; Eisenberg, R. *Journal of the American Chemical Society* **1980**, *102*, 7361.

(114) Beley, M.; Collin, J. P.; Ruppert, R.; Sauvage, J. P. *Journal of the Chemical Society-Chemical Communications* **1984**, 1315.

(115) Beley, M.; Collin, J. P.; Ruppert, R.; Sauvage, J. P. *Journal of the American Chemical Society* **1986**, *108*, 7461.

(116) Collin, J. P.; Jouaiti, A.; Sauvage, J. P. *Inorganic Chemistry* **1988**, *27*, 1986.

(117) Balazs, G. B.; Anson, F. C. *Journal of Electroanalytical Chemistry* **1993**, *361*, 149.

(118) Hammouche, M.; Lexa, D.; Saveant, J. M.; Momenteau, M. *Journal of Electroanalytical Chemistry* **1988**, *249*, 347.

(119) Bhugun, I.; Lexa, D.; Saveant, J. M. *Journal of the American Chemical Society* **1996**, *118*, 1769.

(120) Seshadri, G.; Lin, C.; Bocarsly, A. B. *Journal of Electroanalytical Chemistry* **1994**, *372*, 145.

(121) Cole, E. B.; Lakkaraju, P. S.; Rampulla, D. M.; Morris, A. J.; Abelev, E.; Bocarsly, A. B. *Journal of the American Chemical Society* **2010**, *132*, 11539.

(122) Morris, A. J.; McGibbon, R. T.; Bocarsly, A. B. *Chemsuschem* **2011**, *4*, 191.

(123) Barton, E. E.; Rampulla, D. M.; Bocarsly, A. B. *Journal of the American Chemical Society* **2008**, *130*, 6342.

(124) Ikeda, S.; Takagi, T.; Ito, K. *Bulletin of the Chemical Society of Japan* **1987**, *60*, 2517.

(125) Hoffmann, M. R.; Martin, S. T.; Choi, W. Y.; Bahnemann, D. W. *Chemical Reviews* **1995**, *95*, 69.

(126) Inoue, T.; Fujishima, A.; Konishi, S.; Honda, K. *Nature* **1979**, *277*, 637.

(127) Kumar, B.; Llorente, M.; Froehlich, J.; Dang, T.; Sathrum, A.; Kubiak, C. P. In *Annual Review of Physical Chemistry, Vol 63*; Johnson, M. A. M. T. J., Ed. 2012; Vol. 63, p 541.

(128) Burnside, S.; Moser, J. E.; Brooks, K.; Gratzel, M.; Cahen, D. *Journal of Physical Chemistry B* **1999**, *103*, 9328.

(129) Indrakanti, V. P.; Kubicki, J. D.; Schobert, H. H. *Energy & Environmental Science* **2009**, *2*, 745.

(130) Tseng, I. H.; Wu, J. C. S.; Chou, H. Y. *Journal of Catalysis* **2004**, *221*, 432.

(131) Yamashita, H.; Nishiguchi, H.; Kamada, N.; Anpo, M.; Teraoka, Y.; Hatano, H.; Ehara, S.; Kikui, K.; Palmisano, L.; Sclafani, A.; Schiavello, M.; Fox, M. A. *Research on Chemical Intermediates* **1994**, *20*, 815.

(132) Wu, J. C. S.; Chao-Wei, H. *Frontiers of Chemical Engineering in China* **2010**, *4*.

(133) Tseng, I. H.; Chang, W. C.; Wu, J. C. S. *Applied Catalysis B-Environmental* **2002**, *37*, 37.

(134) Tseng, I. H.; Wu, J. C. S. *Catalysis Today* **2004**, *97*, 113.

(135) Slamet; Nasution, H. W.; Purnama, E.; Kosela, S.; Gunlazuardi, J. *Catalysis Communications* **2005**, *6*, 313.

(136) Wu, J. C. S.; Lin, H. M. *International Journal of Photoenergy* **2005**, *7*, 115.

(137) Ozcan, O.; Yukruk, F.; Akkaya, E. U.; Uner, D. *Topics in Catalysis* **2007**, *44*, 523.

(138) Zhang, Q.-H.; Han, W.-D.; Hong, Y.-J.; Yu, J.-G. *Catalysis Today* **2009**, *148*, 335.

(139) Ishitani, O.; Inoue, C.; Suzuki, Y.; Ibusuki, T. *Journal of Photochemistry and Photobiology a-Chemistry* **1993**, *72*, 269.

(140) Yamashita, H.; Fujii, Y.; Ichihashi, Y.; Zhang, S. G.; Ikeue, K.; Park, D. R.; Koyano, K.; Tatsumi, T.; Anpo, M. *Catalysis Today* **1998**, *45*, 221.

(141) Sasirekha, N.; Basha, S. J. S.; Shanthi, K. *Applied Catalysis B-Environmental* **2006**, *62*, 169.

(142) Choi, W. Y.; Termin, A.; Hoffmann, M. R. *Journal of Physical Chemistry* **1994**, *98*, 13669.

(143) Asahi, R.; Morikawa, T.; Ohwaki, T.; Aoki, K.; Taga, Y. *Science* **2001**, *293*, 269.

(144) Chen, X.; Mao, S. S. *Chemical Reviews* **2007**, *107*, 2891.

(145) Serpone, N. *Journal of Physical Chemistry B* **2006**, *110*, 24287.

(146) Bessekhouad, Y.; Robert, D.; Weber, J. *Journal of Photochemistry and Photobiology a-Chemistry* **2004**, *163*, 569.

(147) Wu, L.; Yu, J. C.; Fu, X. Z. *Journal of Molecular Catalysis a-Chemical* **2006**, *244*, 25.

(148) Ji, S. M.; Jun, H.; Jang, J. S.; Son, H. C.; Borse, P. H.; Lee, J. S. *Journal of Photochemistry and Photobiology a-Chemistry* **2007**, *189*, 141.

(149) Ho, W. K.; Yu, J. C. *Journal of Molecular Catalysis a-Chemical* **2006**, *247*, 268.

(150) Liu, J.; Yang, R.; Li, S. *Rare Metals* **2006**, *25*, 636.

(151) Polo, A. S.; Itokazu, M. K.; Iha, N. Y. M. *Coordination Chemistry Reviews* **2004**, *248*, 1343.

(152) Chatterjee, D.; Mahata, A. *Applied Catalysis B-Environmental* **2001**, *33*, 119.

(153) Chatterjee, D.; Mahata, A. *Journal of Photochemistry and Photobiology a-Chemistry* **2002**, *153*, 199.

(154) Moon, J.; Yun, C. Y.; Chung, K. W.; Kang, M. S.; Yi, J. *Catalysis Today* **2003**, *87*, 77.

(155) Kaur, S.; Singh, V. *Ultrasonics Sonochemistry* **2007**, *14*, 531.

(156) Sayama, K.; Hara, K.; Mori, N.; Satsuki, M.; Suga, S.; Tsukagoshi, S.; Abe, Y.; Sugihara, H.; Arakawa, H. *Chemical Communications* **2000**, 1173.

(157) Kalyanasundaram, K. *Coordination Chemistry Reviews* **1982**, *46*, 159.

(158) Juris, A.; Balzani, V.; Barigelletti, F.; Campagna, S.; Belser, P.; Vonzelewsky, A. *Coordination Chemistry Reviews* **1988**, *84*, 85.

(159) Montalti, M.; Cedi, A.; Prodi, L.; Gandolfi, M. T. *Handbook of Photochemistry*; 3rd edition ed.; Taylor & Francis, 2006.

(160) Asbury, J. B.; Ellingson, R. J.; Ghosh, H. N.; Ferrere, S.; Nozik, A. J.; Lian, T. Q. *Journal of Physical Chemistry B* **1999**, *103*, 3110.

(161) Ramakrishna, G.; Jose, D. A.; Kumar, D. K.; Das, A.; Palit, D. K.; Ghosh, H. N. *Journal of Physical Chemistry B* **2005**, *109*, 15445.

(162) Kuang, D. B.; Ito, S.; Wenger, B.; Klein, C.; Moser, J. E.; Humphry-Baker, R.; Zakeeruddin, S. M.; Gratzel, M. *Journal of the American Chemical Society* **2006**, *128*, 4146.

(163) Benko, G.; Kallioinen, J.; Korppi-Tommola, J. E. I.; Yartsev, A. P.; Sundstrom, V. *Journal of the American Chemical Society* **2002**, *124*, 489.

(164) Kallioinen, J.; Benko, G.; Sundstrom, V.; Korppi-Tommola, J. E. I.; Yartsev, A. P. *Journal of Physical Chemistry B* **2002**, *106*, 4396.

(165) Koops, S. E.; O'Regan, B. C.; Barnes, P. R. F.; Durrant, J. R. *Journal of the American Chemical Society* **2009**, *131*, 4808.

(166) Damrauer, N. H.; Cerullo, G.; Yeh, A.; Boussie, T. R.; Shank, C. V.; McCusker, J. K. *Science* **1997**, *275*, 54.

(167) Ozcan, O.; Yukruk, F.; Akkaya, E. U.; Uner, D. *Applied Catalysis B-Environmental* **2007**, *71*, 291.

(168) Nguyen, T.-V.; Wu, J. C. S.; Chiou, C.-H. *Catalysis Communications* **2008**, *9*, 2073.

(169) Ragsdale, S. W. *Journal of Inorganic Biochemistry* **2007**, *101*, 1657.

(170) Sato, T.; Atomi, H. *Encyclopedia of Life Sciences*; Wiley and Sons, Ltd., 2010.

(171) Huegler, M.; Sievert, S. M. In *Annual Review of Marine Science, Vol 3*; Carlson, C. A. G. S. J., Ed. 2011; Vol. 3, p 261.

(172) Ragsdale, S. W.; Pierce, E. *Biochimica Et Biophysica Acta-Proteins and Proteomics* **2008**, *1784*, 1873.

(173) Ragsdale, S. W. In *Incredible Anaerobes: From Physiology to Genomics to Fuels*; Wiegel, J. M. R. J. A. M. W. W., Ed. 2008; Vol. 1125, p 129.

(174) Ragsdale, S. W.; Wood, H. G. *Journal of Biological Chemistry* **1985**, *260*, 3970.

(175) Doukov, T. I.; Iverson, T. M.; Seravalli, J.; Ragsdale, S. W.; Drennan, C. L. *Science* **2002**, *298*, 567.

(176) Ragsdale, S. W. *Critical Reviews in Biochemistry and Molecular Biology* **2004**, *39*, 165.

(177) Darnault, C.; Volbeda, A.; Kim, E. J.; Legrand, P.; Vernede, X.; Lindahl, P. A.; Fontecilla-Camps, J. C. *Nature Structural Biology* **2003**, *10*, 271.

(178) Doukov, T. I.; Blasiak, L. C.; Seravalli, J.; Ragsdale, S. W.; Drennan, C. L. *Biochemistry* **2008**, *47*, 3474.

(179) Dobbek, H.; Gremer, L.; Kiefersauer, R.; Huber, R.; Meyer, O. *Proceedings of the National Academy of Sciences of the United States of America* **2002**, *99*, 15971.

(180) Dobbek, H.; Gremer, L.; Meyer, O.; Huber, R. *Proceedings of the National Academy of Sciences of the United States of America* **1999**, *96*, 8884.

(181) Gnida, M.; Ferner, R.; Gremer, L.; Meyer, O.; Meyer-Klaucke, W. *Biochemistry* **2003**, *42*, 222.

(182) Lindahl, P. A. *Biochemistry* **2002**, *41*, 2097.

(183) Bender, G.; Pierce, E.; Hill, J. A.; Darty, J. E.; Ragsdale, S. W. *Metallomics* **2011**, *3*, 797.

(184) Svetlitchnyi, V.; Dobbek, H.; Meyer-Klaucke, W.; Meins, T.; Thiele, B.; Romer, P.; Huber, R.; Meyer, O. *Proceedings of the National Academy of Sciences of the United States of America* **2004**, *101*, 446.

(185) Svetlitchnyi, V.; Peschel, C.; Acker, G.; Meyer, O. *Journal of Bacteriology* **2001**, *183*, 5134.

(186) Meyer, O.; Gremer, L.; Ferner, R.; Ferner, M.; Dobbek, H.; Gnida, M.; Meyer-Klaucke, W.; Huber, R. *Biological Chemistry* **2000**, *381*, 865.

(187) Bonam, D.; Ludden, P. W. *Journal of Biological Chemistry* **1987**, *262*, 2980.

(188) Ragsdale, S. W.; Clark, J. E.; Ljungdahl, L. G.; Lundie, L. L.; Drake, H. L. *Journal of Biological Chemistry* **1983**, *258*, 2364.

(189) Svetlichny, V. A.; Sokolova, T. G.; Gerhardt, M.; Ringpfeil, M.; Kostrikina, N. A.; Zavarzin, G. A. *Systematic and Applied Microbiology* **1991**, *14*, 254.

(190) Wu, M.; Ren, Q. H.; Durkin, A. S.; Daugherty, S. C.; Brinkac, L. M.; Dodson, R. J.; Madupu, R.; Sullivan, S. A.; Kolonay, J. F.; Nelson, W. C.; Tallon, L. J.; Jones, K. M.; Ulrich, L. E.; Gonzalez, J. M.; Zhulin, I. B.; Robb, F. T.; Eisen, J. A. *Plos Genetics* **2005**, *1*, 563.

(191) Dobbek, H.; Svetlitchnyi, V.; Gremer, L.; Huber, R.; Meyer, O. *Science* **2001**, *293*, 1281.

(192) Jeoung, J.-H.; Dobbek, H. *Science* **2007**, *318*, 1461.

(193) Drennan, C. L.; Heo, J. Y.; Sintchak, M. D.; Schreiter, E.; Ludden, P. W. *Proceedings of the National Academy of Sciences of the United States of America* **2001**, *98*, 11973.

(194) Kung, Y.; Doukov, T. I.; Seravalli, J.; Ragsdale, S. W.; Drennan, C. L. *Biochemistry* **2009**, *48*, 7432.

(195) Kung, Y.; Drennan, C. L. *Current Opinion in Chemical Biology* **2011**, *15*, 276.

(196) Parkin, A.; Seravalli, J.; Vincent, K. A.; Ragsdale, S. W.; Armstrong, F. A. *Journal of the American Chemical Society* **2007**, *129*, 10328.

(197) Wang, V. C. C.; Pierce, E.; Ragsdale, S. W.; Armstrong, F. A. *Manuscript in preparation* **2012**.

(198) Feng, J.; Lindahl, P. A. *Journal of the American Chemical Society* **2004**, *126*, 9094.

(199) Feng, J.; Lindahl, P. A. *Biochemistry* **2004**, *43*, 1552.

(200) Heo, J.; Halbleib, C. M.; Ludden, P. W. *Proceedings of the National Academy of Sciences of the United States of America* **2001**, *98*, 7690.

(201) Heo, J.; Staples, C. R.; Ludden, P. W. *Biochemistry* **2001**, *40*, 7604.

(202) Spangler, N. J.; Lindahl, P. A.; Bandarian, V.; Ludden, P. W. *Journal of Biological Chemistry* **1996**, *271*, 7973.

(203) Ha, S.-W.; Korbas, M.; Klepsch, M.; Meyer-Klaucke, W.; Meyer, O.; Svetlitchnyi, V. *Journal of Biological Chemistry* **2007**, *282*, 10639.

(204) Gu, W. W.; Seravalli, J.; Ragsdale, S. W.; Cramer, S. P. *Biochemistry* **2004**, *43*, 9029.

(205) Anderson, M. E.; Lindahl, P. A. *Biochemistry* **1996**, *35*, 8371.

(206) Seravalli, J.; Kumar, M.; Lu, W. P.; Ragsdale, S. W. *Biochemistry* **1997**, *36*, 11241.

(207) Volbeda, A.; Fontecilla-Camps, J. C. *Dalton Transactions* **2005**, 3443.

(208) Huang, S. Q.; Lindahl, P. A.; Wang, C. Y.; Bennett, G. N.; Rudolph, F. B.; Hughes, J. B. *Applied and Environmental Microbiology* **2000**, *66*, 1474.

(209) Qiu, D.; Kumar, M.; Ragsdale, S. W.; Spiro, T. G. *Journal of the American Chemical Society* **1996**, *118*, 10429.

(210) Anderson, M. E.; Lindahl, P. A. *Biochemistry* **1994**, *33*, 8702.

(211) Anderson, M. E.; Derose, V. J.; Hoffman, B. M.; Lindahl, P. A. *Journal of the American Chemical Society* **1993**, *115*, 12204.

(212) Dobbek, H.; Svetlitchnyi, V.; Liss, J.; Meyer, O. *Journal of the American Chemical Society* **2004**, *126*, 5382.

(213) Kumar, M.; Lu, W. P.; Liu, L. F.; Ragsdale, S. W. *Journal of the American Chemical Society* **1993**, *115*, 11646.

(214) Lindahl, P. A.; Munck, E.; Ragsdale, S. W. *Journal of Biological Chemistry* **1990**, *265*, 3873.

(215) Hu, Z. G.; Spangler, N. J.; Anderson, M. E.; Xia, J. Q.; Ludden, P. W.; Lindahl, P. A.; Munch, E. *Journal of the American Chemical Society* **1996**, *118*, 830.

(216) Russell, W. K.; Lindahl, P. A. *Biochemistry* **1998**, *37*, 10016.

(217) Gong, W.; Hao, B.; Wei, Z.; Ferguson, D. J., Jr.; Tallant, T.; Krzycki, J. A.; Chan, M. K. *Proceedings of the National Academy of Sciences of the United States of America* **2008**, *105*, 9558.

(218) Jeoung, J.-H.; Dobbek, H. *Journal of the American Chemical Society* **2009**, *131*, 9922.

(219) Chen, J. Y.; Huang, S.; Seravalli, J.; Gutzman, H.; Swartz, D. J.; Ragsdale, S. W.; Bagley, K. A. *Biochemistry* **2003**, *42*, 14822.

(220) Kim, E. J.; Feng, J.; Bramlett, M. R.; Lindahl, P. A. *Biochemistry* **2004**, *43*, 5728.

(221) Cammack, R.; Frey, M.; Robson, R. *Hydrogen as a Fuel: Learning from Nature*; Taylor and Francis: London, 2001.

(222) Lide, D. E. *CRC Handbook of Chemistry and Physics*; CRC Press, 1997.

(223) Burgess, B. K.; Lowe, D. J. *Chemical Reviews* **1996**, *96*, 2983.

(224) Madamwar, D.; Garg, N.; Shah, V. *World Journal of Microbiology & Biotechnology* **2000**, *16*, 757.

(225) Vignais, P. M.; Colbeau, A. *Current Issues in Molecular Biology* **2004**, *6*, 159.

(226) Frey, M. *Chembiochem* **2002**, *3*, 153.

(227) Conrad, R. *Microbiological Reviews* **1996**, *60*, 609.

(228) Ford, T.; Mitchell, R. *Advances in Microbial Ecology* **1990**, *11*, 231.

(229) Lukey, M. J., University of Oxford, 2010.

(230) Lukey, M. J.; Parkin, A.; Roessler, M. M.; Murphy, B. J.; Harmer, J.; Palmer, T.; Sargent, F.; Armstrong, F. A. *Journal of Biological Chemistry* **2010**, *285*, 3928.

(231) Volbeda, A.; Charon, M. H.; Piras, C.; Hatchikian, E. C.; Frey, M.; Fontecillacamps, J. C. *Nature* **1995**, *373*, 580.

(232) Fontecilla-Camps, J. C.; Volbeda, A.; Cavazza, C.; Nicolet, Y. *Chemical Reviews* **2007**, *107*, 4273.

(233) De lacey, A. L.; Fernandez, V. M.; Rousset, M.; Cammack, R. *Chemical Reviews* **2007**, *107*, 4304.

(234) Page, C. C.; Moser, C. C.; Chen, X. X.; Dutton, P. L. *Nature* **1999**, *402*, 47.

(235) Volbeda, A.; Garcin, E.; Piras, C.; deLacey, A. L.; Fernandez, V. M.; Hatchikian, E. C.; Frey, M.; FontecillaCamps, J. C. *Journal of the American Chemical Society* **1996**, *118*, 12989.

(236) Happe, R. P.; Roseboom, W.; Pierik, A. J.; Albracht, S. P. J.; Bagley, K. A. *Nature* **1997**, *385*, 126.

(237) Bleijlevens, B.; van Broekhuizen, F. A.; De Lacey, A. L.; Roseboom, W.; Fernandez, V. M.; Albracht, S. P. J. *Journal of Biological Inorganic Chemistry* **2004**, *9*, 743.

(238) Bagley, K. A.; Vangarderen, C. J.; Chen, M.; Duin, E. C.; Albracht, S. P. J.; Woodruff, W. H. *Biochemistry* **1994**, *33*, 9229.

(239) Bagley, K. A.; Duin, E. C.; Roseboom, W.; Albracht, S. P. J.; Woodruff, W. H. *Biochemistry* **1995**, *34*, 5527.

(240) Stein, M.; van Lenthe, E.; Baerends, E. J.; Lubitz, W. *Journal of the American Chemical Society* **2001**, *123*, 5839.

(241) Volbeda, A.; Martin, L.; Cavazza, C.; Matho, M.; Faber, B. W.; Roseboom, W.; Albracht, S. P. J.; Garcin, E.; Rousset, M.; Fontecilla-Camps, J. C. *Journal of Biological Inorganic Chemistry* **2005**, *10*, 239.

(242) Lamle, S. E.; Albracht, S. P. J.; Armstrong, F. A. *Journal of the American Chemical Society* **2004**, *126*, 14899.

(243) Vincent, K. A.; Parkin, A.; Armstrong, F. A. *Chemical Reviews* **2007**, *107*, 4366.

(244) Wiberg, E. *Inorganic Chemistry*; Academic Press, 2001.

(245) Evans, D. J.; Pickett, C. J. *Chemical Society Reviews* **2003**, *32*, 268.

(246) Darensbourg, M. Y.; Lyon, E. J.; Smee, J. J. *Coordination Chemistry Reviews* **2000**, *206*, 533.

(247) Lubitz, W.; Reijerse, E.; van Gastel, M. *Chemical Reviews* **2007**, *107*, 4331.

(248) Huyett, J. E.; Carepo, M.; Pamplona, A.; Franco, R.; Moura, I.; Moura, J. J. G.; Hoffman, B. M. *Journal of the American Chemical Society* **1997**, *119*, 9291.

(249) Keith, J. M.; Hall, M. B. *Inorganic Chemistry* **2010**, *49*, 6378.

(250) Siegbahn, P. E. M.; Tye, J. W.; Hall, M. B. *Chemical Reviews* **2007**, *107*, 4414.

(251) Armstrong, F. A. *Biochemical Society Transactions* **1999**, *27*, 206.

(252) Hirst, J. *Biochimica Et Biophysica Acta-Bioenergetics* **2006**, *1757*, 225.

(253) Leger, C.; Elliott, S. J.; Hoke, K. R.; Jeuken, L. J. C.; Jones, A. K.; Armstrong, F. A. *Biochemistry* **2003**, *42*, 8653.

(254) Vincent, K. A.; Armstrong, F. A. *Inorganic Chemistry* **2005**, *44*, 798.

(255) Blanford, C. F.; Armstrong, F. A. *Journal of Solid State Electrochemistry* **2006**, *10*, 826.

(256) Hirst, J.; Armstrong, F. A. *Analytical Chemistry* **1998**, *70*, 5062.

(257) Sucheta, A.; Cammack, R.; Weiner, J.; Armstrong, F. A. *Biochemistry* **1993**, *32*, 5455.

(258) Bard, A. J.; Faulkner, L. *Electrochemical Methods: Fundamentals and Applications*; 2nd Edition ed.; John Wiley & Sons, Inc., 2001.

(259) Fisher, A. C. *Electrode Dynamics*; Oxford University Press: New York, U.S.A., 1996.

(260) http://www.basinc.com/products/ec/faqele.html#Ref_Type., Accessed June 2012.

(261) Barbe, C. J.; Arendse, F.; Comte, P.; Jirousek, M.; Lenzmann, F.; Shklover, V.; Gratzel, M. *Journal of the American Ceramic Society* **1997**, *80*, 3157.

(262) Pace, C. N.; Vajdos, F.; Fee, L.; Grimsley, G.; Gray, T. *Protein Science* **1995**, *4*, 2411.

(263) Montalti, M.; Wadhwa, S.; Kim, W. Y.; Kipp, R. A.; Schmehl, R. H. *Inorganic Chemistry* **2000**, *39*, 76.

(264) Cheng, Y.; Wang, Y. S.; Bao, F.; Chen, D. Q. *Journal of Physical Chemistry B* **2006**, *110*, 9448.

(265) Joo, J.; Na, H. B.; Yu, T.; Yu, J. H.; Kim, Y. W.; Wu, F. X.; Zhang, J. Z.; Hyeon, T. *Journal of the American Chemical Society* **2003**, *125*, 11100.

(266) Trammell, S. A.; Moss, J. A.; Yang, J. C.; Nakhle, B. M.; Slate, C. A.; Odobel, F.; Sykora, M.; Erickson, B. W.; Meyer, T. J. *Inorganic Chemistry* **1999**, *38*, 3665.

(267) Gibbons, B. H.; Edsall, J. T. *Journal of Biological Chemistry* **1963**, *238*, 3502.

(268) Ratnasamy, C.; Wagner, J. P. *Catalysis Reviews-Science and Engineering* **2009**, *51*, 325.

(269) Holladay, J. D.; Hu, J.; King, D. L.; Wang, Y. *Catalysis Today* **2009**, *139*, 244.

(270) Newsome, D. S. *Catalysis Reviews-Science and Engineering* **1980**, *21*, 275.

(271) Spencer, M. S. *Topics in Catalysis* **1999**, *8*, 259.

(272) Dry, M. E. *Catalysis Today* **2002**, *71*, 227.

(273) Cheng, X.; Shi, Z.; Glass, N.; Zhang, L.; Zhang, J.; Song, D.; Liu, Z.-S.; Wang, H.; Shen, J. *Journal of Power Sources* **2007**, *165*, 739.

(274) Li, Q. F.; He, R. H.; Gao, J. A.; Jensen, J. O.; Bjerrum, N. J. *Journal of the Electrochemical Society* **2003**, *150*, A1599.

(275) Song, C. S. *Catalysis Today* **2002**, *77*, 17.

(276) Gonzalez, J. C.; Gonzalez, M. G.; Laborde, M. A.; Moreno, N. *Applied Catalysis* **1986**, *20*, 3.

(277) Lloyd, L.; Ridler, D. E.; Twigg, M. V. *Water gas shift reaction, Catalyst Handbook*; 2nd ed.; Mansion Publishing House: London, 1996.

(278) Campbell, C. T.; Koel, B. E. *Surface Science* **1987**, *183*, 100.

(279) Oki, S.; Mezaki, R. *Journal of Physical Chemistry* **1973**, *77*, 1601.

(280) Oki, S.; Mezaki, R. *Journal of Physical Chemistry* **1973**, *77*, 447.

(281) Boreskov, G. K. *Discussions of the Faraday Society* **1966**, 263.

(282) Tinkle, M.; Dumesic, J. A. *Journal of Catalysis* **1987**, *103*, 65.

(283) Kulkova, N. V.; Temkin, M. I. *Zhurnal Fizicheskoi Khimii* **1949**, *23*, 695.

(284) Temkin, M. I.; Eley, D. D., Pines, H., Weisz, P. B., Eds.; Academic Press: New York: 1979, p 173.

(285) Koryabkina, N. A.; Phatak, A. A.; Ruettinger, W. F.; Farrauto, R. J.; Ribeiro, F. H. *Journal of Catalysis* **2003**, *217*, 233.

(286) Rhodes, C.; Hutchings, G. J.; Ward, A. M. *Catalysis Today* **1995**, *23*, 43.

(287) Tanaka, Y.; Utaka, T.; Kikuchi, R.; Takeguchi, T.; Sasaki, K.; Eguchi, K. *Journal of Catalysis* **2003**, *215*, 271.

(288) Utaka, T.; Sekizawa, K.; Eguchi, K. *Applied Catalysis a-General* **2000**, *194*, 21.

(289) Twigg, M. V.; Spencer, M. S. *Applied Catalysis a-General* **2001**, *212*, 161.

(290) Laniecki, M.; Malecka-Grycz, M.; Domka, F. *Applied Catalysis a-General* **2000**, *196*, 293.

(291) Kantschewa, M.; Delannay, F.; Jeziorowski, H.; Delgado, E.; Eder, S.; Ertl, G.; Knozinger, H. *Journal of Catalysis* **1984**, *87*, 482.

(292) Nickolov, R. N.; Edreva-Kardjieva, R. M.; Kafedjiysky, V. J.; Nikolova, D. A.; Stankova, N. B.; Mehandjiev, D. R. *Applied Catalysis a-General* **2000**, *190*, 191.

(293) Andreeva, D.; Idakiev, V.; Tabakova, T.; Andreev, A. *Journal of Catalysis* **1996**, *158*, 354.

(294) Luengnaruemitchai, A.; Osuwan, S.; Gulari, E. *Catalysis Communications* **2003**, *4*, 215.

(295) Andreeva, D.; Idakiev, V.; Tabakova, T.; Ilieva, L.; Falaras, P.; Bourlinos, A.; Travlos, A. *Catalysis Today* **2002**, *72*, 51.

(296) Boccuzzi, F.; Chiorino, A.; Manzoli, M.; Andreeva, D.; Tabakova, T.; Ilieva, L.; Iadakiev, V. *Catalysis Today* **2002**, *75*, 169.

(297) Goerke, O.; Pfeifer, P.; Schubert, K. *Applied Catalysis a-General* **2004**, *263*, 11.

(298) Shido, T.; Iwasawa, Y. *Journal of Catalysis* **1993**, *141*, 71.

(299) Panagiotopoulou, P.; Papavasiliou, J.; Avgouropoulos, G.; Ioannides, T.; Kondarides, D. I. *Chemical Engineering Journal* **2007**, *134*, 16.

(300) Goguet, A.; Meunier, F.; Breen, J. P.; Burch, R.; Petch, M. I.; Ghenciu, A. F. *Journal of Catalysis* **2004**, *226*, 382.

(301) Germani, G.; Schuurman, Y. *Aiche Journal* **2006**, *52*, 1806.

(302) Xue, E.; Okeeffe, M.; Ross, J. R. H. *Catalysis Today* **1996**, *30*, 107.

(303) Panagiotopoulou, P.; Kondarides, D. I. *Journal of Catalysis* **2004**, *225*, 327.

(304) Wang, X.; Gorte, R. J.; Wagner, J. P. *Journal of Catalysis* **2002**, *212*, 225.

(305) http://automobiles.honda.com/fcx-clarity/, accessed May 2012.

(306) Burch, R. *Physical Chemistry Chemical Physics* **2006**, *8*, 5483.

(307) Panagiotopoulou, P.; Kondarides, D. I. *Catalysis Today* **2006**, *112*, 49.

(308) Thinon, O.; Diehl, F.; Avenier, P.; Schuurman, Y. *Catalysis Today* **2008**, *137*, 29.

(309) Shido, T.; Iwasawa, Y. *Journal of Catalysis* **1992**, *136*, 493.

(310) Jacobs, G.; Chenu, E.; Patterson, P. M.; Williams, L.; Sparks, D.; Thomas, G.; Davis, B. H. *Applied Catalysis a-General* **2004**, *258*, 203.

(311) Jacobs, G.; Patterson, P. A.; Graham, U. M.; Sparks, D. E.; Davis, B. H. *Applied Catalysis a-General* **2004**, *269*, 63.

(312) Kim, C. H.; Thompson, L. T. *Journal of Catalysis* **2005**, *230*, 66.

(313) Sokolova, T. G.; Jeanthon, C.; Kostrikina, N. A.; Chernyh, N. A.; Lebedinsky, A. V.; Stackebrandt, E.; Bonch-Osmolovskaya, E. A. *Extremophiles* **2004**, *8*, 317.

(314) Fardeau, M. L.; Salinas, M. B.; L'Haridon, S.; Jeanthon, C.; Verhe, F.; Cayol, J. L.; Patel, B. K. C.; Garcia, J. L.; Ollivier, B. *International Journal of Systematic and Evolutionary Microbiology* **2004**, *54*, 467.

(315) Sokolova, T. G.; Kostrikina, N. A.; Chernyh, N. A.; Tourova, T. P.; Kolganova, T. V.; Bonch-Osmolovskaya, E. A. *International Journal of Systematic and Evolutionary Microbiology* **2002**, *52*, 1961.

(316) Sokolova, T. G.; Gonzalez, J. M.; Kostrikina, N. A.; Chernyh, N. A.; Tourova, T. P.; Kato, C.; Bonch-Osmolovskaya, E. A.; Robb, F. T. *International Journal of Systematic and Evolutionary Microbiology* **2001**, *51*, 141.

(317) Vincent, K. A.; Li, X.; Blanford, C. F.; Belsey, N. A.; Weiner, J. H.; Armstrong, F. A. *Nature chemical biology* **2007**, *3*, 761.

(318) Hexter, S. V.; Grey, F.; Happe, T.; Climent, V.; Armstrong, F. A. *Proceedings of the National Academy of Sciences of the United States of America* **2012**, In press.

(319) Hla, S. S.; Park, D.; Duffy, G. J.; Edwards, J. H.; Roberts, D. G.; Ilyushechkin, A.; Morpeth, L. D.; Nguyen, T. *Chemical Engineering Journal* **2009**, *146*, 148.

(320) Lei, Y.; Cant, N. W.; Trimm, D. L. *Catalysis Letters* **2005**, *103*, 133.

(321) Goldet, G.; Wait, A. F.; Cracknell, J. A.; Vincent, K. A.; Ludwig, M.; Lenz, O.; Friedrich, B.; Armstrong, F. A. *Journal of the American Chemical Society* **2008**, *130*, 11106.

(322) DeLacey, A. L.; Stadler, C.; Fernandez, V. M.; Hatchikian, E. C.; Fan, H. J.; Li, S. H.; Hall, M. B. *Journal of Biological Inorganic Chemistry* **2002**, *7*, 318.

(323) Greco, C.; Bruschi, M.; Heimdal, J.; Fantucci, P.; De Gioia, L.; Ryde, U. *Inorganic Chemistry* **2007**, *46*, 7256.

(324) Pandelia, M.-E.; Ogata, H.; Currell, L. J.; Flores, M.; Lubitz, W. *Biochimica Et Biophysica Acta-Bioenergetics* **2010**, *1797*, 304.

(325) Purec, L.; Krasna, A. I.; Rittenberg, D. *Biochemistry* **1962**, *1*, 270.

(326) Maness, P. C.; Smolinski, S.; Dillon, A. C.; Heben, M. J.; Weaver, P. F. *Applied and Environmental Microbiology* **2002**, *68*, 2633.

(327) Tachibana, Y.; Moser, J. E.; Gratzel, M.; Klug, D. R.; Durrant, J. R. *Journal of Physical Chemistry* **1996**, *100*, 20056.

(328) Pechy, P.; Rotzinger, F. P.; Nazeeruddin, M. K.; Kohle, O.; Zakeeruddin, S. M.; Humphrybaker, R.; Gratzel, M. *Journal of the Chemical Society-Chemical Communications* **1995**, 65.

(329) Gillaizeau-Gauthier, I.; Odobel, F.; Alebbi, M.; Argazzi, R.; Costa, E.; Bignozzi, C. A.; Qu, P.; Meyer, G. J. *Inorganic Chemistry* **2001**, *40*, 6073.

(330) Bae, E. Y.; Choi, W. Y.; Park, J. W.; Shin, H. S.; Kim, S. B.; Lee, J. S. *Journal of Physical Chemistry B* **2004**, *108*, 14093.

(331) Degussa *Technical Information, AEROXIDE and AEROPERL Titanium Dioxide as Photocatalyst*, 2005.

(332) Hagfeldt, A.; Gratzel, M. *Chemical Reviews* **1995**, *95*, 49.

(333) Kavan, L.; Gratzel, M.; Gilbert, S. E.; Klemenz, C.; Scheel, H. J. *Journal of the American Chemical Society* **1996**, *118*, 6716.

(334) Park, H.; Bae, E.; Lee, J. J.; Park, J.; Choi, W. *Journal of Physical Chemistry B* **2006**, *110*, 8740.

(335) Geren, L.; Durham, B.; Millett, F. In *Methods in Enzymology, Vol 456: Mitochondrial Function, Part A: Mitochondrial Electron Transport Complexes and Reactive Oxygen Species*; Allison, W. S., Ed. 2009; Vol. 456, p 507.

(336) Engelbrekt, C.; Sorensen, K. H.; Zhang, J.; Welinder, A. C.; Jensen, P. S.; Ulstrup, J. *Journal of Materials Chemistry* **2009**, *19*, 7839.

(337) Habib, A.; Tabata, M.; Wu, Y. G. *Bulletin of the Chemical Society of Japan* **2005**, *78*, 262.

(338) Zhao, G. H.; Chasteen, N. D. *Analytical Biochemistry* **2006**, *349*, 262.

(339) Li, Q. W.; Luo, G. A.; Feng, J. *Electroanalysis* **2001**, *13*, 359.

(340) Deere, J.; Magner, E.; Wall, J. G.; Hodnett, B. K. *Journal of Physical Chemistry B* **2002**, *106*, 7340.

(341) McKenzie, K. J.; Marken, F. *Langmuir* **2003**, *19*, 4327.

(342) Meier, K. R.; Gratzel, M. *Chemphyschem* **2002**, *3*, 371.

(343) Topoglidis, E.; Campbell, C. J.; Cass, A. E. G.; Durrant, J. R. *Langmuir* **2001**, *17*, 7899.

(344) Topoglidis, E.; Campbell, C. J.; Palomares, E.; Durrant, J. R. *Chemical Communications* **2002**, 1518.

(345) Topoglidis, E.; Cass, A. E. G.; Gilardi, G.; Sadeghi, S.; Beaumont, N.; Durrant, J. R. *Analytical Chemistry* **1998**, *70*, 5111.

(346) Topoglidis, E.; Cass, A. E. G.; O'Regan, B.; Durrant, J. R. *Journal of Electroanalytical Chemistry* **2001**, *517*, 20.

(347) Topoglidis, E.; Lutz, T.; Durrant, J. R.; Palomares, E. *Bioelectrochemistry* **2008**, *74*, 142.

(348) Topoglidis, E.; Lutz, T.; Willis, R. L.; Barnett, C. J.; Cass, A. E.; Durrant, J. R. *Faraday discussions* **2000**, 35.

(349) Bacsa, R. R.; Kiwi, J. *Applied Catalysis B-Environmental* **1998**, *16*, 19.

(350) Fabregat-Santiago, F.; Mora-Sero, I.; Garcia-Belmonte, G.; Bisquert, J. *Journal of Physical Chemistry B* **2003**, *107*, 758.

(351) Kavan, L.; Gratzel, M.; Rathousky, J.; Zukal, A. *Journal of the Electrochemical Society* **1996**, *143*, 394.

(352) Goldet, G.; Brandmayr, C.; Stripp, S. T.; Happe, T.; Cavazza, C.; Fontecilla-Camps, J. C.; Armstrong, F. A. *Journal of the American Chemical Society* **2009**, *131*, 14979.

(353) Wang, V. C. C. *DPhil thesis* **2013**.

(354) Bott, A. W. *Current Separation* **1998**, *17*, 87.

(355) Rothenberger, G.; Fitzmaurice, D.; Gratzel, M. *Journal of Physical Chemistry* **1992**, *96*, 5983.

(356) Haug, H.; Koch, S. W. *Quantum Theory of the Optical and Electronic Properties of Semiconductors*; World Scientific, 1994.

(357) Yun, H. J.; Lee, H.; Joo, J. B.; Kim, N. D.; Yi, J. *Journal of Nanoscience and Nanotechnology* **2011**, *11*, 1688.

(358) Grimme, R. A.; Lubner, C. E.; Bryant, D. A.; Golbeck, J. H. *Journal of the American Chemical Society* **2008**, *130*, 6308.

(359) Lubner, C. E.; Grimme, R.; Bryant, D. A.; Golbeck, J. H. *Biochemistry* **2010**, *49*, 404.

(360) Lubner, C. E.; Knoerzer, P.; Silva, P. J. N.; Vincent, K. A.; Happe, T.; Bryant, D. A.; Golbeck, J. H. *Biochemistry* **2010**, *49*, 10264.

(361) Thampi, K. R.; Kiwi, J.; Gratzel, M. *Nature* **1987**, *327*, 506.

(362) Kaneco, S.; Kurimoto, H.; Shimizu, Y.; Ohta, K.; Mizuno, T. *Energy* **1999**, *24*, 21.

(363) Kaneco, S.; Shimizu, Y.; Ohta, K.; Mizuno, T. *Journal of Photochemistry and Photobiology a-Chemistry* **1998**, *115*, 223.

(364) Slamet; Nasution, H. W.; Purnama, E.; Riyani, K.; Gunlazuardi, J. *World Applied Sciences Journal* **2009**, *6*, 112.

(365) Yang, H.-C.; Lin, H.-Y.; Chien, Y.-S.; Wu, J. C.-S.; Wu, H.-H. *Catalysis Letters* **2009**, *131*, 381.

(366) Michaelis, L.; Hill, E. S. *Jour Gen Physiol* **1933**, *16*, 859.

(367) Yoshikawa, N.; Kimura, T.; Kawase, Y. *Canadian Journal of Chemical Engineering* **2003**, *81*, 719.

(368) Kimura, T.; Yoshikawa, N.; Matsumura, N.; Kawase, Y. *Journal of Environmental Science and Health Part a-Toxic/Hazardous Substances & Environmental Engineering* **2004**, *39*, 2867.

(369) Rajh, T.; Nedeljkovic, J. M.; Chen, L. X.; Poluektov, O.; Thurnauer, M. C. *Journal of Physical Chemistry B* **1999**, *103*, 3515.

(370) Myller, A. T.; Karhe, J. J.; Pakkanen, T. T. *Applied Surface Science* **2010**, *257*, 1616.

(371) Devault, D. *Quarterly Reviews of Biophysics* **1980**, *13*, 387.

(372) Xie, J. M.; Schultz, P. G. *Current Opinion in Chemical Biology* **2005**, *9*, 548.

(373) Yamashita, H.; Kamada, N.; He, H.; Tanaka, K.; Ehara, S.; Anpo, M. *Chemistry Letters* **1994**, 855.

(374) Anpo, M.; Yamashita, H.; Ichihashi, Y.; Fujii, Y.; Honda, M. *Journal of Physical Chemistry B* **1997**, *101*, 2632.

(375) Ikeue, K.; Yamashita, H.; Anpo, M.; Takewaki, T. *Journal of Physical Chemistry B* **2001**, *105*, 8350.

(376) Ikeue, K.; Nozaki, S.; Ogawa, M.; Anpo, M. *Catalysis Letters* **2002**, *80*, 111.

(377) Wu, J. C. S.; Lin, H. M.; Lai, C. L. *Applied Catalysis a-General* **2005**, *296*, 194.

(378) Nguyen, T.-V.; Wu, J. C. S. *Solar Energy Materials and Solar Cells* **2008**, *92*, 864.

(379) Li, X.; Liu, H.; Luo, D.; Li, J.; Huang, Y.; Li, H.; Fang, Y.; Xu, Y.; Zhu, L. *Chemical Engineering Journal* **2012**, *180*, 151.

(380) Heller, A. *Accounts of Chemical Research* **1981**, *14*, 154.

(381) Hambourger, M.; Gervaldo, M.; Svedruzic, D.; King, P. W.; Gust, D.; Ghirardi, M.; Moore, A. L.; Moore, T. A. *Journal of the American Chemical Society* **2008**, *130*, 2015.

(382) Halmann, M. *Nature* **1978**, *275*, 115.

(383) Aurianblajeni, B.; Halmann, M.; Manassen, J. *Solar Energy Materials* **1983**, *8*, 425.

(384) LaTempa, T. J.; Rani, S.; Bao, N.; Grimes, C. A. *Nanoscale* **2012**, *4*, 2245.

(385) Kosmulski, M. *Advances in Colloid and Interface Science* **2002**, *99*, 255.

(386) Serpone, N.; Maruthamuthu, P.; Pichat, P.; Pelizzetti, E.; Hidaka, H. *Journal of Photochemistry and Photobiology a-Chemistry* **1995**, *85*, 247.

(387) Butler, M. A.; Ginley, D. S. *Journal of the Electrochemical Society* **1978**, *125*, 228.

(388) Bolts, J. M.; Wrighton, M. S. *Journal of Physical Chemistry* **1976**, *80*, 2641.

(389) Xu, Y.; Schoonen, M. A. A. *American Mineralogist* **2000**, *85*, 543.

(390) Mathew, X.; Enriquez, J. P.; Romeo, A.; Tiwari, A. N. *Solar Energy* **2004**, *77*, 831.

(391) Fang, Z.; Wang, X. C.; wu, H. C.; Zhao, C. Z. *International Journal of Photoenergy* **2011**.

(392) Britt, J.; Ferekides, C. *Applied Physics Letters* **1993**, *62*, 2851.

(393) Mitchell, K. W.; Fahrenbruch, A. L.; Bube, R. H. *Journal of Applied Physics* **1977**, *48*, 4365.

(394) Weller, H. *Angewandte Chemie-International Edition in English* **1993**, *32*, 41.

(395) Wilcoxon, J. P.; Abrams, B. L. *Chemical Society Reviews* **2006**, *35*, 1162.

(396) Dhyani, H.; Ali, M. A.; Pandey, M. K.; Malhotra, B. D.; Sen, P. *Journal of Materials Chemistry* **2012**, *22*, 4970.

(397) Tang, L.; Zhu, Y.; Yang, X.; Sun, J.; Li, C. *Biosensors & Bioelectronics* **2008**, *24*, 319.

(398) Huang, Y. X.; Zhang, W. J.; Xiao, H.; Li, G. X. *Biosensors & Bioelectronics* **2005**, *21*, 817.

(399) Zhou, H.; Gan, X.; Liu, T.; Yang, Q. L.; Li, G. X. *Journal of Biochemical and Biophysical Methods* **2005**, *64*, 38.

(400) Veinot, J. G. C.; Galloro, J.; Pugliese, L.; Pestrin, R.; Pietro, W. J. *Chemistry of Materials* **1999**, *11*, 642.

(401) Zhang, Q.; Cao, G. *Nano Today* **2011**, *6*, 91.

(402) Zhu, K.; Neale, N. R.; Miedaner, A.; Frank, A. J. *Nano Letters* **2007**, *7*, 69.

# APPENDICES

## A1 USE OF THE NERNST EQUATION TO CALCULATE $E(2H^+/H_2)$ AND $E(CO_2/CO)$ AT PARTICULAR CONDITIONS

The Nernst equation is: $E_{eq} = E^{o} - (RT/n\mathrm{F})\ln Q$

where R is the gas constant, F is the Faraday constant and Q is the reaction quotient. This equation can be used to predict $E_{eq}$ for redox reactions at specified conditions.

In this way it can be used to predict the potential at which the voltammograms in Figure 5A of chapter X intersect the line of zero current. For the *Ec*Hyd2 voltammogram (blue), under a gas mixture of 50% $H_2$, 50% $N_2$ (1 atm. total pressure) at 30 ºC, pH 6:

$$E_{eq} = E^{o} - (RT/n\mathrm{F})\ln Q$$

$Q = a_{H2}/a_{H+}^2$, where $a$ is the activity. Here, $a_{H2} = 0.5$, and $a_{H+}$ (at pH 6) = $10^{-6}$

$$E_{eq} = 0 - (8.314\ \mathrm{J\ K^{-1}\ mol^{-1}} \times 313\ \mathrm{K} / 2 \times 96485\ \mathrm{C\ mol^{-1}})\ln(0.5/10^{-12})$$

$$E_{eq} = -0.36\ \mathrm{V}$$

Similarly, for the $CODH_I$ voltammogram (red) in Figure 5A of chapter X, under a gas mixture of 50% CO, 50% $CO_2$ (1 atm. total pressure) at 30 ºC, pH 6:

$$E_{eq} = E^{o} - (RT/n\mathrm{F})\ln Q$$

$Q = a_{CO} \times a_{H2O} / a_{CO2} \times a_{H+}^2$. Here, $a_{CO} = 0.5$, $a_{CO2} = 0.5$, $a_{H2O} = 1$ and $a_{H+}$ (at pH 6) = $10^{-6}$

$$E_{eq} = -0.11 - (8.314\ \mathrm{J\ K^{-1}\ mol^{-1}} \times 313\ \mathrm{K} / 2 \times 96485\ \mathrm{C\ mol^{-1}})\ln(0.5 \times 1/0.5 \times 10^{-12})$$

$$E_{eq} = -0.48\ \mathrm{V}$$

## A2 THE EYRING EQUATION

The Eyring equation relates the rate constant for a reaction to the standard entropy and enthalpy of activation ($\Delta S^{\ddagger}$ and $\Delta H^{\ddagger}$). It stems from Transition State Theory; that is, the assumption that a reaction between species A and species B proceeds through the formation of a transition state species $C^{\ddagger}$, which goes on to form products P:

$$A + B \text{ Ý } C^{\ddagger} \rightarrow P$$

The Eyring equation is as follows:

$$k = \frac{k_B T}{h} \exp\left(\frac{\Delta S}{R}\right) \exp\left(\frac{-\Delta H^{\ddagger}}{RT}\right)$$

where $k$ is the rate constant for the reaction, $k_B$ is Boltzmann's constant, $T$ is temperature (in Kelvin), h is Planck's constant, R is the gas constant, $\Delta S^{\ddagger}$ is the standard entropy of activation and $\Delta H^{\ddagger}$ is the standard enthalpy of activation. Dividing both sides by $T$ and applying a logarithmic transformation yields:

$$\ln\left(\frac{k}{T}\right) = \frac{-\Delta H^{\ddagger}}{RT} + \ln\left(\frac{k_B}{h}\right) + \frac{\Delta S}{R}$$

Therefore, a plot of $\ln(k/T)$ *vs.* $1/T$ gives a straight line of gradient $(-\Delta H^{\ddagger}/R)$. $\Delta S^{\ddagger}$ can be determined from the $y$-intercept.

## A3 CALCULATION FOR APPROXIMATE NUMBER OF ENZYME UNITS AND PHOTOSENSITISER UNITS PER $TiO_2$ NANOPARTICLE

| | |
|---|---|
| BET surface area of P25 $TiO_2$ | 50 $m^2$ $g^{-1}$ |
| surface area of 5 mg P25 $TiO_2$ | = 5 x $10^{-3}$ g x 50 $m^2$ $g^{-1}$ = 0.25 $m^2$ |
| surface area of one nanoparticle (assuming sphere of diameter 21 nm) | = $4\pi r^2$ = 1.39 x $10^{-15}$ $m^2$ |
| number of nanoparticles in 5 mg sample | 0.25 $m^2$ / 1.39 x $10^{-15}$ $m^2$ = 1.8 x $10^{14}$ |
| 2.40 nmol **CODH** attach to this sample, so **approximate number on each nanoparticle** | = 2.40 x $10^{-9}$ x 6.0 x $10^{23}$ / 1.8 x $10^{14}$ = **8** |
| 56 nmol **RuP** attach to this sample, so **approximate number on each nanoparticle** | = 56 x $10^{-9}$ x 6.0 x $10^{23}$ / 1.8 x $10^{14}$ ≈ **200** |

# A4 EFFECT OF ORDER OF FUNTIONALISATION OF $TiO_2$ NANOPARTICLES ON $CO_2$ PHOTOREDUCTION ACTIVITY

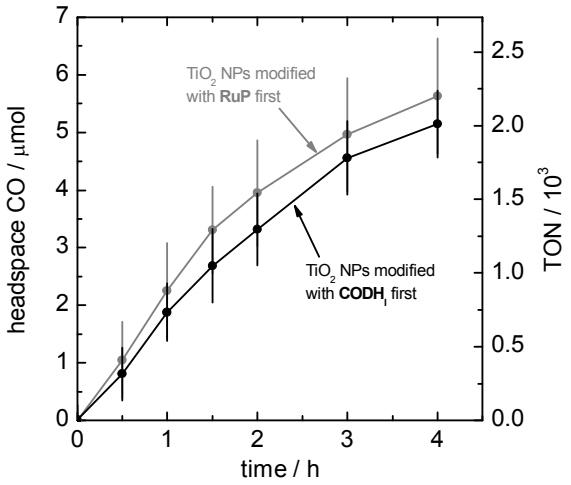


**Influence of order of functionalisation of nanoparticles on $CO_2$ photoreduction at [RuP-$TiO_2$-$CODH_I$].** The black plot shows the production of CO by the system prepared according to the *standard procedure* (*i.e.* nanoparticles were firstly modified with $CODH_I$, and secondly by RuP) and run under *standard conditions*. The grey plot shows CO production by a system in which the P25 $TiO_2$ nanoparticles have been prepared according to the standard procedure, except that the order of functionalisation was switched (*i.e.* nanoparticles were firstly modified by RuP, and secondly by $CODH_I$). The amounts of system components were: 5 mg P25 $TiO_2$, 2.56 nmol $CODH_I$, 56 nmol RuP, 5 mL 0.20 M MES (pH 6.0); and the reaction vessels (initially under a gas atmosphere of 2% $CH_4$ in $CO_2$) were maintained at 20 ºC while under visible light ($\lambda > 420$ nm, 45 mW $cm^{-2}$).

## A5 TEM IMAGES OF $TiO_2$ NANOPARTICLES FUNCTIONALISED WITH $CODH_I$ AND RuP

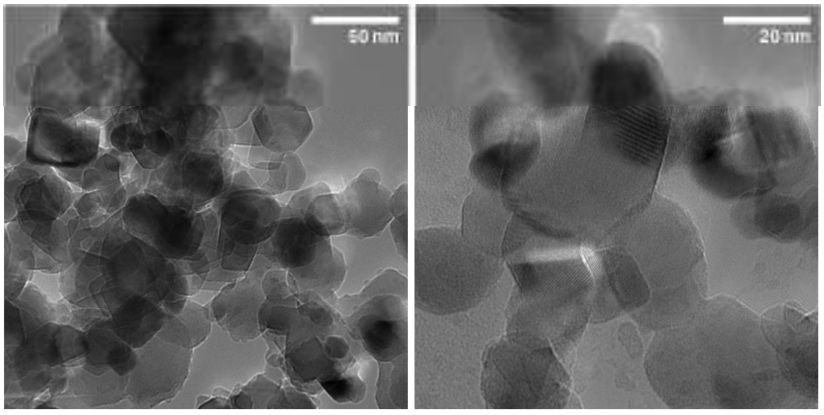


TEM images of [RuP-$TiO_2$-$CODH_I$].

## A6 CALCULATION FOR APPROXIMATE MAXIMUM POSSIBLE COVERAGE OF CODH PER $TiO_2$ NANOPARTICLE

| | |
|---|---|
| dimensions of enzyme molecule | 88 Å x 63 Å x 60 Å |
| assuming 'footprint' dimensions of 88 Å x 60 Å, 'footprint area | = $5.28 \times 10^{-17}$ $m^2$ $molecule^{-1}$ |
| BET surface area of P25 $TiO_2$ | 50 $m^2$ $g^{-1}$ |
| surface area of 5 mg P25 $TiO_2$ | = $5 \times 10^{-3}$ g x 50 $m^2$ $g^{-1}$ = 0.25 $m^2$ |
| **Upper limit for monolayer coverage** | = 0.25 $m^2$ / $5.28 \times 10^{-17}$ $m^2$ $molecule^{-1}$ = 4.73 x $10^{15}$ molecules **= 7.9 nmol** |

## A7 UV-VIS SPECTRA TO DETECT FOR CODH AND RuP DESORPTION FROM $TiO_2$ NANOPARTICLES OVER 4 h

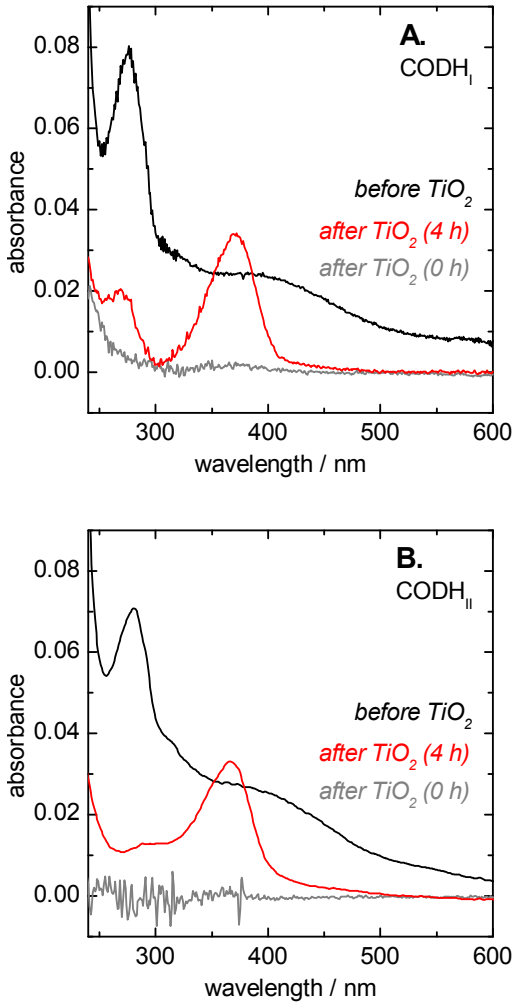


UV-vis absorbance spectra of 2.56 nmol $CODH_I$ (A) or $CODH_{II}$ (B) in 5 mL 0.20 M MES buffer (pH 6.0) before (black) and after (grey) adsorption onto 5 mg P25 $TiO_2$ nanoparticles in suspension. The red spectra were collected after stirring the nanoparticle suspensions for 4 h. Before collecting the grey and red spectra, the nanoparticles were separated from the solution by centrifugation and filtration. The peak at 370 nm is believed to be due to fragments of $TiO_2$.

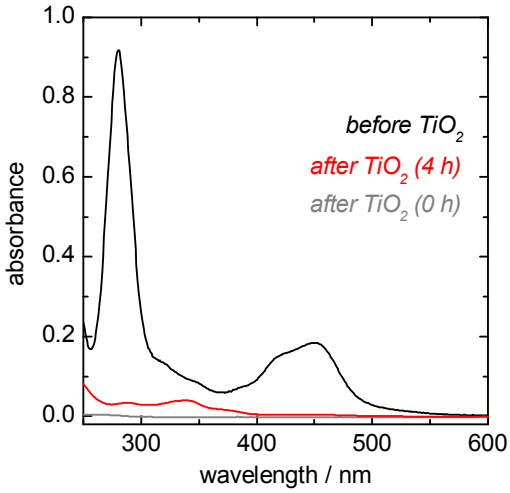


UV-vis absorbance spectra of 56 nmol RuP in 5 mL 0.20 M MES buffer (pH 6.0) before (black) and after (grey) adsorption onto 5 mg P25 $TiO_2$ nanoparticles in suspension. The red spectrum was collected after stirring the suspension of nanoparticles for 4 h. Before collecting the grey and red spectra, the nanoparticles were separated from the solution by centrifugation and filtration.

## A8 APPROXIMATE CALCULATION OF QUANTUM YIELD FOR PHOTOREDUCTION OF $CO_2$ TO CO BY THE [RuP-$TiO_2$-$CODH_I$] *STANDARD SYSTEM*

This calculation is based upon a light intensity at the reaction vessel of 45 mW $cm^{-2}$, and an illuminated facial area of 6 $cm^{-2}$.

| | |
|---|---|
| frequency of 420 nm light, ν | = $c/\lambda$ = 3.0 x $10^{8}$ / 420 x $10^{-9}$ = 7.14 x $10^{14}$ $s^{-1}$ |
| energy of 420 nm photon, E | = h$\nu$ = 6.6 x $10^{-34}$ Js x 7.14 x $10^{14}$ $s^{-1}$ = 4.71 x $10^{-19}$ J |
| total light power at reaction vessel | = 45 x $10^{-3}$ W $cm^{-2}$ x 6 $cm^{2}$ = 0.27 W |
| total light energy arriving at reaction vessel in 4 h | = 0.27 W x 4 h x 60 min $h^{-1}$ x 60 s $min^{-1}$ = 3888 J |
| corresponding number of photons | = 3888 J / 4.71 x $10^{-19}$ J $photon^{-1}$ = 8.25 x $10^{21}$ photons |
| number of electrons used to produce 5.15 µmol CO | = 5.15 x $10^{-6}$ mol x 6.0 x $10^{23}$ molecules $mol^{-1}$ x 2 electrons $molecule^{-1}$ = 6.18 x $10^{18}$ electrons |
| **quantum yield** | = 6.20 x $10^{18}$ / 8.25 x $10^{21}$ **= 7.5 x $10^{-4}$** |

# A9 UV-VIS SPECTROPHOTOMETRY SHOWING ATTACHMENT OF RuP TO A $TiO_2$ THIN FILM

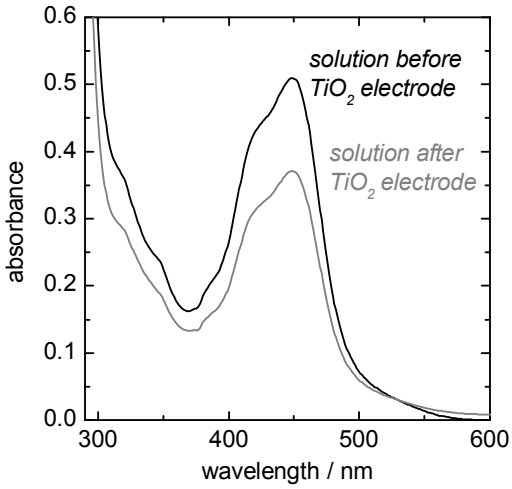


UV-vis absorbance spectra of 5 mL of 40 μM RuP in 0.20 M MES buffer (pH 6.0) before (black) and after (grey) adsorption onto a thin film (~ 25 x 10 mm) of P25 $TiO_2$ nanoparticles. The difference in intensity of the 455 nm absorption corresponds to the attachment of RuP to the $TiO_2$ thin film.

# A10 UV-VIS DATA FOR ATTACHMENT OF CODH AND RuP TO DIFFERENT SEMICONDUCTORS

Spectrophotometric determination of uptake of $CODH_I$ and RuP to different semiconductor nanoparticles. For $CODH_I$, the extent of attachment was determined from the difference in absorbance at 280 nm between a 5 mL solution containing 2.56 nmol $CODH_I$ before (0.0766 ± 0.0016) and after exposure to nanoparticles.[a] For RuP, the extent of attachment was determined from the difference in absorbance at 455 nm between a 5mL solution containing 56 nmol RuP before (0.177 ± 0.003) and after exposure to nanoparticles.

| semiconductor | $A_{455}$ *After* adsorption of RuP to nanoparticles | amount of RuP attached to nanoparticles[b] / nmol | $A_{280}$ *After* adsorption of $CODH_I$ to nanoparticles | amount of enzyme attached to nanoparticles[c] / nmol |
|---|---|---|---|---|
| P25 $TiO_2$ | 0.0036 ± 0.003 | 54.9 ± 1.13 | 0.0047 ± 0.001 | 2.40 ± 0.03 |
| anatase $TiO_2$ | 0.0059 ± 0.006 | 54.1 ± 1.77 | 0.0130 ± 0.005 | 2.13 ± 0.15 |
| ZnO | 0.0644 ± 0.001 | 35.7 ± 0.43 | 0.0171 ± 0.011 | 1.99 ± 0.37 |
| $SrTiO_3$ | 0.0254 ± 0.022 | 48.2 ± 6.87 | 0.0021 ± 0.001 | 2.49 ± 0.02 |

[a] Nanoparticle concentrations were 5 mg nanoparticles / 5 mL 0.20 M MES buffer solution (pH 6.0), except for ZnO (20 mg nanoparticles / 5 mL buffer solution). [b] Out of a maximum of 56 nmol added. [c] Out of a maximum of 2.56 nmol added. Adsorption amounts were calculated using UV-vis absorption data from separate solutions of $CODH_I$ (0.51 μM) and RuP (11.2 μM) before and after exposure to nanoparticles. The concentration of nanoparticles matches those used in the $CO_2$ photoreduction experiments shown in Figure 82.

## A11 XRD PATTERN OF CdS QUANTUM DOTS BEFORE AND AFTER CALCINATION